



TAMPEREEN TEKNILLINEN YLIOPISTO
TAMPERE UNIVERSITY OF TECHNOLOGY

Adnan Qamar Kiayani

**Modeling and Digital Mitigation of Transmitter
Imperfections in Radio Communication Systems**



Julkaisu 1332 • Publication 1332

Tampere 2015

Tampereen teknillinen yliopisto. Julkaisu 1332
Tampere University of Technology. Publication 1332

Adnan Qamar Kiayani

Modeling and Digital Mitigation of Transmitter Imperfections in Radio Communication Systems

Thesis for the degree of Doctor of Science in Technology to be presented with due permission for public examination and criticism in Tietotalo Building, Auditorium TB104, at Tampere University of Technology, on the 27th of October 2015, at 12 noon.

Tampereen teknillinen yliopisto - Tampere University of Technology
Tampere 2015

Supervisor

Mikko Valkama, Dr. Tech., Professor
Department of Electronics and Communications Engineering
Tampere University of Technology
Tampere, Finland

Instructor

Lauri Anttila, Dr. Tech.
Department of Electronics and Communications Engineering
Tampere University of Technology
Tampere, Finland

Pre-examiners

Thomas Eriksson, Ph.D., Professor
Department of Signals and Systems
Chalmers University of Technology
Gothenburg, Sweden

Mario Huemer, Ph. D, Professor
Institute of Signal Processing
Johannes Kepler University
Linz, Austria

Opponents

Ulf Gustavsson, Ph. D.
Ericsson Research
Gothenburg, Sweden

ISBN 978-952-15-3598-7 (printed)
ISBN 978-952-15-3616-8 (PDF)
ISSN 1459-2045

Abstract

To satisfy the continuously growing demands for higher data rates, modern radio communication systems employ larger bandwidths and more complex waveforms. Furthermore, radio devices are expected to support a rich mixture of standards such as cellular networks, wireless local-area networks, wireless personal area networks, positioning and navigation systems, etc. In general, a “smart” device should be flexible to support all these requirements while being portable, cheap, and energy efficient. These seemingly conflicting expectations impose stringent radio frequency (RF) design challenges which, in turn, call for their proper understanding as well as developing cost-effective solutions to address them. The direct-conversion transceiver architecture is an appealing analog front-end for flexible and multi-standard radio systems. However, it is sensitive to various circuit impairments, and modern communication systems based on multi-carrier waveforms such as Orthogonal Frequency Division Multiplexing (OFDM) and Orthogonal Frequency Division Multiple Access (OFDMA) are particularly vulnerable to RF front-end non-idealities.

This thesis addresses the modeling and digital mitigation of selected transmitter (TX) RF impairments in radio communication devices. The contributions can be divided into two areas. First, new modeling and digital mitigation techniques are proposed for two essential front-end impairments in direct-conversion architecture-based OFDM and OFDMA systems, namely inphase and quadrature phase (I/Q) imbalance and carrier frequency offset (CFO). Both joint and de-coupled estimation and compensation schemes for frequency-selective TX I/Q imbalance and channel distortions are proposed for OFDM systems, to be adopted on the receiver side. Then, in the context of uplink OFDMA and Single Carrier FDMA (SC-FDMA), which are the air interface technologies of the 3rd Generation Partnership Project (3GPP) Long Term Evolution (LTE) and LTE-Advanced systems, joint estimation and equalization techniques of RF impairments and channel

distortions are proposed. Here, the challenging multi-user uplink scenario with unequal received power levels is investigated where I/Q imbalance causes inter-user interference. A joint mirror subcarrier processing-based minimum mean-square error (MMSE) equalizer with an arbitrary number of receiver antennas is formulated to effectively handle the mirror sub-band users of different power levels. Furthermore, the joint channel and impairments filter responses are efficiently approximated with polynomial-based basis function models, and the parameters of basis functions are estimated with the reference signals conforming to the LTE uplink sub-frame structure. The resulting receiver concept adopting the proposed techniques enables improved link performance without modifying the design of RF transceivers.

Second, digital baseband mitigation solutions are developed for the TX leakage signal-induced self-interference in frequency division duplex (FDD) transceivers. In FDD transceivers, a duplexer is used to connect the TX and receiver (RX) chains to a common antenna while also providing isolation to the receiver chain against the powerful transmit signal. In general, the continuous miniaturization of hardware and adoption of larger bandwidths through carrier aggregation type non-contiguous allocations complicates achieving sufficient TX-RX isolation. Here, two different effects of the transmitter leakage signal are investigated. The first is TX out-of-band (OOB) emissions and TX spurious emissions at own receiver band, due to the transmitter nonlinearity, and the second is nonlinearity of down-converter in the RX that generates second-order intermodulation distortion (IMD2) due to the TX in-band leakage signal. This work shows that the transmitter leakage signal-induced interference depends on an equivalent *leakage channel* that models the TX path non-idealities, duplexer filter responses, and the RX path non-idealities. The work proposes algorithms that operate in the digital baseband of the transceiver to estimate the TX-RX non-idealities and the duplexer filter responses, and subsequently regenerating and canceling the self-interference, thereby potentially relaxing the TX-RX isolation requirements as well as increasing the transceiver flexibility.

Overall, this thesis provides useful signal models to understand the implications of different RF non-idealities and proposes compensation solutions to cope with certain RF impairments. This is complemented with extensive computer simulations and practical RF measurements to validate their application in real-world radio transceivers.

Preface

The research work reported in this thesis was carried out during the years 2010 – 2015 at the Department of Electronics and Communications Engineering, Tampere University of Technology (TUT), Tampere, Finland.

Foremost, I wish to express my sincere gratitude to my two supervisors Prof. Mikko Valkama and Dr. Lauri Anttila for their support, guidance, and patience during my research work. I am grateful to Prof. Mikko Valkama for two reasons. First, for giving me the opportunity to work under his supervision, which influenced me in numerous ways. Secondly, for teaching me to aim for excellence and conduct high-quality research. He has been a great supervisor and an outstanding role-model. I am indebted to Dr. Lauri Anttila for his infinite tolerance with my questions and incomplete drafts. Without his wise guidance, this thesis would have not been possible. I also express my sincere gratitude to Prof. Markku Renfors, the former head of the department, for creating an inspiring working environment.

I am grateful to my thesis pre-examiners Prof. Thomas Eriksson from Chalmers University of Technology, Sweden, and Prof. Mario Huemer from Johannes Kepler University, Austria, for their insightful comments that have helped me to greatly improve the quality of the thesis. I also wish to thank Dr. Ulf Gustavsson from Ericsson Research, Sweden, for agreeing to act as the opponents on my dissertation defense.

The thesis was financially supported by the Tampere Doctoral Programme in Information Science and Engineering (TISE), the TUT Graduate School, the Finnish Foundation for Technology Promotion (TES), the Finnish Funding Agency for Technology and Innovation (Tekes; under the project “Cross-Layer Modeling and Design of Energy-Aware Cognitive Radio Networks (CREAM)”), the Academy of Finland (under the project 251138 “Digitally-Enhanced RF for Cognitive Radio Devices”), the Linz Center of Mechatronics (LCM) in the framework of the

Austrian COMET-K2 programme, all of which are gratefully acknowledged. Additionally, I would like to express my gratitude to the Nokia Foundation for generous research grant.

I would like to thank my colleagues at the department for the pleasant atmosphere, and devote special thanks to the following colleagues in the RF-DSP research group: Dr. Yaning Zou (co-author), M. Sc. Vesa Lehtinen (co-author), M. Sc. Mahmoud Abdelaziz (co-author), Dr. Sener Dikmese, Dr. Ahmet Gökçeoglu, Dr. Jaakko Marttila, M. Sc. Markus Allén, M. Sc. Janis Werner, M. Sc. Syed Fahad, M. Sc. Mulugeta Fikadu, M. Sc. Simran Singh, and M. Sc. Timo Huusari. I should also thank M. Sc. Joonas Sæ for his friendship and being my Finnish translator. Furthermore, the administrative support of Ulla Siltaloppi, Sari Kinnari, Kirsi Viitanen, Heli Ahlfors, and Soile Lönnqvist is also appreciated.

Thanks to the teams developing open-source softwares such as MikTEX, TeXnic-Center, and OpenOffice, which greatly helped in writing scientific papers and also this thesis.

Special thanks to all Pakistani friends and families in Finland and back at home. Although hard to acknowledge all, I especially wish to thank Usman “Ustad G”, Waqas, Usman Sheikh, Asif, Farhan, Bashir, and Mohsin for their moral support and friendship.

I would like to give my deepest gratitude to my parents, brothers, sister, bhabis, and family. Thanks to my mother and father, for their unconditional love, prayers, sacrifices, and for believing in the importance of education. They deserve the dedication to this work. Last but not least, I would like to give my warmest thanks to: my dear wife Asma Taiba for her continuous support and love, for teaching me that there is life outside the office, and for making our house a pleasant home; and my lovely daughter, Azwa Adnan, for giving meaning to our life.

Tampere, September 2015

Adnan Kiayani

Contents

Abstract	i
Preface	iii
Contents	v
List of Publications	ix
Abbreviations	xi
Mathematical Notations	xv
1 Introduction	1
1.1 Background and Motivation	1
1.2 Scope and Contributions of the Thesis	3
1.3 Outline of the Thesis	5
2 Recent Advances and Challenges in Mobile Radio Communica-	7
tions	
2.1 An Overview of 3GPP Long Term Evolution-Advanced	8
2.1.1 LTE Downlink: OFDMA	9
2.1.2 LTE Uplink: SC-FDMA	11
2.1.3 Carrier Aggregation and Multi-Cluster Transmission	13
2.2 Basics of I/Q Signal Processing	13
2.3 TX RF Imperfections in Direct-Conversion OFDM/OFDMA Sys-	
tems: Influence and Signal Models	16
2.3.1 I/Q Imbalance	16
2.3.2 Carrier Frequency Offset	19
2.4 Transmit Signal Leakage Problems in FDD Transceivers	21
2.4.1 TX Spectral Emissions at Own RX Band due to Nonlinear	
PA	22
2.4.2 Effect of Transmit In-band Signal Leakage on Direct-Conversion	
RX Performance	26

3	Digital Compensation of RF Impairments in OFDM and Uplink OFDMA/SC-FDMA Systems	29
3.1	Compensation of Frequency-Selective TX I/Q Imbalance and Channel Distortions in OFDM Systems	30
3.1.1	Signal and System Model	30
3.1.2	Estimation and Compensation of TX I/Q Imbalance and Channel Distortions	32
3.1.2.1	Joint Estimation and Compensation of TX I/Q Imbalance and Channel Distortions with Preamble Pilot Structure	33
3.1.2.2	De-coupled Estimation and Compensation of TX I/Q Imbalance and Channel Distortions with Sparse Pilot Structure	34
3.2	Compensation of TX RF Impairments and Channel Distortions in Multi-User Uplink OFDMA and SC-FDMA Systems	36
3.2.1	Multi-User Uplink Signal Models Under RF Impairments and Channel Distortions	39
3.2.2	Joint Equalization of TX I/Q Imbalances, Small CFOs, and Channel Distortions	42
3.2.2.1	Extension to Multi-Antenna Receiver	43
3.2.3	Efficient Response Representation with Basis Functions	45
3.2.4	Least-Squares Parameters Estimation with LTE Uplink Reference Signals	46
3.3	Simulation and Measurement Examples	47
3.3.1	TX I/Q Imbalance and Channel Distortions in OFDM Systems	48
3.3.2	TX I/Q Imbalances, Small CFOs, and Channel Distortions in Multi-User SC-FDMA Systems	51
4	Modeling and Digital Mitigation of TX Leakage Signals in Frequency Division Duplex Transceivers	55
4.1	Digital Mitigation of TX Spectral Emissions at Own RX Band	56
4.1.1	TX Out-of-Band Emissions at Own RX Band	56
4.1.1.1	Proposed OOB Emissions Regeneration and Cancellation	58
4.1.2	TX Spurious Emissions at Own RX Band: Special Case of Noncontiguous CA Transmission	60
4.1.2.1	Proposed Spurious IMD Regeneration and Cancellation	63
4.1.3	Comparison of Computational Complexity	65
4.2	Digital Mitigation of TX In-band Leakage Signal-Induced Second-Order Intermodulation Distortion	66
4.2.1	Signal Models with Nonlinear TX-RX Components and Frequency-Selective Duplexer Filter	67
4.2.2	Parallel Augmented Volterra Model for TX In-band Leakage-Induced IMD2	68

4.2.3	Proposed IMD2 Regeneration and Cancellation	70
4.3	Simulation and Measurement Examples	71
4.3.1	Digital Mitigation of Unwanted TX Spectral Emissions at RX Band	71
4.3.2	Digital Mitigation of TX In-band Leakage Signal-Induced IMD2	76
5	Conclusions	79
	Bibliography	83
	Publications	97

List of Publications

This thesis is composed of the following seven publications.

- [P1] A. Kiayani, L. Anttila, Y. Zou, and M. Valkama, “Hybrid Time/Frequency Domain Compensator for RF Impairments in OFDM Systems,” in *Proceedings of IEEE 22nd International Symposium on Personal Indoor and Mobile Radio Communications (PIMRC 2011)*, pp. 1948-1952, Sept. 2011.
- [P2] A. Kiayani, L. Anttila, Y. Zou, and M. Valkama, “Advanced Receiver Design for Mitigating Multiple RF Impairments in OFDM Systems: Algorithms and RF Measurements,” *Journal of Electrical and Computer Engineering*, vol. 2012, article ID 730537, 16 pages, 2012.
- [P3] A. Kiayani, L. Anttila, and M. Valkama, “Mobile Transmitters I/Q Imbalances in LTE Uplink: Analysis and Digital Mitigation,” in *Proceedings of 13th IEEE International Conference on Communication Systems (ICCS 2012)*, pp. 125-129, Nov. 2012.
- [P4] A. Kiayani, L. Anttila, and M. Valkama, “Modeling and Dynamic Cancellation of TX-RX Leakage in FDD Transceivers,” in *Proceedings of IEEE 56th International Midwest Symposium on Circuits and Systems (MWSCAS 2013)*, pp. 1089-1094, Aug. 2013.
- [P5] A. Kiayani, L. Anttila, and M. Valkama, “Digital Suppression of Power Amplifier Spurious Emissions at Receiver Band in FDD Transceivers,” *IEEE Signal Processing Letters*, vol. 21, no. 1, pp. 69-73, Jan. 2014.
- [P6] A. Kiayani, M. Abdelaziz, L. Anttila, V. Lehtinen, and M. Valkama, “DSP-Based Suppression of Spurious Emissions at RX Band in Carrier Aggregation FDD Transceivers,” in *Proceedings of 22nd European Signal Processing Conference (EUSIPCO 2014)*, pp. 591-595, Sept. 2014.

-
- [P7] A. Kiayani, L. Anttila, Y. Zou, and M. Valkama, “Channel Estimation and Equalization in Multi-User Uplink OFDMA and SC-FDMA Systems Under Transmitter RF Impairments,” *IEEE Transactions on Vehicular Technology*, DOI: 10.1109/TVT.2015.2397277, 2015.

Abbreviations

3GPP	3 rd Generation Partnership Project
4G	fourth generation
A/D	analog-to-digital converter
AWGN	additive white Gaussian noise
BPF	bandpass filter
CA	carrier aggregation
CC	component carrier
CFO	carrier frequency offset
CP	cyclic prefix
CPE	common phase error
D/A	digital-to-analog converter
DC	direct current
DFT	discrete Fourier transform
DMRS	demodulation reference signals
DSP	digital signal processing
DVB	digital video broadcasting
FDD	frequency division duplexing
FDMA	frequency division multiple access
FE	front-end
FI	frequency-independent
FIR	finite impulse response
FS	frequency-selective
GSM	Global System for Mobile Communications
HD	harmonic distortion
ICI	intercarrier interference
IDFT	inverse discrete Fourier transform
IEEE	Institute of Electrical and Electronics Engineers
IM	intermodulation

IMD	intermodulation distortion
IMD2	second-order intermodulation distortion
IMD3	third-order intermodulation distortion
IMT	International Mobile Telecommunications
IIP2	second-order intercept point
IRR	image rejection ratio
ISI	inter symbol interference
I/Q	inphase quadrature phase
LAN	local area network
LNA	low noise amplifier
LO	local oscillator
LP	lowpass
LS	least squares
LTE	Long Term Evolution
LTi	linear time-invariant
MFI	mirror frequency interference
ML	maximum-likelihood
MMSE	minimum mean square error
MPR	maximum power reduction
OOB	out-of-band
OFDM	orthogonal frequency division multiplexing
OFDMA	orthogonal frequency division multiple access
P/S	parallel-to-serial
PA	power amplifier
PAPR	peak-to-average power ratio
PH	parallel Hammerstein
PHY	physical layer
PPM	parts per million
PSD	power spectral density
QAM	quadrature amplitude modulation
QPSK	quadrature phase shift keying
RB	resource block
RF	radio frequency
RLS	recursive least squares
RX	receiver
SDR	software defined radio

S/P	serial-to-parallel
SC-FDMA	single carrier frequency division multiple access
SER	symbol error rate
SNR	signal-to-noise ratio
SINR	signal-to-interference plus noise ratio
SRS	sounding reference signal
TX	transmitter
UE	user equipment
VSA	vector signal analyzer
VSG	vector signal generator
WLAN	wireless local area network
ZF	zero-forcing

Mathematical Notations

$\mathfrak{B}\text{Diag}(\cdot)$	square block diagonal matrix
$\text{card}(I_P)$	cardinality of set I_P
$\text{Diag}(\cdot)$	square diagonal matrix
$\mathbb{E}[\cdot]$	expectation operator
$-f$	mirror frequency
Δf	frequency spacing
$-k$	mirror subcarrier of subcarrier k
x	scalar term
$\check{x}(t)$	signal $x(t)$ under I/Q imbalance
\hat{x}	estimate of x
$\underline{\mathbf{x}}/\mathbf{x}$	time-domain vector/matrix
$\underline{\mathbf{X}}/\mathbf{X}$	frequency-domain vector/matrix
$\underline{\mathbf{X}}^\#$	conjugate of the mirror subcarrier vector
$x(t)$	time-domain signal
$x[n]$	discrete-time signal
$X(f)$	frequency-domain signal
$\Re\{x\}$	real part of x
$\Im\{x\}$	imaginary part of x
\star	convolution operator
$(\cdot)^*$	complex conjugate
$(\cdot)^T$	transpose
$(\cdot)^H$	Hermitian transpose
\approx	approximation
ϵ	normalized CFO
$ \cdot $	absolute value
\mathbf{I}_N	$N \times N$ identity matrix
$\mathbf{0}_N$	$N \times N$ zero matrix
\mathbf{F}_N	$N \times N$ FFT matrix

ω	angular frequency
σ	variance
\min	minimum
\max	maximum
\triangleq	defined as
$\lceil \cdot \rceil$	ceiling operator

Chapter 1

Introduction

1.1 Background and Motivation

The wireless communications sector has experienced tremendous growth during the last few decades, with the transition from voice and short text-based messages service offered by the Global System for Mobile Communications (GSM) to the current trend of “always connected”. Considering the accelerating use of multimedia contents on mobile devices, such as music and video streaming, and the Internet browsing, the demand for higher data rates continues to grow. Therefore, the so-called fourth generation (4G) or International Mobile Telecommunications-Advanced (IMT-Advanced) specified data rates within the range of 100 Mbps to 1 Gbps under various mobility conditions [1]. To realize such high data rates, advanced techniques including Carrier Aggregation (CA) to enlarge bandwidth, Multiple Input Multiple Output (MIMO) antenna configuration, Orthogonal Frequency Division Multiplexing (OFDM)-based air interfaces, higher modulation alphabets, and advanced scheduling techniques are deployed in 4G radio systems [2, 3, 4, 5, 6].

In achieving extremely high data rates, a big challenge is *reconfigurability* and *flexibility* of radio devices to simultaneously support a wide variety of wireless standards in different frequency bands. This is in line with the principle of software defined radio (SDR) which calls for reusability of hardware through software updates [7]. Recently, a new concept known as cognitive radio (CR) [8] is proposed, which aims at better spectrum utilization by allowing secondary or non-licensed

users to access the spectrum opportunistically and operate within the frequency bands that are not heavily used by the licensed or primary users.

On one hand, wireless devices should be multimode and multiband. On the other hand, there are big restrictions on their cost, size, and power consumption, particularly on the user equipment (UE) side. These conflicting expectations pose major technical constraints in the evolution of wireless devices, which calls for novel radio architectures with the use of low-cost components. The *direct-conversion (also known as zero-IF or homodyne) radio architecture* [9] offers a good balance between the hardware complexity/size and the performance, and is considered a promising candidate for multi-standard radio devices. In the direct-conversion architecture-based radio transmitters (TXs) and receivers (RXs), the desired signal is directly converted from baseband to radio frequency (RF), and vice versa, without any intermediate frequency (IF) stage. This offers a high level of integration as bulky RF image rejection filters and other off-chip components are not needed. However, the direct-conversion architecture suffers from specific radio frequency (RF) imperfections such as inphase and quadrature phase (I/Q) imbalance stemming from gain, phase, and frequency response mismatch between the signal branches, direct current (DC) offset, local oscillator (LO) signal leakage, even-order intermodulation distortion (IMD) products, and flicker noise, etc. [10, 11, 12, 13, 14, 15]. In general, these impairments cannot be fully avoided in a practical implementation due to inaccuracies in the fabrication process, and their impact becomes more pronounced as the cost and size of analog components decrease and the operating bandwidth and frequency increase [16, 17]. Moreover, modern communication systems employing multicarrier waveforms and higher-order modulation alphabets are particularly vulnerable to these RF imperfections. Hence, one interesting alternative to reduce the impact of these impairments while keeping the cost and size of devices at a reasonable level is to increase the cooperation between the digital baseband and the analog RF. More specifically, sophisticated digital signal processing (DSP) techniques can be applied to reduce the impact of analog RF impairments, as suggested by the “Dirty RF” paradigm [16]. This is the general topic area in this thesis and forms a good motivation for this research work.

1.2 Scope and Contributions of the Thesis

The goal of this thesis is to model and analyze certain TX RF front-end (FE) imperfections, and to propose digital mitigation techniques that enable efficient transceiver operation with flexibility, reconfigurability, and reduced size, power, and cost. The algorithms proposed in this thesis work can be applied in the pilot data-aided OFDM and uplink Orthogonal Frequency Division Multiple Access (OFDMA)/Single Carrier Frequency Division Multiple Access (SC-FDMA) systems, as well as in frequency division duplex (FDD) transceivers with finite isolation duplexer filters and small duplex distance. While it is difficult to cover all essential RF impairments in radio systems in a single thesis, the scope is thus limited to selected TX RF impairments as elaborated in more details in the following paragraphs and technical chapters.

The contributions of this thesis can be divided into two areas. The first is direct-conversion OFDM and uplink OFDMA/SC-FDMA systems, where a hybrid time/frequency-domain compensation structure is proposed, and DSP-based algorithms are developed to combat RF impairments and channel distortions at the receiver side. For OFDM systems, both joint and de-coupled equalization techniques are proposed to mitigate frequency-selective TX I/Q imbalance and channel distortions [P1], [P2]. In the uplink OFDMA/SC-FDMA context, the effect of small carrier frequency offsets (CFOs) is also taken into account together with the frequency-selective TX I/Q imbalances and channel distortions in the challenging multi-user uplink scenario with multiple UEs multiplexed in frequency. Then, motivated by the reduced size and power efficiency for mobile terminals, novel joint estimation and equalization algorithms are developed that operate in the digital baseband of the base station (BS) RX [P3], [P7]. This is one key contribution of this thesis, which allows efficient TX RF impairments and channel distortions estimation and compensation, and are thus highly desirable for OFDM- and uplink OFDMA/SC-FDMA-based RXs.

The second part of this thesis deals with the modeling and mitigation of transmitter leakage signals in FDD transceivers, when a significant portion of transmit signal leaks into the RX chain due to insufficient TX-RX isolation and deteriorate the desired received signal detection. Here, two different self-interference scenarios are considered. The first is TX out-of-band (OOB) emissions and TX

spurious emissions at the own RX band created by the nonlinear power amplifier (PA) in the transmitter chain [P5], [P6], while the second is the nonlinearity of the down-converting mixer in RX that generates second-order IMD (IMD2) due to the transmitter in-band leakage signal [P4]. In both situations, the unwanted self-interference corrupts the reception and may lead to own receiver (RX) desensitization (self-desensitization). We propose algorithms that operate in the digital baseband of the transceiver to regenerate a replica of the self-interference and thereafter suppress it. This is another key contribution, which potentially increases the flexibility of the transceiver by relaxing the TX-RX isolation and duplex distance requirements as well as reducing the overall transceiver cost.

Altogether, this thesis is based on the works reported in [P1] - [P7] and partly also on the work reported in [18], carried out at the Department of Electronics and Communications Engineering, Tampere University of Technology, Finland. The topics were jointly proposed by the thesis supervisors Prof. Mikko Valkama, Dr. Lauri Anttila, and the author himself. The author of the thesis is the first author in all the publications, and was responsible for developing the signal models, analysis, simulations, measurements, and preparations of the publications while the thesis supervisors provided useful guidance and contributed to the technical contents and final appearance of all the publications. The initial idea of developing an overall link-level model with TX and RX I/Q imbalances, CFO, and channel distortions in OFDM systems was proposed by Dr. Lauri Anttila who provided preliminary derivations which the author then formalized and developed compensation solutions in [P1] and [P2] while being advised and aided by the supervisors and co-author Dr. Yaning Zou, who implemented the CFO estimator in [P2]. The author proposed the research concept of RF impairments in uplink OFDMA and SC-FDMA systems inspired by Yoshida *et al.* work in [19], and performed detailed signal modeling, analysis, and simulations. Dr. Lauri Anttila proposed the idea of polynomial approximation for channel estimation, Prof. Mikko Valkama helped in the derivation of joint minimum mean-square error (MMSE) equalizer and also in the analysis of multi-antenna RXs, while Dr. Yaning Zou carried out the complexity analysis in [P7]. The study area of transmitter leakage signal problems in an FDD transceiver was proposed by Prof. Mikko Valkama, and the problem of unwanted transmitter spectral emissions at the RX band [P5] was identified in [P4] for which the author then developed digital mitigation techniques with Prof. Mikko Valkama and Dr. Lauri Anttila guidance. The work on mitigation of transmitter spurious emissions at RX band in CA FDD transceivers [P6] was motivated

by PA predistortion studies in our research group, and the analysis, simulations, measurements, and writing were done by the author. Naturally, thesis supervisors and co-authors M. Sc. Mahmoud Abdelaziz and M. Sc. Vesa Lehtinen provided valuable insight and comments.

1.3 Outline of the Thesis

The remaining chapters of the thesis are organized as follows. Chapter 2 provides essential background aspects, including a compact overview of Long Term Evolution (LTE)-Advanced; I/Q imbalance and CFO problem in direct-conversion architecture-based OFDM systems; and the transmitter leakage signal problems in FDD transceivers. Chapter 3 presents analytic signal models of the received signal as a function of transmitted signals, the TX and RX I/Q imbalances, CFOs, and channel distortions. Then, digital compensation techniques are discussed for TX RF impairments in OFDM and uplink OFDMA/SC-FDMA systems. The chapter ends with the simulation and measurement results. Chapter 4 presents detailed signal modeling and efficient baseband mitigation techniques for different considered TX leakage signal scenarios in FDD transceivers. Again, extensive simulation and measurement results are provided to validate the performance of the proposed methods. Finally, Chapter 5 summarizes the key findings of the thesis.

Chapter 2

Recent Advances and Challenges in Mobile Radio Communications

The number of wireless devices has increased rapidly in the last decade and is expected to reach tens of billions already by 2020 [20]. Along with the increasing number of devices, the consumer demands for extremely high data rates to enable broadband multimedia services have also grown significantly, which requires considerably larger transmission bandwidths and improved spectral efficiency. Meanwhile, the available RF spectrum remains as a scarce resource. In this context, spectrally efficient and flexible transmission schemes such as OFDM have been adopted by many prevailing wireless standards, such as digital audio broadcasting (DAB) [21], digital video broadcasting (DVB) [22], 3rd Generation Partnership Project (3GPP) LTE/LTE-Advanced [6, 10, 23], family of wireless local-area-networks (WLANs) building on 802.11 a/g/n/ac standards [24, 25], and WiMAX standard IEEE 802.16 [26], among others. The OFDM technique is robust against multipath fading, eliminates Inter Symbol Interference (ISI) by inserting a cyclic prefix (CP) between successive symbols, allows the use of MIMO techniques to exploit spatial multiplexing and antenna diversity, and offers high flexibility in resource allocation [27, 28]. The physical layer implementation of OFDM-based systems with a direct-conversion radio architecture represents a promising solution [9], and is currently a prevailing radio architecture in radio transceivers due to its simplified analog FE. However, the direct-conversion architecture is very sensitive to various FE mismatches and imperfections, commonly known as RF impairments [16], stemming from analog hardware inaccuracies that can limit the

system performance. Furthermore, OFDM-based systems are known to be particularly vulnerable to RF impairments, see, e.g., [29, 30, 31, 32, 33, 34, 35, 36] and references therein.

In this chapter, we briefly review the advances in mobile radio communications, namely 3GPP LTE-Advanced, which is based on the OFDM/OFDMA transmission scheme, or some of its variants, and is taken as a case study in this thesis. We also review the most common RF impairments associated with the direct-conversion architecture-based OFDM/OFDMA systems, such as I/Q imbalance and carrier frequency offset (CFO). Finally, the problem of transmit signal leakage in the frequency-division duplex (FDD) transceiver is addressed, and the role of transmitter and receiver non-idealities in this context is covered.

2.1 An Overview of 3GPP Long Term Evolution-Advanced

LTE-Advanced is generally referring to the 3GPP Release 10 and beyond. Here in this section, we introduce only the general properties of LTE and LTE-Advanced that are relevant to this thesis. The reader is referred to [6, 37, 38, 39] and 3GPP 36 series technical specification documents for more details.

Motivated by the ever increasing demands of mobile users for multimedia and other high-speed broadband services, the International Telecommunications Union (ITU) has defined the requirements for the next-generation mobile telecommunication system, known as International Mobile Telecommunications-Advanced (IMT-Advanced). The most notable feature of IMT-Advanced systems is enhanced data rates: 1 Gbps for low mobility users and 100 Mbps for high mobility users. Responding to these requirements [1], 3GPP has been and is still developing the LTE-Advanced standard, which achieves peak data rates by deploying bandwidths up to 100 MHz [3, 40]. Other key features of LTE-Advanced include improved spectral efficiency, scalable bandwidths, low latency, multi-antenna transmission, and backward compatibility with legacy LTE systems (Release 8/9).

LTE supports scalable bandwidths, with current specification of 6 different carrier bandwidths: 1.4, 3, 5, 10, 15 and 20 MHz [2]. However, higher data rates require considerably larger bandwidths. Hence, the *Carrier Aggregation (CA)*

technique is introduced in LTE-Advanced, which enables bandwidth extension beyond 20 MHz by aggregating two or more LTE Release 8 carriers (referred to as component carriers (CCs) in Release 10 onwards). The CCs can possibly be of different bandwidths and can belong to the same frequency band (intra-band CA) or to separate frequency bands (inter-band CA), hence providing increased spectrum flexibility. Furthermore, both contiguous and noncontiguous intra-band CA schemes are specified, depending on whether or not the aggregated carriers are next to each other in frequency-domain.

In addition to transmission bandwidth flexibility, LTE also offers flexibility in duplex arrangements and supports both FDD and Time Division Duplexing (TDD) modes. In TDD mode, uplink and downlink transmissions use the same frequency but take place in non-overlapping time slots. On the other hand, the FDD mode implies that uplink and downlink transmissions can occur simultaneously but using separate frequency bands.

OFDMA-based radio access schemes are adopted in LTE deploying pure OFDMA in downlink and DFT-spread OFDMA, also known as SC-FDMA, in uplink. Properties of LTE uplink and downlink are discussed briefly in the following subsections from the perspective of this thesis work, while the basic physical layer parameters are summarized in Table 2.1. The spectral efficiency of the radio link is further improved by using higher-order subcarrier modulation schemes, that can be quadrature phase shift keying (QPSK) or quadrature amplitude modulation (QAM) with constellation size of 16 and 64, together with efficient error correction coding and MIMO techniques [2, 6, 38].

2.1.1 LTE Downlink: OFDMA

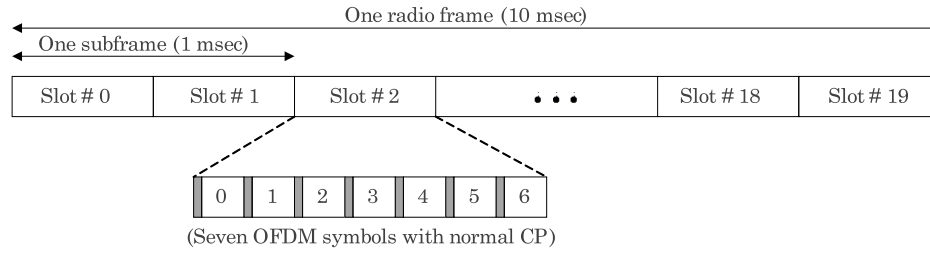
LTE downlink radio access is achieved via OFDMA. OFDMA is a multicarrier transmission and multiple access scheme where available bandwidth is split into several narrow bandwidth orthogonal subcarriers, with each subcarrier carrying data, and different users can be flexibly mapped to different subsets of the overall pool of subcarriers. These make OFDM/OFDMA robust to channel frequency-selectivity and also supports flexibility in bandwidth allocation by varying the number of subcarriers assigned to different users. The orthogonality between subcarriers is achieved through careful selection of carrier spacing such that at the

TABLE 2.1: LTE physical layer parameters

Access scheme	Uplink			SC-FDMA		
	Downlink			OFDMA		
Transmission bandwidths (MHz)	1.4	3	5	10	15	20
FFT Size	128	256	512	1024	1536	2048
No. of RBs	6	15	25	50	75	100
No. of occupied subcarriers	72	180	300	600	900	1200
Subcarrier Spacing (kHz)	15					
Radio subframe duration (msec)	1					
No. of slots in a subframe	2					
No. of symbols per slot	Normal CP			7		
	Extended CP			6		
CP length	Normal			5.2 μ sec for first symbol in a slot, 4.7 μ sec for other symbols in a slot		
	Extended			16.7 μ sec		
Modulation schemes	QPSK, 16–QAM, 64–QAM (<i>only for downlink</i>)					

center of a subcarrier all other subcarriers have zero crossings. In LTE, the subcarrier spacing between consecutive subcarriers is 15 kHz and the number of active subcarriers vary from 72 to 1200 depending on the occupied carrier bandwidth. A group of 12 adjacent subcarriers is called a resource block (RB) and each user may be assigned one or more RBs thus resulting in a minimum bandwidth allocation of 180 kHz. The transmission is arranged in radio frames, and two frame structures are defined for LTE: frame structure type 1 for FDD and frame structure type 2 for TDD mode [10]. In frame structure type 1, a frame is 10 msec in duration and is divided into 10 subframes. A subframe, of duration 1 msec, forms a transmission time interval (TTI) and is further divided into two slots each of 0.5 msec duration. A slot then carries six or seven data symbols, depending on normal or extended cyclic prefix (CP) length. This is illustrated in Fig. 2.1. In LTE OFDMA, the users are scheduled in the time-frequency grid, where in frequency-domain RBs are assigned and in time-domain resource allocation is done with minimum TTI of one subframe [6, 38, 41].

To each OFDM symbol, a CP, which is a copy of the last N_g time-domain samples of an OFDM symbol, is appended to the beginning. When the length of CP is chosen larger than the channel delay spread, no ISI occurs after removing it, properly synchronized, in the receiver. The addition of the CP, however,

FIG. 2.1: *LTE frame structure type 1 for FDD.*

decreases the spectral efficiency of the OFDM system and is a trade-off between the robustness to ISI and spectral efficiency. LTE has two different CP configurations, namely normal CP and extended CP, to account for the channel delay spread. For demodulation in LTE downlink, known *reference signals* are inserted into the time-frequency grid. The reference signals are used, e.g., for the channel estimation on the user equipment (UE). With normal CP, the reference symbols are placed at every sixth subcarrier in frequency-domain, whereas in time-domain, the first and fifth OFDM symbols in a slot carry reference symbols [10].

A drawback of the multicarrier OFDM/OFDMA transmission scheme is that simultaneous transmission of multiple subcarriers leads to large variations in the instantaneous transmit power, i.e. a high peak-to-average power ratio (PAPR). High PAPR drives the PA into its nonlinear region and an input power back-off, which is approximately as large as the PAPR of the transmitted signal, is required to operate in the linear region [11]. This, however, results in inefficient PA operation and increases the cost. Since PA efficiency and cost are more important considerations for the mobile terminals, OFDMA is better suited for downlink transmission. Additionally, OFDM systems are more susceptible to Inter Carrier Interference (ICI) due to the small frequency separation between the subcarriers, and thus Doppler frequency or frequency synchronization errors may destroy the subcarrier orthogonality, resulting in system performance degradation.

2.1.2 LTE Uplink: SC-FDMA

LTE uplink transmission is also based on an OFDMA like access method; however, due to high PAPR of OFDMA signals, DFT-spread OFDMA, also known as SC-FDMA, is selected as the uplink multiple access scheme in 3GPP LTE/LTE-Advanced systems [6, 38, 42]. SC-FDMA is a modified form of OFDMA that

resembles single carrier transmission by pre-coding or spreading the data symbols with a discrete Fourier transform (DFT). Unlike OFDM, where each subcarrier carries a different symbol, in SC-FDMA, the DFT operation spreads the data over all subcarriers. As a consequence, the transmitted signal is single carrier like and has lower PAPR than the OFDM signal. This property makes SC-FDMA favorable for uplink transmission where UEs can benefit in terms of transmitted power efficiency. Interestingly, in LTE Release 11, noncontiguous resource allocation within a single CC, i.e. multi-cluster transmission, is supported where the DFT outputs are not mapped directly to consecutive subcarriers. This allows more flexible channel-dependent scheduling but also increases the PAPR [43, 44]. Another benefit of SC-FDMA is frequency diversity. Since the information on an individual symbol is spread on all data subcarriers, hence if one or more subcarriers are in a deep fade it does not necessarily lead to losing the information transmitted on a symbol. However, at the receiver side, IDFT operation spreads noise over all subcarriers and noise amplification from deep fades has a greater impact on the performance [6, 45, 46, 47].

SC-FDMA has also flexibility in transmission bandwidth and supports both localized and distributed mappings. When a group of successive subcarriers are allocated to a user, i.e. the DFT output is mapped directly to a subset of consecutive subcarriers, it is referred to as localized mapping. Otherwise, it is called distributed mapping where the DFT outputs are mapped to subcarriers over the entire bandwidth. The current working assumptions in LTE/LTE-Advanced assume localized subcarrier mapping [10, 48].

Similar to downlink, the uplink transmission is also organized in the radio frames with 10 msec duration which are further divided into 10 subframes with two slots of 0.5 msec duration each. Furthermore, an uplink RB has 12 subcarriers on the frequency axis and in time, seven SC-FDMA symbols per slot with normal CP configuration and six SC-FDMA symbols when the extended CP is used. There are two types of reference signals: the demodulation reference signals (DMRS) which are used for channel estimation in the BS RX, and the sounding reference signals (SRS) which are used to derive channel quality information for scheduling decisions [10]. Compared to the downlink where the reference signals are distributed in frequency and time, UL DMRS reference signals are in the middle of each slot, i.e., the fourth symbol assuming normal CP configuration, and spans over all subcarriers allocated for uplink transmission. In addition, compared to the data

symbols that are pre-coded by DFT, the reference symbols are directly mapped to the subcarriers in the uplink transmission.

2.1.3 Carrier Aggregation and Multi-Cluster Transmission

In Release 10 of 3GPP specifications, carrier aggregation is introduced that permits aggregating two or more Release 8 CCs, possibly of different bandwidths, for transmission. Up to five CCs can, in principle, be aggregated, resulting in a maximum of 100 MHz transmission bandwidth; however, currently there is support for only two CCs, i.e. a maximum of 40 MHz bandwidth [2, 4, 6, 23, 49, 50]. The number of aggregated CCs can be different in the uplink and downlink, but the number of uplink CCs is always less than or equal to the number of downlink CCs. Initially in Release 10, only intraband contiguous CA was introduced, which was further extended to include downlink intraband noncontiguous and downlink interband CA in Release 11. The uplink intraband noncontiguous and uplink interband CA are then introduced in Release 12. In addition to the bandwidth extension through CA, noncontiguous resource allocation within the contiguously aggregated carriers was proposed in Release 10 and noncontiguous resource allocation within a single CC or the so-called *multi-cluster transmission* is adopted in Release 11 to improve the uplink spectral efficiency [5, 6, 51]. With multi-cluster transmission in uplink, an UE can be allocated 2 nonadjacent clusters within a CC, where a cluster refers to the integer number of RBs. While the multi-cluster transmission has higher scheduling capability than the contiguous RB allocation, the single carrier property is no longer preserved which results in increased PAPR. The evolution and capabilities of CA in different LTE Releases from an uplink perspective are illustrated in Fig. 2.2.

2.2 Basics of I/Q Signal Processing

To establish a basis for discussion in the rest of this thesis, we introduce next the basic concepts of I/Q signal processing in this section.

Complex-valued or I/Q signals are often employed in modern radio signal processing. A complex-valued signal is a pair of two real-valued signals, consisting of *real*

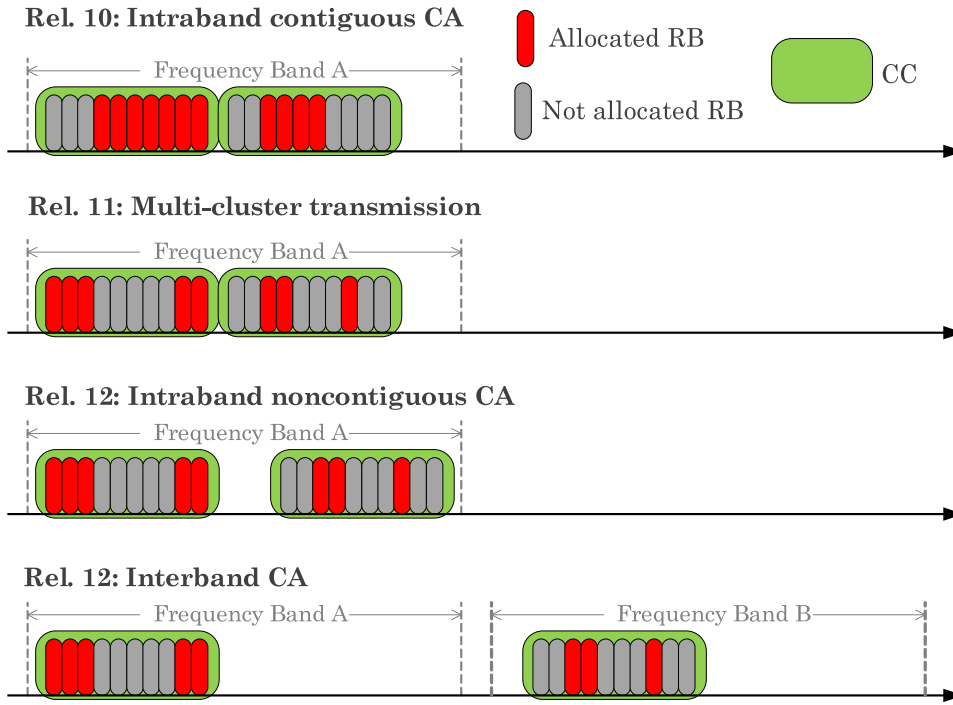


FIG. 2.2: Different types of CA schemes and multi-cluster transmission in LTE-Advanced uplink from single UE perspective.

and *imaginary* components that have 90° phase difference between them. Mathematically, a complex-valued signal is written as $x(t) = x_I(t) + jx_Q(t)$, where the real part of the signal $\Re\{x(t)\} = x_I(t)$ is known as the inphase, and the imaginary part $\Im\{x(t)\} = x_Q(t)$ is known as the quadrature signal. Real-valued signals have *spectral symmetry* around the zero frequency, meaning that $X_{re}(f) = X_{re}^*(-f)$ where $X_{re}(f)$ denotes the Fourier transform of a real-valued signal $x_{re}(t)$, however, complex-valued signals do not need to obey any spectral symmetry [11, 32]

Complex I/Q signal processing is utilized in modern radio transceiver architectures, such as the direct-conversion transmitter and receiver depicted in Fig. 2.3, for up/down-conversion. Here, the frequency translation is performed by multiplying the signal with a complex-valued local oscillator (LO) signal. Conceptually, on the transmitter side, the complex baseband signal $x(t)$ is first multiplied with a complex LO signal $e^{j2\pi f_{LO}t}$, which can be represented as a pair of orthogonal real-valued signals $e^{j2\pi f_{LO}t} = \cos(2\pi f_{LO}t) + j\sin(2\pi f_{LO}t)$ using phasor notation, and the real-part of the RF signal is transmitted on a real-valued channel. This

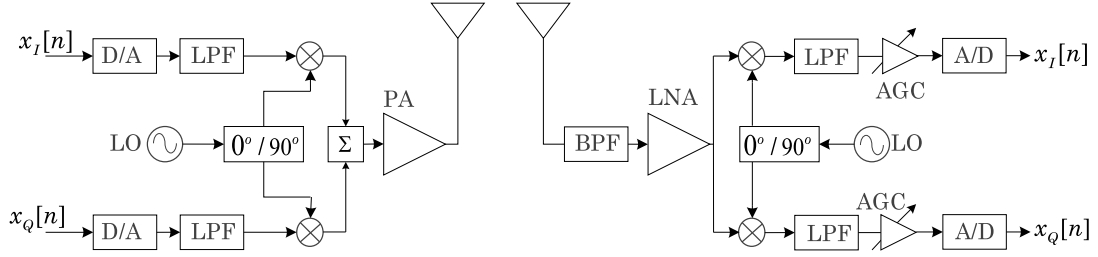


FIG. 2.3: The direct-conversion transmitter (left) and receiver (right) block diagrams using I/Q mixing.

can be mathematically expressed as [52, 53]

$$\begin{aligned}
 x_{RF}(t) &= 2\Re \{x(t)e^{j2\pi f_{LO}t}\} \\
 &= x(t)e^{j2\pi f_{LO}t} + x^*(t)e^{-j2\pi f_{LO}t} \\
 &= 2x_I(t)\cos(2\pi f_{LO}t) - 2x_Q(t)\sin(2\pi f_{LO}t)
 \end{aligned} \tag{2.1}$$

where the last form in above equation is known as *the quadrature carrier form* of the bandpass signal $x_{RF}(t)$, showing that two real-valued signals, or the real and imaginary parts of the complex baseband signal, are being transmitted on the same frequency and over the same bandwidth. The spectrum of above RF signal constitutes both the positive and negative frequency components of the corresponding complex baseband signal, and it is symmetrical about the zero frequency, though non-symmetric about the LO frequency. The spectral symmetry is created by the \Re operator which introduces the $x^*(t)e^{-j2\pi f_{LO}t}$ component in (2.1).

Similarly, on the receiver side, any real-valued RF signal $x_{RF}(t)$ can be down-converted to baseband by first multiplying it with the complex exponential of the opposite frequency, and then recovering the desired baseband signal with lowpass (LP) filtering the frequency translated signal. The equivalent baseband signal can be written as

$$x(t) = LP \{x_{RF}(t)e^{-j2\pi f_{LO}t}\} \tag{2.2}$$

where LP denotes the lowpass filtering operation.

In general, the above I/Q mixing-based transmitter and receiver concepts can also be adopted in multichannel type of scenarios as well as in cases where the lowpass equivalent complex signal $x(t)$ is located not exactly at baseband but, e.g., at a small intermediate frequency (IF). In such cases, the structure of the lowpass equivalent signal simply resembles the structure of the overall processed RF signal, with the zero frequency corresponding to the LO frequency. Good examples of this

are, e.g., Release 11 multi-cluster UE transmitter where the lowpass equivalent signal contains the active RBs within one LTE carrier, or more generally, a dual-carrier CA transmitter where the dual-carrier signal structure is already created in the lowpass equivalent complex signal such that the individual carriers are located at the appropriate complex IF frequencies. In this thesis, we use the direct-conversion transceiver to refer to all these kinds of transmitter and receiver scenarios while the exact signal structure of the lowpass equivalent signals then becomes evident from the more detailed context in different considered system scenarios.

2.3 TX RF Imperfections in Direct-Conversion OFDM/OFDMA Systems: Influence and Signal Models

It is well established in the literature that the direct-conversion architecture is vulnerable to RF impairments of analog FE components [10, 11, 12, 13, 14, 15, 32]. In this thesis, we focus only on certain TX RF impairments in direct-conversion architecture-based OFDM systems, more specifically I/Q imbalance and small uplink CFOs, and deal with the estimation and compensation of these impairments on the receiver side in the presence of channel distortions. The impact of these impairments is now shortly reviewed in the following subsections.

2.3.1 I/Q Imbalance

As discussed in Section 2.2, an I/Q modulator/demodulator is often used for up/down-conversion in the direct-conversion architecture-based TX/RX. The implementation of quadrature up/down-conversion suffers from the mismatch between the analog I and Q paths, typically due to unavoidable fabrication process inaccuracies, and is referred to as I/Q imbalance. Generally speaking, the sinusoids multiplying the quadrature branches may not have equal gain and exactly 90° phase difference, resulting in frequency-independent (FI) I/Q imbalance. In addition, the frequency responses of both signal paths, such as LP filters, amplifiers, digital-to-analog converter (D/A)/analog-to-digital converter (A/D), may not be identical, particularly for wideband signals, hence resulting in frequency-selective

(FS) I/Q imbalance within the signal bandwidth. I/Q imbalance can occur at the TX, RX, or both.

To model such I/Q imbalance, suppose that $g_{TX/RX}$ denotes the relative mismatch, called *gain mismatch*, and $\phi_{TX/RX}$ denotes the relative phase difference, called *phase mismatch*, stemming from the I/Q LO and mixer stages. Furthermore, the relative *impulse response mismatch* between the two quadrature branches is modeled with $h_{TX/RX}(t)$. Then the complex filters $g_{1,TX}(t), g_{2,TX}(t)$ modeling the overall TX I/Q imbalance and $g_{1,RX}(t), g_{2,RX}(t)$ modeling the overall RX I/Q imbalance are defined as [11, 30, 32, 54]

$$\begin{aligned} g_{1,TX}(t) &= (\delta(t) + g_{TX}e^{j\phi_{TX}}h_{TX}(t)) / 2; & g_{2,TX}(t) &= (\delta(t) - g_{TX}e^{j\phi_{TX}}h_{TX}(t)) / 2 \\ g_{1,RX}(t) &= (\delta(t) + g_{RX}e^{-j\phi_{RX}}h_{RX}(t)) / 2; & g_{2,RX}(t) &= (\delta(t) - g_{RX}e^{j\phi_{RX}}h_{RX}(t)) / 2. \end{aligned} \quad (2.3)$$

To quantify the effect of TX I/Q imbalance, let $x(t)$ denote the baseband equivalent transmit signal under perfect I/Q matching. The complex envelope of the transmitted RF signal with I/Q imbalance effect is then given by [11, 54, 55], [P1] - [P3], [P7]

$$\check{x}(t) = g_{1,TX}(t) \star x(t) + g_{2,TX}(t) \star x^*(t). \quad (2.4)$$

The above equation indicates that I/Q imbalance results in a *widely-linear transformation of the ideal complex envelope* [11, 55], since the impaired complex envelope is a weighted sum of the ideal complex envelope and its conjugate. The baseband equivalent signal in (2.4) in the frequency-domain, by taking its Fourier transform, is given by

$$\check{X}(f) = G_{1,TX}(f)X(f) + G_{2,TX}(f)X^*(-f) \quad (2.5)$$

which shows that the undesired image signal $G_{2,TX}(f)X_{TX}^*(-f)$, generated by I/Q imbalance, results in the mirror frequency interference (MFI). Depending on a signal's spectral location, MFI causes *self-interference* through own signal image or *mirror channel interference* through the image signal of mirror channel signals. This is illustrated in Fig. 2.4 for single-channel and multi-channel transmission scenarios, where in the single-channel case when all subcarriers are allocated to a user, the signal suffers from self-interference or intercarrier interference (ICI). However, in the multi-channel case when several users, of possibly different bandwidths and unequal power levels, are sharing the available bandwidth, the interference can

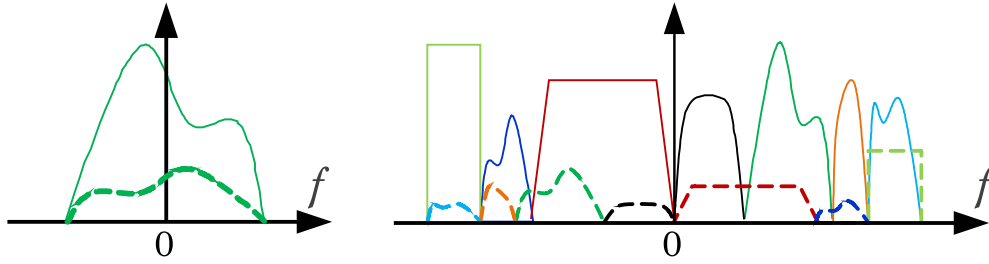


FIG. 2.4: *Example lowpass equivalent spectral illustrations of I/Q imbalance effects on single-channel (left) and multi-channel (right) signals with different bandwidths and power levels.*

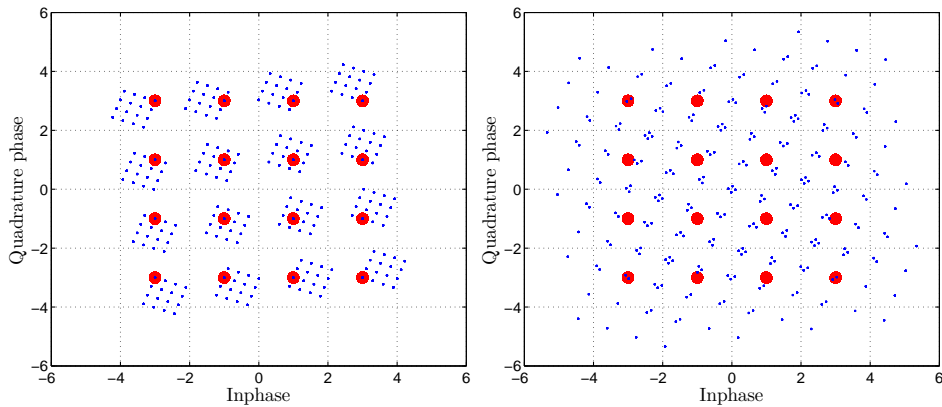


FIG. 2.5: *Effect of TX I/Q imbalance on a noiseless 16-QAM OFDM signal with 15% gain imbalance and 15° phase imbalance. The scatter plot of a single-channel signal (right) and the scatter plot of the weaker signal in a two-channel signal with 10 dB power difference (left). The red circles denote the ideal subcarrier symbols and the blue points denote the imbalanced subcarrier symbols.*

come from one or more mirror channels, resulting in interuser interference (IUI). A strong mirror channel hence generates a more powerful interference which, in turn, results in a high detection error rate for the weak channel signals. The effect of frequency-independent TX I/Q imbalance on a noiseless 16-QAM OFDM symbol constellation is illustrated in Fig. 2.5, showing the ICI effect in the left part of the figure for a single-channel transmission, and the IUI effect in the right part of the figure where the constellation plot of the weak user in a two-channel transmission case is plotted. Notice that the IUI has a noise-like behavior whose level depends on the power difference among the mirror channel users.

The *image rejection ratio* (IRR) can be defined for an individual TX FE using (2.5), expressed in dB, as

$$IRR_{TX}(f) = 10 \log_{10} \left(\frac{|G_{1,TX}(f)|^2}{|G_{2,TX}(f)|^2} \right), \quad (2.6)$$

which quantifies the suppression of the image signal located at the mirror-frequency $-f$ in the lowpass equivalent notation. It is worth mentioning here that for LTE UE terminals, the minimum I/Q image signal suppression is defined to be only 25 dB in the 3GPP standardization [2, 56]. This may not yield sufficient signal suppression especially in the uplink as a considerable power level difference may exist between the uplink users at the BS RX. For example, the in-band dynamic range for an LTE BS RX can be in the order of 21.5 dB [57]. It is also verified with simulations in [P7] that IUI in uplink transmission due to TX I/Q imbalances causes severe performance degradation. This motivates well for the receiver-based suppression of I/Q mismatch-induced interference, especially with higher-order subcarrier modulation in the uplink transmission.

In general, IRR only measures the influence of I/Q imbalance and does not account for other distortion sources such as CFO and channel. Hence, the symbol-error-rate (SER) of a communication system is used as the primary performance metric in this thesis, since it is a most important physical layer performance measure.

2.3.2 Carrier Frequency Offset

An OFDM-based communication system modulates the data symbols to closely spaced orthogonal subcarriers. Such a transmission is very sensitive to frequency synchronization errors, often called CFO. The CFO arises due to the misalignment between TX and RX local RF oscillators and/or Doppler shifts caused by the mobility of users, and destroys subcarrier orthogonality. CFO also results in ICI or IUI, depending on the subcarrier allocation and multiple access scheme, and considerably degrades the system performance [58, 59, 60].

To formulate the effect of CFO, consider an OFDM system with M subcarriers.

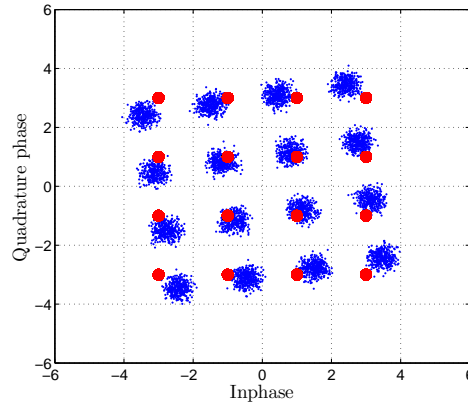


FIG. 2.6: *Effect of normalized CFO = 0.05 on the noiseless 16-QAM OFDM signal with subcarrier spacing of 15 kHz. The rotation of constellation points is due to the CPE and the additional spread around the symbols can be attributed to the ICI.*

The received signal, after CP removal and FFT, in frequency-domain at a subcarrier k is then given by [61, 62], [P1], [P2]

$$Y(k) = X(k)\Omega(k, k, \epsilon) + \sum_{l=0, l \neq k}^{M-1} X(l)\Omega(l, k, \epsilon) \quad (2.7)$$

where ϵ denotes the normalized CFO relative to the subcarrier spacing. The channel multi-path effect and additive noise are ignored here for notational simplicity, but are naturally included in the actual technical developments in the thesis work. The CFO leakage coefficient in (2.7) is defined as

$$\Omega(l, k, \epsilon) = \frac{1}{M} \sum_{q=0}^{M-1} e^{j2\pi \frac{q}{M} (l + \epsilon - k)}. \quad (2.8)$$

The first term in (2.7) represents the transmitted data scaled by the common phase error (CPE) which causes signal rotation, and the second term denotes ICI which is stemming from the lost orthogonality between subcarriers. The effect of CFO on the subcarrier constellation of a noiseless 16-QAM OFDM system is shown in Fig. 2.6.

Contrary to OFDM system where CFO causes ICI, in OFDMA, CFO not only causes ICI among the subcarriers of an individual user but it also introduces IUI due to frequency difference among different users. To better understand the CFO effect in this context, consider an OFDMA system with M subcarriers distributed

between U -users. Then, the frequency-domain received signal of a user- i at sub-carrier k , after CP removal and FFT, is given by [63, 64], [P3], [P7]

$$Y^i(k) = X^i(k)\Omega(k, k, \epsilon^i) + \sum_{l \in \Gamma^i, l \neq k} X^i(l)\Omega(l, k, \epsilon^i) + \sum_{j=1, j \neq i}^U \sum_{l \in \Gamma^j} X^j(l)\Omega(l, k, \epsilon^j) \quad (2.9)$$

where $\epsilon^i; \epsilon^j$ represent the normalized CFO of user- i and user- j , respectively, and Γ^i denotes the subcarrier index set of user- i . Notice that in (2.9) the second term corresponds to ICI observed at the k^{th} subcarrier due to subcarriers allocated to i^{th} user, and the third term represents IUI from subcarriers of all other users.

In addition, the effect of CFO on the downlink transmission is different compared with the uplink transmission. In the downlink transmission where data is sent from a single BS TX to all users, there is a unique CFO per UE receiver. Therefore, a simple CFO compensation scheme based on first estimating the frequency offset and then counter rotating the time-domain samples can be used. However, in the uplink transmission, the CFO problem is more challenging because all simultaneously multiplexed UEs, through the OFDMA/SC-FDMA principle, have their own CFOs relative to the BS receiver. In such a scenario, it is difficult to correct the frequency mismatch in the BS RX as each user may experience a different CFO, and correcting one user's CFO in the composite received signal may result in misalignment of other synchronized users. As a consequence, 3GPP LTE specifications dictate tight frequency synchronization of mobile UE terminals' LOs to the BS LO, and the specified maximum TX LO error is at most ± 0.1 parts per million (PPM) of the carrier frequency [2, 56]. As an example, assuming a carrier frequency of 2 GHz, the maximum allowed frequency error is $2 \times 10^9 \times 0.1 \times 10^{-6} = 200$ Hz.

2.4 Transmit Signal Leakage Problems in FDD Transceivers

As mentioned in Section 2.1, 3GPP LTE/LTE-Advanced supports two duplex modes: FDD and TDD [38, 41]. LTE/LTE-Advanced FDD enables full duplex operation as both TX and RX are operating simultaneously but on separate frequency bands. However, FDD operation is more challenging as sufficient isolation is required between downlink and uplink to prevent the strong TX signal from

saturating/desensitizing the RX [48, 65, 66]. A duplexer filter is commonly used to connect the TX and RX to the same antenna while seeking to provide adequate isolation between them. To cope with high dynamic range between transmit and receive signals, a duplexer filter is constructed with two bandpass filters. In the TX path, the transmitter duplexer filter seeks to suppress the unwanted emissions outside the transmit band, especially the transmitter noise from the PA present at the receiver operating frequency band. The receiver duplexer filter, on the other hand, attenuates the strong transmitter in-band signal. The challenging restrictions on the size and number of components in UEs complicate achieving sufficient TX-RX isolation, and a strong transmit signal may leak into the receiver and be thus present at the receiver input. These aspects are becoming even more demanding when CA, potentially with noncontiguous carriers, is employed and thus the duplexing distance becomes considerably narrower. This has also been recently recognized, e.g., in [5, 67, 68, 69, 70, 71], [P6]. The issue of transmit signal leakage is preliminary addressed in this section, with emphasis on the unwanted transmitter spectral emissions leaking into the RX band and the interaction between the transmitter in-band leakage signal and the receiver nonlinearity.

2.4.1 TX Spectral Emissions at Own RX Band due to Non-linear PA

The PA unit in the TX FE amplifies the transmit signal to a targeted RF power level. A *perfect* PA has a linear response, i.e. the output signal is simply a scaled copy of the input signal. However, *practical* PAs are inherently nonlinear meaning that they perform linearly only up to a certain input power and then the output starts to saturate, creating harmonic distortion (HD) and intermodulation distortion (IMD) products that can degrade the transmission quality. The nonlinearities create new frequency components, and the odd-order IMD products generally appear in the close proximity of the desired signal band [11, 72], causing *spectral regrowth* of the signal, termed as *unwanted spectral emissions* in this thesis. The spectral emissions can in general be divided into three categories: in-band emissions, out-of-band (OOB) emissions, and spurious emissions [2]. In-band emissions refer, by definition, to emissions within the carrier/channel bandwidth and are outside the scope of this thesis. OOB emissions and spurious emissions can, in turn, appear at the RX band causing interference to the desired receiver signal.

In general, the PA nonlinearity problem has become increasingly complex in modern wireless communication systems, such as LTE/LTE-Advanced, where larger bandwidths and non-constant envelope modulations are deployed to achieve higher data rates, and also the duplexing distance can be considerably narrow due to CA deployment. As a result of large variations in the instantaneous power of the transmit signal the PAPR increases. High PAPR signals are generally challenging from PA efficiency/linearity trade-off perspective as in order to keep the PA at a fairly linear region, a substantial back-off needs to be adopted. This, in turn, results in low PA efficiency. SC-FDMA, the access technique for LTE uplink, has typically 3 dB lower PAPR compared to OFDMA [6, 23], giving better efficiency which greatly benefits battery-powered devices such as mobile phones. However, efficiency and linearity are two contradictory requirements (the linearity-efficiency trade-off [73]), therefore, more efficient PA operation inevitably creates more non-linear distortions. In order to avoid interference to adjacent channel signals created by PA nonlinearity, OOB emissions and spurious emissions are generally controlled by the spectral emission mask and the spurious emission mask, defined by the standardization bodies such as 3GPP [2]. When emphasizing PA efficiency, PA-induced unwanted spectral emissions may seriously violate the emission limits [5, 74] and PAs are usually backed-off (increasing the so-called maximum power reduction (MPR) in the context of LTE) from their nominal power level to fulfill the emission limits. The minimum required back-off further increases with non-contiguous CA. Therefore, techniques such as PAPR reduction, PA *linearization* through predistortion and linear transmitter architectures have been and are being investigated to improve PA efficiency and linearity. The reader is referred to [11, 72, 75, 76, 77, 78] and references therein for more details on PA linearization and PAPR mitigation techniques.

Since the effective duplex distance becomes considerably narrower with CA, the spectral emissions of the transmit signal, created by PA nonlinearity, can easily overlap the own receiver operating band, as illustrated in Fig. 2.7. In the noncontiguous intraband CA operation with a single PA transmitter architecture [79], PA nonlinearity also creates spurious IMD products that appear far from the transmitter band and can thus also easily be in the own receiver operating band. The relative strength of these spurious IMD products can be very strong, and they may not be sufficiently suppressed by the duplexer RF filter alone, as in practice, commercial mobile duplexers can achieve only 50...60 dB attenuation [5, 67, 80] with reasonable cost, size, and insertion loss. This is illustrated in

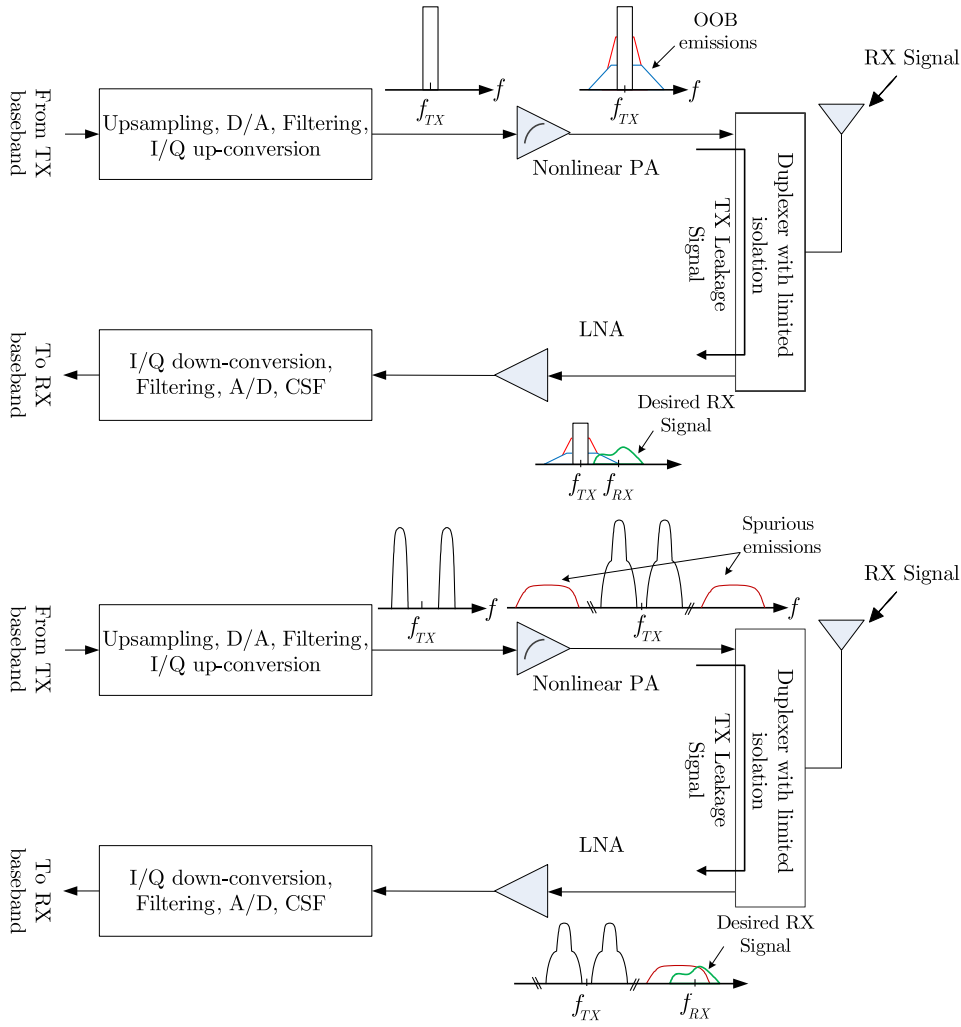


FIG. 2.7: Spectral illustration of unwanted PA OOB emissions (top) and PA spurious emissions (bottom) at the RX band due to a finite isolation duplexer filter.

Fig. 2.8 through an actual RF measurement, where a commercial LTE Band 25 mobile PA and mobile duplexer modules are used. The figure shows that with +23 dBm TX power, the spurious third-order IMD is located at 1.965 GHz, which is within the own RX operating band, and the spurious IMD power after duplexer filtering is still substantial. In such a scenario, RX desensitization can happen even when the transmitted signal satisfies the general spurious emission limit, as we shortly explain with system-level calculations. In summary, the combination of CA and narrow duplexing gaps together with the finite isolation duplexer suggest that nonlinear TX-induced spectral emissions cannot be fully suppressed by RF duplexers alone, and set challenging requirements on the mobile hardware. This is one of the main motivating factors behind this thesis work, particularly related to the publications [P5], [P6], and [18].

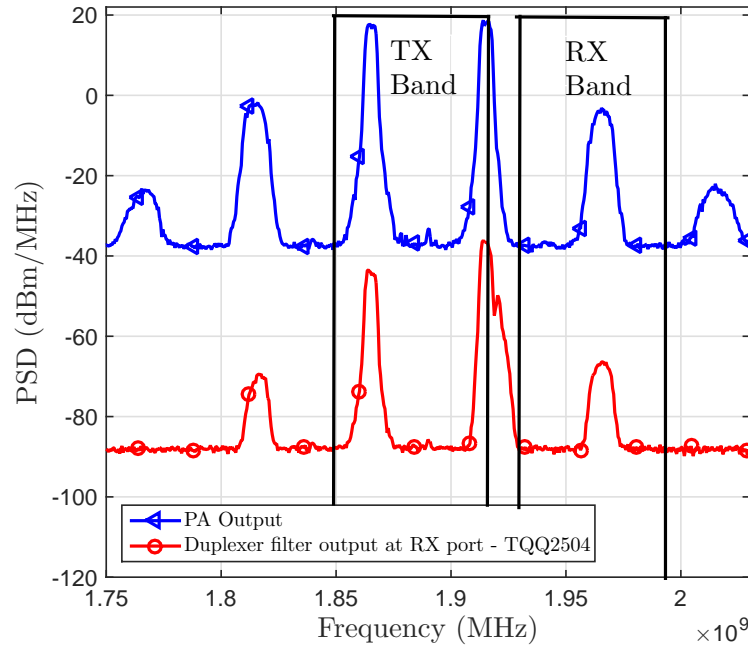


FIG. 2.8: Measured spectra of PA output and duplexer filter output at the RX port. The input signal to PA is a dual-carrier LTE uplink SC-FDMA signal with 5 MHz CCs and 50 MHz gap. The transmit center frequency is 1.89 GHz and the transmit power at antenna is 23 dBm. Own RX center operating frequency is 1.965 GHz.

Next, to shortly demonstrate the impact of TX unwanted spectral emissions at RX band, we consider LTE uplink Band 25 as a practical example and assume intraband CA with two CCs located at the edges of the uplink frequency band. In such carriers configuration, the duplexing distance between 2nd TX carrier and RX carrier is only 15 MHz. Then, in order to avoid performance degradation of the FDD receiver, the TX unwanted spectral emissions at the own RX band should essentially be below the effective thermal noise floor, especially when the receiver is operating close to its sensitivity limit. Assuming that the unwanted spectral emissions at the PA output, prior to the duplexer, can in general be up to -30 dBm/1MHz [2] (general spurious emission limit), and that the duplexer isolation towards the receiver at RX band is typically $50 \cdots 60$ dB [67, 80], the unwanted emissions at RX input can thus be in the order of $-80 \cdots -90$ dBm/1MHz. Compared to the effective thermal noise power with nominal 9dB UE RX noise figure [81], namely $-174 + 60 + 9 = -105$ dBm/1 MHz, this is a substantial interference and can completely block the desired RX signal. Notice that the general coexistence related emission limit of -50 dBm/1MHz [2], applicable also at the own RX band, is measured at the antenna connector after the duplexer filters, and

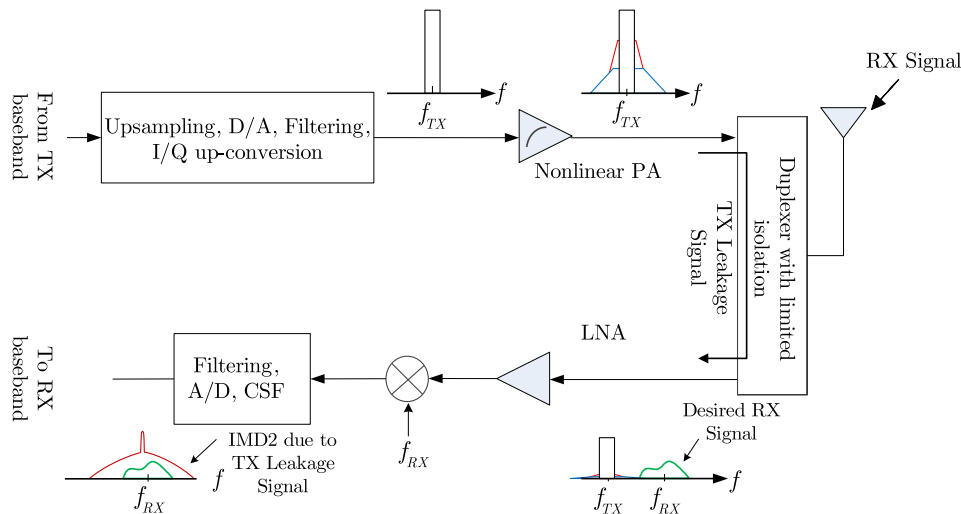


FIG. 2.9: *TX in-band leakage signal-induced IMD2 due to nonlinear mixer in direct-conversion receiver.*

is accordingly totally insufficient to protect the own RX. These system calculations are simply of extreme nature, but demonstrate the particularly challenging problem of the transmitter unwanted spectral emissions at the own receiver band due to transmitter nonlinearities and finite duplexer attenuation. Then, instead of simply backing-off the transmit power, novel digital cancellation solutions to suppress these transmitter nonlinearities-induced self-interference in the transceiver baseband are developed in this thesis work.

2.4.2 Effect of Transmit In-band Signal Leakage on Direct-Conversion RX Performance

The presence of transmitter in-band (portion of the signal that is in the passband of TX duplexer filter) leakage signal at the RX input, due to finite RX filter attenuation for the transmitter passband frequencies, also imposes stringent linearity requirements in the *receiver components*, and can interact with receiver nonlinearities to produce interference in the RX baseband. One specific performance limiting factor related to direct-conversion receivers is their sensitivity to IMD2, which produces a spurious baseband signal having twice the bandwidth of the RF interfering signal and cannot be removed by the channel selection filter [12]. In the down-conversion mixing stage, the transmit in-band leakage signal can couple from the mixer input to the LO port, producing IMD2 that falls directly on top of the weak received signal, as illustrated in Fig. 2.9. To demonstrate and quantify

the relative strength of such IMD2, example transceiver system calculations are again carried out, which indicate that the transmitter in-band leakage signal represents a dominating interference in the direct-conversion receivers. In general, the UE transmit signal can be up to 120 dB stronger than the received signal, when assuming a maximum TX power at the antenna connector of around +23 dBm and the receiver operating close to the sensitivity level, say -96.5 dBm when assuming LTE Band 25 with 5 MHz channel bandwidth and QPSK subcarrier modulation [2]. Then, the value of TX-RX duplexer attenuation for the transmitter passband is typically assumed to be only around 50 dB with 2 dB insertion loss for each TX and RX duplexer filters [5, 67, 80], implying that the transmitter leakage signal power is $+23 - 50 - 2 = -29$ dBm at the receiver LNA input. This signal is next amplified by LNA, having typically a gain of +15dB or so [82], resulting in -14 dBm leakage signal power (P_{TxL}) at the mixer input. The relative strength of IMD2 produced by the down-converter can be characterized by its second order intercept point (IIP2), which indicates its linearity. If the mixer IIP2 is, e.g., +50 dBm [83], then the IMD2 power (P_{TxL}^{IMD2}) at the mixer output is given by $P_{TxL}^{IMD2} = P_{TxL} - (IIP2 - P_{TxL}) = -78$ dBm, where it is assumed that the gain of the mixer is 0 dB for simplicity. If the desired signal itself is assumed to be at the receiver sensitivity level of -96.5 dBm, after LNA gain and mixer stage, its power is -81.5 dBm. This shows that, in this example, the transmitter leakage IMD2 is *stronger* than the desired signal and can cause own RX desensitization. In general, an IIP2 in the order of $60 \cdots 70$ dBm is required for LTE receivers, which can be challenging to achieve [84]. This is again one clear motivating aspect behind this thesis work, in particular in [P4], where a digital regeneration and cancellation solution for this kind of transmitter in-band leakage-induced self-interference is developed.

Chapter 3

Digital Compensation of RF Impairments in OFDM and Uplink OFDMA/SC-FDMA Systems

This chapter presents the digital estimation and compensation methods for certain TX RF impairments and channel distortions in OFDM and multi-user uplink OFDMA and SC-FDMA systems. The analysis and proposed algorithms, originally presented in [P1], [P2], [P3], and [P7], are summarized in this chapter. In [P1] and [P2], both joint and de-coupled compensation techniques for frequency-selective TX I/Q imbalance and channel distortions in OFDM systems are proposed, which are now discussed in Section 3.1. The methods capable of jointly compensating the frequency-selective TX I/Q imbalances, small CFOs, and channel distortions in multi-user uplink OFDMA and SC-FDMA systems were proposed in [P3] and [P7], and are reviewed in Section 3.2. In all these studies, the estimation and compensation processing is done at the RX side, and the channels and impairments filter responses are estimated jointly by utilizing the embedded reference signals within the transmit data. Finally, the performance of the proposed techniques is demonstrated with simulation and measurement examples in Section 3.3.

3.1 Compensation of Frequency-Selective TX I/Q Imbalance and Channel Distortions in OFDM Systems

Most of the existing and emerging wireless systems rely on OFDM, or some of its variants, to provide high data rates under severe frequency-selective fading channels. The direct-conversion architecture represents a promising solution for such systems; however, OFDM systems employing a low-cost direct-conversion front-end are extremely vulnerable to hardware non-idealities such as I/Q imbalance and CFO. These impairments can, in turn, significantly limit the link performance. In recent years, there have been extensive studies on the performance analysis of OFDM systems under RF impairments. Among notable works, digital methods for compensating RF impairments include: TX I/Q imbalance calibration at TX [55, 85, 86, 87] or at RX [86, 88]; RX I/Q imbalance calibration [13, 32, 89, 90, 91, 92]; joint RX I/Q imbalance and channel compensation [93, 94, 95, 96, 97]; and joint TX and RX I/Q imbalance and channel compensation [98, 99, 100, 101, 102, 103]. Furthermore, RX I/Q imbalance and CFO compensation techniques are discussed in [31, 104, 105], while joint estimation and compensation techniques for TX and RX I/Q imbalance, CFO, and channel are discussed in [30, 106, 107, 108].

In contrast to joint TX and RX I/Q imbalance, CFO, and channel distortions compensation schemes, an alternative approach is de-coupled estimation and compensation, where only fast varying parameters in time, such as the channel impulse response or the CFO, are re-estimated and corrected while other parameters remain the same. A hybrid time-domain and frequency-domain compensation structure is proposed here for RF impairments and channel distortions compensation, where state-of-the-art RX I/Q imbalance and CFO compensation schemes are used in conjunction with the proposed TX I/Q imbalance and channel estimation and compensation techniques.

3.1.1 Signal and System Model

Fig. 3.1 shows the general structure of an OFDM system with RF impairments and channel, and the corresponding estimation and compensation blocks. Let \mathbf{X}

be the frequency-domain data symbol vector of size $M \times 1$, which is transformed to time-domain by an M -point inverse FFT. A CP of length N_g samples is then appended at the beginning of each OFDM symbol. After parallel-to-serial (P/S) conversion, the time-domain signal $x(t)$ is fed to a direct-conversion transmitter for transmission, where it is distorted by TX I/Q imbalance. The baseband equivalent of the distorted TX RF signal is of the similar form as given in (2.4). The signal then propagates through the multi-path block fading channel and arrives at the receiver. The CP length is assumed to be sufficiently large that there is no ISI between consecutive OFDM symbols. At the receiver, we assume that the LO of TX and RX are not synchronized and a CFO error is present. Also, the RX down-conversion stage is assumed non-ideal, which induces RX I/Q imbalance. Then, the frequency-domain received symbol at a subcarrier k , after serial-to-parallel (S/P) conversion, CP removal, and FFT operation, can be written as [P1], [P2]

$$\begin{aligned}
 \check{Y}(k) = & G_{1,RX}(k) \left\{ \begin{aligned} & H(k)G_{1,TX}(k)X(k)\Omega(k, k, \epsilon) + \\ & H(k)G_{2,TX}(k)X^*(-k)\Omega(k, k, \epsilon) + \\ & \sum_{l=0, l \neq k}^{M-1} H(l)G_{1,TX}(l)X(l)\Omega(l, k, \epsilon) + \\ & \sum_{l=0, l \neq k}^{M-1} H(l)G_{2,TX}(l)X^*(-l)\Omega(l, k, \epsilon) + \end{aligned} \right\} + \\
 & G_{2,RX}(k) \left\{ \begin{aligned} & H^*(-k)G_{2,TX}^*(k)X(k)\Omega^*(-k, -k, \epsilon) + \\ & H^*(k)G_{1,TX}^*(-k)X^*(-k)\Omega^*(-k, -k, \epsilon) + \\ & \sum_{l=0, l \neq k}^{M-1} H^*(-l)G_{2,TX}^*(-l)X(l)\Omega^*(-l, -k, \epsilon) + \\ & \sum_{l=0, l \neq k}^{M-1} H^*(-l)G_{1,TX}^*(-l)X^*(-l)\Omega^*(-l, -k, \epsilon) + \end{aligned} \right\} + \check{W}(k)
 \end{aligned} \tag{3.1}$$

where $-k$ denotes the mirror subcarrier, $H(k)$ denotes the channel frequency response at subcarrier k , $G_{1,TX;RX}(k)$; $G_{2,TX;RX}(k)$ denote the corresponding frequency-domain TX/RX I/Q imbalance filter responses, at subcarrier k , of the time-domain filters defined in (2.3), $\Omega(k, k, \epsilon)$ is the CFO leakage coefficient defined in (2.8), and $\check{W}(k) = G_{1,RX}(k)W(k) + G_{2,RX}(k)W^*(-k)$ represents the additive white Gaussian noise at the k^{th} subcarrier under RX I/Q imbalance. Based on the above equation, the data at any individual subcarrier k is interfered by the conjugate of the data at mirror subcarrier $-k$, due to I/Q imbalance, as well as by the data on all other subcarriers, due to CFO, therefore, causing ICI in OFDM systems.

In the following, we focus on the frequency-domain compensation of frequency-selective TX I/Q imbalance and channel distortions. It was discussed and verified in [P1] and [P2] that the RX I/Q imbalance can be compensated blindly using

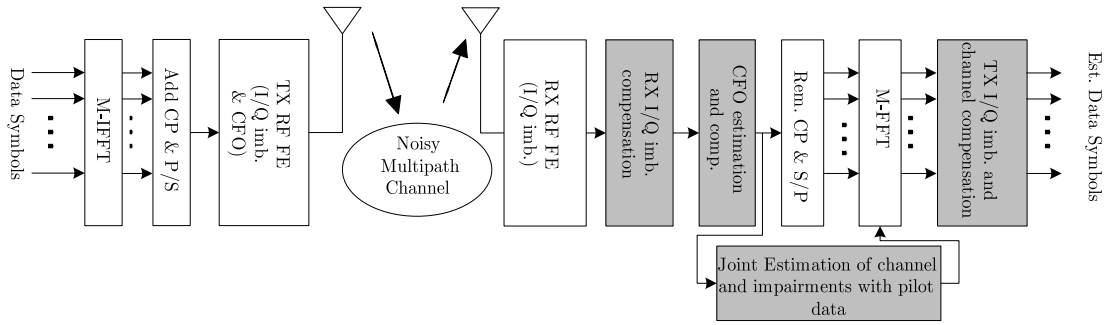


FIG. 3.1: Block diagram of OFDM system with proposed RF impairments and channel distortions estimation and compensation blocks in the receiver.

the technique proposed in [89, 90] and the CFO errors can also be estimated with good accuracy with the techniques proposed in [109], in the presence of TX I/Q imbalance and channel distortions. We thus assume these impairments reasonably well compensated in time-domain as shown in Fig. 3.1. This simplifies (3.1) to the following form

$$Y(k) = G_D(k)X(k) + G_M(k)X^*(-k) + W(k) \quad (3.2)$$

where $G_D(k) \triangleq H(k)G_{1,TX}(k)$ and $G_M(k) \triangleq H(k)G_{2,TX}(k)$ denote the direct and image signal filters, respectively, representing the joint response of TX I/Q imbalance and channel distortion at the k^{th} subcarrier, and filtering the data on mirror subcarriers. Then, with the knowledge of these filter parameters, the original transmitted data symbols can be recovered by applying, e.g., the ZF or ML principles. These aspects are elaborated in details in the next section.

3.1.2 Estimation and Compensation of TX I/Q Imbalance and Channel Distortions

The direct and mirror channel filters in (3.2) can be estimated in time-domain with embedded pilot data in the OFDM signal, which are then used for frequency-domain equalization, as shown in Fig. 3.1. Two different pilot patterns are commonly used in OFDM systems, namely preamble pilots, where an entirely known OFDM symbol is inserted at the beginning of the frame (like in IEEE802.11n and IEEE 802.16d [109]) and is commonly employed for estimating a slowly-varying channel, and sparse pilots, where the pilot symbols are multiplexed with the data in the time-frequency grid (like in 3GPP LTE/LTE-Advanced downlink [10]) and is often used for estimating the fast-varying channels. The time-domain data-aided

estimation with these pilot structures, and frequency-domain joint and de-coupled compensation techniques for TX I/Q imbalance and channel distortions are discussed next in the following subsections.

3.1.2.1 Joint Estimation and Compensation of TX I/Q Imbalance and Channel Distortions with Preamble Pilot Structure

We have observed that the TX I/Q imbalance causes mirror frequency interference, which, in turn, imposes that the impaired signals at mirror frequencies/-subcarriers should be processed jointly. We thus propose here a widely-adopted frequency-domain approach where TX I/Q imbalance and channel impairments are compensated jointly by processing the pairs of mirror subcarriers. This can be done by stacking the frequency-domain received signal at the k^{th} subcarrier $Y(k)$ and the complex conjugate of its mirror subcarrier $Y^*(-k)$ in a vector as

$$\underbrace{\begin{bmatrix} Y(k) \\ Y^*(-k) \end{bmatrix}}_{\tilde{\mathbf{Y}}(k)} = \underbrace{\begin{bmatrix} G_D(k) & G_M(k) \\ G_M^*(-k) & G_D^*(-k) \end{bmatrix}}_{\tilde{\mathbf{G}}(k)} \underbrace{\begin{bmatrix} X(k) \\ X^*(-k) \end{bmatrix}}_{\tilde{\mathbf{X}}(k)} + \underbrace{\begin{bmatrix} W^i(k) \\ W^*(-k) \end{bmatrix}}_{\tilde{\mathbf{W}}(k)} \quad (3.3)$$

where the *total channel matrix* $\tilde{\mathbf{G}}(k)$ represents the joint effect of TX I/Q imbalance and channel distortions for the received data symbols on mirror subcarriers.

Assuming first that the coefficients of $\tilde{\mathbf{G}}(k)$ are known, the original data symbols can then be estimated using, e.g., the joint ZF (J-ZF) equalization, such as

$$\begin{bmatrix} \hat{X}_{ZF}(k) \\ \hat{X}_{ZF}^*(-k) \end{bmatrix} = \tilde{\mathbf{G}}_{ZF}(k) \begin{bmatrix} Y(k) \\ Y^*(-k) \end{bmatrix} = \tilde{\mathbf{G}}^{-1}(k) \begin{bmatrix} Y(k) \\ Y^*(-k) \end{bmatrix}. \quad (3.4)$$

However, ZF equalization is known to suffer from the noise enhancement problem, thus, alternatively; the joint maximum-likelihood (J-ML) detection principle can be employed for detecting the transmitted symbols, which is based on the principle of minimizing the following cost function

$$\begin{bmatrix} \hat{X}_{ML}(k) \\ \hat{X}_{ML}^*(-k) \end{bmatrix} = \arg \min_{\tilde{X}(k), \tilde{X}^*(-k)} \left\| \tilde{\mathbf{G}}(k) \begin{bmatrix} \tilde{X}(k) \\ \tilde{X}^*(-k) \end{bmatrix} - \begin{bmatrix} Y(k) \\ Y^*(-k) \end{bmatrix} \right\|^2 \quad (3.5)$$

where $\check{X}(k)$ denotes the trial value of the data symbol at the k^{th} subcarrier. The ML equalizer can exploit the frequency diversity induced by the TX I/Q imbalance [100, 110, 111] and gives better performance than the ZF equalizer, but the computational complexity associated with ML is very high, which increases with higher-order subcarrier modulation and large number of subcarriers.

The parameters of the total channel matrix can be estimated in time-domain with the LS model fitting principle. For that, we switch to vector-matrix notations and write the time-domain received OFDM symbol corresponding to the preamble pilot transmission as $\underline{\mathbf{y}}_\varrho = \begin{bmatrix} y_\varrho(0) & y_\varrho(1) & y_\varrho(2) & \cdots & y_\varrho(M-1) \end{bmatrix}^T$, where ϱ denotes the preamble pilot OFDM symbol index in a slot. The time-domain direct and mirror channel filters are modeled to have length N_h -taps such that $N_h \ll M$. The received OFDM symbol vector during the pilot transmission is then given by

$$\underline{\mathbf{y}}_\varrho = \mathbf{x}_\varrho \underline{\mathbf{g}}_D + \mathbf{x}_\varrho^* \underline{\mathbf{g}}_M + \underline{\mathbf{w}}_\varrho = \underbrace{\begin{bmatrix} \mathbf{x}_\varrho & \mathbf{x}_\varrho^* \end{bmatrix}}_{\mathbf{x}_\varrho^B} \underbrace{\begin{bmatrix} \underline{\mathbf{g}}_D \\ \underline{\mathbf{g}}_M \end{bmatrix}}_{\underline{\mathbf{g}}^B} + \underline{\mathbf{w}}_\varrho \quad (3.6)$$

where \mathbf{x}_ϱ is the time-domain *circular-convolution matrix* formed by taking inverse FFT of the frequency-domain pilot symbol vector $\underline{\mathbf{X}}_\varrho$. The LS estimate of the direct and mirror channel filters can then be computed as [112]

$$\begin{bmatrix} \hat{\underline{\mathbf{g}}}_D \\ \hat{\underline{\mathbf{g}}}_M \end{bmatrix} = \left(\mathbf{x}_\varrho^{B^H} \mathbf{x}_\varrho^B \right)^{-1} \mathbf{x}_\varrho^{B^H} \underline{\mathbf{y}}_\varrho. \quad (3.7)$$

The estimation procedure is repeated similarly on all subframes, and the frequency-domain expressions of the time-domain estimated filters, which are needed for the equalization/detection in (3.4) and (3.5), are obtained by taking an M -FFT and linearly interpolating them to all OFDM data symbols in different slots.

3.1.2.2 De-coupled Estimation and Compensation of TX I/Q Imbalance and Channel Distortions with Sparse Pilot Structure

The proposed compensation algorithm for the sparse pilot structure, also operating in frequency-domain, is based on compensating the channel distortions and TX I/Q imbalance successively, and is summarized in Table 3.1.

TABLE 3.1: De-coupled compensation of channel distortions and frequency-selective TX I/Q imbalance

1. Estimate the direct channel filter $G_D(k)$ and divide (3.2) by $G_D(k)$ to obtain the equalized subcarriers as

$$\begin{aligned}\check{Y}(k) &= X(k) + \frac{G_M(k)}{G_D(k)}X^*(-k) + \frac{1}{G_D(k)}W(k) \\ &= X(k) + \frac{G_{2,TX}(k)}{G_{1,TX}(k)}X^*(-k) + \frac{1}{G_D(k)}W(k)\end{aligned}\quad (3.8)$$

which shows that the channel effect is removed from the original data symbols and the only impairment present in the signal now is the transmitter I/Q imbalance.

2. Hard-decision-based detection of the mirror subcarriers of the equalized symbol, i.e. $\hat{Y}(-k) = D(\check{Y}(-k))$ where D denotes the decision operator.
3. Now at the pilot locations, the received symbol ϱ at the k^{th} subcarrier is given by

$$\check{Y}_\varrho(k) = X_\varrho(k) + G_\varrho^{comp}(k)\hat{Y}(-k) \quad (3.9)$$

4. From the above equation, we find the compensation filter at the pilot locations as

$$G_\varrho^{comp}(k) = \frac{\check{Y}_\varrho(k) - X_\varrho(k)}{\hat{Y}(-k)} \quad (3.10)$$

5. Interpolate $G_\varrho^{comp}(k)$ to all OFDM symbols as well as to all subcarriers to obtain $G^{comp}(k)$.
6. The estimated symbol at the k^{th} subcarrier is then $\hat{X}(k) = \check{Y}(k) + G^{comp}(k)\hat{Y}(-k)$.

As for the parameter estimation, it can be noticed from Table 3.1 that one needs only the estimates of the direct channel filter $G_D(k)$, which, as discussed in the previous subsection, can be estimated in time-domain as

$$\hat{\mathbf{g}}_D = (\mathbf{x}_\varrho^H \mathbf{x}_\varrho)^{-1} \mathbf{x}_\varrho^H \mathbf{y}_\varrho \quad (3.11)$$

where now $\mathbf{x}_\varrho = \mathbf{F}_{\Gamma^\varrho}^{-1} \mathbf{X}_{\Gamma^\varrho}$ refers to the time-domain circular convolution matrix of the pilot data, and $\mathbf{y}_\varrho = \mathbf{F}_{\Gamma^\varrho}^{-1} \mathbf{Y}_{\Gamma^\varrho}$ is the time-domain received signal, respectively, with the subscript Γ^ϱ denoting the pilot data indexes in a transmission slot, and \mathbf{F}_M denoting the $M \times M$ FFT matrix. The corresponding frequency-domain filter response, used in (3.8), is then obtained by taking the M -point FFT.

Next, we derive the interpolation of filter $G_\rho^{comp}(k)$ in (3.10) to all subcarriers in all OFDM symbols. Assume that the estimates on pilot locations stem from a time-domain impulse response $\underline{\mathbf{g}}_\rho^{comp}$ of length N_g , then the model for the compensation filter, defined in (3.10), becomes $\mathbf{G}_\rho^{comp} = \mathfrak{Diag}(\mathbf{F}_{\Gamma^e, 1:N_g} \underline{\mathbf{g}}_\rho^{comp})$. Let us define the DFT matrix $\mathbf{F}_g = \mathbf{F}_{\Gamma^e, 1:N_g}$ which comprises of the first N_g columns and rows corresponding to the pilot subcarriers of the $M \times M$ DFT matrix \mathbf{F}_M , then $\underline{\mathbf{g}}_\rho^{comp}$ in the LS sense is given by [P2]

$$\underline{\mathbf{g}}_\rho^{comp} = (\mathbf{F}_g^H \mathbf{F}_g)^{-1} \mathbf{F}_g \mathbf{G}_\rho^{comp}. \quad (3.12)$$

The interpolated frequency-domain coefficients can then be directly obtained as $\mathbf{G}^{comp} = \mathbf{F}_{1:M, 1:N_g} \underline{\mathbf{g}}_\rho^{comp}$, and linearly interpolated on all OFDM symbols within the subframe. This is used to detect the original transmit data, as shown in the last step of Table 3.1. The proposed estimation and compensation process is executed independently at every subframe.

3.2 Compensation of TX RF Impairments and Channel Distortions in Multi-User Uplink OFDMA and SC-FDMA Systems

In this section, the joint channel and TX RF impairments estimation and equalization methods are discussed in the context of multi-user multicarrier uplink systems. We study an uplink SC-FDMA system which is the uplink physical layer radio access technique in 3GPP LTE/LTE-Advanced, however, the signal models and proposed algorithms are equally applicable to uplink OFDMA systems also, given that time multiplexed reference signals are used for the parameters estimation. The estimation and compensation are carried out at the BS RX, derived here first for the single antenna receiver and then generalized for a receiver with an arbitrary number of receiver antennas.

In general, the compensation techniques developed for OFDM systems cannot be directly applied to uplink OFDMA/SC-FDMA systems. The TX I/Q imbalance-induced mirror frequency interference causes classical ICI in OFDM systems, whereas in multi-user OFDMA/SC-FDMA type systems, I/Q imbalance induces both ICI and IUI between mirror sub-band/channel users (see Section 2.3.1). The

effect of I/Q imbalances in OFDMA and SC-FDMA systems has been investigated to some extent in recent literature and the notable work, such as [19, 113, 114], always assume known channel and I/Q imbalance parameters for equalization. On the other hand, Mahmoud *et al.* [115] proposed a joint channel and frequency-independent TX I/Q imbalance estimation using a group of mirror subcarrier pairs located symmetrically around the center subcarrier. However, such a technique has a poor spectral efficiency due to a large number of specific pilots being used for the estimation. The impact of joint frequency-selective TX and RX I/Q imbalance on the error vector magnitude (EVM) is investigated in [116], but no estimation or compensation method is proposed. A circularity-based compensation scheme for RX I/Q imbalance in SC-FDMA systems is presented in [117]. Finally, a joint channel and I/Q imbalance and propagation delay estimation technique for multi-user asynchronous uplink OFDMA systems is proposed recently in [110], which assumes distributed subcarrier assignments with mirror subcarriers being always allocated to the same user.

The major contributions of the techniques proposed in this thesis, compared with the existing literature, are as follows:

1. The main challenge in joint estimation and compensation of channel and impairments is the insufficient number of independent equations to solve for the parameters (see equation (3.17)). An efficient approximation of joint channel and RF impairments filter responses with polynomial-based basis functions is presented, which solves this problem. Furthermore, the proposed formulation allows estimation with arbitrary time-multiplexed reference symbols without mirror subcarriers allocated to the same user, and also supports multiple users on the mirror sub-band of a user.
2. A compensation structure utilizing pairs of mirror subcarriers and two joint channel and impairments equalization schemes, stemming from the zero-forcing (ZF) and minimum mean-square error (MMSE) principle, are proposed. The joint mirror subcarrier MMSE equalizer is derived to process uplink mirror sub-band users with unequal received power levels.

The working assumptions in the development of the proposed estimation and compensation framework are closely related to the 3GPP LTE/LTE-Advanced uplink standardization, in terms of I/Q image suppression for UEs, uplink CFO errors,

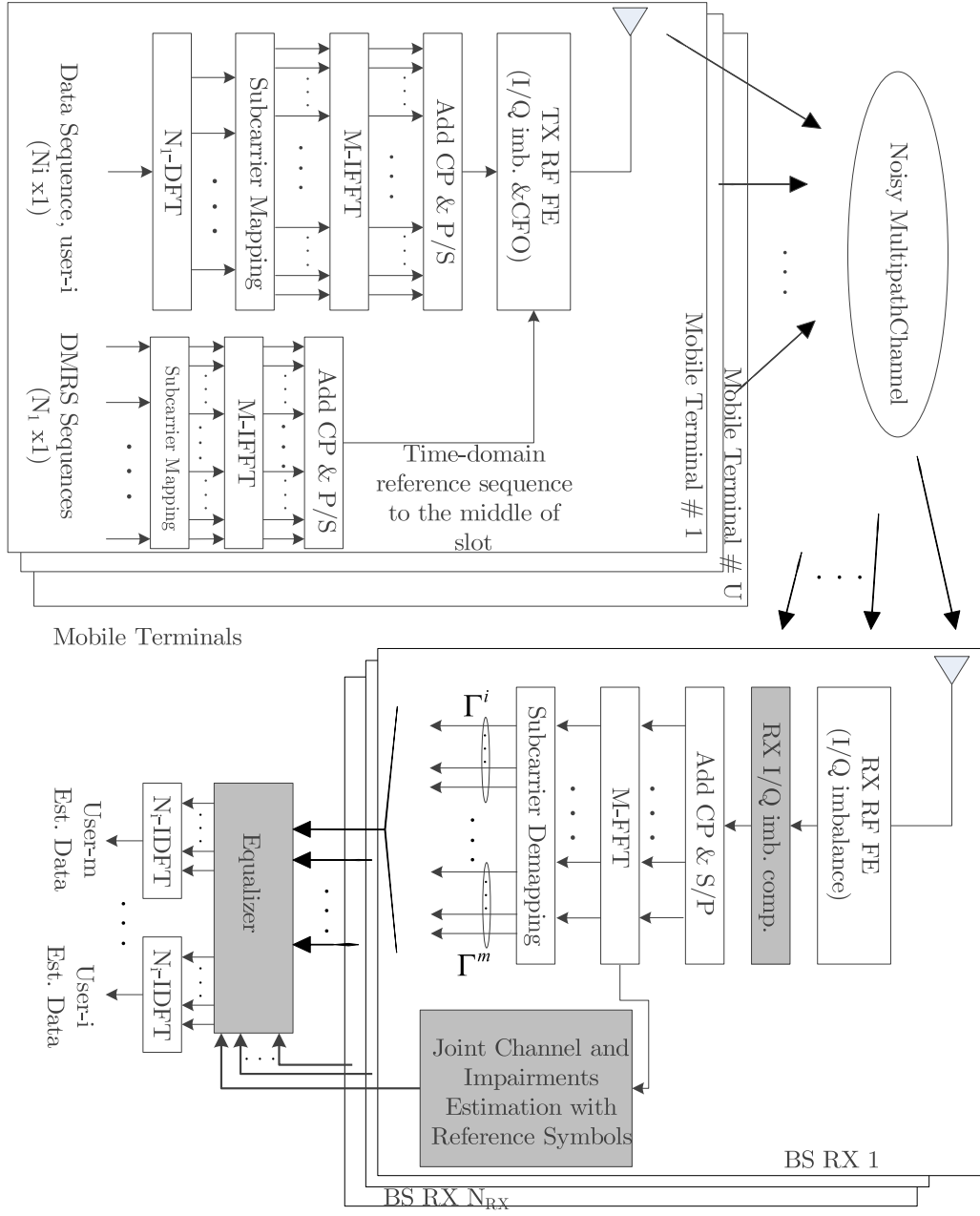


FIG. 3.2: Block diagram of SC-FDMA uplink system with RF impairments and their corresponding equalization/compensation blocks in the BS RX.

and uplink in-band dynamic range for a 3GPP LTE/LTE-Advanced BS receiver. Hence, the proposed solutions can be directly applied in the BS receivers without any modification in the design of the RF transceiver or in the LTE/LTE-Advanced standardization.

3.2.1 Multi-User Uplink Signal Models Under RF Impairments and Channel Distortions

The system model of multi-user uplink SC-FDMA radio link with radio impairments, channels, and the corresponding estimation and compensation blocks is shown in Fig. 3.2. Consider a scenario where U —users are communicating simultaneously with a single BS RX with N_{RX} receiving antennas through their independent multi-path channels. The $N_i \times 1$ data symbol vector of a user- i is first transformed to frequency-domain by means of an N_i —point FFT and then the output samples are mapped to consecutive OFDMA subcarriers, i.e. *localized subcarrier mapping*. The subcarrier mapping is followed by an M —point inverse FFT operation to convert the data to time-domain, after which the CP is appended. The complex baseband signal of user- i , denoted by $x^i(t)$, is distorted by TX I/Q imbalance in the up-conversion stage, and the TX signal then propagates through a multi-path block fading channel whose delay spread is assumed to be shorter than the CP length. At the BS receiver, the overall received signal is composed of the signals received from U —users and additive noise. We assume that the LOs in UE TXs are not perfectly synchronized with the BS LO, thus there exist CFOs. In addition, the RX down-converter is assumed non-ideal such that it induces RX I/Q imbalance. The frequency-domain baseband signal of user- i at subcarrier k after CP removal, FFT, and subcarrier demapping is then given by

[P3], [P7]

$$\begin{aligned}
 Y^i(k) &= G_{1,RX}(k) \left\{ \begin{aligned} &H^i(k)G_{1,TX}^i(k)X^i(k)\Omega(k, k, \epsilon^i) + \\ &H^m(k)G_{2,TX}^m(k)X^m(-k)^*\Omega(k, k, \epsilon^m) + \\ &\sum_{l \in \Gamma^i, l \neq k} H^i(l)G_{1,TX}^i(l)X^i(l)\Omega(l, k, \epsilon^i) + \\ &\sum_{l \in \Gamma^i, l \neq k} H^m(l)G_{2,TX}^m(l)X^m(-l)^*\Omega(l, k, \epsilon^m) + \\ &\sum_{j=1, j \neq i}^U \sum_{l \in \Gamma^j} H^j(l)G_{1,TX}^j(k)X^j(l)\Omega(l, k, \epsilon^j) + \\ &\sum_{j=1, j \neq m}^U \sum_{l \in \Gamma^j} H^j(l)G_{2,TX}^j(l)X^j(-l)^*\Omega(l, k, \epsilon^j) \end{aligned} \right\} + \\
 G_{2,RX}(k) &\left\{ \begin{aligned} &H^i(-k)^*G_{2,TX}^i(-k)^*X^i(k)\Omega(-k, -k, \epsilon^i)^* + \\ &H^m(-k)^*G_{1,TX}^m(-k)^*X^m(-k)^*\Omega(-k, -k, \epsilon^m)^* + \\ &\sum_{l \in \Gamma^i, l \neq k} H^i(-l)^*G_{2,TX}^i(-l)^*X^i(l)\Omega(-l, -k, \epsilon^i)^* + \\ &\sum_{l \in \Gamma^i, l \neq k} H^m(-l)^*G_{1,TX}^m(-l)^*X^m(-l)^*\Omega(-l, -k, \epsilon^m)^* + \\ &\sum_{j=1, j \neq i}^U \sum_{l \in \Gamma^j} H^j(-l)^*G_{2,TX}^j(-l)^*X^j(l)\Omega(-l, -k, \epsilon^j)^* + \\ &\sum_{j=1, j \neq i}^U \sum_{l \in \Gamma^j} H^j(-l)^*G_{1,TX}^j(-l)^*X^j(-l)^*\Omega(-l, -k, \epsilon^j)^* \end{aligned} \right\} + \\
 \check{W}^i(k) & \quad \quad \quad k \in \Gamma^i
 \end{aligned} \tag{3.13}$$

where the superscript m refers to the user located on the mirror sub-band of user- i . Equation (3.13) describes the IUI generated by the image of mirror user- m as a result of TX and RX I/Q imbalances and CFOs, as well as the ICI from the user- i 's own data due to RX I/Q imbalance and CFO. Now, by invoking practical considerations of small uplink CFOs for LTE UEs (i.e. ± 0.1 PPM of carrier frequency [2, 56]) such that it does not induce considerable ICI from the user's own neighboring subcarriers as well as negligibly small IUI, and RX I/Q imbalance compensation *a priori*¹, the signal model in (3.13) then simplifies to

$$Y^i(k) = X^i(k)G_D^i(k) + X^m(-k)^*G_M^i(k) + W^i(k) \tag{3.14}$$

where $G_D^i(k) \triangleq H^i(k)G_{1,T}^i(k)\Omega(k, k, \epsilon^i)$ and $G_M^i(k) \triangleq H^m(k)G_{2,T}^m(k)\Omega(k, k, \epsilon^m)$ denote the direct and mirror channel responses of user- i , respectively.

To emphasize and model the IUI problem in uplink SC-FDMA/OFDMA due to TX I/Q imbalance, we switch to vector-matrix notation. Let $\underline{\mathbf{Y}} = [Y(0) \ Y(1) \ Y(2) \ \cdots \ Y(M-1)]^T$ denote the M samples of the composite received signal vector after CP removal and FFT. The received signal

¹This is a reasonable assumption for BS RX, where the blind technique from [89] can be used for compensating RX I/Q imbalance.

vector of user- i , denoted by $\underline{\mathbf{Y}}^i$ and containing the samples of (3.14), is obtained by left multiplying $\underline{\mathbf{Y}}$ with the demapping matrix of user- i , defined as $\mathbf{M}^i = \begin{bmatrix} \mathbf{0}_{N_i \times (\Gamma_N^i(1)-1)} & \mathbf{I}_{N_i \times N_i} & \mathbf{0}_{N_i \times (M-\Gamma_N^i(N_i))} \end{bmatrix}$. This is given by

$$\underline{\mathbf{Y}}^i = \mathbf{M}^i \underline{\mathbf{Y}} = \mathbf{X}^i \underline{\mathbf{G}}_D^i + \mathbf{X}^{m\#} \underline{\mathbf{G}}_M^i + \underline{\mathbf{W}}^i = \tilde{\mathbf{X}} \tilde{\mathbf{G}}^i + \underline{\mathbf{W}}^i \quad (3.15)$$

where $\tilde{\mathbf{X}} \triangleq \begin{bmatrix} \mathbf{X}^i & \mathbf{X}^{m\#} \end{bmatrix}$ and $\tilde{\mathbf{G}}^i \triangleq \begin{bmatrix} (\underline{\mathbf{G}}_D^i)^T & (\underline{\mathbf{G}}_M^i)^T \end{bmatrix}^T$, and \mathbf{X}^i and $\mathbf{X}^{m\#}$ are the diagonal matrices of FFT pre-coded transmitted data symbols of dimension $N_i \times N_i$ and the direct and mirror channel filter vectors $\underline{\mathbf{G}}_D^i$ and $\underline{\mathbf{G}}_M^i$ are of length $N_i \times 1$. In the multi-user uplink transmission context, the exact structure of the matrix $\mathbf{X}^{m\#}$ and the vector $\underline{\mathbf{G}}_M^i$ depends on the bandwidth occupancy of direct and mirror channel users. To model such a scenario that the uplink users bandwidths are not equal, we denote the number of users located on the mirror sub-band of a user- i by N_u . This results in the following structure of $\mathbf{X}^{m\#}$ and $\underline{\mathbf{G}}_M^i$:

$$\begin{aligned} \mathbf{X}^{m\#} &= \text{Diag} \left(\left[\left(\underline{\mathbf{X}}^{m_1\#} \right)^T \left(\underline{\mathbf{X}}^{m_2\#} \right)^T \dots \left(\underline{\mathbf{X}}^{m_{N_u}\#} \right)^T \right]^T \right) \\ \underline{\mathbf{G}}_M^i &= \left[\left(\underline{\mathbf{G}}_M^{i_1\#} \right)^T \left(\underline{\mathbf{G}}_M^{i_2\#} \right)^T \dots \left(\underline{\mathbf{G}}_M^{i_{N_u}\#} \right)^T \right]^T \end{aligned} \quad (3.16)$$

which implies that for decoding an individual UE's signal, the mirror channel responses and transmitter impairment parameters need to be estimated for multiple mirror UEs. This problem has also been illustrated at a conceptual level in Fig. 2.4 for multi-channel signals.

From the above discussion, it is evident that with current I/Q imaging and CFO specifications in the 3GPP LTE/LTE-Advanced standardization for UEs, the TX I/Q imbalances are expected to play a bigger role than the CFOs, and can severely degrade the system performance, in particular with higher-order subcarrier modulation and considerable power difference between a given UE and its mirror sub-band UEs. It is therefore imperative to estimate and thereafter compensate these impairments. In the following sections, we formulate the joint estimation and compensation solutions for TX I/Q imbalances, small uplink CFOs, and channel distortions.

3.2.2 Joint Equalization of TX I/Q Imbalances, Small CFOs, and Channel Distortions

We first develop the compensation solutions with known channel and impairment parameters and then address the parameter estimation with LTE compliant reference signals.

Again following the same compensation philosophy as in Section 3.1.2.1, that the TX I/Q imbalance causes interference among the users located on mirror sub-band, we propose an equalizer that processes the mirror sub-band users and operates subcarrier-wise. The frequency-domain received signal of a user- i at k^{th} subcarrier $Y^i(k)$ and the complex conjugate of its mirror subcarrier $Y^m(-k)^*$ can be written as

$$\underbrace{\begin{bmatrix} Y^i(k) \\ Y^m(-k)^* \end{bmatrix}}_{\tilde{\mathbf{Y}}(k)} = \underbrace{\begin{bmatrix} G_D^i(k) & G_M^i(k) \\ G_M^m(-k)^* & G_D^m(-k)^* \end{bmatrix}}_{\tilde{\mathbf{G}}(k)} \underbrace{\begin{bmatrix} X^i(k) \\ X^m(-k)^* \end{bmatrix}}_{\tilde{\mathbf{X}}(k)} + \underbrace{\begin{bmatrix} W^i(k) \\ W^m(-k)^* \end{bmatrix}}_{\tilde{\mathbf{W}}(k)} \quad (3.17)$$

where now the total channel matrix $\tilde{\mathbf{G}}(k)$ represents the joint effect of TX I/Q imbalances, small CFOs, and channel distortions for the received signals at mirror subcarriers. Having known coefficients of $\tilde{\mathbf{G}}(k)$, the transmitted data symbols can be estimated by employing a linear equalizer such as the joint MMSE (J-MMSE), which in addition to the total channel matrix parameters, utilizes also the information of signal-to-noise ratio (SNR) of mirror sub-band users. The J-MMSE equalizer uses an equalization filter $\tilde{\mathbf{G}}_{MMSE}(k)$ which filters the received signal as

$$\begin{bmatrix} \hat{X}_{MMSE}^i(k) \\ \hat{X}_{MMSE}^m(-k)^* \end{bmatrix} = \tilde{\mathbf{G}}_{MMSE}(k) \begin{bmatrix} Y^i(k) \\ Y^m(-k)^* \end{bmatrix}. \quad (3.18)$$

The filter $\tilde{\mathbf{G}}_{MMSE}(k)$ minimizes the mean-square error (MSE) between the DFT-spread transmitted samples and the DFT-spread equalized samples, and is of the following form

$$\tilde{\mathbf{G}}_{MMSE}(k) = \begin{bmatrix} \left(\Xi^{-1}(k) \begin{bmatrix} G_D^i(k)^* \\ G_M^m(-k) \end{bmatrix} \right)^T \\ \left(\Xi^{-1}(k) \begin{bmatrix} G_M^i(k)^* \frac{\gamma^m(-k)}{\gamma^i(k)} \\ G_D^m(-k) \frac{\gamma^m(-k)}{\gamma^i(k)} \end{bmatrix} \right)^T \end{bmatrix} \quad (3.19)$$

where $\Upsilon^i(k) \triangleq \sigma_x^{i^2}(k)/\sigma_w^2$ and $\Upsilon^m(-k) \triangleq \sigma_x^{m^2}(-k)/\sigma_w^2$ denote the per subcarrier SNR of direct and mirror users at k^{th} and $(-k)^{th}$ subcarriers, with $\sigma_x^{i^2}(k) = \mathbb{E} \{ |X^i(k)|^2 \}$ and $\sigma_x^{m^2}(-k) = \mathbb{E} \{ |X^m(-k)|^2 \}$ representing the direct and mirror channel signal powers at k^{th} and its mirror $(-k)^{th}$ subcarrier, respectively, σ_w^2 denotes the noise power which is equal on all subcarriers, and the matrix $\Xi(k)$ is defined as [P7]

$$\begin{aligned} \Xi(k) &= \begin{bmatrix} \Xi_{11}(k) & \Xi_{12}(k) \\ \Xi_{21}(k) & \Xi_{22}(k) \end{bmatrix} \\ \Xi_{11}(k) &= |G_D^i(k)|^2 + |G_M^i(k)|^2 \frac{\Upsilon^m(-k)}{\Upsilon^i(k)} + \frac{1}{\Upsilon^i(k)} \\ \Xi_{12}(k) &= (G_D^{i*}(k)G_M^{m*}(-k)) + (G_M^{i*}(k)G_D^{m*}(-k)) \frac{\Upsilon^m(-k)}{\Upsilon^i(k)} \\ \Xi_{21}(k) &= (G_D^i(k)G_M^m(-k)) + (G_M^i(k)G_D^m(-k)) \frac{\Upsilon^m(-k)}{\Upsilon^i(k)} \\ \Xi_{22}(k) &= |G_M^{m*}(-k)|^2 + |G_D^{m*}(-k)|^2 \frac{\Upsilon^m(-k)}{\Upsilon^i(k)} + \frac{1}{\Upsilon^m(-k)}. \end{aligned} \quad (3.20)$$

Alternatively, the joint ZF (J-ZF) equalizer nulls the impairments and channel distortion effects by applying the inverse of the total channel matrix to the received signal as

$$\begin{bmatrix} \hat{X}_{ZF}^i(k) \\ \hat{X}_{ZF}^m(-k)^* \end{bmatrix} = \tilde{\mathbf{G}}_{ZF}(k) \begin{bmatrix} Y^i(k) \\ Y^m(-k)^* \end{bmatrix} = \tilde{\mathbf{G}}^{-1}(k) \begin{bmatrix} Y^i(k) \\ Y^m(-k)^* \end{bmatrix} \quad (3.21)$$

but is known, in general, to suffer from noise enhancement problems.

3.2.2.1 Extension to Multi-Antenna Receiver

The above equalizer formulations can be generalized to a BS RX with multiple receiving antennas, as the one shown in Fig. 3.2. In this case, the signal transmitted by a user from its antenna arrives at the RX antennas through different channels. We assume that the channels between a user's TX antenna and each RX antenna are uncorrelated. With multiple differently faded copies of the same transmitted signal, the RX can then exploit diversity which improves the performance considerably.

With N_{RX} receiving antennas, the received signal at the k^{th} subcarrier of a user $-i$ and its mirror user $-m$ in (3.17) can be re-written by stacking the mirror subcarrier pairs from all N_{RX} antennas as

$$\underbrace{\begin{bmatrix} \tilde{\mathbf{Y}}_1(k) \\ \vdots \\ \tilde{\mathbf{Y}}_{N_{RX}}(k) \end{bmatrix}}_{\tilde{\mathbf{Y}}_{SIMO}(k)} = \underbrace{\begin{bmatrix} \tilde{\mathbf{G}}_1(k) \\ \vdots \\ \tilde{\mathbf{G}}_{N_{RX}}(k) \end{bmatrix}}_{\tilde{\mathbf{G}}_{SIMO}(k)} \tilde{\mathbf{X}}(k) + \underbrace{\begin{bmatrix} \tilde{\mathbf{W}}_1(k) \\ \vdots \\ \tilde{\mathbf{W}}_{N_{RX}}(k) \end{bmatrix}}_{\tilde{\mathbf{W}}_{SIMO}(k)} \quad (3.22)$$

where

$$\begin{aligned} \tilde{\mathbf{Y}}_\chi(k) &= \begin{bmatrix} Y_\chi^i(k) & Y_\chi^m(-k)^* \end{bmatrix}^T; \quad \tilde{\mathbf{G}}_\chi(k) = \begin{bmatrix} G_{D,\chi}^i(k) & G_{M,\chi}^i(k) \\ G_{M,\chi}^m(-k)^* & G_{D,\chi}^m(-k)^* \end{bmatrix} \\ \tilde{\mathbf{W}}_\chi(k) &= \begin{bmatrix} W_\chi^i(k) & W_\chi^m(-k)^* \end{bmatrix}^T \quad \chi \in \{1, 2, \dots, N_{RX}\}. \end{aligned} \quad (3.23)$$

The J-ZF and J-MMSE equalizers are then given directly by

$$\begin{bmatrix} \hat{X}_{ZF}^i(k) \\ \hat{X}_{ZF}^m(-k)^* \end{bmatrix} = \left(\tilde{\mathbf{G}}_{SIMO}^H(k) \tilde{\mathbf{G}}_{SIMO}(k) \right)^{-1} \tilde{\mathbf{G}}_{SIMO}^H(k) \tilde{\mathbf{Y}}_{SIMO}(k) \quad (3.24)$$

and

$$\begin{bmatrix} \hat{X}_{MMSE}^i(k) \\ \hat{X}_{MMSE}^m(-k)^* \end{bmatrix} = \tilde{\mathbf{G}}_{MMSE}^{SIMO}(k) \tilde{\mathbf{Y}}_{SIMO}(k) \quad (3.25)$$

where $\tilde{\mathbf{G}}_{MMSE}^{SIMO}(k)$ is given by [P7]

$$\tilde{\mathbf{G}}_{MMSE}^{SIMO}(k) = \left(\tilde{\mathbf{G}}_{SIMO}^H(k) \mathbf{R}_{\mathbf{W}\mathbf{W}}^{-1} \tilde{\mathbf{G}}_{SIMO}(k) + \mathbf{R}_{\mathbf{X}\mathbf{X}}^{-1}(k) \right)^{-1} \tilde{\mathbf{G}}_{SIMO}^H(k) \mathbf{R}_{\mathbf{W}\mathbf{W}}^{-1}, \quad (3.26)$$

with $\mathbf{R}_{\mathbf{X}\mathbf{X}}(k) = \mathbb{E} \left\{ \tilde{\mathbf{X}}(k) \tilde{\mathbf{X}}^H(k) \right\}$ and $\mathbf{R}_{\mathbf{W}\mathbf{W}} = \mathbb{E} \left\{ \tilde{\mathbf{W}}_{SIMO}(k) \tilde{\mathbf{W}}_{SIMO}^H(k) \right\}$ are diagonal auto-covariance matrices of data and noise, respectively, defined as

$$\begin{aligned} \mathbf{R}_{\mathbf{X}\mathbf{X}}(k) &= \mathfrak{Diag} \left(\sigma_x^{i^2}(k), \sigma_x^{m^2}(-k) \right) \\ \mathbf{R}_{\mathbf{W}\mathbf{W}} &= \mathfrak{Diag} \left(\sigma_{w,1}^2, \sigma_{w,1}^2, \dots, \sigma_{w,N_{RX}}^2, \sigma_{w,N_{RX}}^2 \right) \end{aligned} \quad (3.27)$$

where the noise power is assumed equal on all subcarriers of a single antenna.

The above equalizer formulations in (3.18), (3.21), (3.24), and (3.25) assume that the essential parameters and responses are known, while in practice they need to be estimated. In the next section, we present a basis function representation of

the effective channel response vectors, in order to reduce the estimation parameter space, and then discuss the estimation methods.

3.2.3 Efficient Response Representation with Basis Functions

The effective direct and mirror channel response filters in (3.15) can be efficiently modeled with *basis functions*, where each response filter is expressed as a product of a known *basis function matrix* and an unknown *coefficient vector*. The basis function representation solves the *under-determined problem* of (3.17) and also greatly reduces the size of parameter space.

A simple model of (3.15) based on representing the effective channel response vectors $\underline{\mathbf{G}}_D^i$ and $\underline{\mathbf{G}}_M^i$ with the basis functions can be obtained as

$$\begin{aligned} \underline{\mathbf{Y}}^i &= \mathbf{X}^i \mathbf{B}_D^i \underline{\mathbf{G}}_{D,B}^i + \mathbf{X}^{m\#} \mathbf{B}_M^i \underline{\mathbf{G}}_{M,B}^i + \underline{\mathbf{W}}^i \\ &= \mathbf{X}^i \mathbf{B}_D^i \underline{\mathbf{G}}_{D,B}^i + \mathbf{X}^{m\#} \mathfrak{B} \mathfrak{D} \text{diag} \left(\begin{bmatrix} \mathbf{B}_M^{i_1} \\ \mathbf{B}_M^{i_2} \\ \vdots \\ \mathbf{B}_M^{i_{N_u}} \end{bmatrix} \right) \begin{bmatrix} \underline{\mathbf{G}}_{M,B}^{i_1} \\ \underline{\mathbf{G}}_{M,B}^{i_2} \\ \vdots \\ \underline{\mathbf{G}}_{M,B}^{i_{N_u}} \end{bmatrix} + \underline{\mathbf{W}}^i \\ &= \tilde{\mathbf{X}} \tilde{\mathbf{B}}^i \tilde{\mathbf{G}}_B^i + \underline{\mathbf{W}}^i \end{aligned} \quad (3.28)$$

where

$$\begin{aligned} \mathbf{B}_D^i &= \begin{bmatrix} \underline{\mathbf{B}}_{D,0}^i & \underline{\mathbf{B}}_{D,1}^i & \cdots & \underline{\mathbf{B}}_{D,N_D}^i \end{bmatrix}; \quad \mathbf{B}_M^i = \begin{bmatrix} \underline{\mathbf{B}}_{M,0}^{i_p} & \underline{\mathbf{B}}_{M,1}^{i_p} & \cdots & \underline{\mathbf{B}}_{M,N_M}^{i_p} \end{bmatrix} \\ \underline{\mathbf{G}}_{D,B}^i &= \begin{bmatrix} G_{D,B,1}^i & G_{D,B,2}^i & \cdots & G_{D,B,N_D}^i \end{bmatrix}^T \\ \underline{\mathbf{G}}_{M,B}^{i_p} &= \begin{bmatrix} G_{M,B,1}^{i_p} & G_{M,B,2}^{i_p} & \cdots & G_{M,B,N_M}^{i_p} \end{bmatrix}^T \\ \tilde{\mathbf{B}}^i &= \begin{bmatrix} \mathbf{B}_D^i & \mathbf{0}_{N_i \times N_M} \\ \mathbf{0}_{N_i \times N_D} & \mathbf{B}_M^i \end{bmatrix} \quad \tilde{\mathbf{G}}_B^i \triangleq \begin{bmatrix} (\underline{\mathbf{G}}_{D,B}^i)^T & (\underline{\mathbf{G}}_{M,B}^i)^T \end{bmatrix}^T \\ p &\in \{1, 2, \dots, N_u\}. \end{aligned} \quad (3.29)$$

The matrices $\mathbf{B}_D^i, \mathbf{B}_M^i, \mathbf{B}_M^{i_p}$ are of size $N_i \times N_D; N_i \times N_M; N_i^{i_p} \times N_M$, respectively, that collect the N_D -th; N_M -th; and $N_M^{i_p}$ -th order basis function vectors as columns, and the vectors $\underline{\mathbf{G}}_{D,B}^i; \underline{\mathbf{G}}_{M,B}^i; \underline{\mathbf{G}}_{M,B}^{i_p}$ represent the $N_D \times 1; N_M \times 1; N_M^{i_p} \times 1$ basis

function coefficient vectors, respectively. It can be seen from (3.28) that the procedure is to transform the $N_i \times 1$ -vectors $\underline{\mathbf{G}}_D^i, \underline{\mathbf{G}}_M^i$ into $N_D \times 1$ and $N_M \times 1$ -vectors $\underline{\mathbf{G}}_{D,B}^i, \underline{\mathbf{G}}_{M,B}^i$ for the estimation purposes, and with $N_D + N_M \leq N_i$, the estimation problem is *well-defined*.

The basis function coefficient vectors in (3.28) can be expressed as *polynomial*, *piece-wise polynomial*, and *spline* models. The polynomial basis model approximates the effective response with an N^{th} degree polynomial, and is therefore sensitive to the choice of the polynomial order [118, 119]. The piece-wise polynomial can be used for fast varying responses where the effective response is sliced into small pieces, such as one RB, and each slice is modeled with a low degree polynomial. However, piece-wise polynomials suffers from the discontinuities at the connecting regions between the slices [60, 119], hence it is not efficient for estimating longer channel responses. In order to have least possible oscillations in a way that polynomials in connecting regions join as smoothly as possible while keeping the size of coefficient vectors reasonably small, spline basis model can be used, which is also widely used for the identification of frequency-selective and time-varying channels [120, 121, 122, 123]. In terms of modeling accuracy and complexity, the spline model-based approximation has better performance than the polynomial and piece-wise polynomial-based approximations [P7].

The basis function matrices in (3.28) can be pre-calculated in advance, while the coefficient vectors need to be estimated. The proposed basis function model is now used in the next subsection for estimating the direct and mirror channel filters of all simultaneously scheduled UEs.

3.2.4 Least-Squares Parameters Estimation with LTE Uplink Reference Signals

In LTE, there are two received DMRS in 1 msec TTI, and the proposed estimator, operating in the frequency-domain, exploits these embedded reference signals to estimate the coefficient vectors $\underline{\mathbf{G}}_B$ of all simultaneously scheduled uplink users within a single LTE subframe. A natural approach for estimating the basis function coefficient vectors $\underline{\tilde{\mathbf{G}}}_B^i$ of (3.28) is to use the LS estimator. During the DMRS

transmission, the received signal vector of user- i in (3.28) becomes

$$\begin{aligned}\underline{\mathbf{Y}}_{DMRS(\varrho)}^i &= \underline{\mathbf{X}}_{DMRS(\varrho)}^i \underline{\mathbf{B}}_D^i \underline{\mathbf{G}}_{D,B-DMRS(\varrho)}^i + \underline{\mathbf{X}}_{DMRS(\varrho)}^{m\#} \underline{\mathbf{B}}_M^i \underline{\mathbf{G}}_{M,B-DMRS(\varrho)}^i + \underline{\mathbf{W}}^i \\ &= \tilde{\underline{\mathbf{X}}}_{DMRS(\varrho)} \tilde{\underline{\mathbf{B}}}^i \tilde{\underline{\mathbf{G}}}_{B-DMRS(\varrho)}^i + \underline{\mathbf{W}}^i\end{aligned}\quad (3.30)$$

where ϱ denotes the DMRS index within a 1 msec subframe. The LS estimates of coefficient vectors at the reference signal positions ϱ is then given by [112]

$$\begin{aligned}\hat{\underline{\mathbf{G}}}_{B-DMRS(\varrho)}^i &= \begin{bmatrix} \hat{\underline{\mathbf{G}}}_{D,B-DMRS(\varrho)}^i \\ \hat{\underline{\mathbf{G}}}_{M,B-DMRS(\varrho)}^i \end{bmatrix} \\ &= \left(\tilde{\underline{\mathbf{B}}}^{iH} \tilde{\underline{\mathbf{X}}}_{DMRS(\varrho)}^H \tilde{\underline{\mathbf{X}}}_{DMRS(\varrho)} \tilde{\underline{\mathbf{B}}}^i \right)^{-1} \tilde{\underline{\mathbf{B}}}^{iH} \tilde{\underline{\mathbf{X}}}_{DMRS(\varrho)}^H \underline{\mathbf{Y}}_{DMRS(\varrho)}^i\end{aligned}\quad (3.31)$$

which is implemented for all simultaneously scheduled users $i = 1, 2, \dots, U$ within a subframe, and independently per each receiver antenna in case of a multi-antenna receiver. The actual effective direct and mirror channel filters can then be computed by multiplying the basis function coefficient vectors with the basis functions matrices, as shown in (3.28). Once the estimates of channel filters on both DMRS symbols are obtained, the effective channel responses over all the data-bearing SC-FDMA symbols and subcarriers are obtained through linear interpolation and extrapolation within the subframe. The estimated direct and image channel filter responses are then substituted in (3.18), (3.21), (3.24), or (3.25) to detect the actual transmitted data.

3.3 Simulation and Measurement Examples

In this section, the performance of the proposed estimation and compensation methods under realistic considerations is evaluated in terms of SER. In all simulations, the signal parameters conform to the 3GPP LTE/LTE-Advanced 10 MHz mode with FFT size of $M = 1024$ and subcarrier spacing 15 kHz. The basic sample rate is then $1024 \times 15 \text{ kHz} = 15.36 \text{ MHz}$. The multi-path block fading channel, with a block being one subframe length, is modeled with 39 taps with power delay profile following the Extended Vehicular A model described in [124] and a maximum delay spread of $2.5 \mu\text{s}$.

3.3.1 TX I/Q Imbalance and Channel Distortions in OFDM Systems

We consider an uncoded 64-QAM OFDM system, where the frequency-independent TX gain and phase imbalance values are $g_{TX} = 5\%$ and $\phi_{TX} = 8^\circ$, while the in-phase and quadrature branch filters are modeled with three taps, and their coefficients are $\mathbf{h}_{I,TX} = [0.998, 0.07, 0]^T$, $\mathbf{h}_{Q,TX} = [1, -0.02, 0.01]^T$. The I/Q imbalance values correspond to an average FE IRR of $21 \cdots 24$ dB within the signal BW and represent a challenging yet practical case. To better quantify the performance, the effect of RX I/Q imbalance with IRR of $21 \cdots 24$ dB within the signal BW, and CFO error in the range of -15 kHz \cdots $+15$ kHz is also introduced to the received signal, both of which are estimated and compensated at the RX in time-domain. The I/Q imbalance values, CFO error, and channel impulse response are generated independently in each simulation realization. For an OFDM system with preamble pilot, a known OFDM symbol is inserted at the beginning of the transmission slot. For sparse pilot-based OFDM systems, we adopt the LTE downlink reference pilot structure where pilot symbols are inserted at every sixth subcarrier during the first and fifth OFDM symbol of a transmission slot.

Fig. 3.3 shows the average uncoded SER as a function of the SNR for the preamble pilot structure-based joint estimation and compensation (top), and the sparse pilot structure-based de-coupled estimation and compensation schemes (bottom). Both plots show that the communication system becomes completely unusable in the presence of all radio impairments, and the SER also remains high in the presence of TX I/Q imbalance only. For an OFDM system with preamble pilot, the J-ZF equalizer is able to reduce the SER to the level of the reference system. On the other hand, the J-ML equalizer outperforms the SER performance of the *reference system* which has known channel and impairment estimates. In the low SNR region, the SER is close to the reference system but as the SNR increases, the ML equalizer is able to extract the frequency diversity gain induced by TX I/Q imbalance. For the case of the OFDM system with sparse pilots, good calibration properties of the proposed de-coupled channel distortions and TX I/Q imbalance compensation scheme is evident, where the degradation from the reference system is less than 2 dB.

To further validate the performance, practical RF measurements with commercial I/Q modulator and demodulator chips are given next, which are reproduced from

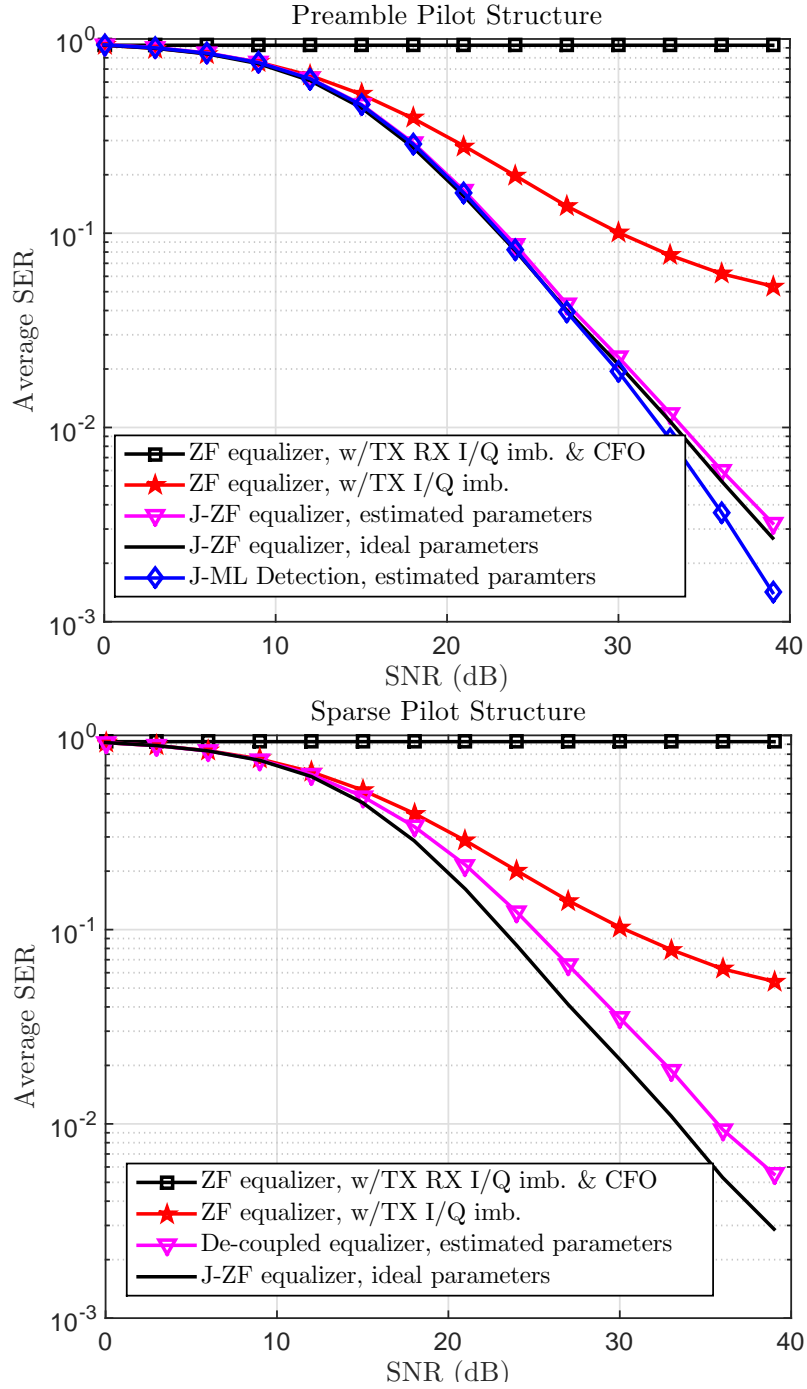


FIG. 3.3: Average SER performance of 64-QAM OFDM system with different pilot structures. TX I/Q imbalance: 21...24 dB, veh. A channel model with a maximum delay spread of 2.5 μ s. The curves are obtained by averaging the results of 3000 independent channel and TX I/Q imbalance parameter realizations.

[P2]. The reader is referred to [P2] for full details on the measurement procedure and extensive measurement examples. Again an OFDM system with 64-QAM subcarrier modulation and parameters conforming to the LTE 10 MHz mode is

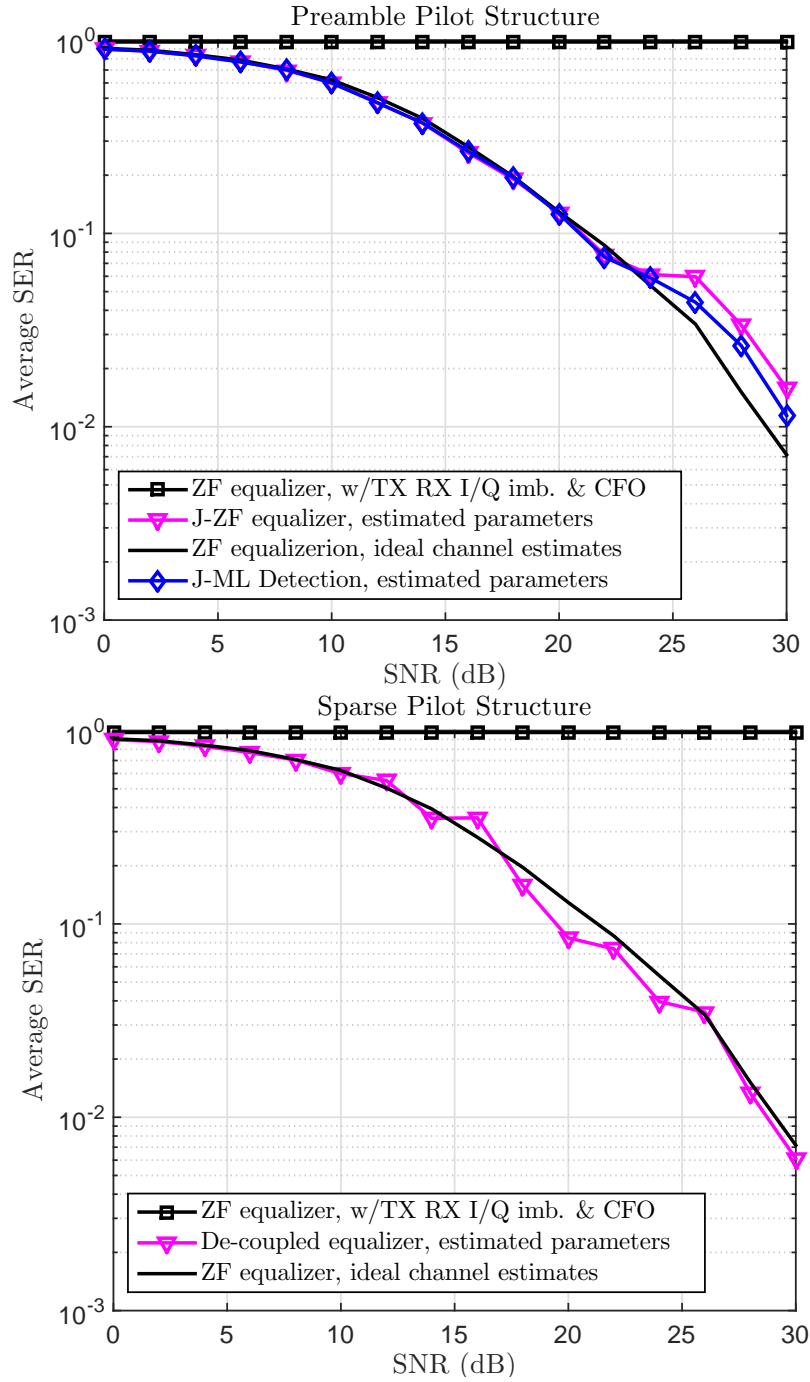


FIG. 3.4: Measured average SER vs SNR for 64-QAM OFDM system with different pilot structures. Veh. A channel model with a maximum delay spread of $2.5 \mu\text{s}$. The curves are obtained by averaging the results of 10 realizations with a fixed channel response.

used. With a fixed channel impulse response, the measured average SER vs SNR curves are plotted in Fig. 3.4 for both pilot structures, which indicate that the proposed estimation and compensation techniques effectively mitigate the effect of radio impairments.

In general, it can be concluded from the above simulation and measurement examples that the proposed RF impairments and channel distortions compensation structure and the estimation methods provide substantial improvements to achievable SER, giving confidence that they can be effectively deployed in practical systems.

3.3.2 TX I/Q Imbalances, Small CFOs, and Channel Distortions in Multi-User SC-FDMA Systems

Here, we consider an uplink multi-user SC-FDMA system, where the TX gain and phase imbalance values are randomly generated in each simulation realization in the range of $g_{TX} = 3\% \cdots 13\%$ and $\phi_{TX} = -5^\circ \cdots 5^\circ$, respectively, while the quadrature branches filter responses are $\mathbf{h}_{I,TX} = [0.998, 0.07, 0]^T$ and $\mathbf{h}_{Q,TX} = [1, -0.02, 0.01]^T$. For the waveform sample rate of 15.36 MHz, the average FE IRR is $23 \cdots 27$ dB within the system bandwidth. The transmit signals pass through independent block-fading multipath channels. The carrier frequency is assumed to be 2 GHz which corresponds to the CFO error in the range of $-200 \cdots 200$ Hz [2, 56]. To realistically quantify the performance, we include the effect of RX I/Q imbalance also but assume that it is well calibrated ideally with an IRR in the order of 55 dB [89, 90, 117]. Aiming at a feasible complexity, the estimator order of direct and mirror channels for a user- i with polynomial approximation is defined as: $(N_i/N_{SC}^{RB}) + 3$. For splines and piece-wise polynomials, each RB is estimated separately with a cubic polynomial giving $(N_i/N_{SC}^{RB}) + 3$ and $(N_i/N_{SC}^{RB}) \times 3$ parameters, respectively.

We first consider a case where two wideband uplink users of equal bandwidths, each spanning 24 RBs, are communicating with a single antenna BS RX. The first user is assumed to be a weaker user and is the *target user*, as being more sensitive to any additional distortion and interference. The second user at the image band of the target user is assumed to be stronger with 15 dB higher average received power than the target user. The subcarrier modulation for both users is 16-QAM. Fig. 3.5 shows the average uncoded SER performance of the target users where the x -axis in the figures represent the received SNR of the target user. For comparison purposes, the solid curve of a reference system with ideal channel estimates and perfect impairments knowledge is also plotted. It can be observed

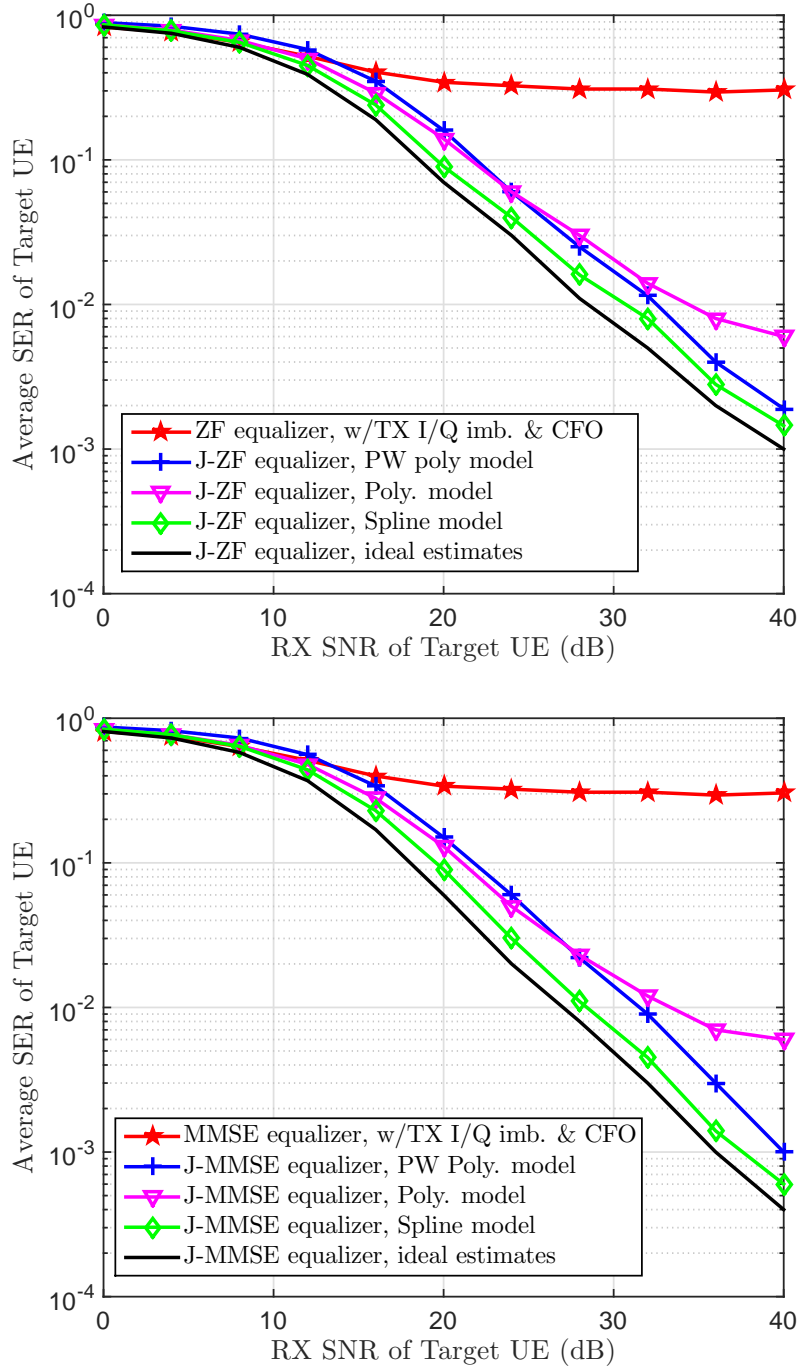


FIG. 3.5: Average SER performance of the target user for a single-antenna RX after estimation and equalization in an uplink SC-FDMA system with 15 dB stronger mirror band UE. CFOs $\in [-200, 200]$ Hz, transmitter I/Q imbalances: $23 \cdots 27$ dB, veh. A channel model with a maximum delay spread of $2.5 \mu\text{sec}$. The curves were obtained by averaging the results of 3000 independent channel, CFO, and I/Q imbalance parameter realizations.

from the figures that without impairment mitigation processing, we observe significant performance degradation of the target user SER due to IUI from the strong UE located on the image band. On the other hand, the proposed methods are

able to greatly reduce the SER degradation. It can also be noticed that the spline approximation, which requires considerably fewer parameters to approximate the channel responses than the piece-wise polynomials, also gives better performance than other approximation techniques. In addition, J-MMSE equalization gives about 2.5 dB improvement in SNR over the J-ZF equalizer.

Next, we present the performance results for an uplink multi-user SC-FDMA system with a dual-antenna BS RX and compare again the performance of the proposed estimation and equalization algorithms with a reference system that has perfect channel and impairments knowledge. Again, the two uplink users case is simulated but with a challenging receiver inband dynamic range in the order of 25 dB. The first user, assumed again as target user, is a weaker user, whereas the mirror band user is stronger and has 16-QAM baseband modulation. The average uncoded SER performance of the target user with different baseband modulation is shown in Fig. 3.6. The steep slopes of the ideal and compensated curves indicate the diversity gain achieved with SIMO. However, in this challenging yet realistic scenario, the target user SER is practically flat when no impairments compensation scheme is employed even though SIMO antenna configuration is adopted. The proposed estimation and equalization technique is again shown to greatly improve the link performance, being very close to the reference system performance bound.

It can be established from the results of the above two experiments that RF impairments, particularly IUI induced by TX I/Q imbalance, can severely limit the obtainable uplink link performance, while the proposed methods can essentially handle the realistic transmission and impairment scenarios. The proposed response approximation methods are shown to approximate the direct and mirror channel filters responses with high accuracy. Furthermore, it is shown that the proposed J-MMSE equalizer gives more than 2 dB performance gain over the J-ZF equalization. Since the channel and impairments are estimated and equalized jointly in the digital domain, the proposed algorithms can thus be directly used in the BS RX without any modification in the uplink LTE/LTE-Advanced pilot structure or in the transceiver's analog/RF hardware design.

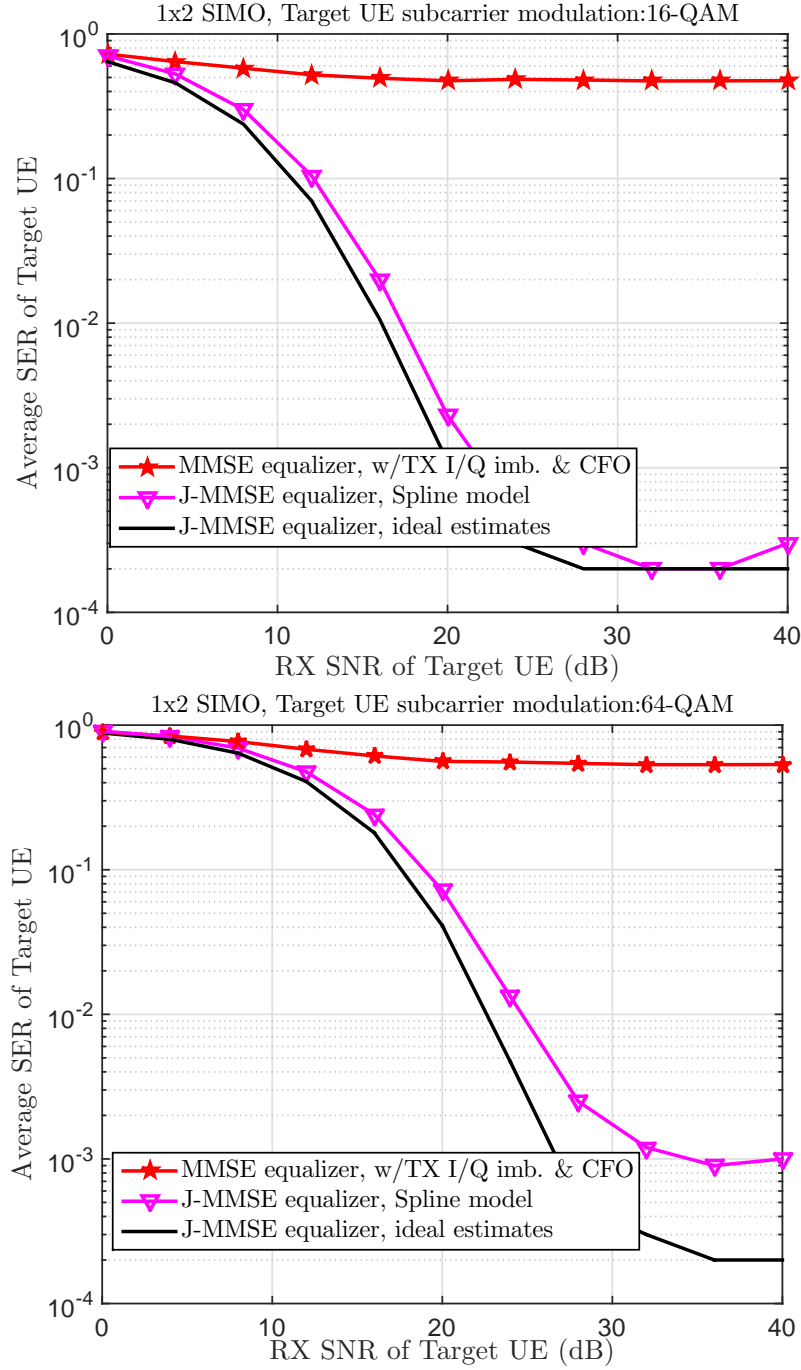


FIG. 3.6: Average SER performance in dual antenna RX setup of the target user after estimation and equalization in an uplink SC-FDMA system with 25 dB stronger mirror band UE. CFOs $\in [-200, 200]$ Hz, transmitter I/Q imbalances: 23...27dB, veh. A channel model with a maximum delay spread of 2.5 μ sec. The curves were obtained by averaging the results of 3000 independent channel, CFO, and I/Q imbalance parameter realizations.

Chapter 4

Modeling and Digital Mitigation of TX Leakage Signals in Frequency Division Duplex Transceivers

In this chapter, we review the contributions to digital mitigation of transmit leakage signal problems in FDD transceivers described originally in [P4], [P5], [P6], and [18]. In [P5], [P6], and [18], the focus is on unwanted transmitter spectral emissions at the own RX band due to nonlinear PA in the TX chain and insufficient duplexer filter isolation. The modeling and mitigation of PA OOB emissions at the RX band is investigated in [P5], which is further extended to spurious emission in the noncontiguous intraband CA scenario in [P6]. The transmitter in-band leakage signal in FDD transceivers can also activate certain RX nonlinearities, and [P4] presents a solution for the mitigation of the transmitter in-band leakage signal-induced spurious IMD2.

The proposed solutions are based on regenerating a replica of the interference and canceling it in the digital baseband of the transceiver, such that the level of interference is reduced, and does not require any additional RF filtering or analog hardware. The validity of the proposed methods is investigated with simulations and RF measurements in a practical 3GPP LTE/LTE-Advanced UE context.

4.1 Digital Mitigation of TX Spectral Emissions at Own RX Band

TX FE non-idealities are typically dominated by PA nonlinearities which produce spectral emissions outside the operating bandwidth. In an FDD transceiver with small duplex distance and finite isolation duplexer filter, OOB emissions or spurious emissions may appear at the own RX operating band which, in turn, may lead to self-desensitization of the RX. To prevent this, one can consider to back-off the transmit power to reduce the level of unwanted spectral emissions, or to increase the duplexing distance. Reducing the transmit power is, however, not desirable as it will directly compromise the uplink coverage. Improving the duplexer stopband attenuation would be, on the other hand, disadvantageous as it will typically increase the insertion loss in the passband, hence reducing power efficiency. In addition, developing duplex filters with high stopband attenuation would significantly increase their complexity and cost. Alternatively, digital cancellation techniques can be employed to reduce the detrimental impact of TX spectral emissions at the own receiver band, see, e.g., [65, 70, 71, 125]. Compared to similar self-interference cancellation schemes reported in literature for PA nonlinearities cancellation in FDD transceivers, the proposed methods in this thesis work have the following advantages:

1. Detailed modeling of the transmitter spectral emissions at the receiver band due to practical nonlinear PA with memory effects and limited isolation duplexer filter with frequency-selective response is carried out. This framework allows efficient estimation of the needed cancellation parameters, including the unknown duplexer response and unknown nonlinear PA with memory.
2. A computationally efficient interference regeneration and cancellation algorithm is derived for a noncontiguous CA transmission scenario by exploiting the specific frequency-domain structure of the aggregated carriers.

4.1.1 TX Out-of-Band Emissions at Own RX Band

We begin the analysis with unwanted PA OOB emissions at the own RX band, for which the discrete-time baseband equivalent model of an FDD transceiver with

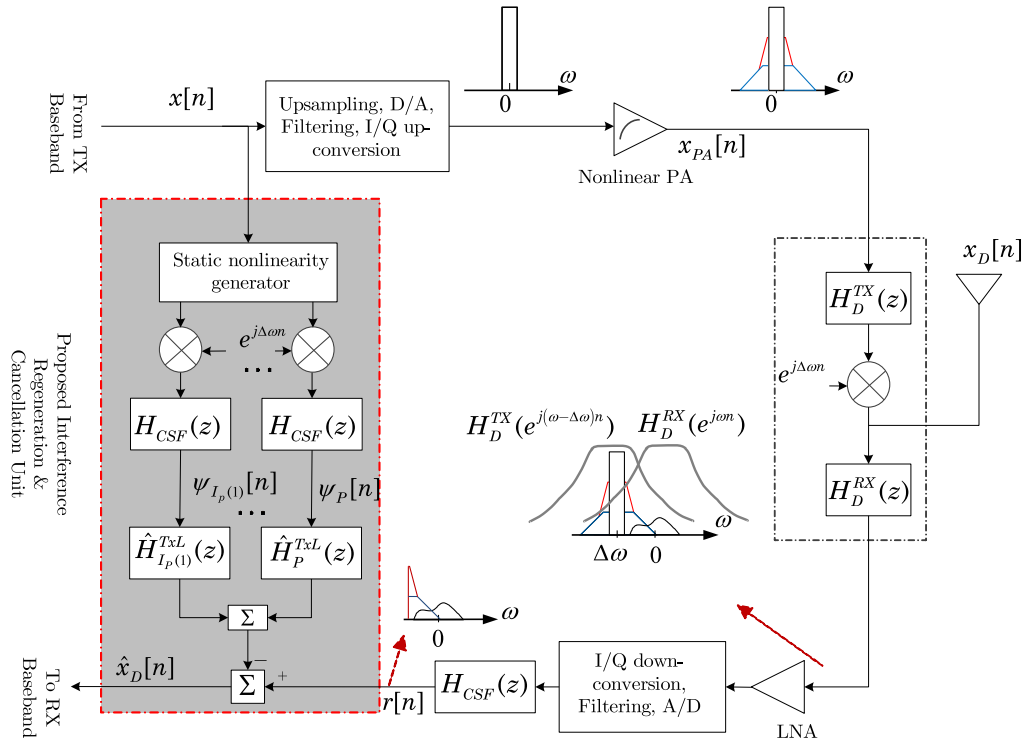


FIG. 4.1: Discrete-time baseband equivalent model and spectral illustrations of TX nonlinear PA-induced OOB emissions at own RX band in an FDD transceiver. The proposed interference regeneration and suppression unit operating at digital baseband of the transceiver is also shown.

associated signal spectra and the proposed interference regeneration and cancellation unit is shown in Fig. 4.1. For analysis and modeling purposes, the frequency separation between the active transmitter carrier and the desired receiver carrier is denoted by Δf , such that $\Delta f = f_{RX} - f_{TX}$, and the complex baseband signal to be transmitted is denoted by $x[n] = x_I[n] + jx_Q[n]$. The baseband transmit signal is up-converted to transmitter carrier frequency f_{TX} with an I/Q modulator, which is assumed perfect here, and the RF signal is then amplified by a PA for transmissions. The parallel Hammerstein (PH) model with polynomial nonlinearities is used to express the PA nonlinearities with memory effects [126]. The baseband equivalent PA output can thus be expressed as

$$x_{PA}[n] = \sum_{\substack{p=1 \\ p \text{ odd}}}^P f_p[n] \star (x[n] |x[n]|^{p-1}) \quad (4.1)$$

where P denotes the polynomial order and $f_p[n]$ denotes the baseband equivalent filter of p^{th} order PH branch. Since odd-order distortion products appear in the vicinity of the transmit signal and contribute to spectral regrowth, hence they

are only considered in (4.1). The amplified TX signal then passes through the duplexer TX filter to the antenna, however, transmitter emissions may not be fully attenuated, as illustrated in Fig. 4.1. At the receiver input, the unwanted TX OOB emissions can be mathematically expressed as

$$x_{Dup}^{leak}[n] = h_D[n] \star (x_{PA}[n]e^{j\Delta\omega n}) \quad (4.2)$$

where $\Delta\omega = 2\pi\Delta f/f_s$ represents the normalized frequency separation, and f_s denotes the sampling frequency. The cumulative duplexer filter response from TX-RX leakage perspective, denoted by $h_D[n]$ in the above equation, is defined as

$$h_D[n] = h_D^{RX}[n] \star (h_D^{TX}[n]e^{j\Delta\omega n}) \quad (4.3)$$

where $h_D^{TX}[n]$ and $h_D^{RX}[n]$ represent the baseband equivalent lowpass models of the bandpass TX and RX duplexer filters, respectively. In addition to the transmitter OOB emissions, the desired received signal, denoted by $x_D[n]$, and the thermal noise, denoted by $w[n]$, are naturally also present at the receiver input. The total received signal, after down-conversion and channel selection filtering, is then given by

$$r[n] = x_D[n] + x_{RxBB}^{leak}[n] + w_{BB}[n] \quad (4.4)$$

where $x_{RxBB}^{leak}[n] = h_{CSF}[n] \star x_{Dup}^{leak}[n]$ denotes the transmitter OOB emissions observed at the RX baseband and $w_{BB}[n] = h_{CSF}[n] \star w[n]$ corresponds to the filtered RX in-band thermal noise.

In the following, stemming from above modeling, we develop an efficient digital technique for dynamically regenerating and suppressing the self-interference inside the FDD transceiver, combined with an appropriate parameter estimation method.

4.1.1.1 Proposed OOB Emissions Regeneration and Cancellation

We now address the regeneration of the transmitter OOB emissions and the corresponding self-interference cancellation. In short, the idea is to regenerate an opposite-phase replica of the interference and then inject it to the receiver baseband, such that the level of the interference is reduced.

First, we note that the OOB emissions term at the receiver baseband $x_{RxBB}^{leak}[n]$ in (4.4) can be equivalently expressed as

$$x_{RxBB}^{leak}[n] = h_{CSF}[n] \star h_D[n] \star \left(\left(\sum_{\substack{p=1 \\ p \text{ odd}}}^P f_p[n] \star (x[n] |x[n]|^{p-1}) \right) e^{j\Delta\omega n} \right). \quad (4.5)$$

In practice, only selected nonlinearity orders p are needed for modeling and cancellation, depending on how the receiver band is located relative to the transmitter emissions. This is quantified with (4.6), which defines the minimum order PA nonlinearities affecting the receiver band as

$$\rho = \left\lceil \frac{|f_{TX} - f_{RX}| - \frac{1}{2}(B_{TX} + B_{RX})}{B_{TX}} \right\rceil \quad (4.6)$$

where B_{TX} and B_{RX} are TX and RX bandwidths, respectively. With this definition, an equivalent form of (4.5) can be written as

$$x_{RxBB}^{leak}[n] = \sum_{p \in I_P} h_p^{TxL}[n] \star \psi_p[n] \quad (4.7)$$

where $I_P = \{2\rho + 1, 2\rho + 3, \dots, P\}$, $h_p^{TxL}[n] = h_D[n] \star (f_p[n] e^{j\Delta\omega n})$ denotes the p^{th} unknown equivalent transmitter leakage channel modeling PA nonlinearities and duplexer filters responses, and $\psi_p[n] = h_{CSF}[n] \star (x[n] |x[n]|^{p-1}) e^{j\Delta\omega n}$ denotes the basis functions formed from the known transmitted baseband signal $x[n]$, filtered by CSF and, then frequency translated to $\Delta\omega$. With the linear-in-parameters model in (4.7), the proposed OOB emissions regeneration and cancellation algorithm requires only the coefficient estimates of the equivalent transmitter leakage channel $h_p^{TxL}[n]$, as the digital transmit data, CSF response, and duplex distance are always known inside the transceiver, and can be used to pre-calculate the filtered basis functions. The principal regeneration and cancellation structure, stemming from this formulation, is illustrated in Fig. 4.1, while the parameter estimation of the equivalent transmitter leakage channel is addressed next.

For the parameter estimation of the transmitter leakage channel, we switch to vector-matrix notations and consider N — samples of the total baseband received signal of (4.4), with transmitter OOB emissions at RX band included, as

$$\mathbf{r} = \mathbf{x}_D + \mathbf{\Psi} \mathbf{h}^{TxL} + \mathbf{w}_{BB} \quad (4.8)$$

where $\underline{\mathbf{h}}^{TxL} = [\underline{\mathbf{h}}_{I_P(1)}^{TxL^T} \quad \underline{\mathbf{h}}_{I_P(2)}^{TxL^T} \quad \cdots \quad \underline{\mathbf{h}}_P^{TxL^T}]^T$ is a vector of dimension $(\text{card}(I_P) \times N_h) \times 1$, with $\text{card}(I_P)$ denoting the cardinality of the set I_P , and N_h denoting the length of $\underline{\mathbf{h}}_p^{TxL}$. Furthermore, $\Psi = [\Psi_{I_P(1)} \quad \Psi_{I_P(2)} \quad \cdots \quad \Psi_P]$ is a block matrix collecting the considered basis function matrices into a single matrix. The p^{th} basis function matrix of dimension $(N + N_h - 1) \times N_h$ is defined as

$$\Psi_p = \begin{bmatrix} \psi_p[0] & 0 & \cdots & 0 \\ \psi_p[1] & \psi_p[0] & \cdots & 0 \\ \vdots & 0 & \cdots & 0 \\ \psi_p[N-1] & \vdots & \ddots & \vdots \\ 0 & \psi_p[N-1] & \cdots & \psi_p[N-N_h] \\ 0 & 0 & \cdots & \psi_p[N-N_h+1] \\ \vdots & \vdots & \ddots & \vdots \\ 0 & 0 & \cdots & \psi_p[N-1] \end{bmatrix}. \quad (4.9)$$

Now, for the parameter estimation purpose, (4.8) can be equivalently written as

$$\underline{\mathbf{r}} = \Psi \underline{\mathbf{h}}^{TxL} + \tilde{\mathbf{w}}_{BB} \quad (4.10)$$

where $\tilde{\mathbf{w}}_{BB} = \underline{\mathbf{x}}_D + \underline{\mathbf{w}}_{BB}$. From the perspective of parameter estimation, the actual received signal $\underline{\mathbf{x}}_D$ acts as additional noise and is thus lumped here into the vector $\tilde{\mathbf{w}}_{BB}$ together with the thermal noise for presentation purposes. The equivalent transmitter leakage channel parameter vector $\underline{\mathbf{h}}^{TxL}$ can now be estimated in the LS sense directly as [112]

$$\hat{\underline{\mathbf{h}}}^{TxL} = (\Psi^H \Psi)^{-1} \Psi^H \underline{\mathbf{r}}. \quad (4.11)$$

Finally, the estimated parameters of the equivalent transmitter leakage channel can then be used in the OOB emissions regeneration and cancellation, as shown in Fig. 4.1.

4.1.2 TX Spurious Emissions at Own RX Band: Special Case of Noncontiguous CA Transmission

The above signal formulations and the proposed regeneration and cancellation solution are, in principle, also applicable to CA FDD transceivers. However, from

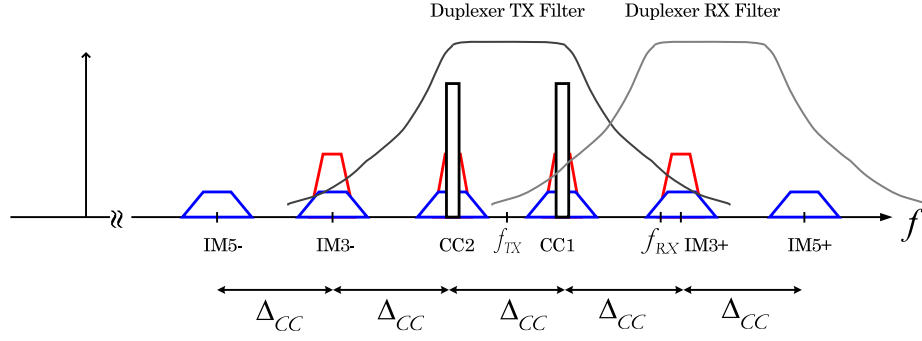


FIG. 4.2: *Example spectral illustration of spurious IMD hitting own receiver band with noncontiguous dual carrier transmitter. In this illustration, only third-order and fifth-order distortions are shown, and the receiver center frequency f_{RX} is located at positive third-order intermodulation band ($IM3_+$).*

a noncontiguous CA transmission perspective where the total frequency span of the transmit signal can be in the order of 100 MHz or even beyond, the proposed technique is computationally very challenging, as it requires processing the whole transmission band to estimate the equivalent transmitter leakage channel. Instead, we now take into account the specific frequency-domain structure of the aggregated carriers to devise a computationally efficient regeneration and cancellation principle for noncontiguous CA transmission scenarios.

First, we notice that when noncontiguous CCs are deployed in the transmission the spectral contents of the spurious IMD due to nonlinear PA are localized around specific frequencies, namely odd-order intermodulation frequencies of the CC center frequencies. These frequencies are referred to as IM3 band, IM5 band, and so forth, as illustrated in Fig. 4.2. In general, a specific IM band contains also higher-order nonlinear products, e.g., the IM3 band contains, in addition to third-order nonlinearity, fifth- and seventh-order nonlinearities. Now considering a general noncontiguous dual-carrier CA FDD transceiver, the baseband transmit signal $x[n]$ in (4.1) is composed of two CCs, denoted by $x_1[n]$ and $x_2[n]$ and separated by $\Delta_{CC} = 2\omega_{IF}$, as $x[n] = x_1[n]e^{j\omega_{IF}n} + x_2[n]e^{-j\omega_{IF}n}$, where ω_{IF} and $-\omega_{IF}$ refer to digital IF frequencies of the individual transmit CCs. In this notation, at composite baseband equivalent signal level, the $IM3_+$ band is then located at three times the IF frequency, i.e. at $+3f_{IF}$. For generality and completeness of the modeling, we again allow the exact center frequency of the own RX to be some Δf off from this frequency, such that $\Delta f = f_{RX} - (f_{TX} + 3f_{IF})$. The baseband equivalent model is illustrated in Fig. 4.3 of such a scenario with the associated signal spectra and the proposed spurious IMD emissions regeneration and cancellation

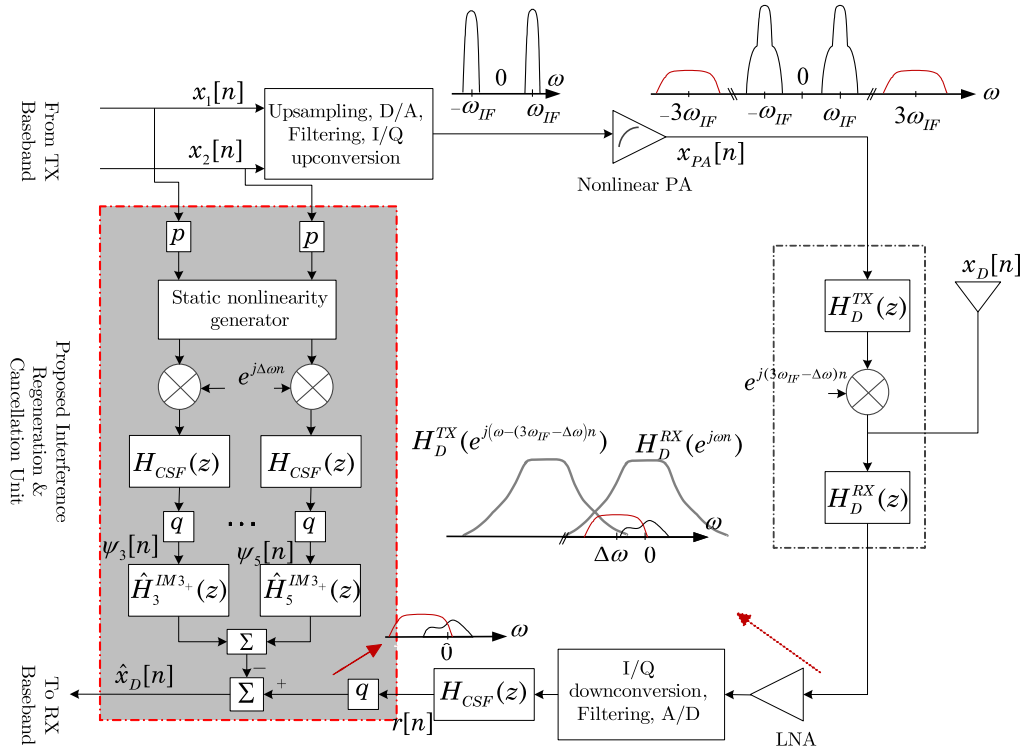


FIG. 4.3: Discrete-time baseband equivalent model and spectral illustrations of TX nonlinear PA-induced spurious IMD leakage at own RX band in CA FDD transceiver with proposed interference regeneration and cancellation unit.

unit. Next, when the noncontiguous CA signal enters the PA, spurious IMDs are created. With the baseband equivalent PA model given in (4.1), and considering PA nonlinearity orders up to $P = 5$ at the IM3 band, the baseband equivalent spurious IMD at the positive and negative IM3 bands can then be shown to read

$$x_{PA}^{IM3+}[n] = f_3^{IM3+}[n] \star (x_1^2[n]x_2^*[n]) + f_5^{IM3+}[n] \star \left(\begin{matrix} 3x_1^2[n]x_2^*[n]|x_2[n]|^2 + \\ 2x_1^2[n]x_2^*[n]|x_1[n]|^2 \end{matrix} \right) \quad (4.12)$$

$$x_{PA}^{IM3-}[n] = f_3^{IM3-}[n] \star (x_1^*[n]x_2^2[n]) + f_5^{IM3-}[n] \star \left(\begin{matrix} 3x_1^*[n]x_2^2[n]|x_1[n]|^2 + \\ 2x_1^*[n]x_2^2[n]|x_2[n]|^2 \end{matrix} \right). \quad (4.13)$$

Here, $f_3^{IM3\pm}[n]$ and $f_5^{IM3\pm}[n]$ are the corresponding baseband equivalent filter responses of third- and fifth-order PH branches $f_3[n]$ and $f_5[n]$ that model the PA's frequency responses for third- and fifth-order nonlinearities at the positive and negative IM3 bands, respectively, and within the assumed receiver bandwidth. They are formally defined as

$$\begin{aligned} f_3^{IM3\pm}[n] &= LP \{ f_3[n] e^{\mp j3\omega_{IF}n} \} \\ f_5^{IM3\pm}[n] &= LP \{ f_5[n] e^{\mp j3\omega_{IF}n} \} \end{aligned} \quad (4.14)$$

where $LP\{\cdot\}$ denotes the lowpass filtering operation with bandwidth equal to the RX bandwidth.

For presentation purposes, we next assume that the positive IM3 band, referred to as IM3₊ hereafter, coincide with the RX band and $x_{PA}^{IM3+}[n]$ appears in the RX operating band. At the receiver input, the TX spurious IMD in (4.12), after passing through the transmitter and receiver duplexer filters, can be mathematically expressed as

$$x_{Dup}^{IM3+}[n] = h_D[n] \star \left(x_{PA}^{IM3+}[n] e^{j\Delta\omega n} \right). \quad (4.15)$$

where $h_D[n] = h_D^{RX}[n] \star \left(h_D^{TX}[n] e^{-j(3\omega_{IF} - \Delta\omega)n} \right)$. Similar to (4.4), the composite baseband received signal at the CSF output is given by

$$r[n] = x_D[n] + x_{RxBB}^{IM3+}[n] + w_{BB}[n] \quad (4.16)$$

where $x_{RxBB}^{IM3+}[n] = h_{CSF}[n] \star x_{Dup}^{IM3+}[n]$ denotes the spurious IMD leakage observed at the RX baseband. As discussed earlier and was shown also in Section 2.4.1 with system level calculations, the TX duplexer filter may not sufficiently attenuate the TX spurious emissions below the noise floor in FDD transceivers of next generation wireless systems such as LTE-Advanced. Hence, in the following, we develop an efficient digital technique for dynamically regenerating and suppressing the spurious IMD leakage at the RX band inside the FDD transceiver.

4.1.2.1 Proposed Spurious IMD Regeneration and Cancellation

We follow a similar principle for the spurious IMD leakage estimation and cancellation as in Section 4.1.1.1 by developing a linear-in-parameters model of the spurious IMD leakage signal. First, we write $x_{RxBB}^{IM3+}[n]$ in (4.16) in its equivalent form as

$$x_{RxBB}^{IM3+}[n] = h_{CSF}[n] \star x_{Dup}^{IM3+}[n] = h_3^{IM3}[n] \star \psi_3[n] + h_5^{IM3}[n] \star \psi_5[n] \quad (4.17)$$

where $h_p^{IM3+}[n], p = \{3, 5\}$ denote the effective IM3₊ channels modeling third- and fifth-order PA nonlinearities and duplexer filters responses at IM3₊ band, defined as

$$\begin{aligned} h_3^{IM3+}[n] &\triangleq e^{j\Delta\omega n} \left(h_D[n] \star f_3^{IM3+}[n] \right) \\ h_5^{IM3+}[n] &\triangleq e^{j\Delta\omega n} \left(h_D[n] \star f_5^{IM3+}[n] \right), \end{aligned} \quad (4.18)$$

while the known component carrier baseband waveforms, duplexing distance, and CSF filter response are combined together to form the *filtered basis functions*, defined below as

$$\begin{aligned}\psi_3[n] &\triangleq h_{CSF}[n] \star (x_1^2[n]x_2^*[n]) e^{j\Delta\omega n} \\ \psi_5[n] &\triangleq h_{CSF}[n] \star \begin{pmatrix} 3x_1^2[n]x_2^*[n]|x_2[n]|^2 + \\ 2x_1^2[n]x_2^*[n]|x_1[n]|^2 \end{pmatrix} e^{j\Delta\omega n}.\end{aligned}\quad (4.19)$$

Next, for the parameter estimation, we again switch to vector-matrix notations and consider N -samples of each CC. By modeling both filters in (4.18) with N_h -taps, the effective IM3 channel filter vector is then of dimension $2N_h \times 1$. The spurious IM3 term in (4.17) then takes the form

$$\begin{aligned}\underline{\mathbf{x}}_{RxBB}^{IM3+} &= \underline{\Psi}_3 \underline{\mathbf{h}}_3^{IM3+} + \underline{\Psi}_5 \underline{\mathbf{h}}_5^{IM3+} = \begin{bmatrix} \underline{\Psi}_3 & \underline{\Psi}_5 \end{bmatrix} \begin{bmatrix} \underline{\mathbf{h}}_3^{IM3+} \\ \underline{\mathbf{h}}_5^{IM3+} \end{bmatrix} \\ &= \underline{\Psi} \underline{\mathbf{h}}^{IM3+}\end{aligned}\quad (4.20)$$

where $\underline{\Psi}_p, p = 3, 5$, in $\underline{\Psi}$ is a matrix of dimension $(N + N_h - 1) \times N_h$, defined similarly as in (4.9). The total baseband received signal in (4.16) then becomes

$$\underline{\mathbf{r}} = \underline{\Psi} \underline{\mathbf{h}}^{IM3+} + \underline{\tilde{\mathbf{w}}}_{BB} \quad (4.21)$$

where again the desired RX signal and noise are lumped into a single variable $\underline{\tilde{\mathbf{w}}}_{BB}$. The LS parameter estimate of $\underline{\mathbf{h}}^{IM3+}$ is then given directly by [112]

$$\hat{\underline{\mathbf{h}}}^{IM3+} = (\underline{\Psi}^H \underline{\Psi})^{-1} \underline{\Psi}^H \underline{\mathbf{r}}. \quad (4.22)$$

Finally, the estimates of the effective IM3₊ channel filters are then used together with the known basis function for regenerating the spurious IMD emissions at the IM3 band and subsequently canceling it, as shown in Fig. 4.3.

Notice that the modeling of the IM3 band contains, in addition to third-order nonlinear distortions, also fifth-order distortions, which is essential for accurate and high-performance cancellation. Similar expressions and canceller developments taking into account nonlinear PA distortions of seventh-order and beyond can also be easily formulated but are not presented in this thesis for the sake of compactness.

Alternatively to the block LS estimation discussed in this section for the transmitter leakage channel estimation, adaptive estimation techniques such as recursive LS (RLS) can also be used, which is practically more appealing as no matrix inversion is needed. The derivation of such adaptive algorithms is straight forward and is not considered in this thesis. Furthermore, since the statistical properties of the transmit data and potentially also the desired received signal are known, linear MMSE (LMMSE) type of estimators can also be developed, which forms an interesting topic for future studies.

4.1.3 Comparison of Computational Complexity

In this section, we shortly discuss the computational complexity aspects of the proposed OOB emissions and the proposed spurious emissions regeneration and cancellation techniques, in terms of the required sample rate and the total number of estimated filter parameters. An attractive feature of the proposed spurious IMD emissions regeneration and cancellation technique is that it is able to exploit the specific nature of noncontiguous carriers and the resulting spurious IMD. To demonstrate this better, consider a noncontiguous intraband CA scenario with two 10 MHz CCs and 50 MHz carrier spacing. The minimum sample rate required for the proposed TX OOB emissions regeneration and cancellation technique to model the fifth order PA nonlinearity at the IM3 band would be 200 MHz, which is calculated based on the individual CCs bandwidths and the IM3 band location. Compared to that, the needed sample rate in the proposed spurious IMD regeneration and cancellation method depends only on the frequency separation between the center of the IM3 band and the desired RX signal center frequency, as well as receiver bandwidth. Denote with B_{RX} the actual RX signal bandwidth, and with B_L and B_U the partial IMD bandwidths below and above the RX bandwidth, respectively. The total spurious IM3₊ bandwidth is then $(B_L + B_U + B_{RX})$ Hz. In order to guarantee that the IMD tails do not alias onto each other within the RX signal band, the minimum sample rate in the regeneration, f_s^{reg} , can then be easily quantified with the following equation

$$f_s^{reg} = \max \{B_L + B_{RX}, B_U + B_{RX}\}. \quad (4.23)$$

For the spurious IMD cancellation technique, this is only 25 MHz if, for simplicity, the center frequency of the RX signal and the IM3₊ band are assumed identical.

Compared to 200 MHz sample rate for the OOB emissions regeneration method, this is a substantial reduction. The cancellation itself can then be performed at the receiver sample rate. Furthermore, the spurious IMD emissions regeneration technique requires less parameters to be estimated as it captures the unknown leakage channel response only at the selected spurious IM3 band.

4.2 Digital Mitigation of TX In-band Leakage Signal-Induced Second-Order Intermodulation Distortion

In direct-conversion receivers, the transmitter in-band leakage signal may impose challenging linearity requirements in receiver components. In particular, the non-linearity of the down-converting mixer generates an IMD2 distortion, which is located at the baseband and interferes with the desired RX signal. The relative strength of such IMD2 may potentially have higher power than the useful received signal, as was discussed in Section 2.4.2. In this section, based on [P4], we report the transmitter in-band signal leakage-induced IMD2 regeneration and cancellation solution in the presence of transmitter non-idealities, which enables efficient dynamic cancellation of such IMD2 in FDD direct-conversion transceivers.

Conventionally, TX in-band leakage signal is suppressed by placing an additional bandpass filter between the LNA and down-converter [127]; however, such a solution limits the flexibility of the receiver and is not appealing for frequency-agile FEs. Other techniques involving cancellation at RF are also proposed, see, e.g., [128, 129, 130] and references therein, nevertheless, they add complexity to the analog front-end. In contrast, digital cancellation techniques for transmitter in-band leakage signal and spurious IMD2 are discussed in [66, 131, 132, 133, 134, 135] assuming an idealized linear transmitter, and in [136] with frequency-flat duplexer stopband. Contrary to these works, we carry out a detailed modeling of the transmitter in-band leakage signal-induced IMD2 taking into account also the effects of nonlinear transmitter chain components. In addition, we develop an efficient model for estimating the frequency-selective duplexer filter response and transmitter-receiver chain nonlinearities, and subsequently canceling the spurious IMD2 in the digital baseband.

equivalent PA output can then be expressed as [P4]

$$\begin{aligned} x_{PA}[n] &= \alpha_1^{PA} \check{x}[n] + \alpha_3^{PA} |\check{x}[n]|^2 \check{x}[n] \\ &\cong \alpha_1^{PA} \check{x}[n] + \alpha_3^{PA} \mu^2 \mu^* |x[n]|^2 x[n] \end{aligned} \quad (4.25)$$

where the simplified form in the second line of the above equation is obtained by assuming that the products with multiplier coefficient $\alpha_3^{PA} \nu$ have diminishing power and will be suppressed below the noise floor by the duplexer filter. The amplified signal then leaks partly into the receiver chain through finite isolation duplexer filter, and the transmit in-band leakage signal can be mathematically expressed similarly as in (4.2). The receiver mixing stage is modeled as having a finite IIP2 number such that it results in the generation of the spurious IMD2 due to the transmitter in-band leakage signal. The baseband received signal after CSF, including also the desired received signal and noise, is then given by

$$r[n] = x_D[n] + \alpha_2^M h_{CSF}[n] \star |x_{Dup}^{leak}[n]|^2 + w_{BB}[n] \quad (4.26)$$

where α_2^M represents the mixer RF-to-LO isolation and is generally complex valued. The signal model in (4.26) indicate that the spurious IMD2 of the transmit in-band leakage signal also appears in the receiver baseband, whose power can be substantial especially when emphasizing a low-cost duplexer and mixer implementation. In the following, we focus on dynamically regenerating and suppressing this spurious IMD2 inside the FDD transceiver.

4.2.2 Parallel Augmented Volterra Model for TX In-band Leakage-Induced IMD2

A parallel augmented Volterra-based framework for transmitter in-band leakage-induced IMD2 is developed first in this section, which is then used to derive an LS parameter estimation and cancellation structure, explained next in the following subsection.

For notational simplicity, assume that the spurious IMD2 signal is contained in the passband of CSF, such that $\alpha_2^M h_{CSF}[n] = \alpha_2^{CSF} \delta[n]$, then the discrete-time

transmit in-band leakage signal IMD2 in (4.26) can be written as

$$x_{IMD2}[n] = \sum_{n_1} \sum_{n_2} h^{IMD2}[n_1, n_2] x_{PA}[n - n_1] x_{PA}^*[n - n_2] \quad (4.27)$$

where $h^{IMD2}[n_1, n_2] = \alpha_2^{CSF} h_D[n_1] h_D^*[n_2]$ is a 2D filter (2^{nd} order *Volterra* kernel), which defines the total IMD2 filter, representing the filtering effect on the transmit in-band leakage signal. Evaluating the product $x_{PA}[n - n_1] x_{PA}^*[n - n_2]$ leads to the following form of (4.27)

$$\begin{aligned} x_{IMD2}[n] = & \sum_{n_1} \sum_{n_2} h_{fund}^{IMD2}[n_1, n_2] \Psi_{fund}[n] + \beta_1^{IM2} \sum_{n_1} \sum_{n_2} h_{fund}^{IMD2}[n_1, n_2] \Psi_1[n] + \\ & \beta_2^{IM2} \sum_{n_1} \sum_{n_2} h_{fund}^{IMD2}[n_1, n_2] \Psi_2[n] + \beta_3^{IM2} \sum_{n_1} \sum_{n_2} h_{fund}^{IMD2}[n_1, n_2] \Psi_3[n] + \\ & \beta_4^{IM2} \sum_{n_1} \sum_{n_2} h_{fund}^{IMD2}[n_1, n_2] \Psi_4[n] \end{aligned} \quad (4.28)$$

where the known basis functions are of the following form

$$\begin{aligned} \Psi_{fund}[n] &= x[n - n_1] x^*[n - n_2] \\ \Psi_1[n] &= x[n - n_1] x[n - n_2]; \\ \Psi_2[n] &= x^*[n - n_1] x^*[n - n_2] \\ \Psi_3[n] &= x[n - n_1] |x[n - n_2]|^2 x^*[n - n_2]; \\ \Psi_4[n] &= |x[n - n_1]|^2 x[n - n_1] x^*[n - n_2] \end{aligned} \quad (4.29)$$

and the unknown parameters are

$$\begin{aligned} h_{fund}^{IMD2}[n_1, n_2] &= h^{IMD2}[n_1, n_2] |\alpha_1^{PA}|^2 |\mu|^2 \\ \beta_1^{IMD2} &= \frac{\nu^*}{\mu^*}; \\ \beta_2^{IMD2} &= \frac{\nu}{\mu} = \beta_1^{IMD2*} \\ \beta_3^{IMD2} &= \frac{|\mu|^2 \alpha_3^{PA*}}{\alpha_1^{PA*}}; \\ \beta_4^{IMD2} &= \frac{|\mu|^2 \alpha_3^{PA}}{\alpha_1^{PA}} = \beta_3^{IMD2*}. \end{aligned} \quad (4.30)$$

With the linear-in-parameters model in (4.28), the digital cancellation algorithm requires the estimates of the set of parameters listed in (4.30) to recreate the

replica of the spurious IMD2. The estimation of these parameters is discussed next.

4.2.3 Proposed IMD2 Regeneration and Cancellation

We first address the parameter estimation, for which N samples of the baseband received signal in (4.26) in a vector-matrix notation can be written as

$$\begin{aligned} \mathbf{r} = & \mathbf{s} + \mathbf{\Psi}_{fund} \mathbf{h}_{fund}^{IMD2} + \beta_1^{IMD2} \mathbf{\Psi}_1 \mathbf{h}_{fund}^{IMD2} + \beta_2^{IMD2} \mathbf{\Psi}_2 \mathbf{h}_{fund}^{IMD2} + \\ & \beta_3^{IMD2} \mathbf{\Psi}_3 \mathbf{h}_{fund}^{IMD2} + \beta_4^{IMD2} \mathbf{\Psi}_4 \mathbf{h}_{fund}^{IMD2} + \mathbf{w}_{BB} \end{aligned} \quad (4.31)$$

where the matrices $\mathbf{\Psi}_{fund}, \mathbf{\Psi}_i, i \in \{1, 2, 3, 4\}$ can be constructed with the known transmit data $x[n]$. From (4.31) following observations can be made: the desired RX signal is in general weaker than the transmit in-band leakage signal-induced IMD2 (see Section 2.4.2); the third and fourth term are transformed by I/Q imbalance and are typically at least 25 dB weaker than the fundamental IMD2 term $\mathbf{\Psi}_{fund} \mathbf{h}_{fund}^{IMD2}$ [2, 56]; the fourth and fifth terms are spectral regrowth created by PA nonlinearity and they are typically at least 30 dB weaker than the fundamental IMD2 term. These facts lead us to derive a two step estimation framework. In the first step, the fundamental IMD2 filter \mathbf{h}_{fund}^{IMD2} is estimated while assuming that rest of the terms are noise. The estimated filter is then used to regenerate the fundamental IMD2 term, which is then subtracted from (4.31); the result of which is next used in the second estimation step to estimate the coefficients $\beta_i^{IMD2}; i \in \{1, 2, 3, 4\}$.

To estimate the fundamental IMD2 filter, we write (4.31) as

$$\mathbf{r}_{IMD2}^{fund} = \mathbf{\Psi}_{fund} \mathbf{h}_{fund}^{IMD2} + \mathbf{w}_1 \quad (4.32)$$

where \mathbf{w}_1 denotes the filtered noise plus weak signal terms, including also the desired RX signal. The LS solution of \mathbf{h}_{fund}^{IMD2} is given by [112]

$$\hat{\mathbf{h}}_{fund}^{IMD2} = (\mathbf{\Psi}_{fund}^H \mathbf{\Psi}_{fund})^{-1} \mathbf{\Psi}_{fund}^H \mathbf{r}_{IMD2}^{fund}. \quad (4.33)$$

Now, with the estimated IMD2 filter $\hat{\mathbf{h}}_{fund}^{IMD2}$ and known basis function matrix $\mathbf{\Psi}_{fund}$, the fundamental IMD2 term is regenerated and subtracted from the down-converted received signal such that the effect of the strongest term in (4.31) is

removed. This is given as

$$\begin{aligned} \tilde{\mathbf{r}} &= \mathbf{r} - \Psi_{fund} \hat{\mathbf{h}}_{fund}^{IM2,LS} \\ &\cong \underbrace{\begin{bmatrix} \Psi_1 \hat{\mathbf{h}}_{fund}^{IM2,LS} & \Psi_2 \hat{\mathbf{h}}_{fund}^{IM2,LS} & \Psi_3 \hat{\mathbf{h}}_{fund}^{IM2,LS} & \Psi_4 \hat{\mathbf{h}}_{fund}^{IM2,LS} \end{bmatrix}}_{\Phi} \underbrace{\begin{bmatrix} \beta_1^{IM2} \\ \beta_2^{IM2} \\ \beta_3^{IM2} \\ \beta_4^{IM2} \end{bmatrix}}_{\underline{\beta}^{IM2}}, \end{aligned} \quad (4.34)$$

and finally the LS estimate of the coefficient vector $\underline{\beta}^{IM2}$ is then given by

$$\underline{\hat{\beta}}^{IM2} = (\Phi^H \Phi)^{-1} \Phi^H \tilde{\mathbf{r}}. \quad (4.35)$$

The estimates of $\hat{\mathbf{h}}_{fund}^{IM2}$ and $\underline{\hat{\beta}}^{IM2}$ are substituted in (4.28) to regenerate the transmit in-band leakage IMD2 interference. The predicted interference is then subtracted from the down-converted received signal in the digital baseband to obtain the desired received signal for detection. A conceptual block diagram of the proposed digital canceller is also shown in Fig. 4.4.

4.3 Simulation and Measurement Examples

In this section, simulation and RF measurement examples are given for the proposed digital regeneration and cancellation algorithms. First, the performance of digital algorithms for the unwanted TX spectral emissions suppression, discussed in Section 4.1, is evaluated. The performance of the transmitter in-band leakage signal-induced IMD2 interference regeneration and cancellation algorithm is then presented.

4.3.1 Digital Mitigation of Unwanted TX Spectral Emissions at RX Band

We first report the performance results with computer simulations. The baseband transmit signal is an LTE/LTE-Advanced uplink SC-FDMA signal with parameters conforming to the 10 MHz channel bandwidth and QPSK subcarrier modulation. In the TX chain, the PA with memory is modeled by a Wiener nonlinearity,

i.e. a linear time-invariant filter (LTI) filter followed by a static nonlinearity. The filter transfer function is $(1 + 0.3z^{-2}) / (1 - 0.2z^{-1})$ [137], while the memoryless nonlinearity is a fifth-order polynomial whose coefficients are calculated from PA gain, IIP3, and 1-dB compression point, which are 20 dB, 17 dBm, and 26 dBm, respectively. The duplexer filter is modeled to have a frequency-selective stopband response with an attenuation of 40...60 dB at the RX band [67, 80]. The desired RX signal is a 10 MHz LTE-A downlink OFDM(A) signal with QPSK subcarrier modulation. The reference thermal noise power at the RX input is assumed to be -104 dBm/10 MHz, the RX noise figure (NF) is 9 dB [81], the reference sensitivity level is -93.5 dBm [2], and the LNA gain is 20 dB. For PA OOB emissions, the duplex gap is assumed to be only 15 MHz to reflect a challenging scenario, whereas for evaluating the performance of PA-induced spurious IMD estimation and cancellation, we deploy a dual-carrier noncontiguous CA signal with each CC modeled as a 10 MHz LTE-Advanced SC-FDMA signal, and 50 MHz spacing between them. The frequency offset between the center of the IM3₊ band and the desired RX signal band is assumed to be 2 MHz.

Fig 4.5 shows the normalized power spectral density (PSD) curves of PA OOB emissions (top) and PA spurious emissions (bottom) at the RX band before and after digital cancellation. A block of 50,000 samples of the filtered baseband received signal and the filtered basis functions are used for estimating the parameters of the canceller. The filter length corresponding to each canceller branch is $N_h = 5$, and the received signal and thermal noise are present during the estimation. Notice that both PA OOB emissions and PA spurious emissions corrupt the desired RX signal reception heavily when the duplex distance is small. However, the proposed techniques are able to push the undesired self-interference below the noise floor within the receiver operating band, especially when a proper set of nonlinearity orders are used.

We further quantify the performance by plotting the receiver signal-to-interference plus noise ratio (SINR) against different TX power levels, and also varying the actual RX signal level. The SINR curves with different RX signal levels for PA OOB emissions and PA spurious IMD emissions are plotted in Fig. 4.6. Both figures show that the proposed techniques are able to substantially reduce the interference and enhance the SINR.

Actual RF measurement examples are next given, where the performance of the

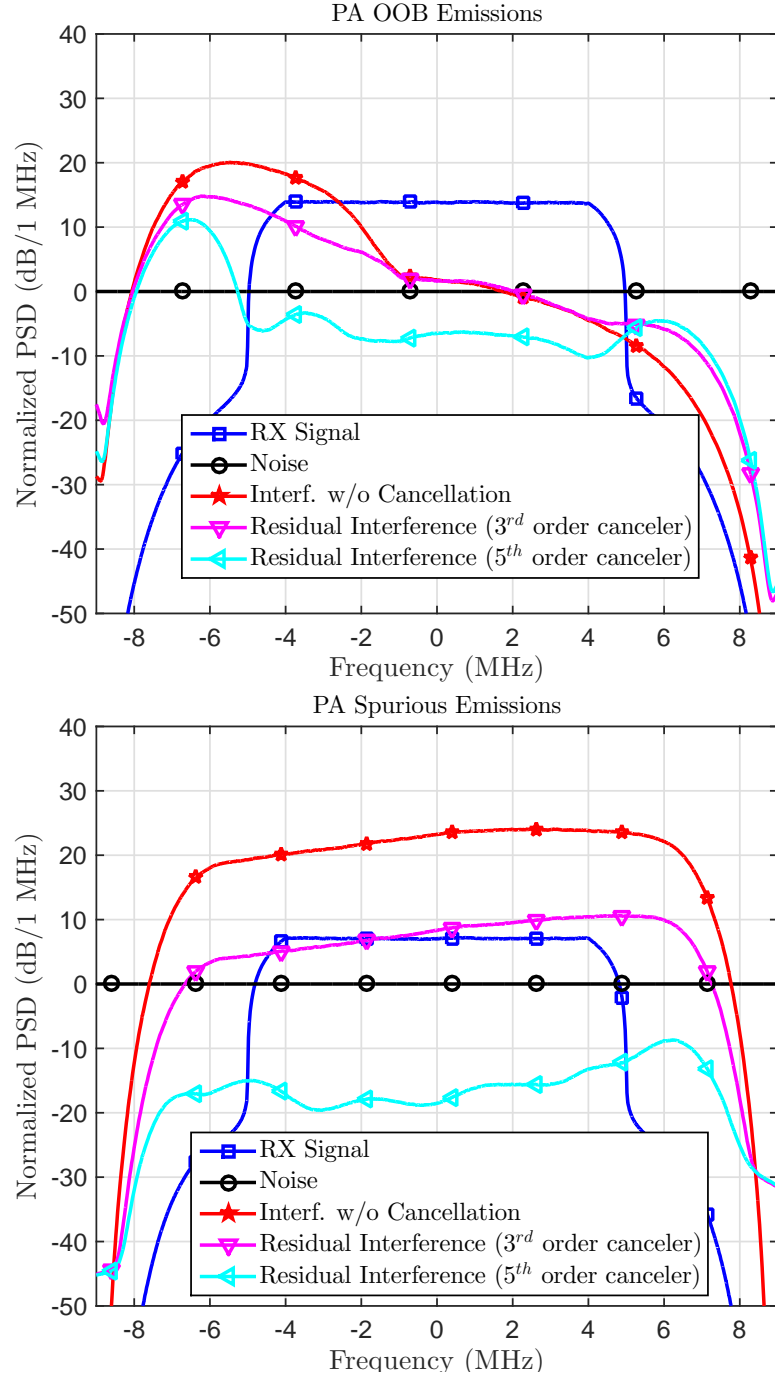


FIG. 4.5: Transmitter nonlinear PA-induced OOB emissions (top) and spurious emissions (bottom) at the RX band before and after cancellation with 23 dBm TX power and 5th order Wiener PA. The RX signal is 10 dB above the reference sensitivity level. PSD curves are normalized to the RX thermal noise power.

PA spurious emissions canceller is evaluated in the context of noncontiguous intraband CA transmission. A state-of-the-art vector signal generator (VSG) and vector signal analyzer (VSA) together with an LTE Band 25 mobile PA module

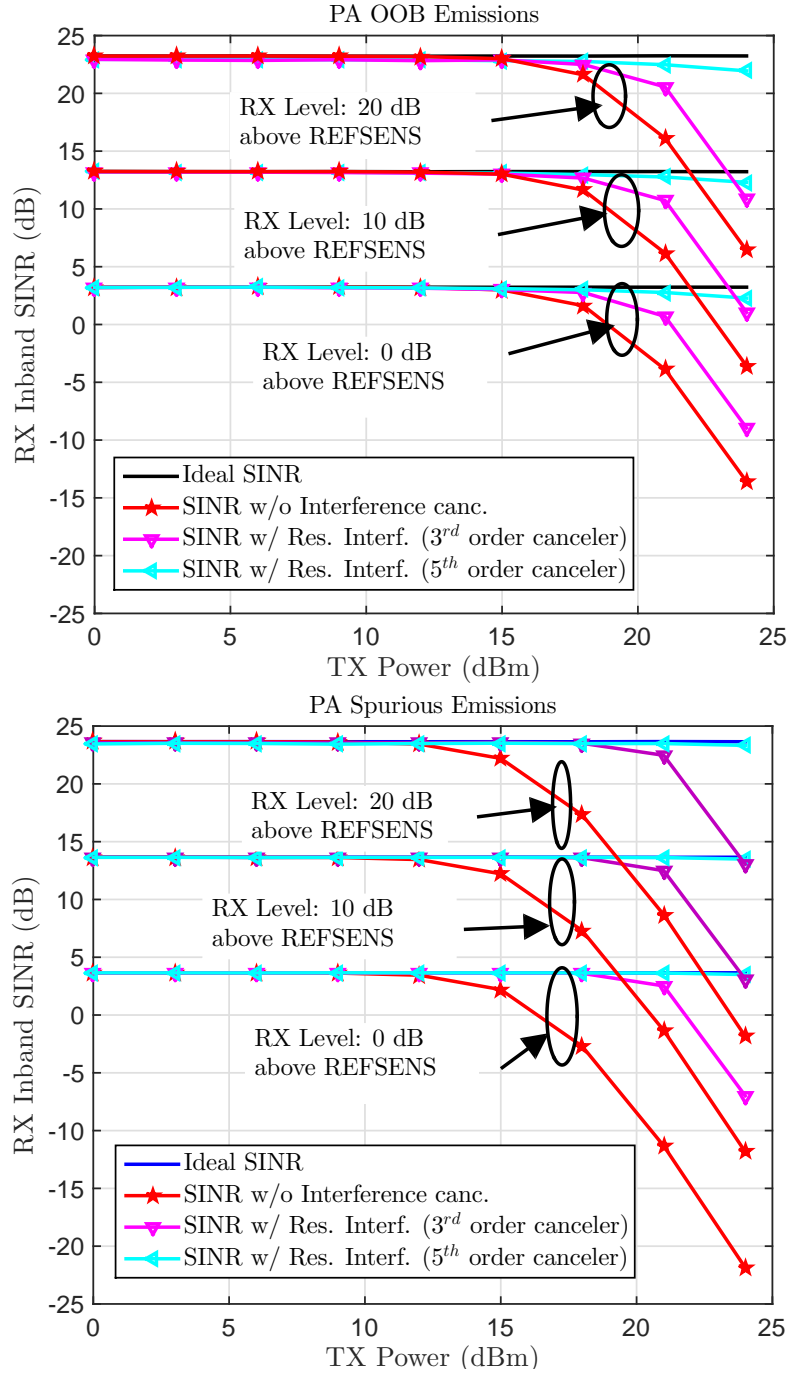


FIG. 4.6: Comparison of average inband SINR vs. TX power before and after the transmitter nonlinear PA-induced OOB emissions (top) and spurious emissions (bottom) cancellation with different RX signal strengths.

and commercial LTE Band 25 mobile duplexer module are used to setup an experimental FDD transceiver. The PA input signal is a dual-carrier LTE-Advanced uplink signal with two 5 MHz CCs and 50 MHz component carriers spacing. The actual RF frequency is 1.89 GHz, and the spurious positive IM3₊ band is located at 1.965 GHz, which is also the own receiver operating band in the measurements.

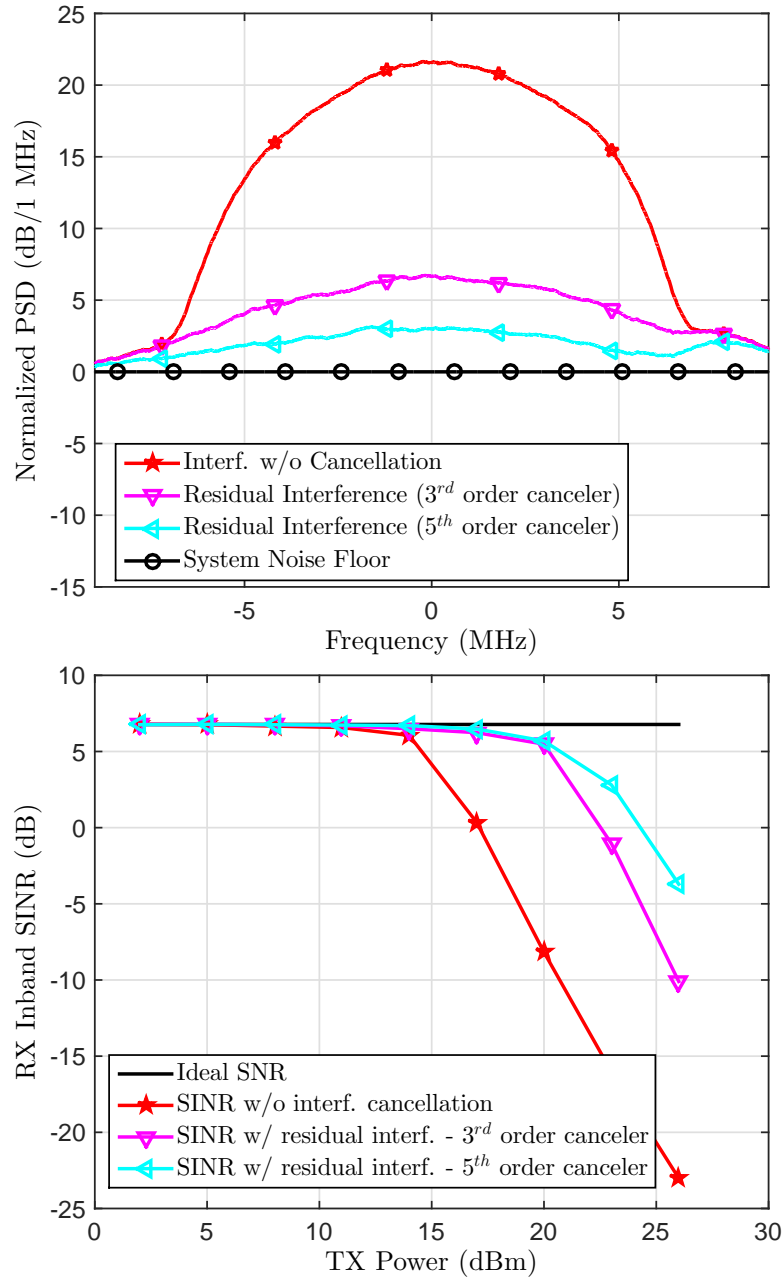


FIG. 4.7: Comparison of measured transmitter nonlinear PA-induced spurious IMD interference spectrum (top) and average measured inband SINR vs. TX power (bottom) before and after digital cancellation. The TX power is +23 dBm and the TX signal is a dual carrier SC-FDMA signal with 5 MHz CCs and 50 MHz CC spacing. The RF frequency is 1.965 GHz.

Fig. 4.7 shows the normalized PSD (top) and the measured SINR vs TX power curves at RX band (bottom) before and after the digital cancellation, showing that the unwanted self-interference can be efficiently suppressed close to the noise

floor with the proposed technique and that more than 18 dB cancellation performance can be achieved. The residual interference present even after the digital cancellation can be attributed to higher than fifth-order nonlinearity terms at the spurious $IM3_+$ band and potential measurement errors, such as the *model mismatch* between the PH model assumed in the estimator and canceler development, and the actual mobile PA, measurement noise, and/or the non-idealities of the measurement equipment.

4.3.2 Digital Mitigation of TX In-band Leakage Signal-Induced IMD2

To evaluate the performance of TX leakage signal-induced IMD2 interference cancellation, the transmit and receive signals are again modeled according to 10 MHz LTE/LTE-Advanced mobile station TX/RX mode. The duplexer filter has a frequency-selective response with $40 \cdots 60$ dB attenuation at the RX band, while the PA gain, PA IIP3, LNA gain, and mixer IIP2 are 24 dB, 15 dBm, 20 dB, and 40 dBm, respectively. The thermal noise power at the LNA input is -104 dBm/10 MHz, the receiver NF is 9 dB, and the desired received signal is 10 dB above the reference sensitivity level that is -93.5 dBm. Frequency-independent transmitter gain and phase imbalances are 5% and 5° , respectively, which correspond to an IRR of 26 dB. With the TX power of +23 dBm, the transmitter leakage IMD2 power at the receiver mixer output is -54 dBm, whereas the desired received signal is at -63.5 dBm. A block of 50,000 samples of the digital baseband transmit signal and the received signal are used in estimation and the fundamental IMD2 2D filter is modeled with 25 parameters. The PSD curves before and after digital cancellation are plotted in Fig. 4.8, showing that the transmitter leakage IMD2 can be suppressed well below the thermal noise floor with the proposed regeneration and cancellation technique. Also, in Fig. 4.9, the average receiver in-band SINR is plotted against different TX powers and for different received signal strengths. The obtained curves show excellent calibration properties of the proposed technique.

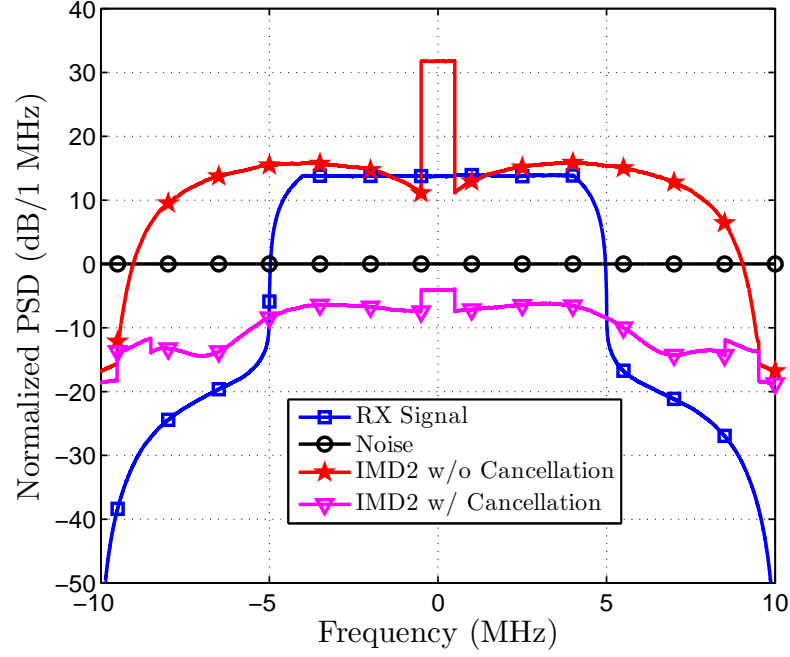


FIG. 4.8: Transmit in-band leakage signal-induced IMD2 interference before and after cancellation with +23 dBm TX power. The RX signal is 10 dB above the reference sensitivity level. PSD curves are normalized to the RX thermal noise power.

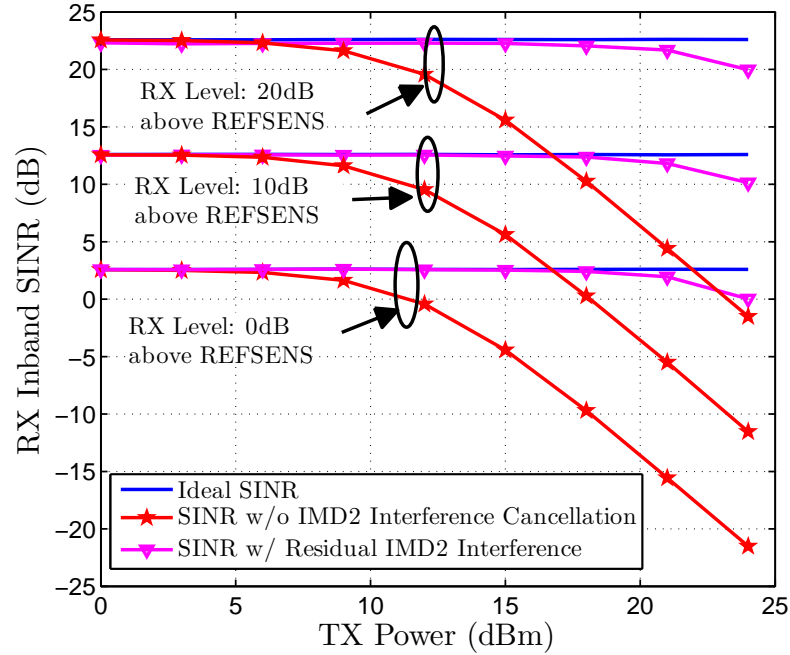


FIG. 4.9: Comparison of average in-band SINR vs. TX power before and after the transmit in-band leakage signal-induced IMD2 interference cancellation with different RX signal strengths.

Chapter 5

Conclusions

This thesis addressed the modeling and digital mitigation of selected RF imperfections in radio communication devices. More specifically, TX RF impairments, namely I/Q imbalance and CFO, and channel distortions were considered in OFDM and uplink OFDMA/SC-FDMA systems, while transmitter leakage signal problems due to nonlinear TX and/or RX components and a finite isolation duplexer filter was investigated for FDD transceivers. Some of the main findings and contributions of this thesis are summarized below.

Receiver-Based Channel and RF Impairments Estimation and Compensation in OFDM Systems: In the first part of Chapter 3, a hybrid time/frequency-domain estimation-compensation structure is proposed for RF impairment and channel distortions mitigation in OFDM systems. Existing efficient algorithms for time-domain RX I/Q imbalance and CFO estimation and correction are incorporated with the proposed frequency-domain TX I/Q imbalance and channel distortions compensation. Both joint and de-coupled TX I/Q imbalance and channel distortions compensation methods are proposed, using preamble pilot or sparse pilot structures for parameter estimation. In addition to simulations, practical RF measurements were also carried out to verify the applicability of the proposed algorithms in OFDM-based receivers.

Uplink OFDMA/SC-FDMA Channel and Impairments Estimation with TX I/Q Imbalances and Small CFOs: In the uplink OFDMA/SC-FDMA context with a direct-conversion architecture, TX I/Q imbalances and CFO cause IUI and ICI. Considering current 3GPP standardization for mobile terminals in terms of I/Q imaging, carrier frequency synchronization, and in-band dynamic range at

the LTE/LTE-Advanced BS RX, IUI due to TX I/Q imbalances is more severe and critical to consider while CFO is relatively small in the uplink, causing very little ICI or IUI. An estimation-compensation structure is proposed in Chapter 3 for joint mitigation of TX I/Q imbalances, small CFOs, and channel distortions, that operates in the BS RX baseband. The joint mirror carrier MMSE equalizer with an arbitrary number of receiver antennas and different power levels of mirror sub-band signals is one key contribution, while an efficient joint parameter estimation with general time-multiplexed reference symbols is another key contribution. Excellent mitigation properties were demonstrated with extensive computer simulations, suggesting that the proposed methods are highly desirable for uplink OFDMA- and SC-FDMA-based BS RXs.

Mitigation of TX Spectral Emissions at Own RX Band in FDD Transceivers:

In this area of thesis work, we proposed a digital mitigation technique for transmitter spectral emissions at the own receiver band due to a nonlinear PA with memory effects in an FDD transceiver. With small duplex gaps, practical nonlinear PAs exhibiting memory effects, and practical duplexers with limited isolation, the transmitter OOB emissions can easily fall in the own RX operating band and can result in own receiver desensitization. In Section 4.1.1, we proposed a nonlinear estimation and regeneration procedure to reproduce essential transmitter OOB emission and subsequently its cancellation in the receiver digital baseband, enabling an efficient cancellation without additional RF filtering. In CA FDD transceivers with noncontiguous CCs, the duplex gap further reduces, and the transmitter spurious emissions created by the nonlinear PA cannot necessarily be sufficiently suppressed. To this end, we proposed a computationally feasible method in Section 4.1.2 that estimates the needed unknown parameters only at the spurious IM3 band, which is assumed to be within the RX operating band, and regenerates and cancels the interference in the receiver baseband. The proposed method is evaluated with simulations as well as in an experimental RF measurement setup, using a commercial LTE mobile device PA and duplexer modules. The obtained results clearly showed the improvement in suppressing unwanted interference and the improved detection of the desired RX signal. Hence, the proposed techniques can be used in FDD transceivers to potentially relax the duplexing gap and the duplexer filtering requirements.

Mitigation of TX In-band Leakage Signal-Induced IMD2: Direct-conversion

receivers are sensitive to second-order intermodulation distortions, where the non-linearity of down-converting mixer may generate IMD2 of the leaking transmit passband signal. In the direct-conversion receiver context, the IMD2 product appears directly in the receiver baseband and interferes with the desired RX signal. A two step LS estimation procedure was described in Section 4.2 to regenerate and cancel the transmitter in-band leakage signal-induced IMD2 in the presence of transmitter nonidealities such as I/Q imbalance and PA nonlinearities. The proposed technique was evaluated with computer simulations and the results demonstrated that the unwanted IMD2 can be efficiently suppressed below the thermal noise floor.

Overall, in this thesis, we investigated some of the important TX RF impairments in OFDM/OFDMA/SC-FDMA-based systems and FDD transceivers, and the proposed algorithms are expected to facilitate the implementation of flexible, reconfigurable, low cost/size and power efficient wireless devices in the future. Meanwhile, some issues have not been addressed in this thesis and can be potential topics for further research. The studies in this thesis assumed uncoded OFDM and OFDMA systems and the algorithms are developed either for single antenna RX configuration or multiple antenna RX configuration, but excluding multiple transmit antennas. In future studies, it would be interesting to generalize the signal models and estimation and compensation algorithms to coded MIMO OFDM/OFDMA type systems with multiple antennas also in all transmitting devices. Furthermore, it would also be interesting to investigate the cost and energy consumption of RF hardware versus the baseband processing adopting the proposed digital algorithms. These form good topics for future work beyond this thesis.

Bibliography

- [1] ITU-R, *Requirements related to technical performance for IMT-advanced radio interface(s)*. Nov. 2008.
- [2] 3GPP, *Evolved Universal Terrestrial Radio Access (E-UTRA); User Equipment (UE) Radio Transmission and Reception*. TS 36.101 V10.3.0, Nov. 2013.
- [3] 3GPP, *Feasibility Study for Further Advancements for E-UTRA (LTE-Advanced)*. TR 36.912,V11.0.0, Oct. 2012.
- [4] G. Yuan, X. Zhang, W. Wang, and Y. Yang, “Carrier aggregation for LTE-advanced mobile communication systems,” *IEEE Communications Magazine*, vol. 48, no. 2, pp. 88–93, 2010.
- [5] T. Lähteensuo, *Linearity Requirements in LTE-Advanced Mobile Transmitter*. Tampere University of Technology, M.Sc. Thesis, 2012.
- [6] E. Dahlman, S. Parkvall, and J. Sköld, *4G LTE/LTE-Advanced for Mobile Broadband*. Amsterdam: Elsevier Ltd., 2011.
- [7] I. Mitola, J., “Software radios: Survey, critical evaluation and future directions,” *IEEE Aerospace and Electronic Systems Magazine*, vol. 8, pp. 25–36, April 1993.
- [8] J. Mitola and G. Q. M. Jr., “Cognitive radio: making software radios more personal,” *IEEE Personal Communications*, vol. 6, pp. 13–18, Aug 1999.
- [9] A. A. Abidi, “Direct-conversion radio transceivers for digital communications,” *IEEE Journal of Solid-State Circuits*, vol. 30, no. 12, pp. 1399–1410, 1995.
- [10] 3GPP, *Evolved Universal Terrestrial Radio Access (E-UTRA); Physical Channels and Modulation*. TS 36.211 V11.1.0, Dec. 2012.

- [11] L. Anttila, *Digital Front-End Signal Processing with Widely-Linear Signal Models in Radio Devices*. Tampere University of Technology, Ph.D. Thesis, 2011.
- [12] M. Faulkner, “DC offset and IM2 removal in direct conversion receivers,” *IEE Proceedings-Communications*, vol. 149, no. 3, pp. 179–184, 2002.
- [13] M. Valkama, M. Renfors, and V. Koivunen, “Compensation of frequency-selective I/Q imbalances in wideband receivers: models and algorithms,” in *IEEE Third Workshop on Signal Processing Advances in Wireless Communications (SPAWC 2001)*, pp. 42–45, 2001.
- [14] B. Razavi, “Design considerations for direct-conversion receivers,” *IEEE Transactions on Circuits and Systems II: Analog and Digital Signal Processing*, vol. 44, pp. 428–435, Jun 1997.
- [15] S. Mirabbasi and K. Martin, “Classical and modern receiver architectures,” *IEEE Communications Magazine*, vol. 38, pp. 132–139, Nov 2000.
- [16] G. Fettweis, M. Lohning, D. Petrovic, M. Windisch, P. Zillmann, and W. Rave, “Dirty RF: A new paradigm,” in *IEEE 16th International Symposium on Personal, Indoor and Mobile Radio Communications (PIMRC 2005)*, vol. 4, pp. 2347–2355 Vol. 4, 2005.
- [17] T. Schenk, *RF Imperfections in High-rate Wireless Systems: Impact and Digital Compensation*. Dordrecht: Springer, 2008.
- [18] A. Kiayani, M. Abdelaziz, L. Anttila, V. Lehtinen, and M. Valkama, “Digital mitigation of transmitter-induced receiver desensitization in carrier aggregation FDD transceivers,” *IEEE Transactions on Microwave Theory and Techniques*, DOI: 10.1109/TMTT.2015.2478005, 2015.
- [19] Y. Yoshida, K. Hayashi, H. Sakai, and W. Bocquet, “Analysis and compensation of transmitter IQ imbalances in OFDMA and SC-FDMA systems,” *IEEE Transactions on Signal Processing*, vol. 57, no. 8, pp. 3119–3129, 2009.
- [20] ABI-Research, *The Internet of Things Will Drive Wireless Connected Devices to 40.9 Billion in 2020*. White pages, [Online]. Available: <https://www.abiresearch.com/press/the-internet-of-things-will-drive-wireless-connect.>, Aug. 2014.

- [21] ETSI, *Radio Broadcasting Systems; Digital Audio Broadcasting (DAB) to mobile, portable and fixed receivers*. May 2001.
- [22] ETSI, *Digital Video Broadcasting (DVB); framing structure, channel coding and modulation for digital terrestrial television*. EN 300 744 V1.5.1., Nov. 2004.
- [23] C. Gessner, *Long Term Evolution - A concise introduction to LTE and its measurement requirements*. Munich: Rohde & Schwarz GmbH & Co., 2001.
- [24] IEEE, *Wireless LAN Medium Access control (MAC) and physical layer (PHY) specifications: High Speed Physical Layer in the 5 Ghz Band*. IEEE Std 802.11a-1999.
- [25] IEEE, *Wireless LAN Medium Access Control (MAC) and Physical Layer (PHY) specifications. Further Higher-Speed Physical Layer Extension in the 2.4 GHz Band*. IEEE Std 802.11g-2003.
- [26] *Mobile WiMAX - Part 1: A technical overview and performance evaluation*. WiMAX Forum, Aug. 2006.
- [27] R. D. can Nee and R. Prasad, *OFDM for Wireless Multimedia Communications*. Artech House, 2000.
- [28] L. W. L. Hanzo, Y. Akhtman and M. Jiang, *MIMO-OFDM for LTE, WiFi amd WiMAX: Coherent versus Non-conherent and Cooperative Turbo Transceivers*. Wiley-IEEE Press, 2011.
- [29] T. C. W. Schenk, *RF Impairments in Multi Antenna OFDM - Influence and Mitigation*. The Netherlands: TU Eindhoven, Ph.D. thesis ed., 2006.
- [30] D. Tandur, *Digital Compensation of Front-End Non-Idealities in Broadband Communication Systems*. Belgium: KU Leuven, Ph.D. thesis ed., 2010.
- [31] G. Xing, M. Shen, and H. Liu, "Frequency offset and I/Q imbalance compensation for OFDM direct-conversion receivers," in *IEEE International Conference on Acoustics, Speech, and Signal Processing (ICASSP 2003)*, vol. 4, pp. IV-708-11 vol.4, 2003.
- [32] M. Windisch, *Estimation and Compensation of I/Q Imbalance in Broadband Communication Receivers*. TU Dresden, Ph.D. Thesis, 2007.

- [33] H. Lin, X. Zhu, and K. Yamashita, "Pilot-aided low-complexity CFO and I/Q imbalance compensation for OFDM systems," in *IEEE International Conference on Communications (ICC 2008)*, pp. 713–717, 2008.
- [34] C.-J. Hsu and W.-H. Sheen, "Joint estimation and compensation of transmitter and receiver radio impairments in MIMO-OFDM receivers," in *IEEE 20th International Symposium on Personal, Indoor and Mobile Radio Communications (PIMRC 2009)*, pp. 2489–2493, 2009.
- [35] J. Feigin and D. Brady, "Joint transmitter/receiver I/Q imbalance compensation for direct conversion OFDM in packet-switched multipath environments," *IEEE Transactions on Signal Processing*, vol. 57, no. 11, pp. 4588–4593, 2009.
- [36] J. Luo, A. Kortke, and W. Keusgen, "Efficient self-calibration of frequency-dependent I/Q-imbalance in direct-conversion OFDM transceivers," in *IEEE International Symposium on Circuits and Systems (ISCAS 2009)*, pp. 413–416, 2009.
- [37] H. Holma and A. Toskala, *LTE-Advanced: 3GPP Solution for IMT-Advanced*. West Sussex: John Wiley & Sons Ltd., 2012.
- [38] H. Holma and A. Toskala, *LTE for UMTS, OFDMA and SC-FDMA Based Radio Access*. West Sussex: John Wiley & Sons Ltd., 2009.
- [39] M. Rumney and A. Technologies, *LTE and the Evolution to 4G Wireless: Design and Measurement Challenges*. Wiley, 2013.
- [40] 3GPP, *Further advancements for E-UTRA physical layer aspects*. TR 36.814, V9.0.0, March 2010.
- [41] 3GPP, *Evolved Universal Terrestrial Radio Access (E-UTRA); Physical Layer; General Description*. TR 36.201 V8.3.0, April 2009.
- [42] H. G. Myung and D. J. Goodman, *Single Carrier FDMA: A New Air Interface for Long Term Evolution*. Wiley, 2008.
- [43] A. Nishio, T. Iwai, A. Matsumoto, and D. Imamura, "System evaluation of mu-mimo and multi-cluster allocation in lte-advanced uplink," in *IEEE 75th Vehicular Technology Conference (VTC Spring 2012)*, pp. 1–5, May 2012.

- [44] H. Wang, H. Nguyen, C. Rosa, and K. Pedersen, "Uplink multi-cluster scheduling with mu-mimo for lte-advanced with carrier aggregation," in *IEEE Wireless Communications and Networking Conference (WCNC 2012)*, pp. 1202–1206, April 2012.
- [45] Z.-N. F.E.Abd El-Samie, F.S.Al-Kamali and M.I.Dessouky, *SC-FDMA for Mobile Communications*. CRC Press, 2013.
- [46] K. Raghunath and A. Chockalingam, "Sc-fdma versus ofdma: Sensitivity to large carrier frequency and timing offsets on the uplink," in *IEEE Global Telecommunications Conference (GLOBECOM 2009)*, pp. 1–6, Nov 2009.
- [47] G. Berardinelli, L. Ruiz de Temino, S. Frattasi, M. Rahman, and P. Mogensen, "Ofdma vs. sc-fdma: performance comparison in local area imt-a scenarios," *IEEE Wireless Communications*, vol. 15, pp. 64–72, October 2008.
- [48] S. Sesia, I. Toufik, and M. Baker, *LTE - The UMTS long Term Evolution, From Theory to Practice*. Sussex: John Wiley & Sons Ltd., 2008.
- [49] M. Iwamura, K. Etemad, M.-H. Fong, R. Nory, and R. Love, "Carrier aggregation framework in 3GPP LTE-advanced [WiMAX/LTE update]," *IEEE Communications Magazine*, vol. 48, no. 8, pp. 60–67, 2010. ID: 1.
- [50] K. I. Pedersen, F. Frederiksen, C. Rosa, H. Nguyen, L. G. U. Garcia, and Y. Wang, "Carrier aggregation for LTE-advanced: functionality and performance aspects," *IEEE Communications Magazine*, vol. 49, no. 6, pp. 89–95, 2011. ID: 1.
- [51] H. Wang, H. Nguyen, C. Rosa, and K. Pedersen, "Uplink multi-cluster scheduling with MU-MIMO for LTE-Advanced with carrier aggregation," *IEEE Wireless Communications and Networking Conference (WCNC 2012)*, pp. 1202–1206, 2012.
- [52] A. B. Carlson, *Communication Systems*. New York: 3rd ed. McGraw-Hill, 1986.
- [53] J. G. Proakis, *Digital Communications*. New York: 3rd ed. McGraw-Hill, 1995.
- [54] Y. Zou, *Analysis and Mitigation of I/Q Imbalances in Multi-Antenna Transmissions Systems*. Tampere University of Technology, Ph.D. Thesis, 2009.

- [55] L. Anttila, M. Valkama, and M. Renfors, "Frequency-selective I/Q mismatch calibration of wideband direct-conversion transmitters," *IEEE Transactions on Circuits and Systems II: Express Briefs*, vol. 55, no. 4, pp. 359–363, 2008.
- [56] 3GPP, *Evolved Universal Terrestrial Radio Access (E-UTRA); User Equipment (UE) Conformance Specification; Radio Transmission and Reception*. Oct. 2013.
- [57] 3GPP, ed., *Evolved Universal Terrestrial Radio Access (E-UTRA); Base Station (BS) Transmission and Reception*. TS36.104, V10.2.0, Release 10, May 2011.
- [58] A. Gomaa and N. Al-Dhahir, "SC-FDMA performance in presence of oscillator impairments: EVM and subcarrier mapping impact," in *IEEE Global Telecommunications Conference (GLOBECOM 2011)*, pp. 1–5, 2011.
- [59] M. Morelli, "Timing and frequency synchronization for the uplink of an OFDMA system," *IEEE Transactions on Communications*, vol. 52, no. 2, pp. 296–306, 2004.
- [60] X. Zhang and H.-G. Ryu, "Suppression of ICI and MAI in SC-FDMA communication system with carrier frequency offsets," *IEEE Transactions on Consumer Electronics*, vol. 56, no. 2, pp. 359–365, 2010.
- [61] C.-P. Li, W.-W. Hu, and T.-Y. Wang, "Frequency offset estimation for ofdm systems using ici self-cancellation schemes," in *IEEE 65th Vehicular Technology Conference (VTC Spring 2007)*, pp. 2305–2309, April 2007.
- [62] Y. Zhao and S.-G. Haggman, "Intercarrier interference self-cancellation scheme for ofdm mobile communication systems," *IEEE Transactions on Communications*, vol. 49, pp. 1185–1191, Jul 2001.
- [63] T. Yucek and H. Arslan, "Carrier frequency offset compensation with successive cancellation in uplink OFDMA systems," *IEEE Transactions on Wireless Communications*, vol. 6, pp. 3546–3551, October 2007.
- [64] X. Zhang and H.-G. Ryu, "Suppression of ICI and MAI in SC-FDMA communication system with carrier frequency offsets," *IEEE Transactions on Consumer Electronics*, vol. 56, pp. 359–365, May 2010.

- [65] M. Omer, R. Rimini, P. Heidmann, and J. S. Kenney, "A compensation scheme to allow full duplex operation in the presence of highly nonlinear microwave components for 4G systems," in *IEEE MTT-S International Microwave Symposium Digest (MTT 2011)*, pp. 1–1, 2011.
- [66] A. Frotzsch and G. Fettweis, "Baseband analysis of Tx leakage in WCDMA zero-IF-receivers," in *3rd International Symposium on Communications, Control and Signal Processing (ISCCSP 2008)*, pp. 129–134, 2008.
- [67] ST-Ericsson and Ericsson, *R4-126946: REFSENS with one UL carrier for NC intra-band CA*.
- [68] ST-Ericsson and Ericsson, *R4-123797, UE reference sensitivity requirements with two UL carriers*.
- [69] C. Park, L. Sundström, A. Wallen, and A. Khayrallah, "Carrier aggregation for lte-advanced: design challenges of terminals," *IEEE Communications Magazine*, vol. 51, pp. 76–84, December 2013.
- [70] H. T. Dabag, H. Gheidi, S. Farsi, P. Gudem, and P. M. Asbeck, "All-digital cancellation technique to mitigate receiver desensitization in uplink carrier aggregation in cellular handsets," *IEEE Transactions on Microwave Theory and Techniques*, vol. 61, no. 12, pp. 4754–4765, 2013.
- [71] H. T. Dabag, H. Gheidi, P. Gudem, and P. M. Asbeck, "All-digital cancellation technique to mitigate self-jamming in uplink carrier aggregation in cellular handsets," in *IEEE MTT-S International Microwave Symposium Digest (IMS 2013)*, pp. 1–3, 2013.
- [72] P. B. Kenington, *High-Linearity RF Amplifier Design*. Artech House, 2000.
- [73] P. Lavrador, T. Cunha, P. Cabral, and J. Pedro, "The linearity-efficiency compromise," *IEEE Microwave Magazine*, vol. 11, pp. 44–58, Aug 2010.
- [74] V. Lehtinen, T. Lähteensuo, P. Vasenkari, A. Piipponen, and M. Valkama, "Gating factor analysis of maximum power reduction in multicluster LTE-A uplink transmission," in *IEEE Radio and Wireless Symposium (RWS 2012)*, pp. 151–153, Jan 2013.

- [75] F. Raab, P. Asbeck, S. Cripps, P. Kenington, Z. Popovic, N. Potheary, J. Sevic, and N. Sokal, "Power amplifiers and transmitters for RF and microwave," *IEEE Transactions on Microwave Theory and Techniques*, vol. 50, pp. 814–826, Mar 2002.
- [76] M. Abdelaziz, L. Anttila, J. Cavallaro, S. Bhattacharyya, A. Mohammadi, F. Ghannouchi, M. Juntti, and M. Valkama, "Low-complexity digital pre-distortion for reducing power amplifier spurious emissions in spectrally-agile flexible radio," in *9th International Conference on Cognitive Radio Oriented Wireless Networks and Communications (CROWNCOM 2014)*, pp. 323–328, June 2014.
- [77] M. Abdelaziz, L. Anttila, A. Mohammadi, F. Ghannouchi, and M. Valkama, "Reduced-complexity power amplifier linearization for carrier aggregation mobile transceivers," in *IEEE International Conference on Acoustics, Speech and Signal Processing (ICASSP 2014)*, pp. 3908–3912, May 2014.
- [78] T. Jiang and Y. Wu, "An overview: Peak-to-average power ratio reduction techniques for OFDM signals," *IEEE Transactions on Broadcasting*, vol. 54, pp. 257–268, June 2008.
- [79] Nokia, *R4-124357: Non-contiguous intra-band reference transmitter architecture*.
- [80] TriQuint, *B4, B25 LTE Duplexer TQQ2504*.
- [81] 3GPP, *Feasibility Study on Interference Cancellation for UTRA FDD User Equipment*. TR 25.963 V7.0.0, April 2007.
- [82] A. T. Phan and R. Farrell, "Reconfigurable multiband multimode LNA for LTE/GSM, WiMAX, and IEEE 802.11.a/b/g/n," in *17th IEEE International Conference on Electronics, Circuits, and Systems (ICECS 2010)*, pp. 78–81, Dec 2010.
- [83] N. Poobuapheun, W.-H. Chen, Z. Boos, and A. Niknejad, "A 1.5-v 0.7-2.5-GHz CMOS quadrature demodulator for multiband direct-conversion receivers," *IEEE Journal of Solid-State Circuits*, vol. 42, pp. 1669–1677, Aug 2007.

- [84] E. Atalla, A. Bellaouar, and P. Balsara, "IIP2 requirements in 4G LTE handset receivers," in *IEEE 56th International Midwest Symposium on Circuits and Systems (MWSCAS 2013)*, pp. 1132–1135, Aug 2013.
- [85] L. Ding, Z. Ma, D. Morgan, M. Zierdt, and G. Zhou, "Compensation of frequency-dependent gain/phase imbalance in predistortion linearization systems," *IEEE Transactions on Circuits and Systems I: Regular Papers*, vol. 55, pp. 390–397, Feb 2008.
- [86] J. Cavers and M. Liao, "Adaptive compensation for imbalance and offset losses in direct conversion transceivers," *IEEE Transactions on Vehicular Technology*, vol. 42, pp. 581–588, Nov 1993.
- [87] R. Marchesani, "Digital precompensation of imperfections in quadrature modulators," Apr 2000.
- [88] J. Tubbax, B. Come, L. V. der Perre, S. Donnay, M. Moonen, and H. D. Man, "Compensation of transmitter IQ imbalance for OFDM systems," in *IEEE International Conference on Acoustics, Speech, and Signal Processing (ICASSP 2004)*, vol. 2, pp. ii–325–8 vol.2, 2004.
- [89] L. Anttila, M. Valkama, and M. Renfors, "Circularity-based I/Q imbalance compensation in wideband direct-conversion receivers," *IEEE Transactions on Vehicular Technology*, vol. 57, no. 4, pp. 2099–2113, 2008.
- [90] L. Anttila and M. Valkama, "On circularity of receiver front-end signals under RF impairments," in *11th European Wireless Conference - Sustainable Wireless Technologies (European Wireless 2011)*, pp. 1–8, 2011.
- [91] G.-T. Gil, Y.-D. Kim, and Y. H. Lee, "Non-data-aided approach to I/Q mismatch compensation in low-IF receivers," *IEEE Transactions on Signal Processing*, vol. 55, pp. 3360–3365, July 2007.
- [92] M. Valkama and M. Renfors, "Advanced DSP for I/Q imbalance compensation in a low-IF receiver," in *IEEE International Conference on Communications (ICC 2000)*, vol. 2, pp. 768–772 vol.2, 2000.
- [93] L. Anttila, M. Valkama, and M. Renfors, "Efficient mitigation of frequency-selective I/Q imbalance in OFDM receivers," in *IEEE 68th Vehicular Technology Conference (VTC 2008-Fall)*, pp. 1–5, 2008.

- [94] E. Lopez-Estraviz, S. De Rore, F. Horlin, and L. Van der Perre, "Optimal training sequences for joint channel and frequency-dependent IQ imbalance estimation in OFDM-based receivers," in *IEEE International Conference on Communications (ICC 2006)*, vol. 10, pp. 4595–4600, June 2006.
- [95] A. Schuchert, R. Hasholzner, and P. Antoine, "A novel IQ imbalance compensation scheme for the reception of OFDM signals," *IEEE Transactions on Consumer Electronics*, vol. 47, no. 3, pp. 313–318, 2001.
- [96] J. Tubbax, B. Come, L. Van der Perre, S. Donnay, M. Moonen, and H. De Man, "Compensation of transmitter IQ imbalance for OFDM systems," in *IEEE International Conference on Acoustics, Speech, and Signal Processing (ICASSP 2004)*, vol. 2, pp. ii–325–8 vol.2, May 2004.
- [97] A. Tarighat, R. Bagheri, and A. H. Sayed, "Compensation schemes and performance analysis of IQ imbalances in OFDM receivers," *IEEE Transactions on Signal Processing*, vol. 53, no. 8, pp. 3257–3268, 2005.
- [98] M. Marey, M. Samir, and O. Dobre, "EM-based joint channel estimation and IQ imbalances for OFDM systems," *IEEE Transactions on Broadcasting*, vol. 58, pp. 106–113, March 2012.
- [99] A. Tarighat and A. H. Sayed, "Joint compensation of transmitter and receiver impairments in OFDM systems," *IEEE Transactions on Wireless Communications*, vol. 6, no. 1, pp. 240–247, 2007.
- [100] Y. Jin, J. Kwon, Y. Lee, J. Ahn, W. Choi, and D. Lee, "Additional diversity gain in OFDM receivers under the influence of IQ imbalances," in *IEEE International Conference on Communications (ICC 2007)*, pp. 5915–5920, 2007.
- [101] E. Lopez-Estraviz and L. Van der Perre, "Em based frequency-dependent transmit/receive IQ imbalance estimation and compensation in OFDM-based transceivers," in *IEEE Global Telecommunications Conference (GLOBECOM 2007)*, pp. 4274–4279, Nov 2007.
- [102] I.-T. Lu and J. Chang, "Joint transmitter and receiver IQ imbalance estimation and compensation for OFDM systems," in *IEEE Radio and Wireless Symposium (RWS 2010)*, pp. 476–479, Jan 2010.

- [103] E. Lopez-Estraviz, S. De Rore, F. Horlin, and A. Bourdoux, "Pilot design for joint channel and frequency-dependent transmit/receive IQ imbalance estimation and compensation in OFDM-based transceivers," in *IEEE International Conference on Communications (ICC 2007)*, pp. 4861–4866, June 2007.
- [104] C.-J. Hsu, R. Cheng, and W.-H. Sheen, "Joint least squares estimation of frequency, DC offset, I-Q imbalance, and channel in MIMO receivers," *IEEE Transactions on Vehicular Technology*, vol. 58, no. 5, pp. 2201–2213, 2009.
- [105] Y. J. Chiu and S. P. Hung, "Estimation scheme of the receiver IQ imbalance under carrier frequency offset in communication system," *IET Communications*, vol. 4, no. 11, pp. 1381–1388, 2010.
- [106] G.-T. Gil, I.-H. Sohn, J.-K. Park, and Y. H. Lee, "Joint ML estimation of carrier frequency, channel, I/Q mismatch, and DC offset in communication receivers," *IEEE Transactions on Vehicular Technology*, vol. 54, no. 1, pp. 338–349, 2005.
- [107] Y.-H. Chung and S.-M. Phoong, "Joint estimation of transmitter and receiver I/Q imbalances, CFO, and channel response for OFDM systems," in *International Conference on Green Circuits and Systems (ICGCS 2010)*, pp. 247–252, 2010.
- [108] D. Tandur and M. Moonen, "Joint adaptive compensation of transmitter and receiver IQ imbalance under carrier frequency offset in OFDM-based systems," *IEEE Transactions on Signal Processing*, vol. 55, no. 11, pp. 5246–5252, 2007.
- [109] J. Gonzalez-Bayon, C. Carreras, and O. Edfors, "A multistandard frequency offset synchronization scheme for 802.11n, 802.16d, LTE, and DVB-T/H systems," *Journal of Computer Systems, Networks, and Communications*, vol. 2010, 2010.
- [110] M. Marey and H. Steendam, "Novel data detection and channel estimation algorithms for BICM-OFDMA uplink asynchronous systems in the presence of IQ imbalance," *IEEE Transactions on Wireless Communications*, vol. 13, no. 5, pp. 2706–2716, 2014.

- [111] E. Au, Z. Lei, and F. Chin, "Exploiting the diversity gain of transmitter I/Q imbalance in single-antenna OFDM systems," in *IEEE Global Telecommunications Conference (GLOBECOM 2009)*, pp. 1–5, 2009.
- [112] S. Haykin, *Adaptive Filter Theory*. NJ: Prentice-Hall, 4 ed. ed., 2002.
- [113] Y. Yoshida, K. Hayashi, and H. Sakai, "On the effect of transmitter IQ imbalance at OFDMA receivers," in *IEEE International Conference on Acoustics, Speech and Signal Processing (ICASSP 2009)*, pp. 2577–2580, April 2009.
- [114] R. Liu, X. Li, L. Ding, and X. Gao, "Low complexity turbo equalization for LTE uplink with transmitter IQ imbalance," in *International Conference on Wireless Communications and Signal Processing (WCSP 2010)*, pp. 1–6, 2010.
- [115] H. A. Mahmoud, H. Arslan, M. K. Ozdemir, and F. E. Retnasothie, "IQ imbalance correction for OFDMA uplink systems," in *IEEE International Conference on Communications (ICC 2009)*, pp. 1–5, 2009.
- [116] A. Gomaa and N. Al-Dhahir, "Multi-user SC-FDMA systems under IQ imbalance: EVM and subcarrier mapping impact," in *IEEE Global Telecommunications Conference (GLOBECOM 2011)*, pp. 1–5, 2011.
- [117] L. Anttila, M. Valkama, and M. Renfors, "3.9G radio reception with SC-FDMA waveforms under I/Q imbalance," in *IEEE International Symposium on Circuits and Systems (ISCAS 2007)*, pp. 25–28, 2007.
- [118] D. K. Borah and B. D. Hart, "Frequency-selective fading channel estimation with a polynomial time-varying channel model," *IEEE Transactions on Communications*, vol. 47, no. 6, pp. 862–873, 1999.
- [119] C. Boor, *A Practical Guide to Splines*. New York: Springer-Verlag, 1978.
- [120] R. N. Khal, Y. V. Zakharov, and J. Zhang, "B-spline based joint channel and frequency offset estimation in doubly-selective fading channels," in *IEEE International Conference on Acoustics Speech and Signal Processing (ICASSP 2010)*, pp. 3214–3217, 2010.
- [121] N. Mai, Y. V. Zakharov, and A. G. Burr, "Iterative channel estimation based on B-splines for fast flat fading channels," *IEEE Transactions on Wireless Communications*, vol. 6, no. 4, pp. 1224–1229, 2007.

- [122] M. Unser, "Splines: a perfect fit for signal and image processing," *IEEE Signal Processing Magazine*, vol. 16, no. 6, pp. 22–38, 1999.
- [123] Y. V. Zakharov and T. C. Tozer, "Local spline approximation of time-varying channel model," *Electronics Letters*, vol. 37, no. 23, pp. 1408–1409, 2001.
- [124] T. B. Sørensen, P. E. Mogensen, and F. Frederiksen, "Extension of the ITU channel models for wideband (ofdm) systems," in *IEEE 62nd Vehicular Technology Conference (VTC-2005-Fall)*, vol. 1, pp. 392–396, 2005.
- [125] M. Omer, R. Rimini, P. Heidmann, and J. S. Kenney, "A PA-noise cancellation technique for next generation highly integrated RF front-ends," in *IEEE Radio Frequency Integrated Circuits Symposium (RFIC 2012)*, pp. 471–474, 2012.
- [126] M. Isaksson, D. Wisell, and D. Ronnow, "A comparative analysis of behavioral models for RF power amplifiers," Jan 2006.
- [127] M. Brandolini, P. Rossi, D. Manstretta, and F. Svelto, "Toward multistandard mobile terminals - fully integrated receivers requirements and architectures," *IEEE Transactions on Microwave Theory and Techniques*, vol. 53, pp. 1026–1038, March 2005.
- [128] V. Aparin, G. Ballantyne, C. Persico, and A. Cicalini, "An integrated lms adaptive filter of tx leakage for cdma receiver front ends," in *IEEE Symposium on Radio Frequency integrated Circuits (RFIC 2005)*, pp. 229–232, June 2005.
- [129] S. Kannangara and M. Faulkner, "Analysis of an adaptive wideband duplexer with double-loop cancellation," *IEEE Transactions on Vehicular Technology*, vol. 56, pp. 1971–1982, July 2007.
- [130] H. Kim, S. Woo, S. Jung, and K.-H. Lee, "A CMOS transmitter leakage canceller for WCDMA applications," *IEEE Transactions on Microwave Theory and Techniques*, vol. 61, pp. 3373–3380, Sept 2013.
- [131] A. Frotzsch and G. Fettweis, "A stochastic gradient LMS algorithm for digital compensation of Tx leakage in zero-IF-receivers," in *IEEE Vehicular Technology Conference (VTC Spring 2008)*, pp. 1067–1071, 2008.

- [132] A. Frotzsch and G. Fettweis, “Least squares estimation for the digital compensation of Tx leakage in zero-IF receivers,” in *IEEE Global Telecommunications Conference (GLOBECOM 2009)*, pp. 1–6, 2009.
- [133] A. Frotzsch, D. Plettemeier, and G. Fettweis, “On the time variance of Tx leakage in FDD zero-IF transceivers,” in *IEEE 70th Vehicular Technology Conference Fall (VTC Fall 2009)*, pp. 1–5, 2009.
- [134] A. Frotzsch and G. Fettweis, “Tx leakage impact on analog-digital conversion in zero-IF receivers,” in *IEEE 70th Vehicular Technology Conference Fall (VTC Fall 2009)*, pp. 1–5, 2009.
- [135] M. Kahrizi, J. Komaili, J. E. Vasa, and D. Agahi, “Adaptive filtering using LMS for digital TX IM2 cancellation in WCDMA receiver,” in *IEEE Radio and Wireless Symposium*, pp. 519–522, 2008.
- [136] C. Lederer and M. Huemer, “Simplified complex LMS algorithm for the cancellation of second-order TX intermodulation distortions in homodyne receivers,” in *Conference Record of the Forty Fifth Asilomar Conference on Signals, Systems and Computers (ASILOMAR 2011)*, pp. 533–537, 2011.
- [137] L. Ding, *Digital Predistortion of Power Amplifiers for Wireless Applications*. Georgia Institute of Technology, Ph.D. Thesis, 2004.

Publications

Publication 1

A. Kiayani, L. Anttila, Y. Zou, and M. Valkama, “Hybrid Time/Frequency Domain Compensator for RF Impairments in OFDM Systems,” in *Proceedings of IEEE 22nd International Symposium on Personal Indoor and Mobile Radio Communications (PIMRC 2011)*, pp. 1948-1952, Sept. 2011.

Copyright ©2011 IEEE. Reprinted, with permission, from the proceedings of IEEE 22nd International Symposium on Personal Indoor and Mobile Radio Communications.

In reference to IEEE copyrighted material which is used with permission in this thesis, the IEEE does not endorse any of Tampere University of Technology's products or services. Internal or personal use of this material is permitted. If interested in reprinting/republishing IEEE copyrighted material for advertising or promotional purposes or for creating new collective works for resale or redistribution, please go to http://www.ieee.org/publications_standards/publications/rights/rights_link.html to learn how to obtain a License from RightsLink.

Hybrid Time/Frequency Domain Compensator for RF Impairments in OFDM Systems

Adnan Kiayani, Lauri Anttila, Yaning Zou, and Mikko Valkama

Department of Communications Engineering

Tampere University of Technology

FI-33101, Tampere, Finland

{adnan.kiayani|lauri.anttila|yaning.zou|mikko.e.valkama}@tut.fi

Abstract—*I/Q* signal processing based communication systems suffer from analog front-end (FE) imperfections such as in-phase and quadrature-phase (I/Q) imbalance and carrier frequency offset (CFO). These impairments are commonly encountered in all practical implementations, and severely degrade the obtainable link performance. Moreover, orthogonal frequency division multiplexing (OFDM)-based systems are particularly sensitive to radio frequency (RF) impairments. In this paper, we analyze the impact of transmitter and receiver I/Q imbalance together with channel distortion and CFO error on an ideal transmit signal, and propose low-complexity DSP algorithms and compensation structure for coping with such imperfections. Based on our proposed estimation/compensation structure, we are able to decouple the impairments and process them individually with rather low-complexity. More specifically, we first apply a blind algorithm for receiver I/Q imbalance compensation, followed by an efficient time domain CFO estimator and compensator. The transmitter I/Q imbalance and channel are then equalized jointly, in the frequency domain, with maximum-likelihood (ML) or zero-forcing (ZF) schemes, respectively. The applied algorithms are either blind working without aid of any training symbol or use only one OFDM symbol for impairments estimation, providing an efficient alternative solution with reduced complexity. The computer simulation results indicate a close to ideal performance of ZF scheme, and suggest that additional performance improvement due to frequency diversity can be obtained when ML estimation technique is employed.

I. INTRODUCTION

The increased demand for high throughput, low-power, cheaper, and flexible radios calls for highly integrable radio transceivers. The so called direct-conversion [1], [2] and low-IF [1], [3] architectures based on I/Q signal processing represent a promising solution due to their simplified RF-FE configuration and the possibility to offer a high degree of integration for the transceiver implementation. These architectures are, nevertheless, exposed to several RF imperfections such as I/Q imbalance, CFO, DC offset, etc. The adoption of higher order modulation techniques (such as 64-QAM) and spectrally efficient modulation schemes (like OFDM) suggests that future wireless systems are highly sensitive to RF impairments. Therefore digital techniques to enhance the dynamic range of FE with minimum additional analog hardware are desirable.

The practical implementation of I/Q up- and down-conversion suffers from the unavoidable gain and phase mismatch between the physical I and Q signal paths, and is

referred to as I/Q imbalance [4]-[6],[9]-[14]. In addition to gain and phase imbalance, other modem components such as digital-to-analog converters (DACs) or analog-to-digital converters (ADCs) and low-pass filters (LPFs) also contribute in general to imbalance effects, and give rise to *frequency selective* I/Q imbalance. I/Q imbalance causes mirror frequency interference and degrades the dynamic range of a transceiver. The performance degradation due to I/Q imbalance has been investigated and compensation schemes have been proposed either for only transmitter I/Q imbalance (e.g. [14]) or for receiver I/Q imbalance (e.g. [4] and [5]). The work in [6], on the other hand, propose joint transmitter and receiver I/Q imbalance compensation algorithms. The algorithms assume frequency-independent I/Q imbalance case which prohibits their application to wideband signals and systems.

Another important RF problem is carrier frequency synchronization. This is especially important for OFDM-based communication systems where subcarriers orthogonality is lost in the presence of CFO. Recently, digital algorithms for joint estimation and compensation of transmitter and receiver I/Q imbalance along with CFO have been proposed. Pilot-based schemes utilizing the training symbols for frequency offset and I/Q imbalance joint compensation are derived in [9] - [13]. The algorithms introduced in [9], [11], and [13] analyze the performance of CFO and I/Q imbalance compensation schemes, but do not take into account the transmitter I/Q imbalance. In [12], joint transmitter receiver I/Q imbalance and CFO compensation techniques are proposed, however *frequency-independent* I/Q imbalance model is assumed. Reference [10] takes a more realistic approach towards the joint estimation and compensation of CFO with frequency-selective transmitter receiver I/Q imbalance, yet the training data require a special symbol structure.

In this paper, we present a comprehensive treatment of frequency-selective transmitter and receiver I/Q imbalance together with CFO error and channel distortion. The novelty of the work is the combination of both blind and data aided estimation, and of time domain and frequency domain compensation, which yields very efficient overall structure in terms of performance and pilot overhead. We utilize our previous work in [5] and [7] to blindly estimate the receiver I/Q imbalance compensation filter. Furthermore, we deploy the sub-space based approach of [8] for CFO estimation and compensation, and propose algorithms for joint transmitter I/Q imbalance and channel estimation and equalization in frequency domain. While receiver I/Q imbalance is compensated blindly, both

The research leading to these results was financially supported by the Technology Promotion Foundation of Finland (TES), the graduate school TISE, and the Austrian Center of Competence in Mechatronics (ACCM).

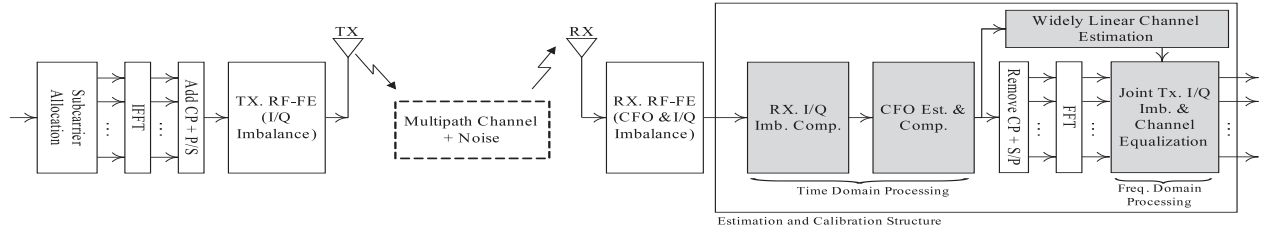


Fig. 1. OFDM system model with transmitter and receiver I/Q imbalance, channel, and CFO compensator.

CFO and joint transmitter I/Q imbalance and channel estimator utilize only a single OFDM pilot symbol, thus reducing pilot overhead and latency. Finally, we evaluate the performance of algorithms in terms of symbol error rate (SER) and show that proposed ML scheme is able to extract the frequency diversity induced by transmitter I/Q imbalance as discussed in [17], and achieve even better performance than the case where no RF impairments except the radio channel and additive noise are present.

The rest of the paper is organized as follows. In Section II, we present the general I/Q imbalance model and describe the impact of I/Q imbalance, CFO, and channel in OFDM system. The estimation and compensation schemes are explained in Section III. Computer simulation results are demonstrated in Section IV and the conclusion is given in Section V.

The notations used in this paper are as follows: scalar parameters are represented by lower-case, vectors in bold lower-case, and matrices in upper-case boldface letters. Superscript $(\cdot)^T$, $(\cdot)^*$ and $(\cdot)^{-1}$ denote the transpose, conjugate, and inverse of a vector, a scalar, or a matrix. The convolution operation is indicated by \star .

II. SIGNAL AND SYSTEM MODEL

A. Frequency-selective transmitter and receiver I/Q imbalance model

We denote the complex baseband signal as $z(t) = z_I(t) + jz_Q(t)$ to be transmitted over the channel. The baseband equivalent of noiseless transmitted RF signal with I/Q imbalance effect is [14]

$$s(t) = g_{1,T}(t) \star z(t) + g_{2,T}(t) \star z^*(t). \quad (1)$$

where the complex imbalance filters $g_{1,T}(t)$ and $g_{2,T}(t)$ model the amplitude, phase, and impulse response mismatch and are expressed in time domain as $g_{1,T}(t) = [h_{I,T}(t) + g_T \exp(j\phi_T) h_{Q,T}(t)]/2$ and $g_{2,T}(t) = [h_{I,T}(t) - g_T \exp(-j\phi_T) h_{Q,T}(t)]/2$. The gain and phase mismatch are designated by g_T and ϕ_T . The mismatch filters $h_{I,T}(t)$ and $h_{Q,T}(t)$ represent the I and Q signal branches response, respectively, and model frequency-selectivity of the overall I/Q imbalance model [14]. In the frequency domain, (1) is transformed into

$$S(f) = G_{1,T}(f)Z(f) + G_{2,T}(f)Z^*(-f). \quad (2)$$

The undesired image signal produced due to the I/Q imbalance results in mirror-frequency interference as shown in (2).

A similar analysis can be carried out on the receiver side, where down-converted baseband equivalent of the received

signal $r(t)$ is of the form [5]

$$x(t) = g_{1,R}(t) \star r(t) + g_{2,R}(t) \star r^*(t) \quad (3)$$

here $g_{1,R}(t)$ and $g_{2,R}(t)$ model the receiver demodulator gain, phase, and impulse response mismatch, and are given in time domain as $g_{1,R}(t) = [h_{I,R}(t) + g_R \exp(-j\phi_R) h_{Q,R}(t)]/2$ and $g_{2,R}(t) = [h_{I,R}(t) - g_R \exp(j\phi_R) h_{Q,R}(t)]/2$. The Fourier transform of (3) is

$$X(f) = G_{1,R}(f)R(f) + G_{2,R}(f)R^*(-f). \quad (4)$$

Again the mirror-frequency interference due to I/Q imbalance is evident from (4). The *image rejection ratio (IRR)* quantifies the image signal suppression, and is defined as the ratio of desired signal power to image signal power, and is expressed in dB as

$$IRR_{TX,RX}(f) \triangleq 10 \log_{10} \left(\frac{|G_{1,T;R}(f)|^2}{|G_{2,T;R}(f)|^2} \right) [dB]. \quad (5)$$

In the ideal case with no I/Q imbalance, $g_{T;R} = 1$, $\phi_{T;R} = 0^\circ$, $h_{I,T;R} = h_{Q,T;R} = 1$, yielding infinite IRR. With careful analog design, IRR's in the order of 25 – 40 dB are stated feasible [2].

B. OFDM signal model with I/Q imbalance, frequency-selective channel, and CFO

We focus here on one symbol block to simplify the analysis. Referring to Fig. 1, let us denote the complex-valued m^{th} OFDM symbol on k^{th} subcarrier by $U_m(k)$, $k = 0, 1, \dots, N-1$. By computing the N -point inverse discrete Fourier transform (IDFT) of the symbol, we obtain the complex baseband signal that can be written in discrete time as

$$z_m(n) = \text{IDFT} \{U_m(k)\}. \quad (6)$$

The cyclic prefix (CP) of length L_{CP} is inserted next by copying the last L_{CP} samples of $z_m(n)$ to its beginning. We assume that the length of the cascade of impulse response of the transmitter I/Q imbalance filters ($g_{1,T}(t)$ and $g_{2,T}(t)$ in (1)) and the multipath radio channel and the receiver I/Q imbalance filters ($g_{1,R}(t)$ and $g_{2,R}(t)$ in (3)) does not exceed the length of CP. It is shown in [5] and [14] that a 3-tap filter is able to correctly estimate the I/Q imbalance filters, thus it is reasonable to estimate the CP length.

First, we assume that an imbalanced quadrature modulator is used to up-convert the baseband signal $z_m(n)$. The resulting distorted signal $s_m(n)$ at the transmitter output is given by (using (1)) [4], [14]

$$s_m(n) = g_{1,T}(n) \star z_m(n) + g_{2,T}(n) \star z_m^*(n). \quad (7)$$

Then, at the receiver side, including the effect of multipath channel, receiver CFO and I/Q imbalance, the signal at the down-conversion stage output appears to be

$$r_m(n) = g_{1,R}(n) \star e^{j2\pi \frac{\Delta f}{NT_s} n} \left(h(n) \star s_m(n) + w_m(n) \right) + g_{2,R}(n) \star e^{-j2\pi \frac{\Delta f}{NT_s} n} \left(h^*(n) \star s_m^*(n) + w_m^*(n) \right) \quad (8)$$

where Δf is the frequency offset, $1/NT_s$ is the subcarrier spacing, $w_m(n)$ is baseband additive white Gaussian noise (AWGN), and $h(n)$ is the impulse response of the baseband equivalent RF radio channel. After some mathematical manipulations, we obtain $r_m(n)$ in terms of transmitter/receiver I/Q imbalance, CFO, and channel as given by (9) (next page). As will be shown in Sec. IV, the presence of all RF impairments severely degrades the system performance, and digital compensation is needed.

III. IMPAIRMENTS ESTIMATION AND COMPENSATION

A. Receiver I/Q imbalance compensation

We continue the analysis in time domain and ignore the noise term. From (9), a straightforward approach to tackle the receiver I/Q imbalance is to use a widely linear compensator of the form $y_m(n) = r_m(n) + w_R(n) \star r_m^*(n)$. The optimum compensator that cancels the mirror frequency interference is of the form $W_R(f) = -G_{2,R}(f)/G_{1,R}^*(-f)$, and is derived in [5]. The basic assumption to obtain the compensation filter in [5] is to utilize the *circular* or *proper* feature of the received signal, which in the presence of transmitter I/Q imbalance is inherently lost. However, it is shown in [7] that either a CFO or a time-varying channel will restore the circularity of the received signal. Motivated by this, we use the blind compensation approach for receiver I/Q imbalance compensation. Applying the optimum compensation filter, (9) becomes

$$y_m(n) \cong g_{1,R}(n) \star e^{j2\pi \frac{\Delta f}{NT_s} n} \left(h(n) \star g_{1,T}(n) \star z_m(n) + h(n) \star g_{2,T}(n) \star z_m^*(n) \right). \quad (10)$$

Comparing (10) with (9) suggests that the compensator is able to fully suppress the image signal term generated by a frequency-selective receiver I/Q imbalance.

B. CFO estimation and compensation

Assuming perfect CFO estimate of Δf , we perform CFO compensation in time domain by multiplying (10) with the complex conjugate of $e^{j2\pi \frac{\Delta f}{NT_s} n}$ which results in

$$\begin{aligned} \tilde{y}_m(n) &= e^{-j2\pi \frac{\Delta f}{NT_s} n} y_m(n) \\ &= \tilde{g}_{1,R}(n) \star h(n) \star g_{1,T}(n) \star z_m(n) + \tilde{g}_{1,R}(n) \star h(n) \star g_{2,T}(n) \star z_m^*(n) \end{aligned} \quad (11)$$

where $\tilde{g}_{1,R}(n) \triangleq e^{-j2\pi \frac{\Delta f}{NT_s} n} g_{1,R}(n)$. There are few algorithms for CFO estimation that can be directly applied here (e.g. [11] and [13]). However, these algorithms assume certain pilot pattern. In this paper, we use the subspace-based approach of [8] for CFO estimation, which utilizes only one OFDM symbol to estimate the CFO. The algorithm does

not account for transmitter I/Q imbalance, but we show with simulations that the impact of transmitter I/Q imbalance on CFO estimation and subsequent compensation is trivial.

C. Joint transmitter I/Q imbalance and channel equalization

We define the direct and image signal filters as $g_D(n) = g_{1,T}(n) \star h(n) \star \tilde{g}_{1,R}(n)$ and $g_M(n) = g_{2,T}(n) \star h(n) \star \tilde{g}_{1,R}(n)$ which transforms (11) to

$$\tilde{y}_m(n) = g_D(n) \star z_m(n) + g_M(n) \star z_m^*(n). \quad (12)$$

In the subsequent derivations, $-k$ refers to the physically opposite (mirror) subcarrier. We now compute the discrete Fourier transform (DFT) of (12) and write it for k^{th} subcarrier of m^{th} received symbol and the complex conjugate of its mirror subcarrier as

$$\begin{bmatrix} \tilde{Y}_m(k) \\ \tilde{Y}_m^*(-k) \end{bmatrix} = \underbrace{\begin{bmatrix} G_D(k) & G_M(k) \\ G_M^*(-k) & G_D^*(-k) \end{bmatrix}}_{G_{total}} \begin{bmatrix} U_m(k) \\ U_m^*(-k) \end{bmatrix} \quad (13)$$

where $G_D(k)$ and $G_M(k)$ are frequency domain representation of the direct and image signal filters. Assuming the coefficients of matrix G_{total} are known, we are able to directly apply the ZF or the ML detection principle on the mirror subcarrier pair.

With ZF scheme, the estimate of original symbol is obtained by solving (13) for each subcarrier k and its mirror $-k$ as

$$\begin{bmatrix} \hat{U}_m(k) \\ \hat{U}_m^*(-k) \end{bmatrix} = \hat{G}_{total}^{-1}(k) \begin{bmatrix} \tilde{Y}_m(k) \\ \tilde{Y}_m^*(-k) \end{bmatrix} \quad (14)$$

As will be shown in Sec. IV, the symbol error rate (SER) vs signal to noise ratio (SNR) analysis show that ZF equalization scheme gives close to ideal performance.

The ML scheme gives the estimate of original symbol by minimizing the cost function of (15) (next page). $\hat{U}_m(k)$ in (15) denotes the trial value of OFDM symbol $U_m(k)$. The computational complexity of ML estimation is generally much higher than ZF method, however, is able to exploit the frequency diversity induced by transmitter I/Q imbalance.

D. LS identification of $g_D(n)$ and $g_M(n)$

We derive a least-squares (LS) estimation technique for imbalance filters $g_D(n)$ and $g_M(n)$. We take a time domain estimation approach similar to [18], where a time domain ML channel estimator was proposed for OFDM. This approach can utilize the frequency domain correlation of the channel implicitly without making any statistical assumptions about the channel, through limiting the length of the estimated channel response estimates as $N_g \ll N$.

We switch to vector-matrix notation to simplify the analysis, and denote the received symbol corresponding to pilot symbol as $\tilde{\mathbf{y}}_p(n) = [\tilde{y}_p(n), \tilde{y}_p(n-1), \dots, \tilde{y}_p(n-L+1)]^T$ and the observable imbalance filter vector by $\hat{\mathbf{g}}_{D;M} = [\hat{g}_{D;M,1}, \hat{g}_{D;M,2}, \dots, \hat{g}_{D;M,N_g}]^T$, where L is the length of observed data and $N_g \leq L_{CP}$ is the length of estimated filters. The received symbol vector during the pilot symbol is then

$$\begin{aligned} \tilde{\mathbf{y}}_p(n) &= \mathbf{Z}_p(n) \hat{\mathbf{g}}_D + \mathbf{Z}_p^*(n) \hat{\mathbf{g}}_M = [\mathbf{Z}_p(n) \quad \mathbf{Z}_p^*(n)] \begin{bmatrix} \hat{\mathbf{g}}_D \\ \hat{\mathbf{g}}_M \end{bmatrix} \\ &= \mathbf{Z}_{p,b}(n) \begin{bmatrix} \hat{\mathbf{g}}_D \\ \hat{\mathbf{g}}_M \end{bmatrix} \end{aligned} \quad (16)$$

$$r_m(n) = g_{1,R}(n) \star e^{j2\pi \frac{\Delta f}{NT_s} n} \left(h(n) \star g_{1,T}(n) \star z_m(n) \right) + g_{1,R}(n) \star e^{j2\pi \frac{\Delta f}{NT_s} n} \left(h(n) \star g_{2,T}(n) \star z_m^*(n) \right) + \\ g_{2,R}(n) \star e^{-j2\pi \frac{\Delta f}{NT_s} n} \left(h^*(n) \star g_{1,T}^*(n) \star z_m^*(n) \right) + g_{2,R}(n) \star e^{-j2\pi \frac{\Delta f}{NT_s} n} \left(h^*(n) \star g_{2,T}^*(n) \star z_m(n) \right) + \\ \left(g_{1,R}(n) \star e^{j2\pi \frac{\Delta f}{NT_s} n} w_m(n) + g_{2,R}(n) \star e^{-j2\pi \frac{\Delta f}{NT_s} n} w_m^*(n) \right). \quad (9)$$

$$\begin{bmatrix} \hat{U}_m(k) \\ \hat{U}_{m,}^*(-k) \end{bmatrix} = \arg \min_{\check{U}_m(k), \check{U}_{m,}^*(-k)} \left\| \hat{G}_{total} \begin{bmatrix} \check{U}_m(k) \\ \check{U}_{m,}^*(-k) \end{bmatrix} - \begin{bmatrix} \check{Y}_m(k) \\ \check{Y}_{m,}^*(-k) \end{bmatrix} \right\|^2 \quad (15)$$

where $\mathbf{Z}_p(n)$ is the *circular-convolution matrix* formed from IDFT of *pilot symbol* $U_p(k)$. The LS estimates of imbalance filters can be computed as [15]

$$\begin{bmatrix} \hat{\mathbf{g}}_D \\ \hat{\mathbf{g}}_M \end{bmatrix} = \mathbf{Z}_{p,b}^\dagger(n) \tilde{\mathbf{y}}_p(n). \quad (17)$$

Here $\mathbf{Z}_{p,b}^\dagger(n)$ represents the *pseudo-inverse* of $\mathbf{Z}_{p,b}(n)$ and is given by $\mathbf{Z}_{p,b}^\dagger(n) = (\mathbf{Z}_{p,b}^H(n) \mathbf{Z}_{p,b}(n))^{-1} \mathbf{Z}_{p,b}^H(n)$ [15]. Frequency domain expressions of the estimated filters, which are needed for equalization/detection in (13)-(15), are then obtained through DFT.

IV. SIMULATION RESULTS

The performance of discussed methods is illustrated in this section using extensive computer simulations. First, we evaluate the performance of CFO estimator in the presence of transmitter I/Q imbalance. In Fig. 2, mean square error (MSE) curve over different CFO values is plotted: $\text{MSE} = E|\Delta \hat{f} - \Delta f|^2$. A 16-QAM OFDM system with transmitter I/Q imbalance parameters corresponding to IRR levels of 20, 30, 40, and INF dB is simulated. These IRR levels map to gain imbalance of 10%, 3%, 1%, 0% and phase imbalance of 10° , 4° , 1° , 0° , respectively. The power delay profile of channel is described in [16] and the results are averaged over 500 independent channel and CFO realizations. The SNR value is fixed to 20 dB and a step size of 0.01 is used for CFO search. The results in Fig. 2 indicate that for small CFO values, we obtain sufficiently accurate estimate i.e. $\Delta \hat{f} \cong \Delta f$, but the performance of estimator deteriorates for large CFO. Despite the biased nature of estimator, it is yet attractive due to number of reasons: *i*) the algorithm delivers reliable estimates, using only a single OFDM symbol. *ii*) the bias is sufficiently small that it does not affect the proposed equalization schemes, as will be shown in following simulations.

Next, we perform the SER simulations and illustrate the performance by plotting SER curves as a function of SNR. A typical 16-QAM OFDM system is considered whose parameters are given in Table I. The I/Q imbalance values stated in the table correspond to 20 – 33 dB IRR within the signal bandwidth. For evaluation, we compare the performance with a system with no FE distortion. A 3-taps compensation filter is built by utilizing the second order statistics of the received signal and is used to compensate for receiver I/Q imbalance as described earlier.

We plot the SER as a function of normalized CFO Δf in Fig. 3. The SNR value is 20 dB. The results are plotted after taking ensemble average of 500 independent CFO and channel

TABLE I
SYSTEM PARAMETERS

Total number of subcarriers	$N = 1024$
Active subcarriers	$N_a = 600$
Cyclic prefix length	$L_{CP} = 52$
Subcarrier spacing	$1/NT_s = 15 \text{ KHz}$
Sampling Frequency	$F_s = 30.72 \text{ MHz}$
Frequency offset	$\Delta f = 10 \text{ KHz}$
Channel Type	vehicular A
No. of channel taps	39
gain imbalance	$g_{T,R} = 5\%$
phase imbalance	$\phi_{T,R} = 5^\circ$
I-branch filter	$\mathbf{h}_{I,T,R} = [1, 0, 0]^T$
Q-branch filter	$\mathbf{h}_{Q,T,R} = [0.97, -0.05, 0.01]^T$

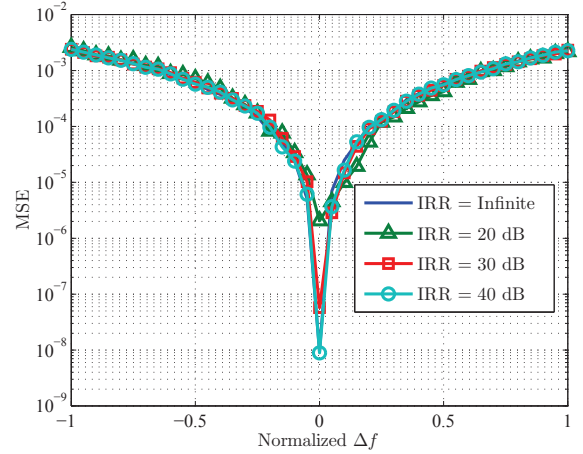


Fig. 2. MSE of CFO estimator vs. true CFO Δf for 16-QAM OFDM system; veh A channel model of length 39; ensemble average of 500 realizations.

realizations, 50 symbols per realization. The excellent calibration property of ML algorithm is evident from the figure. An important observation to note is that the performance is consistent over a wide range of CFO values.

The next simulation example considers a multipath channel with power delay profile of [16] and 39 taps, each having Rayleigh distribution. Fig. 4 compares the SER versus SNR performance curves by taking average over 2000 independent channels and 50 symbols per realization. The channel model also includes AWGN. As can be observed from the figure that the communication system becomes completely unusable when no compensation scheme is in place, and achievable SER remains high in the presence of transmitter receiver I/Q imbalance only. The proposed ZF method is able to

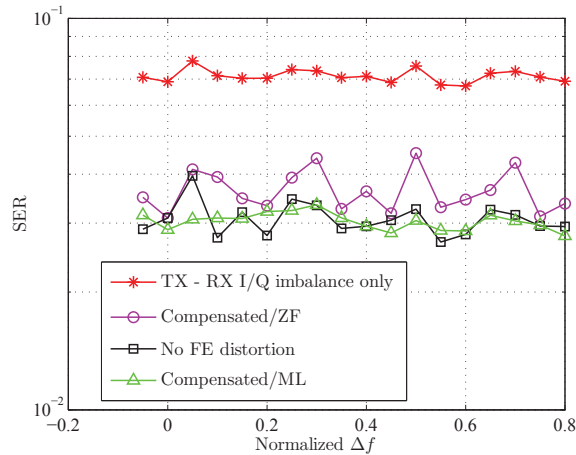


Fig. 3. SER vs. SNR performance curves for 16-QAM OFDM system. TX/RX FE IRR = 20 – 33 dB. Veh A channel model with 39 taps. SNR = 20 dB. Perfect channel knowledge is assumed for the “No FE distortion” and “Tx-Rx I/Q imbalance only” cases. Ensemble average (500 channel realizations).

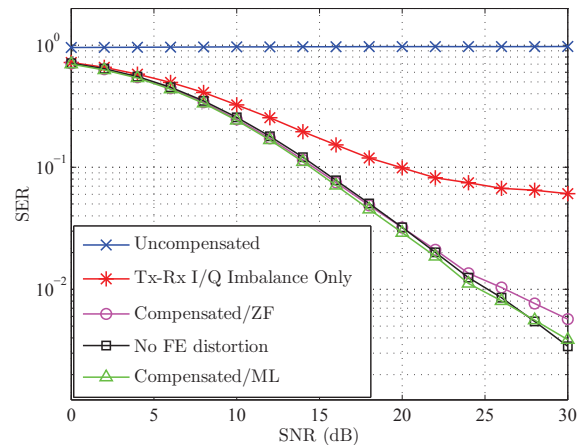


Fig. 4. SER vs. SNR performance curves for 16-QAM OFDM system. TX/RX FE IRR = 20 – 33 dB. Veh A channel model with 39 taps. $\Delta f = 10$ KHz. Perfect channel knowledge is assumed for the “No FE distortion”, “Tx-Rx I/Q imbalance only”, and “Uncompensated” cases. Ensemble average (2000 channel realizations).

produce results close to the ideal case, while ML estimation technique provides frequency diversity due to transmitter I/Q imbalance at low SNR values. The frequency diversity is not very pronounced here as compared to [17], most likely due to residual CFO. However, it is important to note that we are still able to achieve very good performance with a relatively low complexity compensation structure.

V. CONCLUSION AND FUTURE WORK

In this paper, we analyzed the performance of OFDM based communication systems in the presence of transmitter receiver I/Q imbalance, CFO and channel distortion. Based on our signal model, generally applicable digital compensation algorithms are developed. The proposed compensation structure is composed of a time domain compensator and a frequency domain processing compensation part. In the first phase of compensation, we compensate for receiver I/Q imbalance and CFO in an efficient manner in time domain, and two techniques for joint equalization of transmitter I/Q imbalance and channel are presented in frequency domain. It is shown with simulations that the proposed compensator is able to produce symbol estimates very close or even better than ideal available estimates with relatively low implementation complexity. The future work will focus on developing an alternative and more efficient CFO compensator, performing elaborate RF measurements to prove the applicability of the algorithms in real world front-ends, and generalizing the work to MIMO-OFDM and OFDMA systems.

REFERENCES

- [1] A. A. Abidi, “Direct-conversion transceivers for digital communications,” *IEEE J. Solid-State Circuits*, vol. 30, no. 12, pp. 1399-1410, Dec. 1995.
- [2] S. Mirabbasi and K. Martin, “Classical and modern receiver architectures,” *IEEE Communi. Mag.*, vol. 38, pp. 132-139, Nov. 2000.
- [3] J. Crols and M. Steyaert, *CMOS Wireless Transceiver Design*, Kluwer Academic, Dordrecht, the Netherlands, 1997.
- [4] L. Anttila, M. Valkama, and M. Renfors, “Efficient mitigation of frequency-selective I/Q imbalance in OFDM receivers,” in *Proc. IEEE Veh. Technol. Conf. (VTC-F’08)*, Calgary, Canada, Sept. 2008.
- [5] L. Anttila, M. Valkama, and M. Renfors, “Circularity-based I/Q imbalance compensation in wideband direct-conversion receivers,” *IEEE Trans. Veh. Technol.*, vol. 57, pp. 2099-2113, July 2008.
- [6] A. Tarighat, R. Bagheri, and A. Sayed, “Compensation schemes and performance analysis of IQ imbalances in OFDM receivers,” *IEEE Trans. Signal Processing*, vol. 53, no. 8, pp. 3257-3268, Aug 2005.
- [7] L. Anttila and M. Valkama, “On circularity of receiver front-end signals under RF impairments,” in *Proc. 17th European Wireless Conf.*, pp. 610-617, Vienna, Austria, April 2011.
- [8] T. Roman and V. Koivunen, “Carrier frequency synchronization for mobile television receivers,” *IEEE International Symposium on Circuits and Systems (ISCAS-2007)*, pp. 261-264, May 2007.
- [9] C. Hsu, R. Cheng, and W. Sheen, “Joint least-squares estimation of frequency, DC offset, I-Q imbalance, and channel in MIMO receivers,” *IEEE Trans. Veh. Technol.*, vol. 58, no. 5, pp. 2201-2213, June 2009.
- [10] D. Tandur, C. Lee, and M. Moonen, “Efficient Compensation of RF Impairments for OFDM Systems,” *IEEE Wireless Communications and Networking Conference (WCNC-2009)*, pp. 1-6, April 2009.
- [11] J. Tubbax *et al.*, “Joint compensation of IQ imbalance and frequency offset in OFDM systems,” in *Proc. Global Telecommunications Conference (GLOBECOM 03)*, vol. 4, pp. 2365-2369, Dec 2003.
- [12] Y. Chung and S. Phoong, “Joint estimation of transmitter and receiver I/Q imbalances, CFO, and channel response for OFDM systems,” *International Conference on Green Circuits and Systems (ICGCS-2010)*, pp. 247-252, June 2010.
- [13] G. Xing, M. Shen, and H. Liu, “Frequency offset and I/Q imbalance compensation for direct-conversion receivers,” *IEEE Trans. Wireless Communication*, vol. 4, no. 2, pp. 673-680, March 2005.
- [14] L. Anttila, M. Valkama, and M. Renfors, “Frequency-selective I/Q mismatch calibration for wideband direct-conversion transmitters,” *IEEE Trans. Circuits Syst. II, Exp. Breifs*, vol. 55, pp. 359-361, April 2008.
- [15] S. Haykin, *Adaptive Filter Theory*, 4th ed. Upper Saddle River, NJ: Prentice-Hall, 2002.
- [16] T. B. Sorensen, P. E. Mogensen, and F. Frederksen, “Extension of the ITU channel models for wideband (OFDM) systems,” in *Proc. IEEE Veh. Technol. Conf. (VTC’05)*, pp. 392-396, Dallas, Texas, USA, Sept. 2005.
- [17] Y. Jin *et al.*, “Additional diversity gain in OFDM receivers under the influence of IQ imbalances,” in *Proc. IEEE Intl. Conf. Comm. (ICC’07)*, pp. 5915-5920, Glasgow, Scotland, June. 2007.
- [18] L. Deneire, P. Vandenameele, L. Perre, B. Gyselinckx, M. Engels, “A low-complexity ML channel estimator for OFDM,” *IEEE Trans. Comm.*, vol. 51, no. 2, pp. 135-140, Feb. 2003.
- [19] A. Tarighat and A. Sayed, “Joint compensation of transmitter and receiver impairments in OFDM systems,” *IEEE Trans. Wireless Communications*, vol. 6, no. 1, pp. 240-247, Jan 2007.

Publication 2

A. Kiayani, L. Anttila, Y. Zou, and M. Valkama, “Advanced Receiver Design for Mitigating Multiple RF Impairments in OFDM Systems: Algorithms and RF Measurements,” *Journal of Electrical and Computer Engineering*, vol. 2012, article ID 730537, 16 pages, 2012.

Copyright ©2012 Adnan Kiayani et al. This is an open access article distributed under the Creative Commons Attribution License, which permits unrestricted use, distribution, and reproduction in any medium, provided the original work is properly cited.

Research Article

Advanced Receiver Design for Mitigating Multiple RF Impairments in OFDM Systems: Algorithms and RF Measurements

Adnan Kiayani, Lauri Anttila, Yaning Zou, and Mikko Valkama

Department of Communications Engineering, Tampere University of Technology, 33101 Tampere, Finland

Correspondence should be addressed to Adnan Kiayani, adnan.kiayani@tut.fi

Received 15 July 2011; Accepted 12 October 2011

Academic Editor: Ming-Der Shieh

Copyright © 2012 Adnan Kiayani et al. This is an open access article distributed under the Creative Commons Attribution License, which permits unrestricted use, distribution, and reproduction in any medium, provided the original work is properly cited.

Direct-conversion architecture-based orthogonal frequency division multiplexing (OFDM) systems are troubled by impairments such as in-phase and quadrature-phase (I/Q) imbalance and carrier frequency offset (CFO). These impairments are unavoidable in any practical implementation and severely degrade the obtainable link performance. In this contribution, we study the joint impact of frequency-selective I/Q imbalance at both transmitter and receiver together with channel distortions and CFO error. Two estimation and compensation structures based on different pilot patterns are proposed for coping with such impairments. The first structure is based on preamble pilot pattern while the second one assumes a sparse pilot pattern. The proposed estimation/compensation structures are able to separate the individual impairments, which are then compensated in the reverse order of their appearance at the receiver. We present time-domain estimation and compensation algorithms for receiver I/Q imbalance and CFO and propose low-complexity algorithms for the compensation of channel distortions and transmitter IQ imbalance. The performance of the compensation algorithms is investigated with computer simulations as well as with practical radio frequency (RF) measurements. The performance results indicate that the proposed techniques provide close to the ideal performance both in simulations and measurements.

1. Introduction

With the ever-increasing demand for high data rates and high quality of services for end users, bandwidth-efficient transmission schemes such as orthogonal frequency division multiplexing (OFDM) are being adopted in emerging wireless communication systems (e.g., WLAN 802.11a/g/n [1], WiMAX IEEE 802.16 [2], DVB-T [3], DVB-H [4], 3GPP LTE [5]). The physical layer implementation of OFDM-based systems with direct-conversion (zero-IF or homodyne) radio architecture represents a promising solution for future wireless systems. The direct-conversion architecture offers a simplified analog front end (FE) as it performs the frequency translation in one step and thus eliminates the need of bulky image rejection filters [6, 7]. This yields an easy integration of analog and digital components of the FE on a single chip and consequently results in lower-cost and less power consumption. From the perspective of

practical implementation, a trade-off exists between the high integrability and the performance. The direct-conversion architecture-based transceivers are extremely vulnerable to the nonidealities of analog front-end components. The main impairments that degrade the system performance are in-phase quadrature-phase (I/Q) imbalance, DC offset, and carrier frequency offset (CFO) [6, 7]. The adoption of higher-order modulation alphabets (such as 64-QAM) in OFDM systems suggests that they are increasingly sensitive to any impairments in the underlying analog hardware. Rather than trying to improve the quality of individual analog modules, it is more cost-efficient to tolerate these RF impairments to a certain degree in the analog domain and afterward compensating them in the digital domain.

The frequency up- and downconversion in the direct-conversion architectures are implemented by I/Q mixing, which suffers from the amplitude and phase mismatch between the I- and Q- branches [8–24]. This problem

is mainly inflicted by the modulators/demodulators which employ the principle of having equal gain and exact 90° phase difference between the quadrature branches. However, other analog front-end components such as DACs or ADCs and LPFs also contribute in general to the imbalance effects, resulting in *frequency-selective* I/Q imbalance [8–10]. Estimation and compensation schemes dealing with I/Q imbalance have been proposed in several papers including [8–12] and references therein.

CFO is another important RF impairment, particularly associated with OFDM-based communication systems. It is caused by the instability of local oscillator and also due to the mobility of users [25, 26]. OFDM systems divide the available bandwidth into many orthogonal subcarriers with a small subcarrier spacing. The subcarriers orthogonality is lost in the presence of CFO, leading to intercarrier interference. Because the CFO cannot be perfectly estimated in the presence of I/Q imbalances, most of the recent works (e.g., [18–24, 27]) treat them jointly. The algorithms introduced in [18–21] analyze the performance degradation and propose compensation scheme coping with CFO and receiver I/Q imbalance, but do not take into account the transmitter I/Q imbalance. Gil et al. [22], Chung and Phoong [23], and Tandur and Moonen [24] developed the joint estimation algorithm of the I/Q imbalance, CFO, and channel, however frequency-independent I/Q imbalance model is assumed. Finally, in [27], compensation methods for the mitigation of frequency-selective transmitter and receiver I/Q imbalance combined with CFO and channel distortions are proposed by the authors of this article. But the application of proposed algorithms is restricted to systems with a preamble pilot, and also the computational complexity for CFO estimation is very large.

In this paper, we consider DSP-based compensation of frequency-selective transmitter and receiver I/Q imbalance together with frequency-selective channel and CFO in the OFDM system context. The central theme is to first systematically formulate the baseband equivalent of the received signal. Based on this signal model, we propose new low-complexity decoupled estimation and compensation algorithms. Unlike the joint estimation algorithms (e.g., [22, 24]) where the compensator parameters have to be reestimated with channel variations, the decoupled schemes are advantageous in the sense that only the varying parameter has to be reestimated, while the other parameters remain the same. More precisely, at the estimation and compensation stage, we first compensate the generally time-invariant receiver I/Q imbalance in time domain with blind methods proposed in authors' earlier work [11, 13]. The subsequent estimation and compensation of nonidealities including CFO, channel distortions, and transmitter IQ imbalance is done for pilot symbol-assisted modulation (PSAM) OFDM systems in each transmission. With practical considerations, two pilot patterns are taken into account in this work, namely, the preamble pilot pattern, where one complete OFDM symbol in a transmission frame is assumed known, and the sparse pilot pattern, where pilot symbols are placed over different subcarriers of certain OFDM symbols. We propose two alternative estimation and compensation

structures depending on the pilot pattern. The leading principle in CFO estimation and compensation for both pilot patterns is to use an already existing technique of [28] and apply it in time domain. For the preamble pilot-based estimation, we propose zero-forcing (ZF) and maximum-likelihood (ML) estimation methods for joint channel distortions and transmitter I/Q imbalance compensation, whereas an algorithm for successive compensation of channel distortions and transmitter I/Q imbalance is proposed for sparse pilot-based structure. The performance of algorithms is evaluated with extensive computer simulations as well as with laboratory measurement setup.

The novelty of this paper is as follows:

- (1) We do not make any specific assumption about the location of pilots for sparse pilot-based estimation and compensation structure. The existing algorithms, for example [29], allocate the pilots to mirror frequency pairs which is generally not valid in practical radio systems like LTE [5].
- (2) In this work, instead of proposing comprehensive and brand new algorithms to cope with multiple RF impairments at once, we simplify the complexity of the problem by reforming overall receiver design and decoupling the effects of individual RF impairments. Then incorporating already existing efficient algorithms with new proposed methods, a hybrid time-and-frequency domain compensation architecture with very reasonable complexity and good performance is achieved.
- (3) Practical RF measurements are used to verify the applicability of algorithms in real-world receiver design which, to the best of authors' knowledge, has not been addressed so far in the literature. The performance of individual impairments has been evaluated though, for example, [9, 11], but RF performance evaluation in the presence of all the considered impairments is still new.
- (4) Here we use two widely deployed pilot patterns in the current and upcoming OFDM-based radio systems (e.g., IEEE 802.11n [1], DVB-H/T [3, 4], and LTE [5] systems), namely, the preamble-based and sparsely located pilot structures for parameter estimations. As a result, the proposed algorithms can be directly applied in the corresponding receiver design without any modification.

An attractive feature of receiver I/Q imbalance compensation algorithm is that it is able to track the time-variation of I/Q imbalance and updates the coefficients of compensation filter appropriately.

The paper is organized as follows. I/Q imbalance model and its impact, OFDM signal model under frequency-selective I/Q imbalances, channel distortions, and CFO are described in Section 2. Section 3 presents the estimation and compensation techniques for the mitigation of impairments. Computer simulation results are shown in Section 4. In Section 5, the measurement setup and obtained results are presented. Finally, the conclusions are drawn in Section 6.

Preliminaries. The notations used in this paper are as follows. Scalar parameters are represented by lower case letters a and frequency domain quantities with upper case letters A . We denote the time domain vectors/matrices by lower case bold face with over-bar $\bar{\mathbf{a}}/\bar{\mathbf{A}}$ and frequency domain vectors/matrices by bold face letters \mathbf{a}/\mathbf{A} . Superscript $(\cdot)^T, (\cdot)^*$, and $(\cdot)^{-1}$ denote the transpose, conjugate, and inverse of a vector, a scalar, or a matrix, respectively. The (i, j) th quantity of a matrix is defined by A_{ij} and (i, i) th quantity by A_i . The convolution operation is indicated by \star . If $\mathbf{a} = [a_1, a_2, \dots, a_{N/2}, \dots, a_N]^T$ is an OFDM symbol with N subcarriers then $\mathbf{a}^\# = [a_1^*, a_N^*, \dots, a_{N/2}^*, \dots, a_2^*]^T$ is the conjugate of mirror subcarriers vector. The discrete Fourier transform operation is denoted by a matrix \mathbf{F} of size $N \times N$ defined as $[\mathbf{F}]_{mn} = e^{-j(2\pi mn/N)}$, $m = 0, 1, \dots, N-1$; $n = 0, 1, \dots, N-1$.

2. Signal and System Model

2.1. Frequency-Selective I/Q Imbalance Model. The direct-conversion transmitter architecture is based on the principle of directly I/Q upconverting the baseband signal to the RF frequency. The upconversion is performed in the analog domain by a quadrature mixer, which theoretically provides infinite image signal attenuation. This eliminates the need for image rejection filter, relaxing the overall requirement for RF filtering. A perfectly balanced modulator corresponds to equal gain and 90° phase difference between the quadrature branches. However, in practice, this requirement is not fully satisfied. In addition to that, other modem components such as DACs and LPFs in the I- and Q- branch are not perfectly matched [7, 8]. These effects are called I/Q imbalance, and it results in the limited suppression of the image signal [8, 9]. In the wideband system context, the *reconstruction filters* in the modulator exhibit frequency-dependent response, which causes the I/Q imbalance to vary as a function of frequency. Consequently, we can characterize the I/Q imbalance with transmitter gain imbalance and phase imbalance parameter g_T and ϕ_T , respectively [8, 27]. In addition, the relative nonideal filter transfer function between in the I- and Q-branches is modeled with the filter $h_T(t)$. A conceptual block diagram is illustrated in Figure 1. To see the impact of I/Q imbalance on the transmitted signal, we denote the baseband equivalent ideal transmit signal as $z(t) = z_I(t) + jz_Q(t)$. The complex envelope of the transmitted RF signal with I/Q imbalance effects is [8]

$$s(t) = g_{1,T}(t) \star z(t) + g_{2,T}(t) \star z^*(t), \quad (1)$$

where the complex filters $g_{1,T}(t)$ and $g_{2,T}(t)$ correspond to imbalance filters and are defined as

$$\begin{aligned} g_{1,T}(t) &= \frac{\delta(t) + g_T \exp(j\phi_T) h_T(t)}{2}, \\ g_{2,T}(t) &= \frac{\delta(t) - g_T \exp(j\phi_T) h_T(t)}{2}. \end{aligned} \quad (2)$$

The baseband equivalent signal in frequency domain is

$$S(f) = G_{1,T}(f)Z(f) + G_{2,T}(f)Z^*(-f). \quad (3)$$

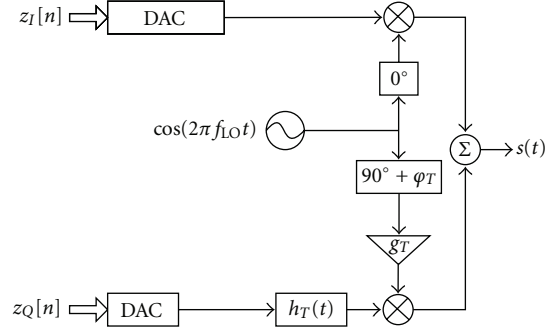


FIGURE 1: Block diagram of Frequency-selective transmitter I/Q imbalance model.

The above equation indicates that the imbalanced baseband signal is weighted sum of the desired signal $Z(f)$ and the undesired image signal $Z^*(-f)$. The undesired image signal term is produced by the I/Q imbalance and results in the mirror frequency interference.

On the receiver side, the RF signal is downconverted to baseband using a quadrature demodulator. The downconverted baseband equivalent of the received signal $r(t)$ is of the form [11]

$$x(t) = g_{1,R}(t) \star r(t) + g_{2,R}(t) \star r^*(t) \quad (4)$$

with the receiver I/Q imbalance filters $g_{1,R}(t)$ and $g_{2,R}(t)$ given as

$$\begin{aligned} g_{1,R}(t) &= \frac{\delta(t) + g_R \exp(-j\phi_R) h_R(t)}{2}, \\ g_{2,R}(t) &= \frac{\delta(t) - g_R \exp(j\phi_R) h_R(t)}{2}. \end{aligned} \quad (5)$$

The Fourier transform of (4) is

$$X(f) = G_{1,R}(f)R(f) + G_{2,R}(f)R^*(-f). \quad (6)$$

Again the mirror-frequency interference due to I/Q imbalance is evident from (6).

The *image rejection ratio* (IRR) quantifies the image signal suppression and is defined as the ratio of desired signal power to image signal power, expressed in dB as

$$\text{IRR}_{T;R}(f) \triangleq 10 \log_{10} \left(\frac{|G_{1,T;R}(f)|^2}{|G_{2,T;R}(f)|^2} \right) [\text{dB}]. \quad (7)$$

With careful analog design, IRR's in the order of 25–40 dB are stated feasible [6–8].

2.2. OFDM Signal Model with RF Impairments. We consider an OFDM system with N subcarriers. At the transmitter, OFDM symbols are generated by computing the N -point inverse discrete Fourier transform (IDFT) of the data symbols \mathbf{u} . A cyclic prefix (CP) of length L_{CP} is appended ahead of each OFDM symbol which is removed at the receiver after DFT.

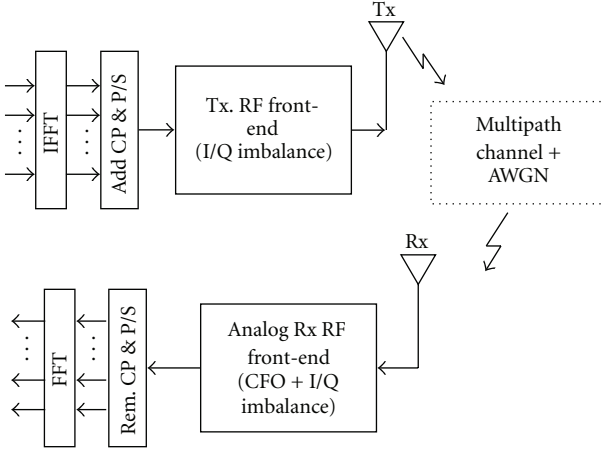


FIGURE 2: OFDM system model with I/Q imbalance and CFO.

Referring to Figure 2, consider the transmission of i th symbol of size $N \times 1$, the frequency domain transmitted signal corresponding to i th OFDM symbol is then given by

$$\mathbf{s}^i = \mathbf{G}_{1,T}\mathbf{u}^i + \mathbf{G}_{2,T}\mathbf{u}^{i\#}, \quad (8)$$

where $\mathbf{G}_{1,T}$ and $\mathbf{G}_{2,T}$ are $N \times N$ frequency domain diagonal matrices whose diagonal elements possess frequency responses of transmitter I/Q imbalance filters ($g_{1,T}$; $g_{2,T}$ in (2)). We consider the transmission over a block fading channel whose impulse response is denoted by $\mathbf{h} = [h(0), h(1), \dots, h(L-1)]^T$ with channel length L . The received frequency domain signal can then be expressed as

$$\mathbf{r}^i = \mathbf{H}\mathbf{G}_{1,T}\mathbf{u}^i + \mathbf{H}\mathbf{G}_{2,T}\mathbf{u}^{i\#} + \mathbf{n}, \quad (9)$$

where \mathbf{H} is $N \times N$ frequency domain matrix that contains the channel frequency response on its main diagonal and \mathbf{n} is additive white Gaussian noise (AWGN).

Assume now that the local oscillator of transmitter and receiver are not synchronized and a CFO Δf is present. If we denote the time domain received signal vector as $\bar{\mathbf{r}}^i$, then the signal in the presence of CFO can be modeled as $\bar{\mathbf{r}}^i = \bar{\Omega}^i \mathbf{r}^i$, where $\bar{\Omega}^i = \text{diag}\{\bar{\mathbf{c}}^i\}$ is the CFO matrix with main diagonal entries

$$\bar{\mathbf{c}}^i = e^{j2\pi\Delta f T_s \{(i-1)N + iL_{CP}\}} \times [1, e^{j2\pi\Delta f T_s}, \dots, e^{j2\pi\Delta f T_s(N-1)}]^T. \quad (10)$$

Here Δf is the frequency offset in Hertz and T_s is the sampling rate. The frequency domain $N \times N$ CFO matrix $\Omega^i = \mathbf{F}\bar{\Omega}^i$ is circulant in nature and has $c(0)$ on its main diagonal and $c^i(1)$ and $c^i(N-1)$ on the first sub- and superdiagonal [30]. Including the CFO effect to (9), we obtain

$$\mathbf{r}^i = \Omega^i \mathbf{H}\mathbf{G}_{1,T}\mathbf{u}^i + \Omega^i \mathbf{H}\mathbf{G}_{2,T}\mathbf{u}^{i\#} + \mathbf{n}. \quad (11)$$

Finally taking into account the receiver I/Q imbalance, the signal at the downconversion stage appears as

$$\mathbf{x}^i = \mathbf{G}_{1,R}\mathbf{r}^i + \mathbf{G}_{2,R}\mathbf{r}^{i\#}, \quad (12)$$

where again $\mathbf{G}_{1,R}$ and $\mathbf{G}_{2,R}$ are $N \times N$ frequency domain diagonal matrices whose diagonal elements are DFT of receiver I/Q imbalance filters ($g_{1,R}$; $g_{2,R}$ in (5)). After some simple mathematical manipulations, the complex baseband equivalent of the received signal in terms of transmitter/receiver I/Q imbalance, channel, and CFO is given by

$$\mathbf{x}^i = \left(\mathbf{G}_{1,R}\Omega^i \mathbf{H}\mathbf{G}_{1,T} + \mathbf{G}_{2,R}\Omega^{i\#} \mathbf{H}^{\#} \mathbf{G}_{2,T}^{\#} \right) \mathbf{u}^i + \left(\mathbf{G}_{1,R}\Omega^i \mathbf{H}\mathbf{G}_{2,T} + \mathbf{G}_{2,R}\Omega^{i\#} \mathbf{H}^{\#} \mathbf{G}_{1,T}^{\#} \right) \mathbf{u}^{i\#} + \mathbf{v}, \quad (13)$$

where $\Omega^{i\#}$, $\mathbf{H}^{\#}$, $\mathbf{G}_{1,T}^{\#}$, $\mathbf{G}_{2,T}^{\#}$ are the mirrored matrix of Ω^i , \mathbf{H} , $\mathbf{G}_{1,T}$, $\mathbf{G}_{2,T}$, respectively. The noise term now becomes $\mathbf{v} = \mathbf{G}_{1,R}\mathbf{n} + \mathbf{G}_{2,R}\mathbf{n}^{\#}$, whose elements are still complex circular Gaussian, but with correlated mirror subcarriers. In the ideal case when there is perfect transmitter/receiver modulator/demodulator matching as well as perfect synchronization between the transmitter/receiver local oscillator, the model in (13) reduces to $\mathbf{x}^i = \mathbf{H}\mathbf{u}^i + \mathbf{n}$ which can be equalized with one complex multiplication for each subcarrier in each OFDM symbol. As evident from (13), both I/Q imbalances and CFO introduce ICI and severely degrade the system performance, thus digital compensation is needed.

In this paper, we assume that the length of the cascade of impulse responses of the transmitter I/Q imbalance filters ($g_{1,T}(t)$ and $g_{2,T}(t)$ in (1)), the multipath radio channel, and the receiver I/Q imbalance filters ($g_{1,R}(t)$ and $g_{2,R}(t)$ in (4)) does not exceed the length of CP. It is reasonable to make such an assumption as the frequency-selective transceiver I/Q imbalance is rather moderate and can be estimated with sufficient accuracy with only a few taps [8, 11, 27].

3. Estimation and Compensation of Nonidealities

The estimation and compensation of radio frequency impairments in OFDM systems can be performed blindly and/or with the aid of training (a.k.a. pilot) symbols. For forming such pilot-symbol-assisted OFDM systems, it involves inserting the known symbols in the stream of data symbols. With practical system design, two types of pilot patterns are widely used—the preamble pilot pattern that amends an entirely known OFDM symbol at the beginning of the frame and the sparse pilot pattern where pilot symbols are sparsely inserted at some subcarriers of specific OFDM symbols. Figure 3 illustrate these two ways of inserting pilots among the data symbols.

In the following, we discuss receiver-based estimation and compensation algorithms for mitigating all the considered RF impairments. With developed signal model and given pilot patterns, we are able to isolate them individually and then process them for estimation and compensation in the reverse order of their appearance in the transmitter and receiver front end. We first discuss the receiver I/Q imbalance estimation and compensation, which is performed in time domain and is independent of the pilot pattern. Then, two low-complexity and novel structures are proposed for CFO, channel, and transmitter I/Q imbalance compensation with both preamble and sparse pilot structures. The CFO

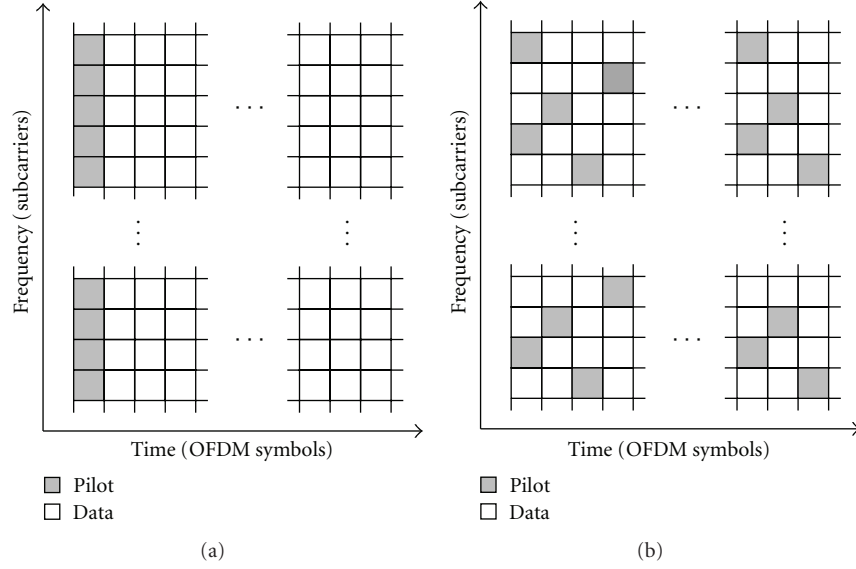


FIGURE 3: Pilot structure (a) preamble (b) scattered.

estimation and compensation is also carried out in time domain, while the channel and transmitter IQ imbalance are compensated in frequency domain.

3.1. Blind Receiver I/Q Imbalance Compensation. For receiver I/Q imbalance estimation and compensation, we propose to utilize the statistical signal processing-based blind I/Q imbalance compensation algorithms, developed in authors' earlier work [11, 13, 14]. In general, most complex communication waveforms based on M -PSK and M -QAM (with $M > 2$) are proper or circular [31]. The OFDM signal constructed from these alphabets is thus also circular. I/Q imbalance destroys this property and makes the signal noncircular. The strategy used in [11] is to recover the circularity using second-order statistics-based approach, under the assumption that the received signal (without receiver I/Q imbalance) is circular. The circularity of received signal is inherently lost in the presence of transmitter I/Q imbalance, potentially hindering the applicability of the I/Q imbalance compensation algorithms of [11]. However, it is shown in [13] that either a CFO or a fading channel will restore the circularity of the received signal (without receiver I/Q imbalance), thus making it possible to utilize the circularity-based algorithms of [11]. These blind algorithms are also beneficial from the point of view that they do not affect the subsequent signal processing of CFO, channel, and transmitter I/Q imbalance estimation and compensation.

For notational simplicity, we drop the noise term in (13) and continue the analysis. Notice that even though the actual compensation processing is done partly in the time domain (for receiver I/Q imbalance and CFO), the following analysis is done completely in the frequency domain. From (12), we recognize that the signal \mathbf{x}^i is the linear combination of the received signal \mathbf{r}^i and its mirror conjugate $\mathbf{r}^{i\#}$. For such a system model, the natural compensator is of the form

$$\mathbf{y}^i = \mathbf{x}^i + \mathbf{W}_R \mathbf{x}^{i\#}. \quad (14)$$

Substituting the observed signal \mathbf{x}^i of (12) into the compensator in (14), the output can be written as

$$\mathbf{y}^i = (\mathbf{G}_{1,R} + \mathbf{W}_R \mathbf{G}_{2,R}^\#) \mathbf{r}^i + (\mathbf{G}_{2,R} + \mathbf{W}_R \mathbf{G}_{1,R}^\#) \mathbf{r}^{i\#}. \quad (15)$$

From (15), it follows that the optimum compensation filter \mathbf{W}_R canceling the mirror-frequency interference is, in frequency domain $N \times N$ diagonal matrix, of the form $\mathbf{W}_{\text{OPT}} = -\mathbf{G}_{2,R}(\mathbf{G}_{1,R}^\#)^{-1}$ and is derived in [11].

Applying the optimum compensation filter to (15) cancels the mirror conjugate term $\mathbf{r}^{i\#}$ and results in the output signal as

$$\begin{aligned} \mathbf{y}^i = & \left(\mathbf{G}_{1,R} \Omega^i \mathbf{H} \mathbf{G}_{1,T} - \mathbf{G}_{2,R} \mathbf{G}_{2,R}^\# (\mathbf{G}_{1,R}^\#)^{-1} \Omega^i \mathbf{H} \mathbf{G}_{1,T} \right) \mathbf{u}^i \\ & + \left(\mathbf{G}_{1,R} \Omega^i \mathbf{H} \mathbf{G}_{2,T} - \mathbf{G}_{2,R} \mathbf{G}_{2,R}^\# (\mathbf{G}_{1,R}^\#)^{-1} \Omega^i \mathbf{H} \mathbf{G}_{1,T} \right) \mathbf{u}^{i\#}. \end{aligned} \quad (16)$$

It is well known that $|\mathbf{G}_{1,T,R}| > |\mathbf{G}_{2,T,R}|$ and $|\mathbf{G}_{1,T,R}| \approx 1$ for any practical imbalance values; thus the contributions of the second terms inside the parentheses are relatively very small compared to the first term and can be omitted, leading to the following form:

$$\mathbf{y}^i \approx \mathbf{G}_{1,R} \Omega^i \mathbf{H} (\mathbf{G}_{1,T} \mathbf{u}^i + \mathbf{G}_{2,T} \mathbf{u}^{i\#}). \quad (17)$$

Comparing (16) with (13) suggests that, given \mathbf{W}_{OPT} , the compensator is able to fully suppress the image signal term generated by a frequency-selective receiver I/Q imbalance in the presence of CFO, channel distortions, and transmitter I/Q imbalance. The estimation of \mathbf{W}_{OPT} is described in [11, 13] and is not reproduced here. Next, we discuss the pilot-based estimation and compensation schemes for CFO, channel distortions, and transmitter I/Q imbalance.

3.2. Estimation and Compensation with Preamble Pilot Structure. The compensation structure proposed in this section

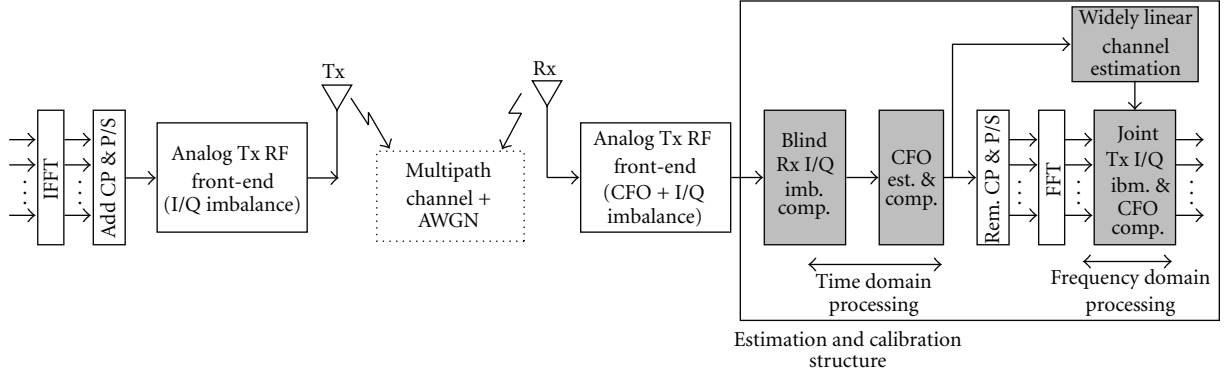


FIGURE 4: OFDM system model with preamble pilot compensator structure.

utilizes one complete pilot OFDM symbol embedded in the OFDM frame. The preamble pilot symbol is transmitted at the beginning of the transmission to estimate the RF impairments. This kind of pilot pattern assumes that the channel remains static over several OFDM symbols and has the benefit of efficiently using the available bandwidth. OFDM-based systems such as IEEE 802.11 n and IEEE 802.16d have a preamble at the beginning of the frame [25]. Figure 4 shows the system model with RF impairments estimation and compensation block in place. In the following, we discuss the algorithms for the estimation and compensation of RF impairments.

3.2.1. CFO Estimation and Compensation. There exists an abundant literature on CFO estimation (see, e.g., [18–25] and references therein), but most of these algorithms assume a specific pilot structure which restrict their use in our problem. The subspace-based CFO estimation approach proposed in [26] utilizes only one OFDM symbol, and can be directly used here at the expense of increased computational complexity. We rather suggest to use the CFO estimation algorithm of [28] as discussed in [25]. More specifically, the actual CFO estimation is performed in two stages: first the fractional part of CFO is estimated and corrected in time domain by using the CP correlation. The integer part is then estimated in frequency domain in the second stage. Even though the presence of transmitter I/Q imbalance is not taken into account in this method, we show with simulations that the algorithm is still able to achieve reasonable good CFO estimation performance.

Assuming perfect CFO estimate is obtained, we perform CFO compensation in time domain by multiplying the time domain equivalent of (17) with the complex conjugate of $\tilde{\Omega}^i$, which, in time domain, can be written as

$$\begin{aligned} \tilde{\mathbf{y}}^i &= \mathbf{F}[\tilde{\Omega}^{i*} \tilde{\mathbf{y}}^i] \\ &= \tilde{\mathbf{G}}_{1,R} \mathbf{H}(\mathbf{G}_{1,T} \mathbf{u}^i + \mathbf{G}_{2,T} \mathbf{u}^{i*}), \end{aligned} \quad (18)$$

where $\tilde{\mathbf{G}}_{1,R} \triangleq \Omega^{i*} \mathbf{G}_{1,R}$.

3.2.2. Joint Transmitter I/Q Imbalance and Channel Equalization. The joint transmitter I/Q imbalance and channel

equalization are carried out in frequency domain. To simplify the analysis further, let us define the direct and image signal filters as $\mathbf{G}_D \triangleq \tilde{\mathbf{G}}_{1,R} \mathbf{H} \mathbf{G}_{1,T}$ and $\mathbf{G}_M \triangleq \tilde{\mathbf{G}}_{1,R} \mathbf{H} \mathbf{G}_{2,T}$, which transforms (18) into

$$\tilde{\mathbf{y}}^i = \mathbf{G}_D \mathbf{u}^i + \mathbf{G}_M \mathbf{u}^{i*}. \quad (19)$$

We now switch to the subcarrier model and write the CFO compensated symbol for the k th subcarrier and the complex conjugate of its mirror subcarrier. In the subsequent derivations, the subcarrier index $-k$ refers to the physically opposite mirror subcarrier

$$\begin{bmatrix} \tilde{Y}_k^i \\ \tilde{Y}_{-k}^{i*} \end{bmatrix} = \underbrace{\begin{bmatrix} G_{D,k} & G_{M,k} \\ G_{M,-k}^* & G_{D,-k}^* \end{bmatrix}}_{\mathbf{G}_{\text{total},k}} \begin{bmatrix} U_k^i \\ U_{-k}^{i*} \end{bmatrix}. \quad (20)$$

The matrix $\mathbf{G}_{\text{total},k}$ represents the joint transmitter I/Q imbalance and channel response. Assuming the coefficients of matrix $\mathbf{G}_{\text{total},k}$ are known, we are able to directly apply the ZF or the ML detection principle on the mirror subcarrier pair to estimate the transmitted symbol.

With ZF equalization scheme, the estimate of original transmit symbols is obtained by solving (20) for each subcarrier k and its mirror subcarrier $-k$ as

$$\begin{bmatrix} \hat{U}_k^i \\ \hat{U}_{-k}^{i*} \end{bmatrix} = \hat{\mathbf{G}}_{\text{total},k}^{-1} \begin{bmatrix} \tilde{Y}_k^i \\ \tilde{Y}_{-k}^{i*} \end{bmatrix}. \quad (21)$$

It is well known that ZF equalization suffers from the noise enhancement problem, yet it gives good calibration performance as will be shown in Section 4.

Alternatively, the transmitted symbols can be estimated using ML detection principle which is based on the principle of minimizing the cost function

$$\begin{bmatrix} \hat{U}_k^i \\ \hat{U}_{-k}^{i*} \end{bmatrix} = \arg \min_{\tilde{U}_k^i, \tilde{U}_{-k}^{i*}} \left\| \hat{\mathbf{G}}_{\text{total},k} \begin{bmatrix} \tilde{U}_k^i \\ \tilde{U}_{-k}^{i*} \end{bmatrix} - \begin{bmatrix} \tilde{Y}_k^i \\ \tilde{Y}_{-k}^{i*} \end{bmatrix} \right\|^2, \quad (22)$$

where \tilde{U}_k^i in (22) denotes the trial value of OFDM symbol U_k^i . The ML equalizer is able to exploit the frequency diversity induced by transmitter I/Q imbalance and gives better performance than ZF, but the computational complexity associated with ML is very large which increases with higher-order constellations and large number of subcarriers.

3.2.3. LS Identification of $G_{total,K}$. We consider the LS estimation of the joint transmitter I/Q imbalance and channel filters \mathbf{G}_D and \mathbf{G}_M . The filters are estimated in time domain similar to [32], where a time-domain ML channel estimator was proposed for OFDM. This approach can utilize the frequency domain correlation of the channel implicitly without making any statistical assumptions about the channel, through limiting the length of the estimated channel response estimates as $N_g \ll N$.

We switch to matrix-vector algebra and write the time-domain received symbol corresponding to preamble pilot as $\tilde{\mathbf{y}}^p(n) \triangleq [\tilde{y}^p(n), \tilde{y}^p(n-1), \dots, \tilde{y}^p(n-N+1)]^T$ and the observable imbalance filters as $\hat{\mathbf{g}}_{D;M} = [\hat{g}_{D;M,1}, \hat{g}_{D;M,2}, \dots, \hat{g}_{D;M,N_g}]^T$, where N is the length of pilot data and $N_g < L_{CP}$ is the length of estimated filters. The received symbol vector during the pilot symbol is then

$$\begin{aligned} \tilde{\mathbf{y}}^p(n) &= \bar{\mathbf{U}}^p(n) \hat{\mathbf{g}}_D + \bar{\mathbf{U}}^{p*}(n) \hat{\mathbf{g}}_M \\ &= [\bar{\mathbf{U}}^p(n) \quad \bar{\mathbf{U}}^{p*}(n)] \begin{bmatrix} \hat{\mathbf{g}}_D \\ \hat{\mathbf{g}}_M \end{bmatrix} \\ &= \bar{\mathbf{U}}_b^p(n) \begin{bmatrix} \hat{\mathbf{g}}_D \\ \hat{\mathbf{g}}_M \end{bmatrix}, \end{aligned} \quad (23)$$

where $\bar{\mathbf{U}}^p(n)$ is the time-domain *circular-convolution matrix* formed from IDFT of *pilot symbol* \mathbf{u}_p . The LS estimates of imbalance filters can be computed as [33]

$$\begin{bmatrix} \hat{\mathbf{g}}_D \\ \hat{\mathbf{g}}_M \end{bmatrix} = \bar{\mathbf{U}}_b^{p\dagger}(n) \tilde{\mathbf{y}}^p(n). \quad (24)$$

Here $\bar{\mathbf{U}}_b^{p\dagger}(n)$ represents the *pseudoinverse* of $\bar{\mathbf{U}}_b^p(n)$ and is given by $\bar{\mathbf{U}}_b^{p\dagger}(n) = (\bar{\mathbf{U}}_b^{pH}(n) \bar{\mathbf{U}}_b^p(n))^{-1} \bar{\mathbf{U}}_b^{pH}(n)$ [33]. Frequency domain expressions of the estimated filters \mathbf{G}_D and \mathbf{G}_M , which are needed for equalization/detection in (20)–(22), are then obtained through DFT.

3.3. Estimation and Compensation with Sparse Pilot Structure. OFDM systems such as LTE and DVB-T/H do not include a preamble pilot in their frame, rather the pilot tones are inserted sparsely in the OFDM symbols. DVB-T/H standard defines both continual and scattered pilots, on the other hand, LTE includes pilot subcarriers only on specified OFDM symbols. Figure 5 shows the reference pilot structure for LTE system with pilot symbols at every sixth subcarrier during the first and fifth OFDM symbol of each slot.

One big challenge with sparse located pilot structure is that the pilots are most likely not allocated to mirror-frequency pairs which is required by most of the pilot-based algorithms developed in literature, for example, [29]. The compensation algorithms proposed in this section consist of estimating the impairments at the pilot frequencies and then interpolating the estimates over all the subcarriers. Therefore, no pilot structure modification is needed, and they can be directly applied for the development of, for example, LTE receiver. The estimation and compensation structure is illustrated in Figure 6. Again, notice that the receiver I/Q imbalance has already been compensated with the blind method discussed in Section 3.1.

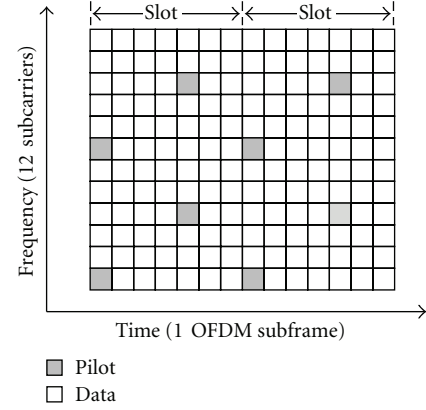


FIGURE 5: LTE reference pilot structure.

3.3.1. CFO Estimation and Compensation. For the CFO estimation, we again apply the two-step time-domain approach of [25] as discussed in the previous subsection, resulting in the time domain CFO compensated signal similar to (18) as

$$\begin{aligned} \tilde{\mathbf{y}}^i &= \tilde{\mathbf{G}}_{1,R} \mathbf{H} \mathbf{G}_{1,T} \mathbf{u}^i + \tilde{\mathbf{G}}_{1,R} \mathbf{H} \mathbf{G}_{2,T} \mathbf{u}^{i*} \\ &= \mathbf{G}_D \mathbf{u}^i + \mathbf{G}_M \mathbf{u}^{i*}. \end{aligned} \quad (25)$$

3.3.2. Decoupled Transmitter I/Q Imbalance and Channel Equalization. With the sparse pilot structure, we propose to compensate the channel and transmitter I/Q imbalance successively. Algorithm 1 summarizes the algorithm for the estimation of transmitted symbols.

Algorithm 1 (It is for estimation of channel distortions and transmitter I/Q imbalance).

- (1) Estimate widely-linear filter $G_{D,k}$ (see Section 3.3.3).
- (2) Switch to subcarrier model and write (25) in frequency domain for subcarrier k as

$$\tilde{Y}_k^i = G_{D,k} U_k^i + G_{M,k} U_{-k}^{i*}. \quad (26)$$

- (3) Divide (26) by $G_{D,k}$ to obtain the equalized subcarriers as

$$\begin{aligned} \tilde{S}_k^i &= \frac{1}{G_{D,k}} \tilde{Y}_k^i = U_k^i + \frac{G_{M,k}}{G_{D,k}} U_{-k}^{i*} \\ &= U_k^i + \frac{G_{2,T,k}}{G_{1,T,k}} U_{-k}^{i*}. \end{aligned} \quad (27)$$

Clearly, the channel effect is removed and the only impairment present in the signal now is the transmitter I/Q imbalance.

- (4) Hard-decision-based detection of the mirror subcarriers of equalized symbol, given by

$$\tilde{S}_{-k}^i = D(\tilde{S}_{-k}^i), \quad (28)$$

where D denotes the decision.

- (5) At the pilot subcarriers, we now have

$$\tilde{S}_k^p = U_k^p - W_k^p \tilde{S}_{-k}^p. \quad (29)$$

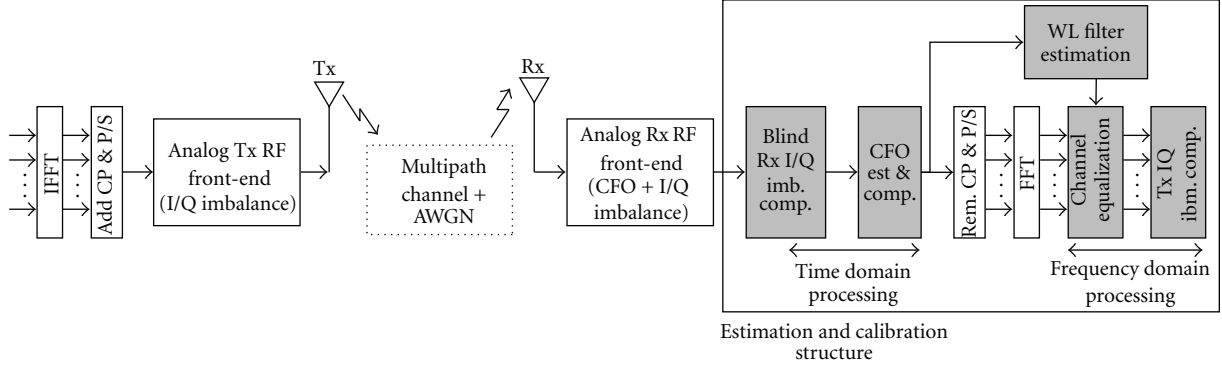


FIGURE 6: OFDM system model with sparse pilot compensator structure.

- (6) From above equation, we find the compensation filter at the pilot subcarriers as

$$W_k^p = \frac{U_k^p - \hat{S}_k^p}{\hat{S}_{-k}^p}. \quad (30)$$

- (7) Interpolate W_k^p to all subcarriers to obtain W_k (see Section 3.3.4).

- (8) The estimated symbols are then given as

$$\hat{U}_k^i = \hat{S}_k^i + W_k \hat{S}_{-k}^i. \quad (31)$$

3.3.3. Estimation of Widely Linear Filter $G_{D,K}$. The filter $G_{D,K}$ can also be estimated in the time domain as discussed in the previous subsection. For the i th received OFDM symbol after receiver I/Q imbalance and CFO compensation, we perform the DFT operation and pick the data on pilot subcarriers. The time domain OFDM symbol corresponding to pilot subcarriers can then be written as $\tilde{\mathbf{y}}^p(n) \triangleq [\tilde{y}^p(n), \tilde{y}^p(n-1), \dots, \tilde{y}^p(n-N_p+1)]^T$ and the observable imbalance filter as $\hat{\mathbf{g}}_D = [\hat{g}_{D,1}, \hat{g}_{D,2}, \dots, \hat{g}_{D,N_g}]^T$, where again N_p is the length of sparse pilot symbols and $N_g < L_{CP}$ is the length of estimated filters. The LS estimate of $\hat{\mathbf{g}}_D$ is then

$$\hat{\mathbf{g}}_D = (\bar{\mathbf{U}}^{pH}(n) \bar{\mathbf{U}}^p(n))^{-1} \bar{\mathbf{U}}^{pH}(n) \tilde{\mathbf{y}}^p(n), \quad (32)$$

where $\bar{\mathbf{U}}^p(n)$ is the time-domain circular-convolution matrix formed from by taking the IDFT of pilot symbols \mathbf{u}_p .

3.3.4. Interpolation of W_k^p . Here, we derive the transformation for the interpolation of filter W_k^p in (30). Assume that the pilot estimates stem from a time domain impulse response $\bar{\mathbf{w}}$ of length N_w , then the model expressed in (30) becomes

$$\mathbf{W}^p = \mathbf{F}_{\{\text{ind}P, 1:N_w\}} \bar{\mathbf{w}}, \quad (33)$$

where \mathbf{W}^p is $N_p \times N_p$ diagonal matrix and $\text{ind}P$ denotes the indices of pilot subcarriers. Now, let us define the DFT matrix \mathbf{F}_M comprised of first N_w columns and rows corresponding to the pilot subcarriers, formally given as

$$\mathbf{F}_M = \mathbf{F}_{\{\text{ind}P, 1:N_w\}}, \quad (34)$$

then the impulse response vector is estimated based on minimizing the mean square error

$$\arg \min_{\bar{\mathbf{w}}} \|\mathbf{W}^p - \mathbf{F}_M \bar{\mathbf{w}}\|^2 \quad (35)$$

which can be found by minimizing the LS scheme, corresponding to left multiplying the pseudo-inverse of \mathbf{F}_M to (30) yielding

$$\bar{\mathbf{w}}_{LS} = (\mathbf{F}_M^H \mathbf{F}_M)^{-1} \mathbf{F}_M^H \mathbf{W}^p. \quad (36)$$

The interpolated frequency-domain coefficients are then obtained as

$$\mathbf{W}_{LS} = \mathbf{F}_{\{1:N, 1:N_w\}} \bar{\mathbf{w}}_{LS}. \quad (37)$$

The estimates obtained from the above equation are then plugged in (31) to obtain transmitted symbols estimate.

In practice, some of the coefficients of \mathbf{W}_{LS} might be very biased due to deep channel fading. These biased estimates can be improved by using weighted-least-squares (WLS) solution. There are many possibilities for defining the weight matrix, for example, giving more weight to the subcarriers that have strong mirror subcarrier. In this work, we define the weight matrix as

$$\mathbf{P}_k = \text{diag} \left\{ \frac{|\hat{U}_{-k}^*|^2}{|\hat{U}_k|^2} \right\}, \quad (38)$$

which transform the original LS problem into WLS as

$$\bar{\mathbf{w}}_{WLS} = (\mathbf{F}_M^H \mathbf{P} \mathbf{F}_M)^{-1} \mathbf{F}_M^H \mathbf{P} \mathbf{W}^p \quad (39)$$

or equivalently in frequency domain as

$$\mathbf{W}_{WLS} = \mathbf{F}_{\{1:N, 1:N_w\}} \bar{\mathbf{w}}_{WLS}. \quad (40)$$

3.4. Compensation Complexity. In Table 1, we summarize the complexity in terms of number of the complex multiplications required by each compensation stage.

The overall complexity of the proposed compensation schemes is $(N_w + 1) \times (N + L_{CP}) + 2N_a$.

TABLE 1: Computational complexities per OFDM symbol for different compensation stages.

Algorithms	Complex multiplications
Rx. I/Q imbalance compensation	$N_w \times (N + L_{CP})$
CFO compensation	$N + L_{CP}$
Channel equalization	N_a
Tx. I/Q imbalance compensation	N_a

Conceptually, a conventional channel equalizer in the absence of CFO and I/Q imbalances operates on a per-subcarrier basis, requiring 1 complex multiplication per active subcarrier. However, a joint equalizer for channel, CFO, and Tx. Rx. imbalances has to take into account the contribution of all active subcarriers. Therefore, for such an equalizer with N_a active subcarriers, N_a^2 complex multiplications would be required. Comparing this complexity with the complexity of proposed decoupled schemes clearly signifies the benefit of decoupled compensation.

4. Simulation Results

The performance of proposed algorithms is illustrated in this section with computer simulations. We first evaluate the performance of CFO estimator in the presence of transmitter I/Q imbalance and channel distortions and do not take into account receiver I/Q imbalance, for both preamble and sparse pilot structures. Then, SER simulations are performed to evaluate the detection performance of compensation schemes in the presence of transmitter and receiver I/Q imbalance, channel distortions, and CFO.

4.1. Performance of CFO Estimator. The parameters considered for CFO estimator simulations are as follows: OFDM-based system with 64-QAM subcarrier modulation, total number of subcarriers $N = 1024$, of which 600 are active, 50 OFDM symbols, and the subcarrier spacing is 15 KHz. In the case of preamble pilot, the first complete OFDM symbol is considered as pilot and used for the CFO estimation. For sparse pilot example, pilot symbols are inserted at every sixth subcarrier. The multipath channel is 39 taps long with maximum delay spread of 2.5 ms and power delay profile as described in [34]. The transmitter I/Q imbalance filters impulse responses are $\bar{\mathbf{h}}_{I;T} = [1, 0, 0]^T$; $\bar{\mathbf{h}}_{Q;T} = [0.97, -0.1, 0.01]^T$. Frequency-independent gain g_T and phase ϕ_T are chosen corresponding to IRR levels of 20 dB, 30 dB, 40 dB, and infinite (INF.). These IRR levels map to gain imbalance of 10%, 3%, 1%, 0% and phase imbalance of 10° , 4° , 1° , 0° , respectively. The mean received SNR is 20 dB. The performance results are illustrated by plotting the mean square error (MSE) over normalized CFO values with 500 independent channel realizations: $\text{MSE} = E|\Delta\hat{f} - \Delta f|^2$.

Figures 7 and 8 show the performance of CFO estimation scheme of [25] for preamble and sparse pilot cases, respectively. For the sparse pilot example, we assume that the system under consideration is LTE for which normalized CFO can be higher than one [25], and we simulate the algorithm over the normalized CFO range of $[-5, 5]$. As

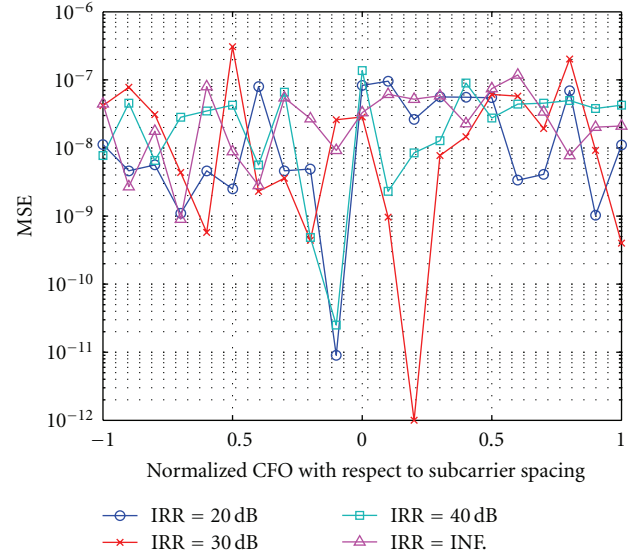


FIGURE 7: MSE of preamble pilot-based CFO estimator versus normalized CFO for 64-QAM OFDM system; 39-tap veh. A channel model; ensemble average of 500 independent channel realizations.

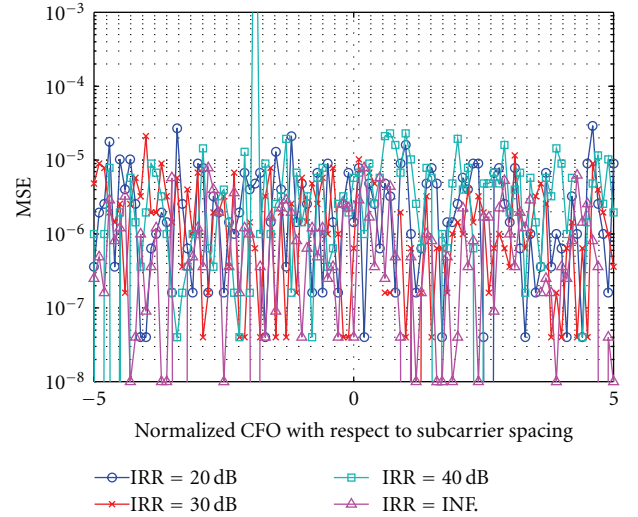


FIGURE 8: MSE of sparse pilot-based CFO estimator versus normalized CFO for 64-QAM OFDM system; 39-tap veh. A channel model; ensemble average of 500 independent channel realizations.

evident from the results, the algorithm delivers sufficiently reliable estimates for small to large imbalance values. The MSE remains below 10^{-7} with preamble and in the order of 10^{-5} when pilots are inserted sparsely at SNR = 20 dB.

4.2. SER Performance. Now, we perform the SER simulations and illustrate the results by plotting the mean SER as a function of received SNR. A typical 64-QAM OFDM system is considered whose parameters are given in Table 2. The OFDM signal parameters are similar to 3GPP long-term evolution (LTE) specifications [35]. The I/Q imbalance

TABLE 2: System parameters.

Total number of subcarriers	$N = 1024$
Active subcarriers	$N_a = 600$
Cyclic prefix length	$L_{CP} = 52$
Subcarrier spacing	$1/NT_s = 15 \text{ KHz}$
Sampling Frequency	$F_s = 15.36 \text{ MHz}$
Channel type	vehicular A
No. of channel taps	39
Gain imbalance	$g_{T,R} = 5\%$
Phase imbalance	$\phi_{T,R} = 5^\circ$
I-branch filter	$\bar{\mathbf{h}}_{I,T;R} = [1, 0, 0]^T$
Q-branch filter	$\bar{\mathbf{h}}_{Q,T;R} = [0.97, -0.05, 0.01]^T$

values stated in the table correspond to 23–30 dB front-end IRR and represent a practical example case.

In the following figures, legend “No FE Distortion” refers to the case when no transmitter and receiver I/Q imbalance and CFO is present and known channel estimates are used for channel equalization, “W/o Compensation” refers to when all radio impairments are present and only channel is equalized with known estimates, and “W/Tx Rx IQ Imbalance only” for the case when only transmitter and receiver IQ imbalance is present and channel is equalized with known estimates. “W/ZF Compensation” “W/ML Compensation” “W/LS Compensation”, and “W/WLS Compensation” legends exemplify the schemes proposed in Section 3. The results depicted are averaged over 10^3 independent channel realizations.

For preamble pilot-based compensation, we transmit 50 OFDM symbols and use first OFDM symbol as pilot. In each simulation run, we generate a random CFO in the range $[-1, 1]$ and introduce it to the signal (with transmitter I/Q imbalance and channel distortions). The receiver I/Q imbalance is compensated with 3-tap compensation filter, built by utilizing the second-order statistics of the received signal. This is followed by CFO estimation and compensation, performed in time domain. ZF and ML estimation techniques are applied next. It can be seen in Figure 9 that communication system becomes completely unusable when no compensation scheme is in place and SER remains very high when only I/Q imbalance is present at both transmitter and receiver. The ZF equalizer is able to reduce the SER to the level of a system with no front-end distortion. On the other hand, the ML equalizer even outperforms the SER performance of system with no RF impairments and known channel estimates. In the low SNR region, the SER is close to the ideal system but as the SNR increases, the equalizer is able to extract the frequency diversity gain induced by transmitter I/Q imbalance. A similar diversity effect is also reported in [29] where only transmitter I/Q imbalance and channel distortions are considered.

The OFDM signal model for sparse pilot-based compensation is similar to LTE frame structure shown in Figure 10, consisting of one frame that is composed of ten subframes; each subframe is further divided into two slot. A slot consists of seven OFDM symbols, and pilot symbols are

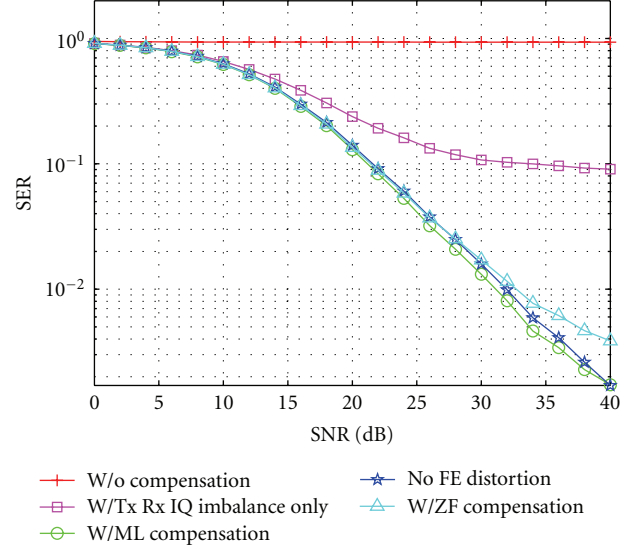


FIGURE 9: Preamble pilot-based SER versus SNR performance curves for 64-QAM OFDM system. Tx/Rx FE IRR = 20–30 dB; veh. A channel model with 39 taps; ensemble average over 1000 independent channel realizations.

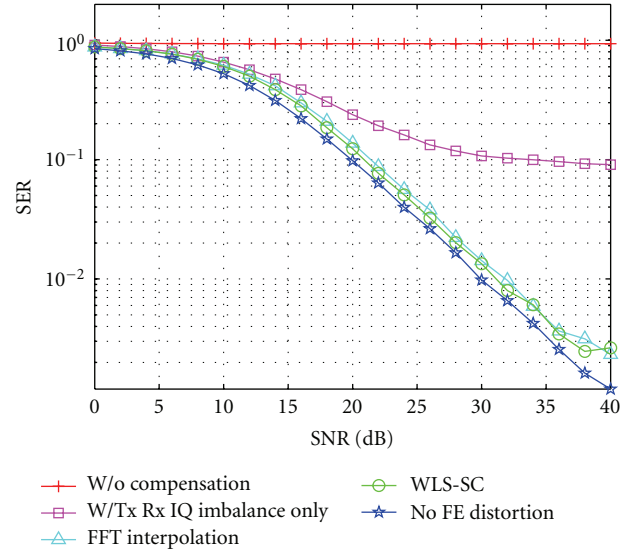


FIGURE 10: Sparse pilot-based SER versus SNR performance curves for 64-QAM OFDM system. Tx/Rx FE IRR = 20–30 dB; veh. A channel model with 39 taps; ensemble average over 1000 independent channel realizations.

located at every sixth subcarrier of first and fifth OFDM symbol of each slot. Thus, in total, we transmit 140 OFDM symbols with pilot tones on 20 symbols. As discussed in the previous subsection, the normalized frequency offset is randomly generated in the range $[-5, 5]$ during each channel realization (CFO in LTE is much smaller, in fact it can be greater than one), and its effect is added to the signal. At the algorithm compensation level, we again apply a 3-tap compensation filter for receiver I/Q compensation, followed by CFO estimation and compensation. The LS and WLS compensation algorithms are applied in frequency

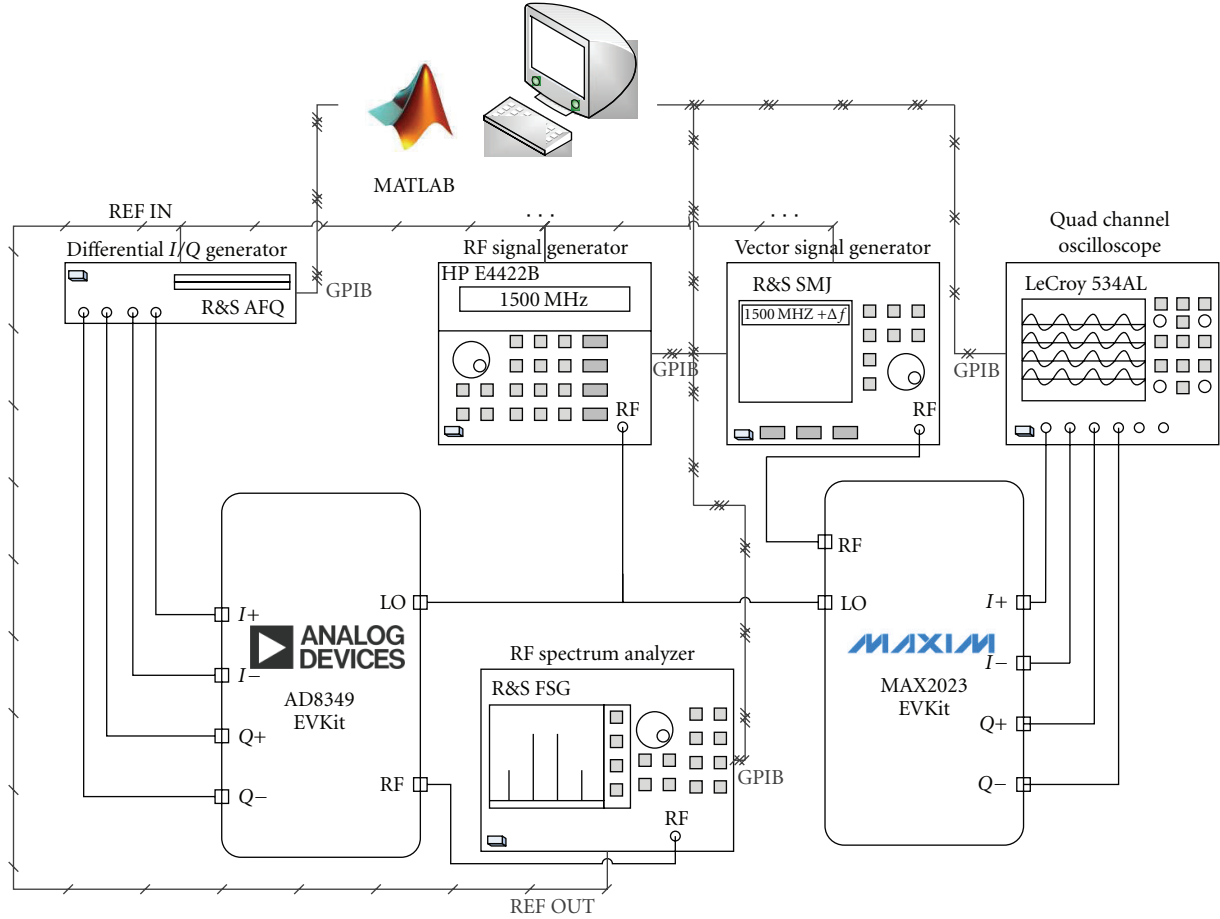


FIGURE 11: General structure of the measurement setup consisting of laboratory instruments and I/Q modulator and demodulator.

domain for channel distortions and transmitter I/Q imbalance calibration. Figure 10 illustrates the simulation results that renders excellent calibration property of proposed algorithms, with WLS achieving close to SER of a system with no FE distortions.

5. Experimental RF Measurements Results

In order to further validate the performance of proposed compensation algorithms, real-world RF measurements have been performed. We first summarize the overall measurement setup and then describe the measurement procedure in detail.

5.1. Prototype Implementation. The generic structure of the measurement setup is identical to the one shown in Figures 4 and 6, and the corresponding block diagram is depicted in Figure 11. The prototype implementation integrates Rohde and Schwarz (R&S) AFQ100A baseband I/Q signal generator, R&S FSG spectrum and signal analyzer, R&S SMJ vector signal generator, HP E4422B RF signal generator, LeCroy 534AL quad-channel oscilloscope, Analog Devices (AD) AD8349 direct conversion modulator evaluation kit, and Maxim 2023 demodulator evaluation kit. All the instruments are connected to a computer via general purpose interface bus (GPIB) for remote control operation.

5.2. Measurement Setup. A computer with MATLAB is used for performing digital signal processing-related tasks and also for instrument control. The baseband OFDM signal with parameters similar to simulations as in Section 4 is generated in computer, and its samples are loaded into the memory of R&S AFQ. The analog I/Q signal output by R&S AFQ is up-converted to RF frequency by AD8349 modulator. In order to introduce the channel distortions and noise, we capture the baseband equivalent of the RF signal using built-in I/Q subsystem of R&S FSG. The I/Q subsystem first translates the signal to an intermediate frequency (IF) of 20.4 MHz, followed by IF filtering. The filtered signal is then digitized by a built-in ADC at a rate of 81.6 MHz. Finally the sampled signal is digitally downconverted to complex baseband, low-pass filtered, and resampled to desired sampling frequency. The samples are then read out in block of 512,000 each in ASCII format. The channel distortions and noise are then added, and the samples of signal (with transmitter I/Q imbalance, channel distortions, and noise) are loaded into R&S SMJ memory, which outputs the RF signal. The CFO effect is introduced at the transmitter side by drifting the LO frequency of R&S SMJ relative to the RF frequency of HP E4422B. The LO frequency is used in the measurements in 1.5 GHz. On the receiver side, MAX2023 demodulator downconverts the signal from RF to baseband.

The output of analog frontend of MAX2023 is captured with a quad channel oscilloscope. The samples recorded by the oscilloscope are then sent to MATLAB for offline processing.

5.3. Performance Analysis

5.3.1. Front-End IRR without Calibration. We first shortly address the estimation of front-end IRR of AD8349 and MAX2023 chips, without any compensation. Although the exact values of gain and phase imbalance of these chips are unknown, the IRR analysis is still possible using LS fitting approach as follows. We denote the reference time domain signal \bar{z} to be transmitted. The complex envelope of RF signal can be written as in (41). $\bar{Z}(n)$ and $\bar{Z}^*(n)$ are time domain convolution matrix and conjugate convolution matrix formed from reference signal $\bar{z}(n)$ and its conjugate $\bar{z}^*(n)$, respectively. Assuming perfect synchronization in time, frequency, and phase, the LS estimates of the front-end imbalance filters are then given by (42) [8, 11].

In Figure 12, IRR curves with different I/Q imbalance filter lengths, utilizing 50,000 samples and ensemble averaged over ten independent simulation runs, are plotted. The LO frequency is 1.5 GHz, and the signal is a 16-QAM modulated signal with 18 MHz two-sided bandwidth, six times oversampling, and root raised cosine pulse shaping. The results suggest that both chips have frequency selective image rejection, varying between 27–29 dB for AD8349 (transmitter modulator) and 30–33 dB for Maxim 2023 (receiver demodulator):

$$\begin{aligned} \bar{s}(n) &= \begin{bmatrix} s(n) \\ s(n-1) \\ \vdots \\ s(n-L+1) \end{bmatrix} \\ &= \begin{bmatrix} \bar{\mathbf{g}}_{1,T}^T(n)\bar{z}(n) + \bar{\mathbf{g}}_{2,T}^T(n)\bar{z}^*(n) \\ \bar{\mathbf{g}}_{1,T}^T(n)\bar{z}(n-1) + \bar{\mathbf{g}}_{2,T}^T(n)\bar{z}^*(n-1) \\ \vdots \\ \bar{\mathbf{g}}_{1,T}^T(n)\bar{z}(n-L+1) + \bar{\mathbf{g}}_{2,T}^T(n)\bar{z}^*(n-L+1) \end{bmatrix} \\ &= \begin{bmatrix} \bar{Z}(n) & \bar{Z}^*(n) \end{bmatrix} \begin{bmatrix} \bar{\mathbf{g}}_{1,T}(n) \\ \bar{\mathbf{g}}_{2,T}(n) \end{bmatrix} = \bar{Z}_b(n) \begin{bmatrix} \bar{\mathbf{g}}_{1,T}(n) \\ \bar{\mathbf{g}}_{2,T}(n) \end{bmatrix}, \end{aligned} \quad (41)$$

$$\begin{bmatrix} \bar{\mathbf{g}}_{1,T}(n) \\ \bar{\mathbf{g}}_{2,T}(n) \end{bmatrix} = \bar{Z}_b^\dagger(n) \bar{s}(n). \quad (42)$$

5.3.2. Blind Receiver I/Q Imbalance Compensation. The performance of blind receiver I/Q imbalance compensation algorithm is evaluated next. Here, R&S SMJ acts as transmitter to produce RF signal (with no transmitter IQ imbalance and channel distortions) and MAX2023 to demodulate the signal. The digitized baseband signal (with receiver I/Q imbalance) is transferred to computer through GPIB, where we apply blind DSP algorithm for compensation. The data captured from oscilloscope, however, cannot be used directly for compensation but rather it is first processed to remove the RF chain errors. That involves resampling, delay removal, phase synchronization, offset cancellation, and scaling. After

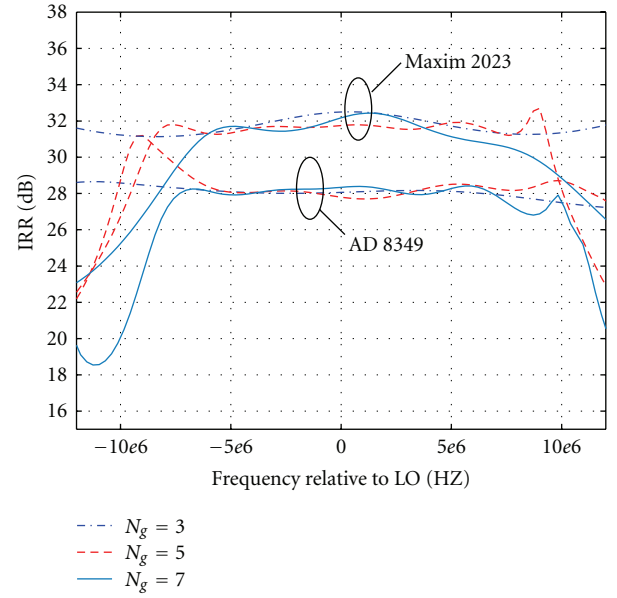


FIGURE 12: Comparison of averaged FE IRR versus frequency for different imbalance filter lengths. LO frequency = 1.5 GHz.

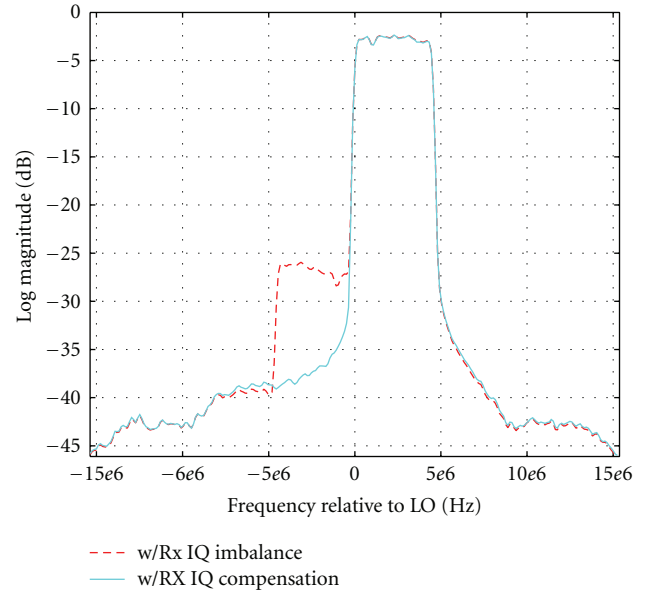


FIGURE 13: Comparison of measured I/Q demodulator output before and after I/Q imbalance compensation.

these steps, we apply the compensation algorithm. For illustration purpose, we use a half-loaded OFDM signal with 300 active subcarriers (out of total 1024). The LO frequency is 1.5 GHz. Figure 13 shows the measured spectra before and after compensation, evidencing a clear improvement obtained with the compensation algorithm.

5.3.3. Characterization of Pilot-Based Compensation Schemes. The performance analysis of pilot-based compensation schemes is carried out by creating an OFDM waveform with parameters given in Table 2 as per LTE standard. The

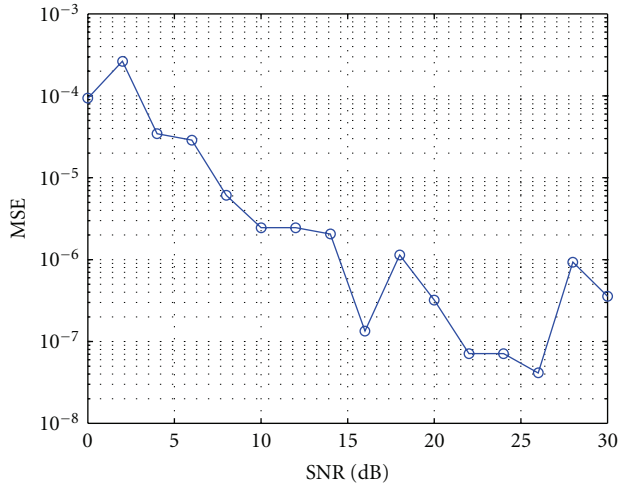


FIGURE 14: Preamble pilot-based measured MSE of CFO versus SNR performance curve. CFO = 10 KHz.

baseband OFDM signal is sampled at $2 \times 1024 \times 15 \text{ KHz} = 30.72 \text{ MHz}$, oversampled by 2, and output by R&S AFQ. The *I/Q subsystem* of R&S FSG implements the down conversion, filtering, and sampling from 81.6 MHz to $2 \times 30.72 \text{ MHz} = 61.44 \text{ MHz}$. Blocks of 512,000 samples are read from R&S FSG memory and loaded into MATLAB memory. The samples are processed for delay estimation, timing synchronization, and LO leakage removal. After the data conditioning, the channel distortions and noise are added, before feeding the signal to R&S SMJ. The CFO effect is also introduced in R&S SMJ by changing the RF frequency. The RF signal is downconverted and sampled at 50 M Samples/second. These samples are extracted from oscilloscope and again processed in MATLAB for resampling to 30.72 MHz, delay estimation, phase synchronization, and scaling. After these processing stages, we have the baseband equivalent model of the signal that has transmitter/receiver I/Q imbalance, channel distortion, noise, and CFO effects included.

The example waveform used for preamble pilot-based compensation algorithms is an OFDM signal with same parameters as were in simulations. In the measurements, we transmit 10 OFDM symbols and use one known OFDM symbol during the estimation and calibration phase. The CFO is 10 KHz and a 3-tap compensation filter for receiver I/Q imbalance compensation and also for transmitter I/Q imbalance estimation. Both ML and ZF equalization schemes are applied to the signal, after receiver I/Q imbalance and CFO compensation. With a fixed channel, the obtained results ensemble averaged over 10 independent measurements are plotted. Figure 14 shows the measurement results of CFO estimation over different SNR values. The results indicate that the estimator performance improves with increasing SNR. Even for small SNR, the MSE remains very low. In Figure 15, measured SER versus SNR is plotted. The figure also shows a reference curve ("No FE Distortion,") obtained with MATLAB simulation with no I/Q imbalances, perfect CFO, and channel compensation with known

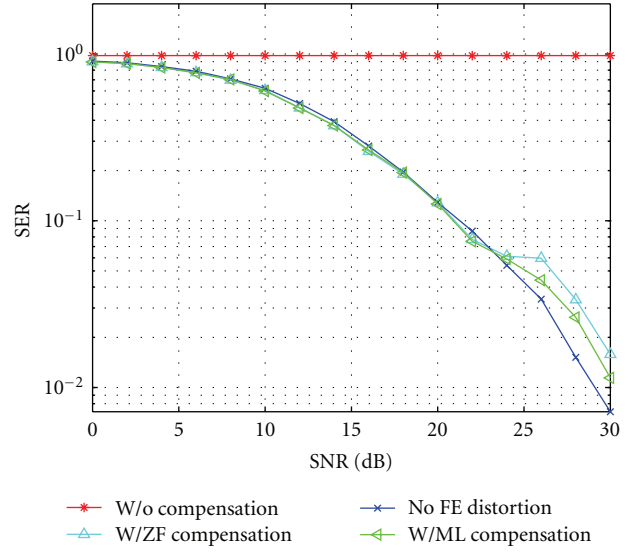


FIGURE 15: Measured SER versus SNR performance curves for 64-QAM OFDM system with preamble pilot; CFO = 10 KHz; veh. A channel model with 39 taps; ensemble average over 10 realizations with a fixed channel.

estimates. As evident from Figure 15, the algorithms give very consistent performance with SER close to simulated SER. Also, the ML technique provides better performance than ZF technique. Notice that for SNR greater than 26, there is a little performance degradation which is most likely due to measurement noise. In Figure 16, we also plot the symbol constellation after compensation with ZF equalization scheme. The excellent calibration property of algorithms is also visible here.

In the second measurement example, the signal is an OFDM signal having 10 symbols and pilots located at every sixth subcarrier. The signal has altogether 600 active subcarriers out of 1024 subcarriers, with 15 KHz subcarrier spacing. Therefore, in total, there are 1000 pilot symbols. The signal is oversampled by 2. The CFO is now 45 KHz that is greater than the subcarrier spacing. Again the receiver I/Q imbalance is compensated with 3-taps, and the LS and WLS approaches discussed in Section 3 are employed for transmitter I/Q imbalance and channel equalization. The CFO estimation in terms of MSE between the estimated and the true CFO value versus SNR is plotted in Figure 17, which demonstrates a similar behavior to previous preamble pilot-based estimation example. The measured SER versus SNR curve in Figure 18 and symbols after compensation are plotted in Figure 19. The results suggest that the proposed methods are able to deliver very accurate estimates. An important implication of Figure 18 is that with more pilot data available over different symbols, we are able to reduce the effect of measurement noise which was very dominant in the previous measurement example (Figure 15).

In general, it can be concluded from the measurements results of Figures 15 and 18 that the proposed estimator and compensator structures provide considerable improvements to achievable SER, giving confidence to deploy them in practical systems.

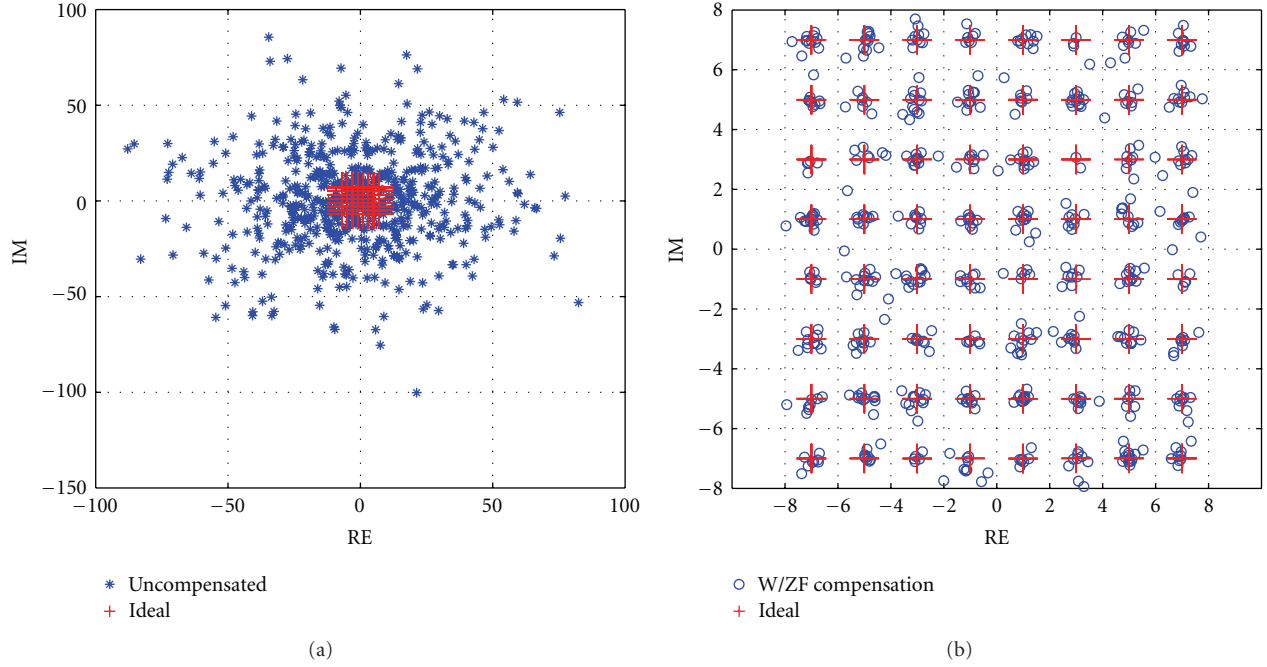


FIGURE 16: Measured constellation diagram of 64-QAM OFDM system before and after RF impairments mitigation. (a) Uncompensated (b) Compensated with ZF equalization.

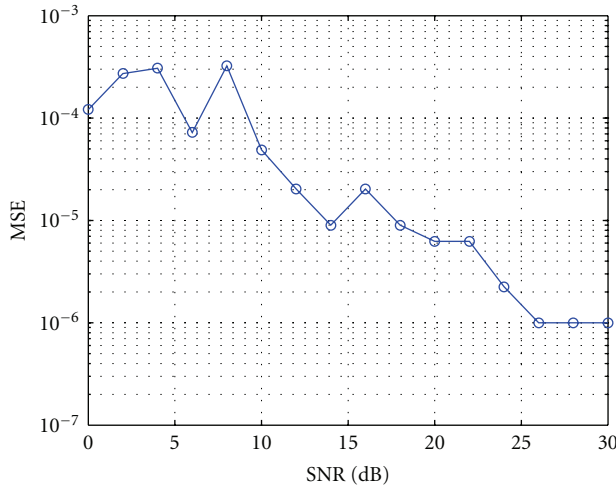


FIGURE 17: Sparse pilot-based measured MSE of CFO versus SNR performance curve. CFO = 45 KHz.

5.4. Implementation Challenges. In practice, the measurement setup is exposed to variety of errors, which must be corrected before introducing the channel distortion and noise as well as before applying the compensation algorithms. We briefly review these errors now.

The downconversion of RF signal (with transmitter I/Q imbalance) using R&S *I/Q subsystem* is subject to unavoidable residual errors such as synchronization, LO leakage, delay between original and measured signal, nonlinearities of components, and noise of its own. Frequency synchronization between the instruments is achieved by connecting the instruments to same reference clock of R&S FSG, as shown

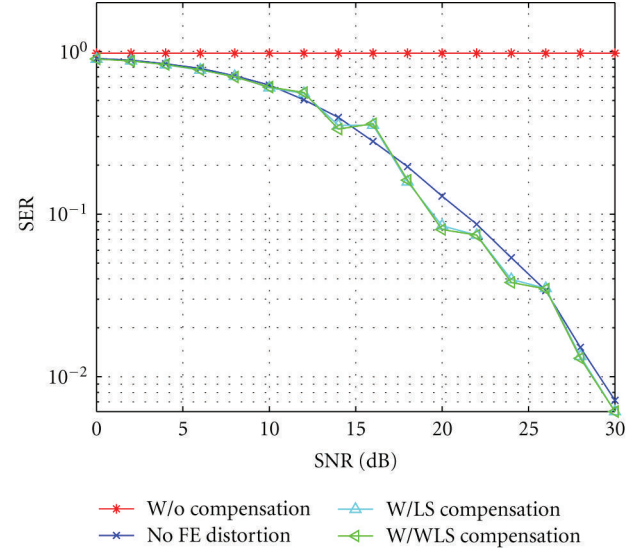


FIGURE 18: Measured SER versus SNR performance curves for 64-QAM OFDM system with sparse pilot; CFO = 45 KHz; veh. A channel model with 39 taps; ensemble average over 10 realizations with a fixed channel.

in Figure 11. Symbol timing synchronization is performed prior to downsampling the signal to symbol rate with ML algorithm. LO leakage results due to finite isolation between the LO and RF ports of the modulator/demodulator. Consequently, when RF signal is up-/downconverted, LO leakage causes offset. It can be mitigated by removing the sample mean of the measured signal. The delay estimation is performed in two steps: first integer delay is removed with

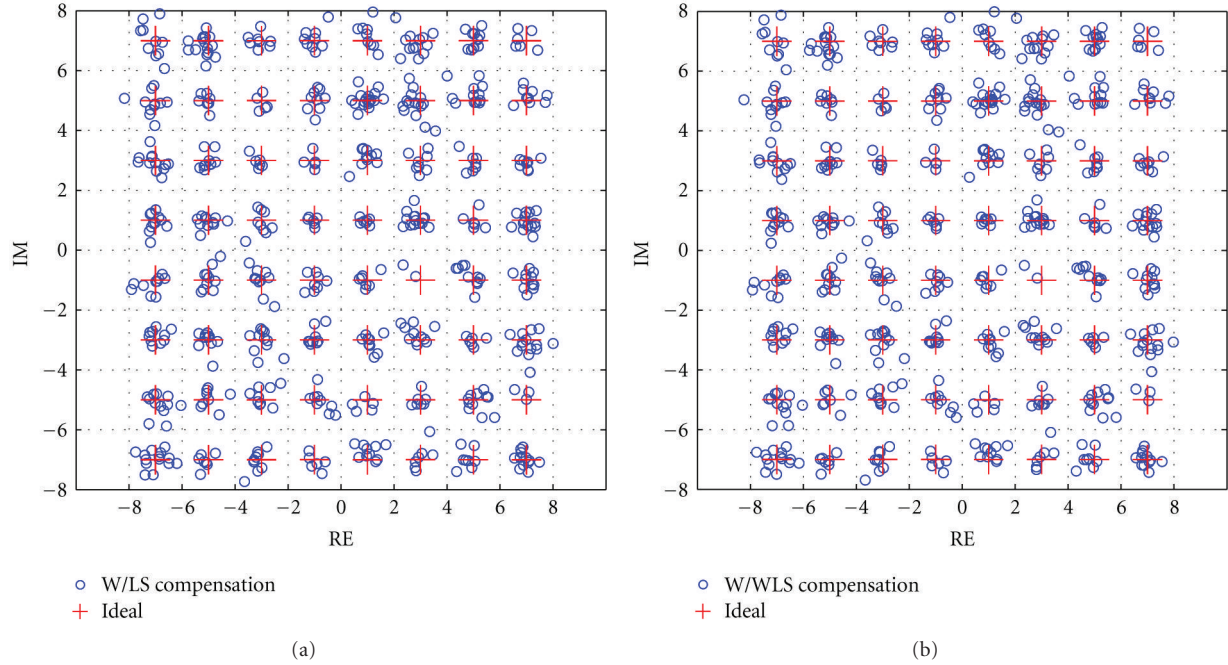


FIGURE 19: Measured constellation diagram of 64-QAM OFDM system with RF impairments mitigation. (a) Compensated with LS method (b) Compensated with WLS method.

FFT-based correlator, allowing non-data-aided (NDA) ML algorithm for fractional delay estimation and compensation. Detailed review of synchronization algorithms can be found in [36].

Similar to R&S FSG, the data captured from oscilloscope must be DSP conditioned before being used in actual estimation and compensation. The data conditioning involves resampling to original signal sample rate, delay estimation, and offset removal with already-mentioned algorithms.

6. Conclusion

In this paper, the performance of OFDM-based communication systems is studied in the presence of frequency-selective I/Q imbalance, channel distortions and CFO. Based on our signal model, generally applicable algorithms have been developed for the compensation of such impairments. The proposed methods are composed of time domain and frequency domain compensation. It is shown with simulations that the proposed, estimator and compensator structures produce symbol error rates close to the ideal ones. A laboratory measurement setup is also proposed and extensive measurements are carried out to prove the practical value of the algorithms. The measurements results show that the achievable SER is close to the ideal. Hence, the compensation algorithms provide significant improvement to obtainable link performance and can be used in real world radio transceivers. Future work will focus on generalizing the work to MIMO-OFDM and a real-time prototype implementation using FPGA's for the digital parts and integrated RF-ASIC's for the analog circuitry.

Acknowledgments

This work was supported by the Technology Promotion Foundation of Finland (TES), the Nokia Foundation, the graduate school TISE, the Austrian Center of Competence in Mechatronics (ACCM), the Academy of Finland (under the projects “Digitally-Enhanced RF for Cognitive Radio Devices” and “Joint Analysis and DSP-Based Mitigation of Multiple RF Impairments in Future Radio Devices”), and the Finnish Funding Agency for Technology and Innovation (Tekes; under the project “Enabling Methods for Dynamic Spectrum Access and Cognitive Radio”), all of which are gratefully acknowledged. The authors would also like to thank the anonymous reviewers for their helpful comments and suggestions.

References

- [1] “Wireless LAN medium access control (MAC) and physical layer (PHY) specifications: high speed physical layer in 2.4 GHz band,” Tech. Rep., IEEE, 1999.
- [2] “IEEE standard for local and metropolitan area networks part 16: air interface for fixed broadband wireless access systems,” Tech. Rep., IEEE 802.16, 2004.
- [3] U. Ladebusch and C. A. Liss, “Terrestrial DVB (DVB-T): a broadcast technology for stationary portable and mobile use,” *Proceedings of the IEEE*, vol. 94, no. 1, pp. 183–192, 2006.
- [4] G. Faria, J. A. Henriksson, E. Stare, and P. Talmola, “DVB-H: digital broadcast services to handheld devices,” *Proceedings of the IEEE*, vol. 94, no. 1, pp. 194–209, 2006.
- [5] A. B. Ericsson, “Long term evolution (LTE): an introduction,” White Paper, 2007.

- [6] S. Mirabbasi and K. Martin, "Classical and modern receiver architectures," *IEEE Communications Magazine*, vol. 38, no. 11, pp. 132–139, 2000.
- [7] A. A. Abidi, "Direct-conversion radio transceivers for digital communications," *IEEE Journal of Solid-State Circuits*, vol. 30, no. 12, pp. 1399–1410, 1995.
- [8] L. Anttila, M. Valkama, and M. Renfors, "Frequency-selective I/Q mismatch calibration of wideband direct-conversion transmitters," *IEEE Transactions on Circuits and Systems II: Express Briefs*, vol. 55, no. 4, pp. 359–363, 2008.
- [9] L. Ding, Z. Ma, D. R. Morgan, M. Zierdt, and G. T. Zhou, "Compensation of frequency-dependent gain/phase imbalance in predistortion linearization systems," *IEEE Transactions on Circuits and Systems I: Regular Papers*, vol. 55, no. 1, pp. 390–397, 2008.
- [10] M. Valkama, M. Renfors, and V. Koivunen, "Advanced methods for I/Q imbalance compensation in communication receivers," *IEEE Transactions on Signal Processing*, vol. 49, no. 10, pp. 2335–2344, 2001.
- [11] L. Anttila, M. Valkama, and M. Renfors, "Circularity-based I/Q imbalance compensation in wideband direct-conversion receivers," *IEEE Transactions on Vehicular Technology*, vol. 57, no. 4, pp. 2099–2113, 2008.
- [12] L. Anttila, M. Valkama, and M. Renfors, "Efficient mitigation of frequency-selective I/Q imbalance in OFDM receivers," in *Proceedings of the IEEE Vehicular Technology Conference (VTC-F '08)*, Calgary, Canada, September 2008.
- [13] L. Anttila and M. Valkama, "On circularity of receiver front-end signals under RF impairments," in *Proceedings of the 17th European Wireless Conference*, pp. 610–617, Vienna, Austria, April 2011.
- [14] L. Anttila, M. Valkama, and M. Renfors, "Blind moment estimation techniques for I/Q imbalance compensation in quadrature receivers," in *Proceedings of the IEEE International Symposium on Personal, Indoor and Mobile Radio Communications (PIMRC '06)*, Helsinki, Finland, September 2006.
- [15] A. Tarighat, R. Bagheri, and A. H. Sayed, "Compensation schemes and performance analysis of IQ imbalances in OFDM receivers," *IEEE Transactions on Signal Processing*, vol. 53, no. 8, pp. 3257–3268, 2005.
- [16] M. Lipardi, D. Mittera, and F. Sterle, "MMSE equalization in presence of transmitter and receiver IQ imbalance," in *Proceedings of the International Waveform Diversity and Design Conference (WDD '07)*, pp. 165–168, Pisa, Italy, June 2007.
- [17] A. Tarighat and A. H. Sayed, "Joint compensation of transmitter and receiver impairments in OFDM systems," *IEEE Transactions on Wireless Communications*, vol. 6, no. 1, pp. 240–247, 2007.
- [18] J. Tubbax, A. Fort, L. V. Der Perre et al., "Joint Compensation of IQ imbalance and Frequency Offset in OFDM systems," in *Proceedings of the IEEE Global Telecommunications Conference (GLOBECOM '03)*, vol. 4, pp. 2365–2369, San Francisco, Calif, USA, December 2003.
- [19] G. Xing, M. Shen, and H. Liu, "Frequency offset and I/Q imbalance compensation for direct-conversion receivers," *IEEE Transactions on Wireless Communications*, vol. 4, no. 2, pp. 673–680, 2005.
- [20] C. J. Hsu, R. Cheng, and W. H. Sheen, "Joint least squares estimation of frequency, DC offset, I-Q imbalance, and channel in MIMO receivers," *IEEE Transactions on Vehicular Technology*, vol. 58, no. 5, pp. 2201–2213, 2009.
- [21] Y. J. Chiu and S. P. Hung, "Estimation scheme of the receiver IQ imbalance under carrier frequency offset in communication system," *IET Communications*, vol. 4, no. 11, pp. 1381–1388, 2010.
- [22] G.-T. Gil, I.-H. Sohn, J.-K. Park, and Y. H. Lee, "Joint ML estimation of carrier frequency, channel, I/Q mismatch, and DC offset in communication receivers," *IEEE Transactions on Vehicular Technology*, vol. 54, no. 1, pp. 338–349, 2005.
- [23] Y.-H. Chung and S.-M. Phoong, "Joint estimation of transmitter and receiver I/Q imbalances, CFO, and channel response for OFDM systems," in *Proceedings of the 1st International Conference on Green Circuits and Systems (ICGCS '10)*, pp. 247–252, Shanghai, China, June 2010.
- [24] D. Tandur and M. Moonen, "Joint adaptive compensation of transmitter and receiver IQ imbalance under carrier frequency offset in OFDM-based systems," *IEEE Transactions on Signal Processing*, vol. 55, no. 11, pp. 5246–5252, 2007.
- [25] J. González-Bayón, C. Carreras, and O. Edfors, "A multistandard frequency offset synchronization scheme for 802.11n, 802.16d, LTE, and DVB-T/H systems," *Journal of Computer Systems, Networks, and Communications*, vol. 2010, Article ID 628657, 9 pages, 2010.
- [26] T. Roman and V. Koivunen, "Carrier frequency synchronization for mobile television receivers," in *Proceedings of the IEEE International Symposium on Circuits and Systems (ISCAS '07)*, pp. 261–264, May 2007.
- [27] A. Kiayani, L. Anttila, Y. Zou, and M. Valkama, "Hybrid time/frequency domain compensator for RF impairments in OFDM systems," in *Proceedings of the 22nd IEEE International Symposium on Personal, Indoor and Mobile Radio Communications (PIMRC '11)*, Toronto, Canada, September 2011.
- [28] M. Speth, S. Fechtel, G. Fock, and H. Meyr, "Optimum receiver design for OFDM-based broadband transmission—part II: a case study," *IEEE Transactions on Communications*, vol. 49, no. 4, pp. 571–578, 2001.
- [29] J. Younghwan, K. Jihyun, L. Yuro, A. Jaemin, C. Wongyu, and L. Dongchan, "Additional diversity gain in OFDM receivers under the influence of IQ imbalances," in *Proceedings of the IEEE International Conference on Communications (ICC '07)*, pp. 5915–5920, Glasgow, Scotland, June 2007.
- [30] S. Narayanan, B. Narasimhan, and N. Al-Dhahir, "Digital baseband compensation of joint TX/RX I/Q imbalance in mobile MIMO SC-FDE transceivers in the presence of CFO," in *Proceedings of the IEEE International Conference on Acoustics, Speech, and Signal Processing (ICASSP '10)*, pp. 3510–3513, March 2010.
- [31] J. G. Proakis, *Digital Communications*, McGraw-Hill, New York, NY, USA, 3rd edition, 1995.
- [32] L. Deneire, P. Vandenameele, L. Van der Perre, B. Gyselinckx, and M. Engels, "A low-complexity ML channel estimator for OFDM," *IEEE Transactions on Communications*, vol. 51, no. 2, pp. 135–140, 2003.
- [33] S. Haykin, *Adaptive Filter Theory*, Prentice-Hall, Upper Saddle River, NJ, USA, 4th edition, 2002.
- [34] T. B. Sorensen, P. E. Mogensen, and F. Frederksen, "Extension of the ITU channel models for wideband (OFDM) systems," in *Proceedings of the IEEE Vehicular Technology Conference (VTC '05)*, pp. 392–396, Dallas, Tex, USA, September 2005.
- [35] 3GPP Technical Specification Group Radio Access Network, "Evolved universal terrestrial radio access (E-UTRA) and evolved universal terrestrial radio access (E-UTRAN); overall description; stage 2," Tech. Rep. TS 36.300, V1.0.0, 2007.
- [36] U. Mengali and A. N. D. Andrea, *Synchronization Techniques for Digital Receivers*, Plenum Press, New York, NY, USA, 1997.

Publication 3

A. Kiayani, L. Anttila, and M. Valkama, "Mobile Transmitters I/Q Imbalances in LTE Uplink: Analysis and Digital Mitigation," in *Proceedings of 13th IEEE International Conference on Communication Systems (ICCS 2012)*, pp. 125-129, Nov. 2012.

Copyright ©2012 IEEE. Reprinted, with permission, from the proceedings of 13th IEEE International Conference on Communication Systems.

In reference to IEEE copyrighted material which is used with permission in this thesis, the IEEE does not endorse any of Tampere University of Technology's products or services. Internal or personal use of this material is permitted. If interested in reprinting/republishing IEEE copyrighted material for advertising or promotional purposes or for creating new collective works for resale or redistribution, please go to http://www.ieee.org/publications_standards/publications/rights/rights_link.html to learn how to obtain a License from RightsLink.

Mobile Transmitters I/Q Imbalances in LTE Uplink: Analysis and Digital Mitigation

Adnan Kiayani, Lauri Anttila, and Mikko Valkama
Department of Communications Engineering
Tampere University of Technology
FI-33101, Tampere, Finland
{adnan.kiayani|lauri.anttila|mikko.e.valkama}@tut.fi

Abstract—The single-carrier frequency-division multiple access (SC-FDMA), also known as discrete Fourier transform (DFT)-spread OFDMA, has been adopted as uplink transmission scheme for the 3GPP Long Term Evolution (LTE). Such OFDM-based systems are known to be particularly sensitive to radio frequency (RF) impairments. The major sources of these RF impairments are in-phase and quadrature-phase imbalance (IQI) and carrier frequency offset (CFO). In this paper, we investigate the impact of radio impairments on the LTE uplink by mathematically formulating the received signal as a function of transmitted signals, IQI, CFO, and channel distortions. Then, two alternative joint equalization schemes are proposed for coping with such impairments, stemming from the minimum mean square error (MMSE) and the zero forcing (ZF) principles, respectively. LTE uplink computer simulations are then carried out to assess the validity and performance of the proposed equalizers. The results demonstrate that the proposed schemes significantly improve the uplink performance, the performance of the MMSE solution being very close to the zero RF impairments scenario.

I. INTRODUCTION

The demand for high data rates to support broadband multimedia applications pushes the future wireless systems to utilize more wider bandwidth. In this context, orthogonal frequency division multiplexing (OFDM)-based multiple access schemes have garnered much attention and are being adopted in emerging wireless communication systems (e.g. WLAN 802.11a/g/n [1], WiMAX IEEE 802.16 [2], DVB-T [3], DVB-H [4], 3GPP LTE [5]). The inherent orthogonal subcarriers nature of OFDM offers different users ability to transmit their data simultaneously on different subcarriers. This is usually referred to as OFDMA and is adopted as downlink transmission technique in LTE. Compared with the OFDMA, SC-FDMA, also known as DFT-spread OFMA, has low peak-to-average power ratio (PAPR) which enables high power efficiency of mobile terminals in the uplink communications. Therefore, SC-FDMA has been proposed as uplink multiple access scheme for 3GPP LTE.

The physical layer implementation of SC-FDMA systems with direct-conversion (zero-IF or homodyne) radio architecture represents a low-cost solution for mass deployment. The direct-conversion architecture has the advantage of low power consumption and decreases the hardware complexity

by avoiding bulky image rejection filters [6]. However, hardware inaccuracies stemming from the impairments associated with the analog components in direct conversion radio lead to the degradation of signal quality. The most pronounced radio impairment in direct-conversion based radios is in-phase and quadrature-phase imbalance (IQI), i.e., amplitude and phase mismatches between the I- and Q- branch signals [6]. Unmitigated IQI results in the mirror frequency interference (MFI) between the subcarriers located symmetrically around the center frequency. In SC-FDMA and OFDMA systems, the IQI problem is particularly severe as it causes inter-user interference (IUI) among users that are allocated to mirror subcarriers blocks. In general, digital techniques can be employed to efficiently eliminate such RF impairments. There exists several estimation and compensation approaches for IQI in OFDM systems (e.g. [7], [12] and references therein) that deal with the combined effect of transmitter and receiver IQI. In [10], the IQI problem in the uplink of an OFDMA systems is investigated and the joint estimation and compensation of IQI and channel distortion is carried out with the aid of a pilot pattern. [11] and [12] addressed the problem in SC-FDMA systems from the aspect of compensation of transmitter and receiver IQI, respectively.

In addition to IQI, SC-FDMA systems are also sensitive to carrier frequency synchronization errors, which is induced by the instability of local oscillator and/or the mobility of the users [13]. The effect of CFO on SC-FDMA systems is different than on the OFDM systems, where in the latter, CFO causes the inter-carrier interference (ICI) and destroys the orthogonality among the subcarriers. On the other hand, in the uplink communication of a SC-FDMA system, CFO not only introduces ICI among the subcarriers of a same user but it also causes multi-access interference (MAI) among different users. Furthermore, it is difficult to correct the frequency mismatch in the uplink as different users always experience different CFO, which severely degrade the system performance. There exists abundant literature on the estimation and compensation of CFO in multi-carrier radio systems [13] - [17]. CFO estimation and compensation schemes for OFDMA systems are summarized in [13] - [15]. These schemes could also be used in SC-FDMA systems. The compensation schemes focusing on SC-FDMA systems are proposed in [16] and [17]. In [16], the authors proposed schemes based on MMSE and MMSE+parallel interference cancellation (PIC) to correct the CFO error in the uplink SC-FDMA systems. A suppression method utilizing block-type pilots is discussed in [17].

The research leading to these results was financially supported by the Tampere Doctoral Programme in Information Science and Engineering (TISE), the Nokia Foundation, the Austrian Center of Competence in Mechatronics (ACCM), the Academy of Finland (under the project "Digitally-Enhanced RF for Cognitive Radio Devices"), and the Finnish Funding Agency for Technology and Innovation (Tekes; under the project "Enabling Methods for Dynamic Spectrum Access and Cognitive Radio")

In this paper, we investigate the impact of various RF impairments on the uplink of a SC-FDMA system, and also propose signal processing methods on the base station side to mitigate their impact. As discussed in the previous paragraphs, some work has been reported on the problem of IQI and CFO compensation in SC-FDMA systems, however, the joint treatment of these problems has still not been addressed. Thus, the contribution of this work is as follows: 1) we present a detailed analysis of impairments that are commonly encountered in practical radio systems, and together with channel distortions, we derive an analytic expression of the received uplink signal of a SC-FDMA system, 2) based on our formulation, we derive two joint equalization schemes based on MMSE and ZF criterion, and also propose a compensation structure to efficiently mitigate the effects of radio impairments. The computer simulation results show the significant performance degradation brought by the impairments, while the proposed signal processing schemes are then able to considerably reduce their effect.

Notations: the scalar parameters are represented by lower case letters a and frequency domain quantities with upper case letters A . Vectors are denoted by lowercase boldface letters \mathbf{a} and matrices with uppercase boldface letters \mathbf{A} . The convolution operator is indicated by \star . Superscript $(\cdot)^T$, $(\cdot)^H$, $(\cdot)^{-1}$, and $(\cdot)^*$ denote the transpose, hermitian transpose, inverse, and conjugate of a scalar, a vector, or a matrix. The ij^{th} element of a matrix \mathbf{A} is denoted by a_{ij} .

II. SYSTEM MODEL WITH RADIO IMPAIRMENTS

Consider an SC-FDMA system where U -users are communicating with a single base station (BS) through independent multi-path channels. We assume that a user- i is allocated N_i -subcarriers out of total available M -subcarriers. The indices of subcarriers allocated to a user i are in the set Γ_i . There are two choices of mapping subcarriers among users: localized and distributed. We study the SC-FDMA system with localized subcarrier assignment as adopted in 3GPP LTE [5].

For a user- i , a block of N_i data symbols $\{x_i(n)\}$, $0 \leq n \leq N_i - 1$ drawn from a QAM-constellation are first fed to an N_i -point discrete Fourier transform (DFT) block for a frequency domain representation. The output at l^{th} -subcarrier can be expressed as

$$X_i(l) = \sum_{n=0}^{N_i-1} x_i(n) e^{-j2\pi \frac{nl}{N_i}}, \quad 0 \leq l \leq N_i - 1. \quad (1)$$

The outputs are mapped according to localized pattern to Γ_i , which is followed by an M -point inverse fast Fourier transform (IFFT) to convert the data into a time domain complex signal. After the guard interval (cyclic prefix) insertion, the time domain signal for user- i can be written as

$$s_i(m) = \sum_{l \in \Gamma_i} X_i(l) e^{j2\pi \frac{ml}{M}}, \quad -N_g \leq m \leq M - 1. \quad (2)$$

The complex signal is then passed to the RF module for up-conversion, whose output under IQI is given by

$$\tilde{s}_i(m) = s_i(m) \star g_{1T,i}(m) + s_i^*(m) \star g_{2T,i}(m) \quad (3)$$

where the complex imbalance filters $g_{1T,i}(m)$, $g_{2T,i}(m)$ model the gain g_T , phase ϕ_T , and impulse responses

$h_{IT;QT}$ mismatch, and are expressed as $g_{1T,i}(m) = (h_{IT,i}(m) + g_{T,i} \exp(j\phi_{T,i}) h_{QT,i}(m)) / 2$ and $g_{2T,i}(m) = (h_{IT,i}(m) - g_{T,i} \exp(j\phi_{T,i}) h_{QT,i}(m)) / 2$ [9].

The signal is then transmitted over a multi-path channel, and the received signal is comprised of signals transmitted from U -users and additive noise, and is of the following form

$$y(m) = \sum_{i=0}^U r_i(m) + n(m) \quad (4)$$

where $r_i(m)$ is the received signal of i^{th} user, defined as

$$r_i(m) = \sum_l \tilde{s}_i(l) h_i(m-l). \quad (5)$$

Assuming now that the local oscillators of transmitter and receiver are not perfectly synchronized, there exists CFO such that $y(m) = \sum_{i=0}^U r_i(m) e^{j2\pi \epsilon_i m / M} + n(m)$, where ϵ_i is normalized frequency offset of i^{th} user. Also, the down-conversion stage is not ideal and induces IQI. The frequency domain signal of user- i at the k^{th} -subcarrier after CP removal, FFT, and subcarrier demapping is given by (6) (next page), where $-k$ denotes the mirror subcarrier, subscript m refers to mirror user, $H_i(k)$, $H_m(k)$ are the channel responses of user i and m at k^{th} subcarrier, $G_{1T,i}(k)$, $G_{2T,i}(k)$ are frequency domain responses of Tx. IQI filters $g_{1T,i}$, $g_{2T,i}$ at k^{th} subcarrier, and $G_{1R}(k)$, $G_{2R}(k)$ are frequency domain responses of Rx. IQI filters, and $N(k)$ represent noise term [9]. The CFO leakage coefficient is defined as [17]

$$\Omega(l, k, \epsilon_i) = \frac{1}{M} \sum_{m=0}^{M-1} e^{j2\pi \frac{m}{M} (l + \epsilon_i - k)}. \quad (7)$$

Equation (6) describes the MFI due to IQI and also the ICI from the same user data and the MAI from the other users data.

We assume that the base station receiver IQI has already been corrected using e.g. the technique of [18]. In general, CFO between the base station and a mobile user is estimated in the downlink and there is a small part of CFO present in the uplink (0.1ppm of LO frequency as per 3GPP specifications) [19]. Thus, in the presence of small CFO and no receiver IQI, (6) simplifies to

$$Y_i(k) = H_i(k) G_{1T,i}(k) X_i(k) \Omega(k, k, \epsilon_i) + H_m(k) G_{2T,m}(k) X_m^*(-k) \Omega(k, k, \epsilon_m) + N(k). \quad (8)$$

III. JOINT EQUALIZATION OF TRANSMITTER IQI, CFO, AND CHANNEL

We now develop schemes for joint equalization of transmitter IQI, channel distortions, and carrier frequency offset at the base station of SC-FDMA system. The proposed receiver structure is illustrated in Fig. 1, which shows that the equalization is carried out in the frequency domain for each user after subcarrier demapping. As indicated by (8), the IQI causes MFI leading to the inter-user interference (IUI) between the users located at the mirror subcarriers. By utilizing the pair of mirror subcarriers, we develop the joint equalization schemes based on ZF and MMSE criterion. We assume that the parameters of channel, IQI, and CFO are already estimated at the base station.

$$\begin{aligned}
Y_i(k) = G_{1R}(k) & \left\{ \begin{aligned} & H_i(k)G_{1T,i}(k)X_i(k)\Omega(k, k, \epsilon_i) + H_m(k)G_{2T,m}(k)X_m^*(-k)\Omega(k, k, \epsilon_m) + \\ & \sum_{l \in \Gamma_i, l \neq k} H_i(l)G_{1T,i}(l)X_i(l)\Omega(l, k, \epsilon_i) + \\ & \sum_{l \in \Gamma_i, l \neq k} H_m(l)G_{2T,m}(l)X_m^*(-l)\Omega(l, k, \epsilon_m) + \\ & \sum_{j=1, j \neq i}^U \sum_{l \in \Gamma_j} H_j(l)G_{1T,j}(k)X_j(l)\Omega(l, k, \epsilon_j) + \\ & \sum_{j=1, j \neq m}^U \sum_{l \in \Gamma_j} H_j(l)G_{2T,j}(l)X_j^*(-l)\Omega(l, k, \epsilon_j) \end{aligned} \right\} \\
+ G_{2R}(k) & \left\{ \begin{aligned} & H_i^*(-k)G_{2T,i}^*(-k)X_i(k)\Omega^*(-k, -k, \epsilon_i) + H_m^*(-k)G_{1T,m}^*(-k)X_m^*(-k)\Omega^*(-k, -k, \epsilon_m) + \\ & \sum_{l \in \Gamma_i, l \neq k} H_i^*(-l)G_{2T,i}^*(-l)X_i(l)\Omega^*(-l, -k, \epsilon_i) + \\ & \sum_{l \in \Gamma_i, l \neq k} H_m^*(-l)G_{1T,m}^*(-l)X_m^*(-l)\Omega^*(-l, -k, \epsilon_m) + \\ & \sum_{j=1, j \neq i}^U \sum_{l \in \Gamma_j} H_j^*(-l)G_{2T,j}^*(-l)X_j(l)\Omega^*(-l, -k, \epsilon_j) + \\ & \sum_{j=1, j \neq i}^U \sum_{l \in \Gamma_j} H_j^*(-l)G_{1T,j}^*(-l)X_j^*(-l)\Omega^*(-l, -k, \epsilon_j) \end{aligned} \right\} \\
+ N(k) & \quad k \in \Gamma_i
\end{aligned} \quad (6)$$

$$\underbrace{\begin{bmatrix} Y_i(k) \\ Y_m^*(-k) \end{bmatrix}}_{\mathbf{y}(k)} = \underbrace{\begin{bmatrix} H_i(k)G_{1T,i}(k)\Omega(k, k, \epsilon_i) & H_m(k)G_{2T,m}(k)\Omega(k, k, \epsilon_m) \\ H_i^*(-k)G_{2T,i}^*(-k)\Omega^*(-k, -k, \epsilon_i) & H_m^*(-k)G_{1T,m}^*(-k)\Omega^*(-k, -k, \epsilon_m) \end{bmatrix}}_{\mathbf{H}(k)} \underbrace{\begin{bmatrix} X_i(k) \\ X_m^*(-k) \end{bmatrix}}_{\mathbf{x}(k)} + \underbrace{\begin{bmatrix} N(k) \\ N^*(-k) \end{bmatrix}}_{\mathbf{n}(k)}. \quad (9)$$

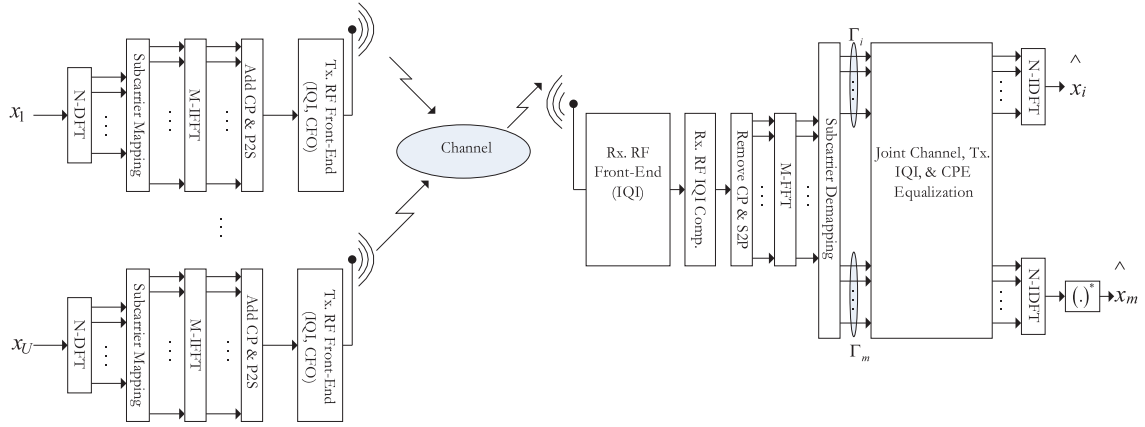


Fig. 1. Structure of uplink SC-FDMA system with equalization/compensation blocks of RF impairments in base station receiver.

After M-FFT and subcarrier demapping, the received signal for the i^{th} -user at subcarrier k is given by (8). We stack the received carrier and complex conjugate of the mirror-carrier in a vector as given by (9).

The ZF equalizer for the i^{th} -user builds on the inverse of the total “system” matrix $\mathbf{H}(k)$ in (9) and processes the pair of subcarriers as

$$\begin{bmatrix} \hat{X}_i^{ZF}(k) \\ \hat{X}_m^{*ZF}(-k) \end{bmatrix} = \mathbf{H}^{-1}(k) \begin{bmatrix} Y_i(k) \\ Y_m^*(-k) \end{bmatrix}. \quad (10)$$

Note that ZF equalizers suffer from the noise enhancement problem, however, the simulation results indicate that it is still able to produce satisfactory results. Another important observation from (10) is that the ZF equalizer fails to compensate the impairments if the matrix $\mathbf{H}(k)$ is ill-conditioned. The simulations show that such a situation is very unlikely to occur. Alternatively, we can employ the MMSE criterion where the received signal vector is filtered by the equalization filter $\mathbf{G}^{MMSE}(k)$

$$\begin{bmatrix} \hat{X}_i^{MMSE}(k) \\ \hat{X}_m^{*MMSE}(-k) \end{bmatrix} = \mathbf{G}^{MMSE}(k) \begin{bmatrix} Y_i(k) \\ Y_m^*(-k) \end{bmatrix} \quad (11)$$

which is the solution to

$$\mathbf{G}^{MMSE}(k) = \underset{\mathbf{G}(k)}{\operatorname{argmin}} \left\| \underbrace{\begin{bmatrix} X_i(k) \\ X_m^*(-k) \end{bmatrix}}_{\mathbf{x}(k)} - \mathbf{G}(k) \underbrace{\begin{bmatrix} Y_i(k) \\ Y_m^*(-k) \end{bmatrix}}_{\mathbf{y}(k)} \right\|^2 \quad (12)$$

to obtain the estimates of transmitted symbols. Let us define the correlation matrix $\mathbf{R}_{yy}(k) \triangleq E[\mathbf{Y}^H(k)\mathbf{Y}(k)]$ of the received signal and the cross-correlation vector $\mathbf{p}_{xy}^H(k) \triangleq E[\mathbf{x}^H(k)\mathbf{Y}(k)]$ where

$$\mathbf{Y}(k) = \begin{bmatrix} \mathbf{y}(k) & \mathbf{0}_{2 \times 1} \\ \mathbf{0}_{2 \times 1} & \mathbf{y}(k) \end{bmatrix}. \quad (13)$$

Expanding the correlation matrix and the cross-correlation vector yields

$$\mathbf{R}_{yy}(k) = \sigma_x^2 \begin{bmatrix} \mathbf{W}(k) & \mathbf{0}_{2 \times 2} \\ \mathbf{0}_{2 \times 2} & \mathbf{W}(k) \end{bmatrix} \quad (14)$$

$$\mathbf{p}_{xy}^H(k) = \sigma_x^2 [h_{11} \ h_{21} \ h_{12} \ h_{22}] \quad (15)$$

where $h_{ij}; i, j \in \{1, 2\}$ are the elements of matrix $\mathbf{H}(k)$ and $\mathbf{W}(k)$ is given by

$$\mathbf{W}(k) = \begin{bmatrix} |h_{11}|^2 + |h_{12}|^2 + 1/\text{SNR} & h_{11}^* h_{21} + h_{12}^* h_{22} \\ h_{11} h_{21}^* + h_{12} h_{22}^* & |h_{21}|^2 + |h_{22}|^2 + 1/\text{SNR} \end{bmatrix}. \quad (16)$$

With the given formulation, the MMSE solution of (12) is

$$\begin{bmatrix} g_{11}^{MMSE}(k) \\ g_{12}^{MMSE}(k) \\ g_{21}^{MMSE}(k) \\ g_{22}^{MMSE}(k) \end{bmatrix} = \begin{pmatrix} \mathbf{W}^{-1}(k) \begin{bmatrix} h_{11}^*(k) \\ h_{21}^*(-k) \end{bmatrix} \\ \mathbf{W}^{-1}(k) \begin{bmatrix} h_{12}^*(k) \\ h_{22}^*(-k) \end{bmatrix} \end{pmatrix} \quad (17)$$

where $g_{ij}^{MMSE}(k)$ are the coefficients of the matrix $\mathbf{G}^{MMSE}(k)$.

IV. SIMULATION RESULTS

To evaluate the performance of proposed schemes, we carry out extensive computer simulations. We consider an uplink SC-FDMA systems with $M = 1024$ subcarriers, and 600 data subcarriers. The subcarrier spacing is 15kHz and the occupied bandwidth is 9MHz. The data subcarriers are grouped into sets of 12 consecutive subcarriers and each user is allocated randomly a block of 12 subcarriers or multiple of that. We also assume that all the users transmit in one uplink slot that consists of seven SC-FDMA symbols. The transmitter gain and phase imbalance values are between 5 – 17% and $5^\circ - 10^\circ$, respectively, while the frequency selective inphase and quadrature branch impulse responses are $h_I = [1, 0, 0]$ and $h_Q = [0.97, -0.1, 0.01]$, respectively. All the transmitted signals pass through a 39 taps block fading channel with maximum delay spread of $2.5\mu\text{s}$ and power delay profile as described in [20]. LTE specifications states that mobile station (MS) frequency should be accurate to within 0.1ppm [19], and with 2GHz LO frequency this maps to CFO of $\pm 200\text{Hz}$ [19]. This is assumed also in the simulations. The simulation results are plotted by measuring the total symbol error rate (SER) at the receiver and averaging it over 2000 independent channel realizations. The channel coefficients, IQI parameters, and CFO are known at the receiver.

In all the simulations, we first consider the case when there are no radio impairments introduced in the signal and the channel is equalized with known estimates. The curve corresponding to this case in the following figures is labeled with “No FE distortion”, where FE stands for front-end. The uplink signals distorted by transmitter IQI, CFO, and the combined effect of both IQI and CFO is labeled with “W/Tx. IQI (PCE)”, “W/CFO (PCE)”, and “W/o Compensation (PCE)”, respectively. In these three cases, the channel is equalized on per carrier basis (PCE) with known estimates and the CPE term in corrected in the latter two examples. Finally, we employ the proposed ZF and MMSE equalization methods to jointly equalize the IQI, CFO, and channel distortions. The ZF and MMSE equalization utilize mirror-carriers jointly and are referred as joint mirror-carrier equalization (JMCE). The legend in the following figures corresponding to these equalization techniques are “W/ZF (JMCE) Scheme” and “W/MMSE (JMCE) Scheme”.

In the first simulation scenario, we randomly generate users with bandwidths of multiple of 12 subcarriers for each channel realization, with equal average received power and

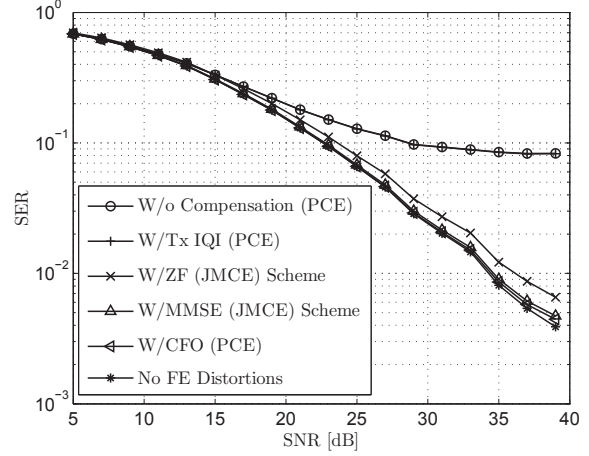


Fig. 2. Simulated average SER vs. SNR of localized SC-FDMA uplink system with random UE bandwidths of multiple of 12 subcarriers. 16-QAM data modulation and equal received power levels. Block-fading vehicular-A channels with $2.5\mu\text{s}$ delay spread. (2000 channel realizations)

16-QAM modulation. In each simulation, we generate users with random bandwidths as well as the CFO, IQI, and channel parameters. These impairments are introduced to the signal and the SER at the receiver is plotted in Fig. 2, illustrating the effect of the radio impairments. The results show that there is huge distortion brought by the IQI to the signal, however, the effect of CFO is very moderate. We have shown in the analysis that IQI results in the IUI among the uplink users and it clearly degrades the performance significantly. On the other hand, the proposed ZF and MMSE equalizers greatly improve the performance and reduce the SER considerably. The MMSE equalizer outperforms the ZF equalizer due to its less susceptibility to noise.

In the second simulation case, we consider the situation when there are four users communicating with the base station and each user has a bandwidth of 2.25 MHz. The first two users have QPSK modulated symbols while the latter two utilize 16-QAM modulation scheme. Again, the users suffer from the radio impairments whose parameters are generated randomly during each channel realization. To make the simulations more realistic, we allocate different receiver power levels to each user which are $[0, 5, 10, 15]$ dB respectively. First, we plot the average received SER of all users in Fig. 3 and compare it with Fig. 2. The results suggest that the total received SER for fixed users is notably higher than the case with random users. This is because for the fixed user case, we have different power levels and modulation schemes allocated to different users and it increases the SER of weak users leading to the overall increase in SER. Nevertheless, the proposed equalization schemes are able to bring the SER close to the case where there are no FE distortions. Notice also that MMSE equalizer has better performance than the ZF equalizer. To get a deeper insight, we also plot the user-by-user SER performance curves against average received SNR after MMSE equalization in Fig. 4. From figure we observe the major performance degradation in user-1 and user-

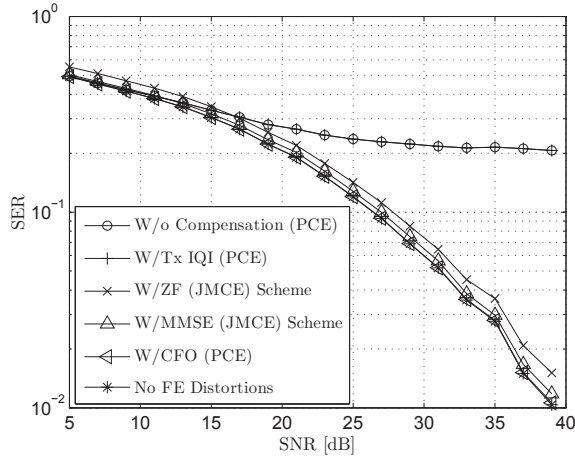


Fig. 3. Simulated average SER vs. SNR of localized SC-FDMA uplink system with 4 fixed bandwidth UE's. Two UE's use QPSK and the other two 16-QAM data modulation, while relative received powers are 0dB, 5dB, 10dB and 15dB. Block-fading vehicular-A channels with $2.5\mu s$ delay spread. (2000 channel realizations)

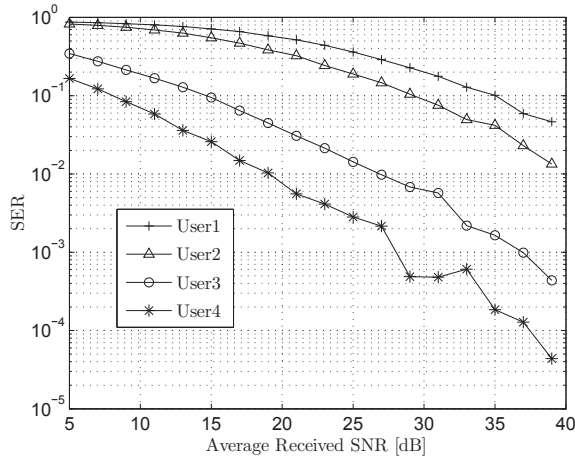


Fig. 4. Simulated individual UE SER vs. SNR of localized SC-FDMA uplink system with 4 fixed bandwidth UE's. Two UE's use QPSK and the other two 16-QAM data modulation, while relative received powers are 0dB, 5dB, 10dB and 15dB. Block-fading vehicular-A channels with $2.5\mu s$ delay spread. (2000 channel realizations)

2 signals. As described already, the transmitter IQI causes interference among users located at the mirror subcarriers, therefore, the weak users 1 & 2 suffer from the IUI due to the image component of user 4 & 3, respectively. Since the latter two users have quite higher power than the former two, the degradation is inevitable.

V. CONCLUSION

In this paper, we investigated the effect of radio impairments on a SC-FDMA system. We mathematically modeled the received uplink signal as a function of transmitter and receiver IQI, CFO, and channel. This analysis revealed the IUI due to IQI and also the ICI and MAI due to CFO. For the compensation of impairments, we made the assumption

that base station receiver IQI has already been corrected and CFO is relatively small. With these fairly reasonable assumptions, we simplified the signal model and proposed a joint compensation structure with two equalization schemes that were carried out in the frequency domain. It was shown with computer simulations that the proposed compensator was able to produce symbols estimates close to the ideal ones by employing the joint equalization schemes. The future work will focus on developing joint estimation techniques of the radio impairments and generalizing the work to MIMO-SCFDMA systems.

REFERENCES

- [1] *Wireless LAN medium access control (MAC) and physical layer (PHY) specifications: high speed physical layer in 2.4 GHz band*, IEEE, April 1999.
- [2] *IEEE standard for local and metropolitan area networks part 16: air interface for fixed broadband wireless access systems*, IEEE 802.16, 2004.
- [3] U. Ladebusch, C. A. Liss, "Terrestrial DVB (DVB-T): A broadcast technology for stationary portable and mobile use," *Proc. IEEE*, vol.94, no.1, pp.183-193, Jan. 2006.
- [4] G. Faria, J. A. Henriksson, E. Stare, and P. Talmola, "DVB-H: digital broadcast services to handheld devices," *Proc. IEEE*, vol.94, no.1, pp.194-209, Jan. 2006.
- [5] 3GPP Technical Specification Group Radio Access Network, "Evolved Universal Terrestrial Radio Access (E-UTRA) and Evolved Universal Terrestrial Radio Access (E-UTRAN); Overall Description; Stage 2," Technical Report TS 36.300, V1.0.0, March 2007.
- [6] A. A. Abidi, "Direct-conversion transceivers for digital communications," *IEEE J. Solid-State Circuits*, vol. 30, no. 12, pp. 1399-1410, Dec. 1995.
- [7] A. Tarighat and A. H. Sayed, "Joint compensation of transmitter and receiver impairments in OFDM systems," *IEEE Trans. Wireless Comm.*, vol.6, no.1, pp.240-247, Jan. 2007.
- [8] Y. H. Chung, and S. M. Phoong, "Joint estimation of transmitter and receiver IQ imbalances, CFO, and channel response for OFDM systems," *Intl. Conf. Green Circuits and Systems (ICGCS)*, Shanghai, China, June 2010.
- [9] A. Kiayani, L. Anttila, Y. Zou, and M. Valkama, "Advanced Receiver Design for Mitigating Multiple RF Impairments in OFDM Systems: Algorithms and RF Measurements," *Journal of Electrical and Computer Engineering*, vol. 2012.
- [10] H. A. Mahmoud, H. Arslan, M. K. Ozdemir, F. E. Retnasothie, "IQ imbalance correction for OFDMA uplink systems," in *Proc. IEEE Intl. Conf. Communications (ICC)*, pp.1-5, June 2009.
- [11] Y. Yoshida, K. Hayashi, H. Sakai, W. Bocquet, "Analysis and compensation of transmitter IQ imbalances in OFDMA and SC-FDMA Systems," *IEEE Trans. Signal Processing*, vol.57, no.8, pp.3119-3129, Aug. 2009.
- [12] L. Anttila, M. Valkama, M. Renfors, "3.9G Radio reception with SC-FDMA waveforms under I/Q imbalance," in *Proc. IEEE Intl. Symposium Circuits and Systems (ISCAS)*, pp.25-28, May 2007.
- [13] M. Morelli, "Timing and frequency synchronization for the uplink of an OFDMA system," *IEEE Trans. Commun.*, Vol. 52, Issue 2, pp. 296-306, Feb. 2004.
- [14] X. Dai, "Carrier frequency offset estimation and correction for OFDMA uplink," *IET Communications*, Vol. 1, Issue 2, pp. 273-281, April 2007.
- [15] H. Defeng, K. B. Letaief, "An interference-cancellation scheme for carrier frequency offsets correction in OFDMA systems," *IEEE Trans. Commun.*, vol.53, no.7, pp. 1155-1165, July 2005.
- [16] F. S. Al-kamali, M. I. Dessouky, B. M. Sallam, F. Shawki, and F. E. A. El-Samie, "Carrier Frequency Offsets Problem in DCT-SC-FDMA System: Investigation and Compensation," *ISRN Communications and Networking*, vol. 2011.
- [17] X. P. Zhang and H. G. Ryu, "Suppression of ICI and MAI in SC-FDMA communication system with carrier frequency offsets," *IEEE Trans. Consumer Electronics*, vol.56, no.2, pp.359-365, May 2010.
- [18] L. Anttila and M. Valkama, "On Circularity of Receiver Front-end Signals Under RF Impairments," in *Proc. 11th European Wireless Conference*, pp.1-8, 27-29 April 2011.
- [19] 3GPP Technical Specifications, TS 25.104, *Technical Specification Group Radio Access Network; Base Station (BS) radio transmission and reception (FDD)* 3GPP, V11.1.0 March 2012.
- [20] T. B. Sorensen, P. E. Mogensen, and F. Frederksen, "Extension of the ITU channel models for wideband (OFDM) systems," in *Proc. IEEE Veh. Technol. Conf. (VTC'05)*, pp. 392-396, Dallas, Texas, USA, Sept. 2005.

Publication 4

A. Kiayani, L. Anttila, and M. Valkama, "Modeling and Dynamic Cancellation of TX-RX Leakage in FDD Transceivers," in *Proceedings of IEEE 56th International Midwest Symposium on Circuits and Systems (MWSCAS 2013)*, pp. 1089-1094, Aug. 2013.

Copyright ©2013 IEEE. Reprinted, with permission, from the proceedings of IEEE 56th International Midwest Symposium on Circuits and Systems.

In reference to IEEE copyrighted material which is used with permission in this thesis, the IEEE does not endorse any of Tampere University of Technology's products or services. Internal or personal use of this material is permitted. If interested in reprinting/republishing IEEE copyrighted material for advertising or promotional purposes or for creating new collective works for resale or redistribution, please go to http://www.ieee.org/publications_standards/publications/rights/rights_link.html to learn how to obtain a License from RightsLink.

Modeling and Dynamic Cancellation of TX-RX Leakage in FDD Transceivers

Adnan Kiayani, Lauri Anttila, and Mikko Valkama

Department of Electronics and Communications Engineering,

Tampere University of Technology, FI-33101, Tampere, Finland.

Email: adnan.kiayani@tut.fi, lauri.anttila@tut.fi, mikko.e.valkama@tut.fi

Abstract—Frequency division duplex (FDD) transceivers employing the direct-conversion radio architecture are known to suffer from transmitter-receiver signal leakage problems. The presence of such leakage signal can impose stringent linearity requirements in receiver components that are difficult to fulfill in practice. Good example is second-order intermodulation distortion (IM2) due to transmitter leakage signal, stemming from finite IIP2 of receiver mixers, falling directly on top of the weak received signal. This paper carries out detailed modeling and proposes a dynamic cancellation technique for such TX-RX leakage, enabling sufficient TX-RX isolation in FDD mode without any extra analog/RF filtering. The technique is based on creating a replica of the undesired transmitter leakage signal and subtracting it from the down-converted signal in the receiver path, taking also the essential transmitter nonidealities into account. Simulation results show that the proposed method is able to effectively push transmitter leakage induced IM2 below the receiver noise floor.

Keywords—Calibration, direct-conversion receiver, duplexer isolation, dynamic cancellation, FDD, intermodulation distortion, second-order distortion, self-healing, transmitter leakage signal.

I. INTRODUCTION

During the last decade, radio transceiver architectures have received a great deal of attention, fueled by the desire to reduce cost, size, and power consumption of wireless devices. Among several radio architectures, the direct-conversion (or zero-IF) is the most promising approach, which offers a possibility of frequency agile radio front-ends and high level of component integration on a single chip. In general, to implement high-speed electronics, CMOS technology has evolved to 14 nm and BJT technology has evolved with addition of SiGe HBTs. However, there are discouraging predictions regarding the yield of RF circuits in these sub-micron technologies [1]. As a result, future RF transceivers in these sub-micron technologies need to be thoroughly tested before reaching to the customers. Since RF testing is quit costly (around 30% of manufacturing cost), on-chip testing has been proposed for RF circuits and systems [2]–[5]. Also, on-chip calibration techniques have been proposed to increase the yield of RF systems [6]–[9].

On the direct-conversion receiver side, one specific performance limiting factor related to RF circuit implementation challenges is the sensitivity to second-order intermodulation distortion (IM2). Such IM2 may be caused by strong out-of-band blocking signals entering the receiver, or in frequency division duplex (FDD) based systems, by the transceiver's

own transmit signal leaking into the receiver path. In FDD transceivers, both the transmitter and receiver are working simultaneously while operate on different frequency bands. The concurrent transmission is generally facilitated by a duplexer filter that connects the transmitter and receiver to the same antenna and separates their signals, such that the strong transmit signal cannot saturate the receiver. A duplexer generally consists of two band-pass filters (BPFs) to protect the sensitive receiver circuitry from the powerful transmit signals. The transmit signal may, however, leak to the receiver due to finite isolation of the duplexer [13] and is thus present at the receiver input. This leakage signal may potentially have substantially higher power than the useful received signal and its IM2 will then directly interfere with the weak received signal. This imposes stringent linearity requirements for the receiver. An attractive alternative to this problem is to use digital signal processing (DSP) based techniques for dynamic cancellation of the transmitter leakage signal in the receiver chain. First ideas in that direction have been reported in [12] – [14]. Another possible source of TX-RX leakage is transmitter out-of-band emissions which may also be substantial and desensitize the receiver chain, especially if the duplexing gap between TX and RX bands is small [11].

For the proper operation of FDD transceivers, leakage from the TX channel to RX channel should be controlled or minimized while the RF components like the duplexer and the power amplifier (PA) work within their specification limits. Thus, post-manufactured RF circuits need to be tested and possibly further calibrated. Therefore, in this paper, to minimize the testing cost of RF FDD transceivers and to increase the yield of these sub-systems, a novel dynamic cancellation technique of TX-RX leakage is developed, specifically tailored to the IM2 problem. In this technique, a replica of the undesired IM2 induced by the transmitter leakage signal is created and then subtracted from the down-converted signal in the receiver path. Since all essential estimation and cancellation signal processing takes place in the transceiver digital front-end (DFE), the proposed technique is generally independent of the underlying IC technology and can also be used for assembled and on-chip FDD based transceivers.

In the existing literature, digital compensation approaches for mitigation of transmitter leakage signals are discussed in [12]–[15], where in [12] a baseband model of transmitter leakage signal in zero-IF receiver is presented and its impact on system performance is simulated, but the study is neglecting the effects of nonlinear transmitter components. The authors have then described two different approaches for the estimation of transmitter leakage signal in [13], again assuming an idealized linear transmitter. The cancellation of IM2 due to transmitter leakage signal is, in turn, proposed in [14], but the study is simplified in the sense that the frequency-selective nature of

This work was supported by the Academy of Finland (under the project 251138 “Digitally-Enhanced RF for Cognitive Radio Devices”), the Finnish Funding Agency for Technology and Innovation (Tekes, under the project “Cross-Layer Modeling and Design of Energy-Aware Cognitive Radio Networks (CREAM)”), the Graduate School TISE, and the Austrian Center of Competence in Mechatronics (ACCM).

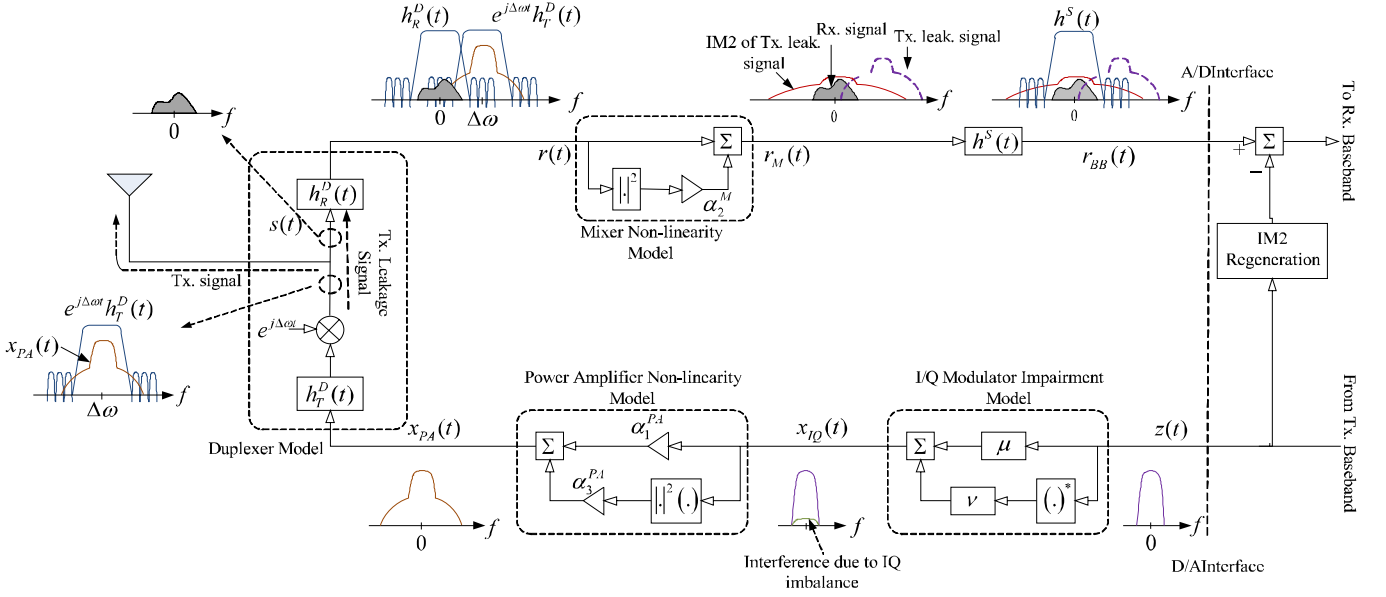


Fig. 1: Baseband equivalent model of a FDD transceiver with IM distortion, transmitter leakage signal, and I/Q imbalance.

duplexer stopband is neglected. Finally, [15] deals with the compensation of transmitter out-of-band (OOB) emissions in the receiver band and no receiver nonlinearities are considered. Contrary to the previous work, in this paper, we present a comprehensive treatment on the effect of nonlinearities of both the transmitter and receiver chain components and develop a complete baseband model of the overall received signal containing the impacts of transmitter leakage induced IM2 as well as the transmitter OOB emissions due to power amplifier (PA) spectral re-growth. We then focus in detail on the suppression of the IM2 and develop an efficient parametric nonlinear model for its estimation and cancellation. Compared to existing literature, the modeling and developed dynamic cancellation architecture takes into account the frequency-selective nature of the duplexer stopband response as well as the nonlinear signal distortion in the transmitter chain which are missing in the existing literature.

Notations: the scalar parameters are represented by lower case letters a and vectors/matrices in boldface letters \mathbf{a} . We distinguish the vectors from matrices by a bold face letter with underline $\underline{\mathbf{a}}$. The convolution operator is indicated by \star . Superscript $(\cdot)^T$, $(\cdot)^H$, $(\cdot)^{-1}$, and $(\cdot)^*$ denote the transpose, hermitian transpose, inverse, and conjugate of a scalar, a vector, or a matrix.

II. FDD TRANSCEIVER SIGNAL MODELING

Fig. 1 illustrates the baseband equivalent model of a complete FDD transceiver system, and the associated signal spectra, with finite isolation in the duplexing filters and nonlinear transmitter and receiver components. For analysis and modeling purposes, the frequency separation between the transmitter and receiver center-frequencies is denoted by $\Delta\omega$. In the following, we carry out the essential signal modeling for the whole chain starting from transmitter baseband up to power amplifier output, and thereon towards the receiver chain employing the direct conversion principle.

A. Fundamental Signal Modeling

For signal modeling, we denote the complex baseband signal to be transmitted as $z(t) = z_I(t) + jz_Q(t)$. This signal is up-converted to the transmitter carrier frequency with an I/Q modulator. The mismatch between the I and Q branch

of the modulator causes I/Q imbalance that results in mirror-frequency crosstalk. The complex envelope of I/Q modulated signal under I/Q imbalance is given by [16]

$$x_{IQ}(t) = \mu z(t) + \nu z^*(t) \quad (1)$$

where μ and ν model the gain and phase imbalance between the I and Q branches of the modulator, defined as $\mu = [1 + ge^{j\phi}]/2$; $\nu = [1 - ge^{j\phi}]/2$. The modulated signal is next amplified by a PA for transmission purposes. PA is inherently a non-linear device and for simplified modeling purposes, we approximate its nonlinear behavior with a simple 3rd order polynomial model. The baseband equivalent model for PA output with 3rd order non-linearity (IM3) can then be expressed as

$$x_{PA}(t) = \alpha_1^{PA} x_{IQ}(t) + \alpha_3^{PA} |x_{IQ}(t)|^2 x_{IQ}(t) \quad (2)$$

where $\alpha_1^{PA}, \alpha_3^{PA}$ are the complex polynomial coefficients. Substituting (1) in (2) yields

$$\begin{aligned} x_{PA}(t) = & \alpha_1^{PA} (\mu z(t) + \nu z^*(t)) \\ & + \alpha_3^{PA} |\mu z(t) + \nu z^*(t)|^2 \mu z(t) \\ & + \alpha_3^{PA} |\mu z(t) + \nu z^*(t)|^2 \nu z^*(t) \end{aligned} \quad (3)$$

Notice in the above equation that the second and third terms that are multiplied with the coefficient α_3^{PA} are in practice at least 30dB weaker than the first term. Also the terms with I/Q imbalance coefficient ν are in minimum 25dB weaker than the fundamental term $\mu z(t)$ [10]. This implies that the products of the form $\alpha_3^{PA} \nu$ have diminishing power and the contribution of terms having such products as multipliers are insignificant. This simplifies (3) to

$$x_{PA}(t) \cong \alpha_1^{PA} (\mu z(t) + \nu z^*(t)) + \alpha_3^{PA} \mu^2 |z(t)|^2 z(t). \quad (4)$$

The PA output signal then passes through the duplexer to antenna. A duplexer is constructed with two BPFs. In the transmitter path, the transmitter duplex filter suppresses the unwanted emissions outside the transmission band and the transmitter noise from PA present at the receiver frequency band, while the receiver duplex filter attenuates the transmitter signal leaking into the receiver chain. With finite isolation

of duplexing filters, the transmitter signal emissions are not completely suppressed from the receiver chain. At receiver input, this transmitter leakage signal can now be mathematically expressed as

$$\begin{aligned} s_L(t) &= h_R^D(t) \star (h_T^D(t) \star x_{PA}(t)) e^{j\Delta\omega t} \\ &= (h^D(t) \star x_{PA}(t)) e^{j\Delta\omega t} \end{aligned} \quad (5)$$

where

$$h^D(t) = h_T^D(t) \star (h_R^D(t) e^{-j\Delta\omega t}) \quad (6)$$

denotes the total response of duplexer filters from TX-RX leakage perspective. Thus, the total signal at the input of the receiver chain consists of the actual weak desired received signal and the leaking transmitter signals. The baseband equivalent form for this total receiver input signal is then

$$r(t) = s_D(t) + s_L(t) + n(t) \quad (7)$$

where $s_D(t)$ is the desired received signal and $n(t)$ denotes thermal noise.

The receiver mixer stage is next modeled as having a finite IIP2 number resulting in the generation of the undesired IM2. This can be modeled by the square of mixer input signal which is essentially the squared envelope of the total signal entering the mixers. The IM2 is present in additive form at the mixer output, written here as

$$\begin{aligned} r_M(t) &= r(t) + \alpha_2^M |r(t)|^2 \\ &= s_D(t) + s_L(t) + n(t) + \alpha_2^M |s_D(t)|^2 \\ &\quad + \alpha_2^M |s_L(t)|^2 + \alpha_2^M |n(t)|^2 + 2\alpha_2^M \Re\{s_D(t)s_L^*(t)\} \\ &\quad + 2\alpha_2^M \Re\{n(t)s_D^*(t)\} + 2\alpha_2^M \Re\{n(t)s_L^*(t)\} \end{aligned} \quad (8)$$

where α_2^M represents the mixer RF-to-LO isolation and is generally complex valued. The fourth term in (8) is the IM2 of the actual received signal and the seventh term is cross-product between the received and transmitter leakage signals. Assuming the actual received signal is weak, both of these terms are very small and can be neglected. Furthermore, the sixth, eighth, and ninth term describe the IM2 of noise $n(t)$, the cross product of the noise with the received signal, and the transmitter leakage signal. Since α_2^M is very small, these terms can be considered much weaker than the down-converted noise and can be ignored, thus simplifying (8) to

$$r_M(t) = s_D(t) + s_L(t) + \alpha_2^M |s_L(t)|^2 + n(t). \quad (9)$$

In above, the first term is the desired received signal, second term is the leaking transmit signal at a frequency distance of $\Delta\omega$ from the received signal, and the third term is the IM2 due to leaking transmit signal with twice the bandwidth of the original transmit signal including the OOB emission. The filtering process by channel selection filter (CSF), denoted by $h^S(t)$, is given by

$$\begin{aligned} r_{BB}(t) &= h^S(t) \star r_M(t) \\ &= s_D(t) + \alpha_2^M h^S(t) \star |s_L(t)|^2 + h^S(t) \star s_L(t) + n_h(t) \\ &= s_D(t) + s_{IM2}(t) + s_{OOBE}(t) + n_h(t) \end{aligned} \quad (10)$$

where $n_h(t) = h^S(t) \star n(t)$ and

$$s_{IM2}(t) = \alpha_2^M h^S(t) \star |h^D(t) \star x_{PA}(t)|^2 \quad (11a)$$

$$s_{OOBE}(t) = h^S(t) \star (h^D(t) \star x_{PA}(t)) e^{j\Delta\omega t}. \quad (11b)$$

Thus from (10), two different effects of distortion or interference can be clearly observed as written in (11a), (11b). These are discussed further below.

B. IM2 Distortion at Baseband

The second term $s_{IM2}(t)$ in (10), written in (11a), represents the IM2 due to transmitter leakage signal which appears directly at baseband and may be partially attenuated by CSF due to its doubled bandwidth, as shown in Fig. 1. This transmitter leakage induced IM2 signal can be strong, depending on the achieved duplexer attenuation and mixer IIP2, and generally causes severe interference to the received signal which cannot be mitigated with linear filtering alone. To demonstrate and quantify the relative strength of such IM2, example transceiver system calculations are carried out next. Using LTE FDD mode as an example, the mobile station (MS) transmit signal can be up to 120dB stronger than the received signal, assuming maximum TX power at the antenna connector of around +23dBm (power class 3) and receiver sensitivity level of -97dBm [10]. The typical value of TX-RX duplexer attenuation, in turn, assumed e.g. in standardization [11] is only 50dB. Thus with power class 3 mobile transmitter, the transmitter leakage signal power is +23 - 50 = -27dBm at the receiver input. This signal is next amplified by LNA, having typically a gain of +20dB or so, resulting in -7dBm leakage signal power (P_{TxL}) at the mixer input. Then, if the mixer IIP2 is e.g. +40dBm, then the IM2 power (P_{TxL}^{IM2}) at the mixer output is given by $P_{TxL}^{IM2} = P_{TxL} - (IIP2 - P_{TxL}) = -54dBm$, where it is assumed that the gain of the mixer is 0dB for simplicity. If then the desired signal itself is assumed to be at receiver sensitivity level of -97dBm, after LNA gain and mixer stage, its power is -77dBm. Hence, the transmitter leakage IM2 is in this example 23dB *stronger* than the desired signal, thus calling for efficient suppression. The above calculation certainly represents an extreme worst-case scenario but still the problem is practical and severe, especially when trying to keep the duplexer complexity and costs at a reasonable level.

C. Transmitter OOB Emissions at RX Band

As shown in Fig. 1, the spectral re-growth of transmitter signal due to PA non-linearity can also directly overlap with the received signal if the duplexing gap between the transmitter and receiver is small. Again, if such OOB emission is not completely suppressed by transmitter duplex filter, this interference is directly on the receiver band and can heavily reduce the receiver sensitivity. In our modeling, the third term $s_{OOBE}(t)$ in (10), written out explicitly in (11b), represents this interference and its dependence on the PA output signal and associated filtering.

To demonstrate the relative strength of this kind of interference, we shortly study LTE uplink band 25 [10] and assume intra-band carrier aggregation scenario with two carriers. In this scenario, the duplexing gap between 2nd TX carrier and RX band is only 15MHz and the transmitter emissions are controlled by Spurious Emission Limit which limits the emissions to maximum of -30dBm per 1MHz measurement bandwidth. Assuming an example figure of -35dBm/1MHz, being then further suppressed by duplex filter by 50dB's, the resulting OOBE is -85dBm/1MHz or -75dBm/10MHz. Compared to reference sensitivity of -93.5dBm for 10MHz RX bandwidth, the TX OOB is still significantly higher than the received signal ($\sim 18.5dB$) and can completely block the receiver in case it is operating close to sensitivity level.

From above discussions, it can be deduced that both IM2 and OOB type signal leakage problems can be substantial in FDD devices, especially when emphasizing low-cost duplexer implementations. In the following, we focus in detail on the IM2 problem and develop an efficient digital signal processing based estimation-cancellation architecture for dynamically regenerating and suppressing the leakage signal inside the transceiver.

III. DIGITAL ESTIMATION AND CANCELLATION METHOD FOR TRANSMITTER LEAKAGE IM2

With the homodyne receiver topology, the desired received signal is directly down-converted to the baseband while the even-order nonlinear distortions also fall to baseband on top of the received signal. In the following, a parallel augmented Volterra based framework is first developed for leakage IM2 modeling, which is then used to derive LS parameter estimation and cancellation structure. The subsequent derivations are carried out in discrete time domain.

A. Parallel Augmented Volterra Model for Transmitter Leakage IM2

We define $h_2^S(t) = \alpha_2^M h^S(t)$ and assume that the transmitter leakage IM2 signal is contained in the passband of CSF, such that $h_2^S(t) = \alpha_2^M \alpha^S \delta(t) = \alpha_2^S \delta(t)$. The resulting discrete time model of transmitter leakage IM2 from (11a) is then

$$s_{IM2}[n] = \alpha_2^S \star |h^D[n] \star x_{PA}[n]|^2 = \sum_{m_1} \sum_{m_2} h^{IM2}[m_1, m_2] x_{PA}[n - m_1] x_{PA}^*[n - m_2] \quad (12)$$

where $h^{IM2}[m_1, m_2] = \alpha_2^S h^D[m_1] h^{D*}[m_2]$ is a 2D filter (2^{nd} order Volterra kernel) which defines the total IM2 filter, representing the filtering effect on the transmitter leakage signal. The above formulation leads to a model which is linear in parameters at the expense of increase in dimensionality of the problem. Evaluating the product $x_{PA}[n - m_1] x_{PA}^*[n - m_2]$ and using the same reasoning as stated before that terms with multiplier coefficients such as $\nu^2, \alpha_3^{PA} \nu$ are sufficiently weak and can be omitted in the analysis, leading to (13), where the

known basis functions are

$$\begin{aligned} \Psi_{fund}[n] &= z[n - m_1] z^*[n - m_2] \\ \Psi_1[n] &= z[n - m_1] z[n - m_2] \\ \Psi_2[n] &= z^*[n - m_1] z^*[n - m_2] \\ \Psi_3[n] &= z[n - m_1] |z[n - m_2]|^2 z^*[n - m_2] \\ \Psi_4[n] &= |z[n - m_1]|^2 z[n - m_1] z^*[n - m_2] \end{aligned} \quad (14)$$

while the unknown parameters are

$$\begin{aligned} h_{fund}^{IM2}[m_1, m_2] &= h^{IM2}[m_1, m_2] |\alpha_1^{PA}|^2 |\mu|^2 \\ \beta_1^{IM2} &= \frac{\nu^*}{\mu^*} \\ \beta_2^{IM2} &= \frac{\nu}{\mu} = \beta_1^{IM2*} \\ \beta_3^{IM2} &= \frac{|\mu|^2 \alpha_3^{PA*}}{\alpha_1^{PA*}} \\ \beta_4^{IM2} &= \frac{|\mu|^2 \alpha_3^{PA}}{\alpha_1^{PA}} = \beta_3^{IM2*}. \end{aligned} \quad (15)$$

With the model in (13), the digital cancellation algorithm requires the estimates of the set of parameters listed in (15) to recreate the replica of undesired transmitter leakage IM2.

B. LS Estimation of Parameters

We switch to vector-matrix notation and write the L samples of down-converted baseband signal with transmitter leakage IM2 as

$$\begin{aligned} \mathbf{r}_{BB} &= \mathbf{s} + \mathbf{s}_{IM2} + \mathbf{n}_h \\ &= \mathbf{s} + \mathbf{\Psi}_{fund} \mathbf{h}_{fund}^{IM2} + \beta_1^{IM2} \mathbf{\Psi}_1 \mathbf{h}_{fund}^{IM2} + \beta_2^{IM2} \mathbf{\Psi}_2 \mathbf{h}_{fund}^{IM2} \\ &\quad + \beta_3^{IM2} \mathbf{\Psi}_3 \mathbf{h}_{fund}^{IM2} + \beta_4^{IM2} \mathbf{\Psi}_4 \mathbf{h}_{fund}^{IM2} + \mathbf{n}_h \end{aligned} \quad (16)$$

where the matrix $\mathbf{\Psi}_{fund}$ and vector \mathbf{h}_{fund}^{IM2} are given by (17). The matrices $\mathbf{\Psi}_i, i \in \{1, 2, 3, 4\}$ can also be constructed in a similar way as $\mathbf{\Psi}_{fund}$. Recalling the system calculations in section II-B, we observe following facts from (16):

- 1) the received signal \mathbf{s} is generally weaker than the transmitter leakage IM2 (e.g. -23dB below if received signal is at sensitivity level and transmitter transmits at maximum power),

$$s_{IM2}[n] = \sum_{m_1} \sum_{m_2} h_{fund}^{IM2}[m_1, m_2] \Psi_{fund}[n] + \beta_1^{IM2} \sum_{m_1} \sum_{m_2} h_{fund}^{IM2}[m_1, m_2] \Psi_1[n] + \beta_2^{IM2} \sum_{m_1} \sum_{m_2} h_{fund}^{IM2}[m_1, m_2] \Psi_2[n] + \beta_3^{IM2} \sum_{m_1} \sum_{m_2} h_{fund}^{IM2}[m_1, m_2] \Psi_3[n] + \beta_4^{IM2} \sum_{m_1} \sum_{m_2} h_{fund}^{IM2}[m_1, m_2] \Psi_4[n] \quad (13)$$

$$\begin{aligned} \mathbf{\Psi}_{fund} &= [\mathbf{\Psi}_{fund}(0), \mathbf{\Psi}_{fund}(1), \dots, \mathbf{\Psi}_{fund}(M-1)], \quad \text{with} \\ \mathbf{\Psi}_{fund}(m) &= \begin{bmatrix} z[n-m] z^*[n] & z[n-m] z^*[n-1] & \dots & z[n-m] z^*[n-M+1] \\ z[n-m-1] z^*[n-1] & z[n-m-1] z^*[n-2] & \dots & z[n-m-1] z^*[n-M] \\ \vdots & \vdots & \ddots & \vdots \\ z[n-m-L+1] z^*[n-L+1] & z[n-m-L+1] z^*[n-L] & \dots & z[n-m-L+1] z^*[n-L-M+2] \end{bmatrix} \\ \mathbf{h}_{fund}^{IM2} &= [\mathbf{h}_{fund}^{IM2,T}(0), \mathbf{h}_{fund}^{IM2,T}(1), \dots, \mathbf{h}_{fund}^{IM2,T}(M-1)]^T, \quad \text{with} \\ \mathbf{h}_{fund}^{IM2}(m) &= [h^{IM2}[m, 0], h^{IM2}[m, 1], \dots, h^{IM2}[m, M-1]]^T; \quad m \in \{1, 2, \dots, M-1\}. \end{aligned} \quad (17)$$

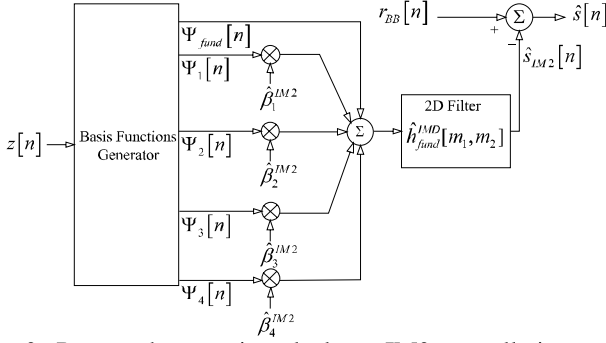


Fig. 2: Proposed transmitter leakage IM2 cancellation architecture.

- 2) the third and fourth term of (17) are transformed by I/Q imbalance and they are at least 25dB weaker than the fundamental IM2 term $\Psi_{fund}\mathbf{h}_{fund}^{IM2}$ [10],
- 3) the fourth and fifth terms of (17) are spectral regrowth created by PA and they are at least 30dB weaker than the fundamental IM2 term.

These facts lead us to derive a two step estimation framework. In the first step, the fundamental filter \mathbf{h}_{fund}^{IM2} is estimated while assuming that rest of the terms are noise. The estimated filter is used to regenerate the fundamental IM2 which is subtracted from (16), the result of which is then used in second estimation step to estimate the coefficients $\beta_i^{IM2}; i \in \{1, 2, 3, 4\}$.

Now, to estimate the fundamental IM2 filter, we write (17) as

$$\mathbf{r}_{BB,IM2}^{fund} = \Psi_{fund}\mathbf{h}_{fund}^{IM2} + \mathbf{w}_1 \quad (18)$$

where \mathbf{w}_1 denotes the filtered noise plus weak signal terms. The least-squares (LS) solution of \mathbf{h}_{fund}^{IM2} is given by [17]

$$\hat{\mathbf{h}}_{fund}^{IM2,LS} = \left(\Psi_{fund}^H \Psi_{fund} \right)^{-1} \Psi_{fund}^H \mathbf{r}_{BB,IM2}. \quad (19)$$

Next, with estimated IM2 filter $\hat{\mathbf{h}}_{fund}^{IM2,LS}$, we subtract the term $\Psi_{fund}\hat{\mathbf{h}}_{fund}^{IM2,LS}$ from the down-converted baseband signal \mathbf{r}_{BB} to remove the effect of strongest term and use the estimates of $\hat{\mathbf{h}}_{fund}^{IM2,LS}$ which gives us

$$\begin{aligned} \tilde{\mathbf{r}}_{BB} &= \mathbf{r}_{BB} - \Psi_{fund}\hat{\mathbf{h}}_{fund}^{IM2,LS} \\ &\cong \mathbf{s} + \Phi_1\beta_1^{IM2} + \Phi_2\beta_2^{IM2} + \Phi_3\beta_3^{IM2} + \Phi_4\beta_4^{IM2} + \mathbf{n}_h \\ &\cong \Phi\beta^{IM2} + \mathbf{w}_2 \end{aligned} \quad (20)$$

where

$$\begin{aligned} \Phi_1 &= \Psi_1\mathbf{h}_{fund}^{IM2} \\ \Phi_2 &= \Psi_2\mathbf{h}_{fund}^{IM2} \\ \Phi_3 &= \Psi_3\mathbf{h}_{fund}^{IM2} \\ \Phi_4 &= \Psi_4\mathbf{h}_{fund}^{IM2} \\ \Phi &= [\Phi_1 \quad \Phi_2 \quad \Phi_3 \quad \Phi_4] \\ \beta^{IM2} &= [\beta_1^{IM2} \quad \beta_2^{IM2} \quad \beta_3^{IM2} \quad \beta_4^{IM2}]^T \\ \mathbf{w}_2 &= \mathbf{s} + \mathbf{n}_h. \end{aligned} \quad (21)$$

The LS estimator of coefficient vector β^{IM2} is then

$$\hat{\beta}^{IM2,LS} = \left(\Phi^H \Phi \right)^{-1} \Phi^H \tilde{\mathbf{r}}_{BB}. \quad (22)$$

TABLE I: Algorithm for the estimation and cancellation of transmitter leakage IM2 from the baseband received signal

- 1) Construct the basis function matrices $\Psi_{fund}, \Psi_1, \Psi_2, \Psi_3, \Psi_4$ from the transmitter data $z[n]$ according to (14) and (17).
- 2) Estimate the fundamental filter vector \mathbf{h}_{fund}^{IM2} in the least-squares sense as given in (19).
- 3) Subtract the fundamental term of \mathbf{s}_{IM2} which is a product $\Psi_{fund}\hat{\mathbf{h}}_{fund}^{IM2,LS}$ from the baseband signal vector \mathbf{r}_{BB} to obtain $\tilde{\mathbf{r}}_{BB}$ as in (20).
- 4) Use (22) to estimate the coefficient vector $\hat{\beta}^{IM2,LS}$.
- 5) Plug in the estimates of $\hat{\mathbf{h}}_{fund}^{IM2,LS}; \hat{\beta}^{IM2,LS}$ together with basis matrices of step-1 to recreate the interference \mathbf{s}_{IM2} .
- 6) Subtract \mathbf{s}_{IM2} from the signal \mathbf{r}_{BB} to get the desired received signal \mathbf{s} .

C. Transmitter Leakage IM2 Cancellation

An estimate of transmitter leakage IM2 can be regenerated using the baseband digital transmitter data $z[k]$ together with the estimated parameters of (15) obtained using (19) and (22). The estimates of $\hat{\mathbf{h}}_{fund}^{IM2,LS}; \hat{\beta}^{IM2,LS}$ are substituted in (13) to regenerate the transmitter leakage IM2 interference. The predicted interference is then subtracted from the down-converted signal $r_{BB}[n]$ to obtain a cleaned received signal for detection. A conceptual block diagram of the proposed digital canceller is shown in Fig. 2, and the proposed estimation and cancellation principle is summarized in Table I.

D. Practical Aspects and Limitations

There are certain implementation related aspects that may affect the modeling and cancellation behavior of the proposed technique. First, a model mismatch between the behavioral models and the true nonlinear response of the RF components may compromise the performance. Possible mismatch sources include memory effects in PA nonlinearity and I/Q mismatch, as well as LNA nonlinearity. In addition to that, accurate time alignment of the reference and the received IM2 signal is also crucial for precise estimation. From the complexity point of view, the proposed algorithm has increased resource requirements compared to [13] and [14], but as will be shown in the next section, will also exhibit much better cancellation performance with higher transmit powers. Such a complexity-performance tradeoff is typical in nonlinear system identification problems. All of these issues will be addressed in detail in future work.

IV. SIMULATION RESULTS

To evaluate the performance of proposed estimation and cancellation scheme, we setup a FDD simulation chain where the transmit and receive signals are modeled according to LTE mobile station 10MHz TX/RX mode. The duplexer filter is modeled to have an attenuation of 50dB on the transmitter band, while the PA gain, PA IIP3, LNA gain, and mixer IIP2 are 24dB, 15dBm, 20dB, and 40dBm, respectively. The thermal noise power at the LNA input is -104.5 dBm and the received signal power is -90 dBm. In LTE 10MHz FDD mode, the maximum transmit signal power at antenna connector is $+23$ dBm thus producing a transmitter leakage signal at LNA input with power of -27 dBm. The LNA adds 20dB gain to the received signal and the transmitter leakage signal. At the output of mixer, assuming 0dB mixer gain, the received

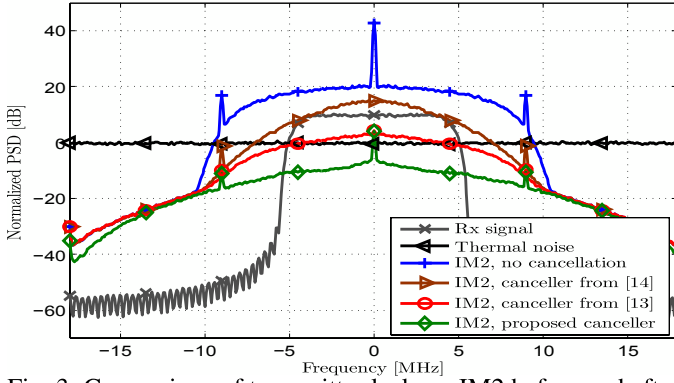


Fig. 3: Comparison of transmitter leakage IM2 before and after cancellation with 23dBm transmit power.

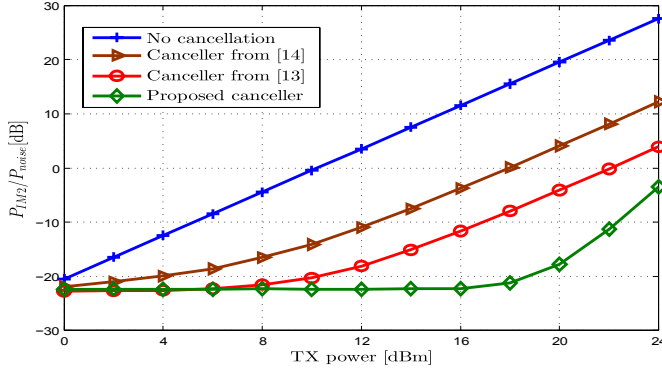


Fig. 4: Comparison of transmitter leakage IM2-to-noise power ratio vs. TX power before and after cancellation.

signal is at -70dBm compared to the transmitter leakage IM2 power of -54dBm . Blocks of 100k samples of digital baseband transmit signal and down-converted received signal are used in estimation and the fundamental IM2 2D filter is modeled with $25(M = 5)$ parameters. The estimated interference is then subtracted from composite received signal comprising of desired signal, leakage IM2, and thermal noise. We compare our method with the transmitter leakage IM2 cancellers proposed in [13] and [14], where transmitter nonidealities are not considered.

In the first simulation, we plot the signal spectrum and compare the transmitter leakage IM2 suppression before and after proposed digital cancellation. The results indicate that the transmitter leakage IM2 signal after suppression using canceller of [14] is still stronger than the desired received signal. On the other hand, the LS technique of [13] is able to significantly reduce the transmitter leakage IM2 effect but does not remove it completely and a small interference remains in the cleaned received signal. This is due to the fact that this technique effectively estimates only the fundamental IM2 filter \mathbf{h}_{fund}^{IM2} and performs cancellation in one step, while the residual I/Q imbalance and PA regrowth terms remain in the signal. Contrary to that, our proposed technique first estimates the fundamental IM2 term and then utilizes it to estimate the scalar parameters in a second estimation step, resulting in the transmitter leakage IM2 suppressed below the thermal noise floor. We also plot the transmitter leakage IM2-to-noise power ratio versus the TX power and show the substantial improvement brought with the proposed estimation and cancellation technique.

V. CONCLUSION

The paper addressed the issue of transmitter leakage in FDD transceiver systems, and the impacts of transmitter leak-

age IM2 and transmitter OOB emission on receiver chain were analyzed. The paper proposed a two step LS estimation procedure to reproduce the transmitter leakage induced IM2 in the presence of transmitter nonidealities enabling efficient dynamic cancellation of such IM2 in FDD direct-conversion transceivers. The proposed technique was evaluated with computer simulations which demonstrated that the IM2 interference can be efficiently suppressed below the noise floor, despite the transmitter nonidealities. Future work will focus on prototype implementations to demonstrate the calibration capabilities of the proposed algorithm on real RF hardware. It is also imperative to perform an analysis on the RF hardware cost, such as linearity of mixers, PA, and modulators, and duplexer attenuation, versus the baseband processing cost of DSP based algorithms.

REFERENCES

- [1] <http://www.darpa.org/> (Broad Agency Announcement, DARPA-BAA-08-40, May 19, 2008).
- [2] R. Voorakaranam, S. Cherubal, and A. Chatterjee, "A signature test framework for rapid production testing of RF circuits," in *Proc. Design, Automation and Test in Europe Conference and Exhibition*, pp. 186-191, 2002.
- [3] A. Goyal, M. Swaminathan, and A. Chatterjee, "One-port resonance based test technique for RF interconnect and filters embedded in RF substrates," *IEEE Trans. Compon. Packag. Technol.*, vol. 3, no. 2, pp. 236-246, Feb. 2013.
- [4] A. Goyal, M. Swaminathan, and A. Chatterjee, "Low-cost specification based testing of RF amplifier circuits using oscillation principles," *J. Electron. Testing Theory and Applicat.*, vol. 26, no. 1, pp. 13-24, Feb. 2010.
- [5] A. Goyal, M. Swaminathan, and A. Chatterjee, "Low-frequency and low-cost test methodology for integrated RF substrates," *IEEE Adv. Packag.*, vol. 33, no. 3, pp. 669-680, Aug. 2010.
- [6] N. Kupp, He Huang, Y. Makris, and P. Drineas, "Improving analog and RF device yield through performance calibration," *IEEE Des. Test Comput.*, vol. 28, no. 3, pp. 64-75, May-June 2011.
- [7] A. Goyal, M. Swaminathan, A. Chatterjee, D. Howard, and J. D. Cressler, "A new self-healing methodology for RF amplifier circuits based on oscillation principles," *IEEE Trans. Very Large Scale Integr. (VLSI) Syst.*, vol. 32, no. 4, pp. 1835-1848, Oct. 2012.
- [8] J. Liaperdos, A. Arapoyanni, and Y. Tsiatouhas, "A built-in voltage measurement technique for the calibration of RF mixers," *IEEE Trans. Instrum. Meas.*, vol. 62, no. 4, pp. 732-742, April 2013.
- [9] R. Ayadi, S. Mahresi, and M. Masmoudi, "Self-calibration of output match and reverse isolation in LNAs based switchable resistor," *J. of Electron. Testing*, vol. 28, no. 2, pp. 167-176, April 2012.
- [10] *3GPP Spec. LTE; Evolved Universal Terrestrial Radio Access (E-UTRA); User Equipment (UE) radio transmission and reception (3GPP TS 36.101 version 11.2.0 Release 11)*, Nov. 2012.
- [11] *3GPP Spec.; R4-126964, REFSENS with one UL carrier for NC intra-band CA*, Ericsson, ST-Ericsson.
- [12] A. Frotzsch, and G. Fettweis, "Baseband analysis of Tx leakage in WCDMA zero-IF-receivers," in *Proc. 3rd Int. Symp. Commun., Control and Signal Process. (ISCCSP'08)*, pp. 129-134, March 2008.
- [13] A. Frotzsch, G. Fettweis, "Digital compensation of transmitter leakage in FDD zero-IF receivers," *Trans. Emerging Telecommun. Tech.*, vol. 23, no. 2, pp. 105-120, March 2012.
- [14] C. Lederer, and M. Huemer, "Simplified complex LMS algorithm for the cancellation of second-order TX intermodulation distortions in homodyne receivers," in *Proc. 45th Asilomar Conf. Signals, Syst. and Comput. (ASILOMAR)*, pp. 533-537, Nov. 2011.
- [15] M. Omer, R. Rimini, P. Heidmann, J. S. Kenney, "A compensation scheme to allow full duplex operation in the presence of highly nonlinear microwave components for 4G systems," in *Proc. IEEE MTT-S Int. Microwave Symp. Dig. (MTT)*, pp. 1-4, June 2011.
- [16] L. Anttila, M. Valkama, and M. Renfors, "Frequency-selective I/Q mismatch calibration for wideband direct-conversion transmitters," *IEEE Trans. Syst. II, Exp. Breifs*, vol. 55, no. 4, pp. 359-361, April 2008.
- [17] S. Haykin, *Adaptive Filter Theory*, 4th ed. Upper Saddle River, NJ: Prentice-Hall, 2002.

Publication 5

A. Kiayani, L. Anttila, and M. Valkama, "Digital Suppression of Power Amplifier Spurious Emissions at Receiver Band in FDD Transceivers," *IEEE Signal Processing Letters*, vol. 21, no. 1, pp. 69-73, Jan. 2014.

Copyright ©2014 IEEE. Reprinted, with permission, from IEEE Signal Processing Letters, vol. 21, no. 1, Jan. 2014.

In reference to IEEE copyrighted material which is used with permission in this thesis, the IEEE does not endorse any of Tampere University of Technology's products or services. Internal or personal use of this material is permitted. If interested in reprinting/republishing IEEE copyrighted material for advertising or promotional purposes or for creating new collective works for resale or redistribution, please go to http://www.ieee.org/publications_standards/publications/rights/rights_link.html to learn how to obtain a License from RightsLink.

Digital Suppression of Power Amplifier Spurious Emissions at Receiver Band in FDD Transceivers

Adnan Kiayani, *Student Member, IEEE*, Lauri Anttila, *Member, IEEE*, and Mikko Valkama, *Member, IEEE*

Abstract—As the duplexing distances in emerging wireless systems are getting more and more narrow, achieving sufficient isolation between transmit and receive chains using radio frequency (RF) filtering alone becomes increasingly complex. Particularly challenging problem in this context is the spectral regrowth of nonlinear power amplifiers (PAs) in the transmit chain, and other transmitter out-of-band (OOB) emissions, which can heavily desensitize the receiver chain. In this letter, we first carry out detailed modeling of transmitter OOB emissions due to practical wideband PAs with memory effects. Stemming from this modeling, and using the known digital transmit data inside the transceiver as reference, we then propose an efficient nonlinear digital cancellation technique to suppress the transmitter OOB emissions in the receiver path. The proposed technique is verified and analyzed using extensive computer simulations, rendering excellent suppression properties, hence enabling sufficient TX-RX isolation in frequency division duplexing (FDD) transceivers without any extra analog/RF filtering or PA linearization.

Index Terms—Cancellation, duplexer isolation, frequency-division duplexing, nonlinear distortion, out-of-band emission, power amplifier, transmitter leakage signal.

I. INTRODUCTION

THE next generation mobile communication systems are expected to provide high data rates to support multimedia and other broadband services. 3GPP Long-Term Evolution (LTE) and LTE-Advanced (LTE-A) systems are being optimized to support high data rates, low latency, multiantenna transmission, and flexible bandwidths and RF spectrum use [1]. LTE-A, Release 10, is introducing carrier aggregation (CA) which allows efficient use of spectrum and enables bandwidth expansion beyond 20 MHz by aggregating two or more component carriers, while maintaining backwards compatibility to Release 8/9 [2], [3]. While LTE and LTE-A system specifications support both frequency division duplexing (FDD) and time division duplexing (TDD), we focus in this article on FDD and associated RF and linearity challenges.

Concurrent transmission and reception in FDD systems is generally made possible by RF duplexer filters, which connect the transmitter and receiver to the same antenna such that the strong transmit signal cannot saturate the receiver. Due to increased pressure for efficient and flexible spectrum utilization,

future wireless systems such as LTE-A will have narrower duplexing gaps between the uplink and downlink bands (down to 15 MHz in some LTE-A bands [4]), therefore making it more difficult for the duplexer filter to achieve sufficient attenuation for the transmit signal. In such scenarios, the out-of-band (OOB) emissions induced by transmitter nonlinearities, such as the power amplifier (PA), may directly overlap the receiver band. These OOB emissions can potentially be of similar magnitude, or even higher, than the actual received signal when operating close to receiver sensitivity level, thus possibly leading to own receiver desensitization [6].

To demonstrate the desensitization phenomenon, consider LTE uplink band 25 [4] and assume intra-band CA with two carriers. In this scenario, the duplexing gap between 2nd TX carrier and RX is only 15MHz. The transmitter emissions are controlled by the Spurious Emission Limit which limits the emissions to maximum of -30dBm per 1MHz measurement bandwidth. Assuming an example figure of, say, $-35\text{dBm}/1\text{MHz}$ for the OOB emissions, being then further suppressed by the duplexer filter whose typical attenuation assumed in standardization is 50dB [6], the resulting OOB emissions at own receiver input are thus $-85\text{dBm}/1\text{MHz}$, or equivalently $-75\text{dBm}/10\text{MHz}$. Compared to the reference sensitivity level of -93.5dBm for 10MHz RX bandwidth [4], the TX OOB emission is significantly higher than the minimum received signal level (by $\sim 18.5\text{dB}$) and can completely block the received signal if operating close to the sensitivity level.

Classical solution to prevent own receiver desensitization is to improve the duplexer TX filtering. This is, however, costly and may not be feasible especially in devices with very small duplexing gap. An alternative fascinating idea is to suppress the spurious emissions using digital signal processing in the receiver path. Recently, a compensation technique for transmitter OOB emission at receiver band is proposed in [7] but the study is highly simplified by assuming that the duplexer filters responses are known and also a memoryless PA model is assumed, both of which limit the applicability of the reported algorithms to practical wideband transceiver scenarios with unknown duplexer responses and nonlinear PAs. In this article, we first carry out detailed modeling for the transmitter OOB emission at the receiver band due to practical nonlinear PAs with memory effects. With sophisticated nonlinear signal processing stemming from the modeling, and using the known digital TX data as the reference, a proper replica of OOB emission at the receiver band is regenerated and then subtracted from the received signal at digital baseband. The proposed formulation allows efficient estimation of the needed cancellation parameters, including the unknown duplexer response and unknown nonlinear PA with memory, and can thus be seen as a strong extension of [7]. Notice that transmitter

Manuscript received September 26, 2013; accepted November 07, 2013. Date of publication November 14, 2013; date of current version November 20, 2013. This work was supported by the Academy of Finland (under the project 251138 “Digitally-Enhanced RF for Cognitive Radio Devices”), the Finnish Funding Agency for Technology and Innovation (Tekes, under the project “Cross-Layer Modeling and Design of Energy-Aware Cognitive Radio Networks (CREAM)”), the Graduate School TISE, and the Austrian Center of Competence in Mechatronics (ACCM).

The authors are with the Department of Electronics and Communications Engineering, Tampere University of Technology, Tampere, FI-33101, Finland. (e-mail: adnan.kiayani@tut.fi, lauri.anttila@tut.fi, mikko.e.valkama@tut.fi)

Color versions of one or more of the figures in this paper are available online at <http://ieeexplore.ieee.org>.

Digital Object Identifier ...

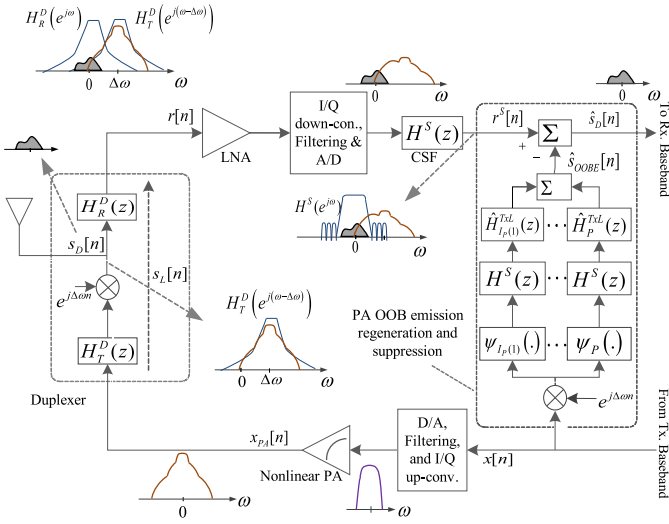


Fig. 1. Discrete-time baseband equivalent model and spectra of transmitter nonlinear PA induced OOB emission at receiver band in an FDD transceiver. The proposed OOB emission regeneration and suppression unit operating at digital baseband is also shown.

induced receiver interference is also considered in [8], [9], but focusing on the receiver related nonlinear distortion instead of transmitter out-of-band emissions at receiver band.

Notations: scalar parameters are represented by lower case letters a and vectors/matrices in boldface letters \mathbf{a} . We distinguish the vectors from matrices by a bold face letter with underline $\underline{\mathbf{a}}$. The convolution operator is indicated by \star . Superscripts $(\cdot)^T$ and $(\cdot)^H$ denote the transpose and hermitian transpose, respectively, while $(\cdot)^{-1}$ denotes matrix inverse.

II. SIGNAL MODELS FOR TX OOB EMISSION AT RECEIVER BAND IN FDD TRANSCEIVER

Fig. 1 shows the discrete-time baseband equivalent OOB emission model of an FDD transceiver and the associated signal spectra, with finite isolation in the duplexing filters and nonlinear transmitter PA. For analysis and modeling purposes, the frequency separation between the transmitter and receiver RF center-frequencies is denoted by $\Delta\omega$. The complex baseband signal to be transmitted is denoted by $x[n] = x_I[n] + jx_Q[n]$. This signal is up-converted to the transmitter carrier-frequency with an I/Q modulator and the modulated signal is then amplified by a PA for transmission. The PA is inherently a nonlinear device which exhibits memory effects for wideband signals. We use the parallel Hammerstein model with polynomial nonlinearities to express the nonlinearity of PA with memory effects, as it has been shown in the literature to have very good modeling capability for practical wideband PAs [10]. The baseband equivalent output of PA is therefore expressed as

$$x_{PA}[n] = \sum_{\substack{p=1 \\ p \text{ odd}}}^P f_p[n] \star \psi_p(x[n]) \quad (1)$$

where P denotes the polynomial order and the polynomial basis functions $\psi_p(x[n])$ are given by $\psi_p(x[n]) = x[n] |x[n]|^{p-1}$. In general, only odd-order distortions products appear in the vicinity of the desired received signal, thus only odd polynomial orders are considered in (1).

The PA output signal then passes through the duplexer to the antenna. A duplexer is constructed with two BPFs. In the transmitter path, the transmitter duplex filter suppresses the unwanted emissions outside the transmit band, especially the transmitter noise from PA present at the receiver frequency band, while the receiver duplex filter attenuates the transmitter passband signal leaking into the receiver chain. With finite attenuation of duplexing filters, the transmitter signal emissions are not completely suppressed from the receiver chain.

At receiver input, this transmitter leakage signal can now be mathematically expressed as

$$s_L[n] = (h^D[n] \star x_{PA}[n]) e^{j\Delta\omega n} \quad (2)$$

where $h^D[n] = e^{-j\Delta\omega n} h_R^D[n] \star h_T^D[n]$ denotes the total response of duplexer filters from TX-RX leakage perspective, and $h_T^D[n]$ and $h_R^D[n]$ are the baseband lowpass models of the bandpass TX and RX duplexer filters, respectively. Thus, the total signal at the input of the receiver chain consists of the actual weak desired received signal and the leaking transmitter signal. The baseband equivalent form for this total receiver input signal is then

$$r[n] = s_D[n] + s_L[n] + w[n] \quad (3)$$

where $s_D[n]$ is the desired received signal and $w[n]$ denotes the thermal noise. The signal is then downconverted from RF to baseband, followed by channel selection filter (CSF) which is denoted by $h^S[n]$. The baseband signal at the CSF output is given by

$$r^S[n] = h^S[n] \star r[n] = s_D[n] + s_{OOBE}[n] + w^S[n] \quad (4)$$

where $s_{OOBE}[n] = h^S[n] \star s_L[n]$ denotes the transmitter OOB emission interference directly on top of received baseband signal and $w^S[n] = h^S[n] \star w[n]$ is the filtered inband noise. As discussed already earlier, the transmitter duplexer filter may not have sufficient attenuation to push the OOB emission, shown above, below the thermal noise floor in the transceivers of next generation wireless systems such as LTE. Hence, in the following, we develop an efficient digital technique for dynamically regenerating and suppressing the RX band OOB emission signal inside the FDD transceiver.

III. DIGITAL ESTIMATION AND CANCELLATION OF TRANSMITTER OOB EMISSION

Stemming from previous modeling, we now develop an appropriate framework for transmitter-induced OOB emission regeneration and suppression, together with efficient LS parameter estimation supporting unknown duplex filter responses and unknown nonlinear PA with memory.

A. Linear-in-Parameters Model for TX OOB Emission

We first write the transmitter OOB emission term $s_{OOBE}[n]$ in (4) in its equivalent form as

$$s_{OOBE}[n] = h^S[n] \star \left(\sum_{\substack{p=1 \\ p \text{ odd}}}^P h^D(n) \star f_p[n] \star \psi_p(x[n]) \right) e^{j\Delta\omega n}. \quad (5)$$

In practice, only selected nonlinearity orders p are needed for the modeling and cancellation, depending on how the RX

band is located relative to the TX emissions. This is quantified with (6), which defines the minimum order PA intermodulation distortion affecting the RX band as

$$\rho = \left\lceil \frac{|f_{TX} - f_{RX}| - \frac{1}{2}(B_{TX} + B_{RX})}{B_{TX}} \right\rceil \quad (6)$$

where f_{TX} and f_{RX} are the RF center-frequencies of the transmit and receive signals, respectively, and B_{TX} and B_{RX} are the corresponding bandwidths. With given definition of ρ , the first $2\rho - 1$ terms of (5) are outside the desired RX signal band and thus not necessary to take into account in the modeling and cancellation. This leads to an alternative form of (5) written as

$$s_{OOBE}[n] = \sum_{p \in I_P} h^S[n] \star (h^D(n) \star f_p[n] \star \psi_p(x[n])) e^{j\Delta\omega n} \quad (7)$$

where $I_P = \{2\rho + 1, 2\rho + 3, \dots, P\}$. We next define the transmitter leakage channel, which refers to the composite linear responses of duplexer filters and PA, as $h_p^L[n] \triangleq (h^D[n] \star f_p[n]) e^{j\Delta\omega n}$, and the CSF filtered polynomial basis functions as $\psi_p^S(x[n]) \triangleq h^S[n] \star \psi_p(x[n] e^{j\Delta\omega n})$, which enable transforming (7) into

$$s_{OOBE}[n] = \sum_{p \in I_P} h_p^L[n] \star \psi_p^S(x[n]). \quad (8)$$

Now, with the model in (8), the digital OOB emission regeneration and cancellation algorithm requires only the coefficient estimates of $h_p^L[n]$, as digital transmit data and filtered basis functions are always known inside the device. The principal regeneration and cancellation structure, stemming from above, is also illustrated in Fig. 1.

B. LS Estimation of Transmitter Leakage Parameters

For parameter estimation purposes, we switch to vector matrix notation and write N samples of the total baseband received signal, with transmitter OOB emission included, as

$$\begin{aligned} \mathbf{r}^S &= \mathbf{s}_D + \mathbf{s}_{OOBE} + \mathbf{w}^S \\ &= \mathbf{s}_D + \mathbf{\Psi}_x^S \mathbf{h}^L + \mathbf{w}^S \end{aligned} \quad (9)$$

where $\mathbf{h}^L = [\mathbf{h}_{I_P(1)}^L, \mathbf{h}_{I_P(2)}^L, \dots, \mathbf{h}_{I_P}^L]^T$ is a vector of dimension $|I_P| \cdot N_L \times 1$, with $|I_P|$ denoting the cardinality of the set I_P , and N_L denotes the length of \mathbf{h}_p^L . Furthermore, $\mathbf{\Psi}_x^S$ is a matrix of the form $\mathbf{\Psi}_x^S = [\mathbf{\Psi}_{I_P(1)}^S(\mathbf{x}), \mathbf{\Psi}_{I_P(2)}^S(\mathbf{x}), \dots, \mathbf{\Psi}_P^S(\mathbf{x})]$ with $\mathbf{x} = [x_0 \ x_1 \ x_2 \ \dots \ x_{N-1}]^T$, and $\mathbf{\Psi}_p^S(\mathbf{x})$ is of dimension $(N + N_L - 1) \times N_L$ and is defined as

$$\mathbf{\Psi}_p^S(\mathbf{x}) = \begin{bmatrix} \psi_p^S(x_0) & 0 & \dots & 0 \\ \psi_p^S(x_1) & \psi_p^S(x_0) & \dots & 0 \\ \vdots & 0 & \dots & 0 \\ \psi_p^S(x_{N-1}) & \vdots & \ddots & \vdots \\ 0 & \psi_p^S(x_{N-1}) & \dots & \psi_p^S(x_{N-N_L}) \\ 0 & 0 & \dots & \psi_p^S(x_{N-N_L+1}) \\ \vdots & \vdots & \ddots & \vdots \\ 0 & 0 & \dots & \psi_p^S(x_{N-1}) \end{bmatrix}. \quad (10)$$

In order to estimate the transmitter leakage channel parameters, we re-write (9) now as

$$\mathbf{r}^S = \mathbf{\Psi}_x^S \mathbf{h}^L + \mathbf{w}_1 \quad (11)$$

where $\mathbf{w}_1 = \mathbf{s}_D + \mathbf{w}^S$. The LS parameter estimate of \mathbf{h}^L is then given directly by

$$\hat{\mathbf{h}}^L = (\mathbf{\Psi}_x^{S,H} \mathbf{\Psi}_x^S)^{-1} \mathbf{\Psi}_x^{S,H} \mathbf{r}^S. \quad (12)$$

These leakage channel parameter estimates are then used in the OOB emission regeneration and cancellation, as shown in Fig. 1.

IV. SIMULATION RESULTS

To evaluate the performance of the proposed estimation and cancellation scheme, we setup an FDD transceiver simulation chain according to Fig. 1 where the transmit and receive signals are modeled according to LTE mobile station 5MHz TX/RX mode. The transmit signal passes through the dynamic PA with memory, which is modeled as a Wiener system with a linear filter, whose impulse response is $\mathbf{h} = [1, 0.2, 0.34, 0.068, 0.0136, 0.0027, 0.0005]^T$, and the memoryless nonlinearity polynomial coefficients are calculated from PA gain, IIP3, and 1-dB compression point, which are 20dB, 17dBm, and 26dBm, respectively. The signal then goes through the duplexer filter which is modeled with 5-taps and has an average attenuation of 50dB at the RX band, containing also frequency-selectivity following typical commercial duplexer stopband responses. The duplexing spacing in the device is assumed to be small, only 1.5 times the channel width, to reflect a challenging scenario. The reference thermal noise power level at receiver input is assumed to be -104.5 dBm per 5MHz, RX noise figure (NF) is 4.5dB, and the reference sensitivity level is -95 dBm (minimum SNR ~ 5 dB). In the estimation phase, a block of 100k samples of filtered baseband received signal \mathbf{r}^S and the filtered basis function outputs $\mathbf{\Psi}_x^S$ (generated from frequency shifted baseband transmit data) is used for estimating the transmitter leakage channel parameters, which is modeled in the cancellation processing with 6-taps per nonlinearity order. The estimated parameters are then used to regenerate the interference and subtract it from the composite baseband received signal.

For illustration purposes, we first plot the OOB emission spectrum before and after the proposed nonlinear digital cancellation in Fig. 2, together with the actual received signal and noise floor. It can be observed that without suppression, the transmitter OOB emission is corrupting the receiver band substantially. However, the proposed technique is able to push the interference below the noise floor in the receiver band, especially when proper set of nonlinearity orders are used. Notice that there is still residual interference when only 3rd order canceller is considered, whereas taking into account also the 5th order nonlinearity effectively mitigates the interference. This is intuitive since the receiver band is containing both 3rd and 5th order intermodulation of the PA. To further quantify the performance of the proposed technique, the desired received signal-to-interference plus noise ratio (SINR) is evaluated against different TX power levels. The average SINR curves with different RX signal levels are depicted in Fig. 3, which shows that the higher transmission powers cause

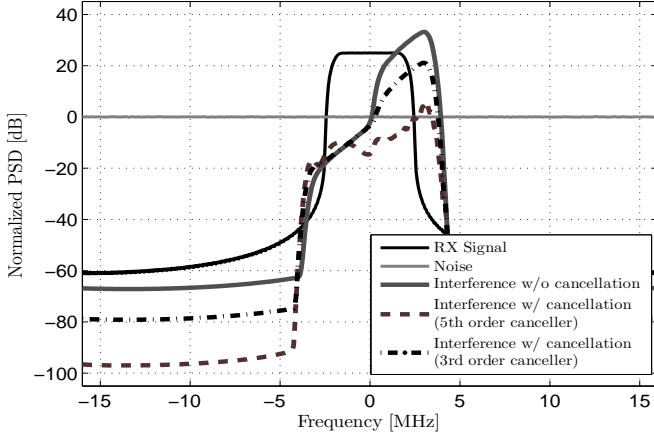


Fig. 2. Transmitter OOB emission before and after cancellation with 23dBm TX power. The RX signal is 20dB above the reference sensitivity level.

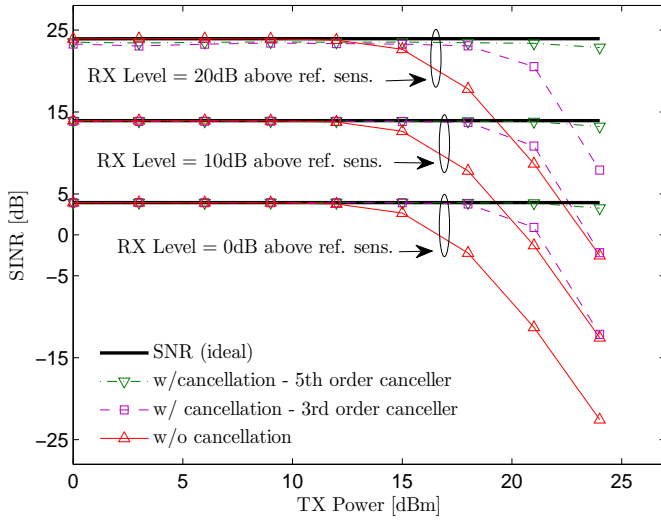


Fig. 3. Comparison of average SINR vs. TX power before and after cancellation with different RX signal strengths.

more powerful OOB emissions to the RX band and therefore degrades the receiver SINR. With practical 23dBm TX power, the difference between the interference-free SNR and the SINR with interference is about 26dB, whereas this difference becomes less than 1dB when the cancellation technique is employed. It is also noted that the proposed technique is able to efficiently estimate the transmitter leakage filters even in the presence of a strong RX signal. The final example simulates the SINR versus different received signal powers with different estimator sample lengths. The average SINR curves are plotted in Fig. 4, which reveal that increasing the RX power level starts eventually degrading the cancellation performance, but this can be alleviated by increasing the estimation block size. On the other hand, for achieving typical SINR between 10 – 20dB, a block of 10k samples is already enough. Furthermore, note that without interference cancellation, reliable reception can only be guaranteed if the desired received signal is at least 30dB or so above the reference sensitivity level which, in practice, is very rare. Thus, the effectiveness of proposed cancellation technique is evident and indisputable.

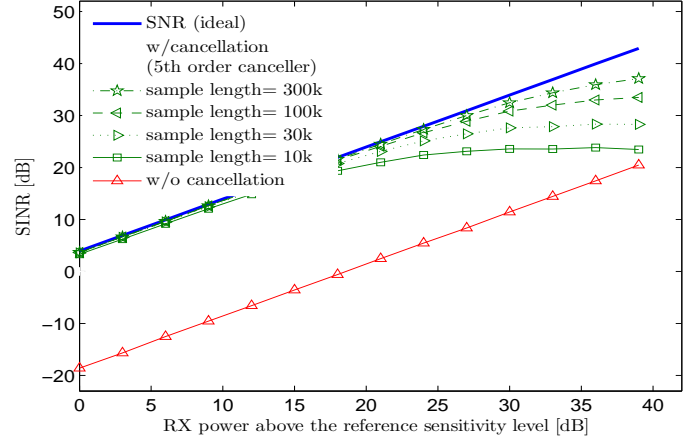


Fig. 4. Average SINR vs. RX power above the reference sensitivity level with different sample blocks lengths. The TX signal power is 23dBm.

V. CONCLUSION

This article addressed the issue of transmitter spurious emissions at receiver band due to a dynamic PA with memory effects in an FDD transceiver. Especially with small duplex gaps, practical PAs and practical duplexers, these emissions can easily result to own receiver desensitization. The paper proposed a nonlinear estimation and regeneration procedure to reproduce the essential transmitter OOB emission signal, at own receiver digital baseband, enabling its efficient cancellation without additional RF filtering. The proposed technique can operate under unknown frequency-selective duplexer responses and unknown nonlinear PAs with memory, and was evaluated with computer simulations demonstrating that the OOB emissions can be efficiently suppressed below the noise floor. Future work will focus on a prototype implementation to demonstrate the suppression properties of the proposed algorithms with real RF duplexers and PAs and also on analyzing the impact of TX leakage signal induced RX nonlinearities.

REFERENCES

- [1] S. Sesia, I. Toufik, and M. Baker, *LTE-The UMTS Long Term Evolution, From Theory to Practice*, Chichester, West Sussex, John Wiley & Sons Ltd., 2008.
- [2] M. Iwamura *et al.*, “Carrier aggregation framework in 3GPP LTE-advanced”, *IEEE Commun. Mag.*, vol. 48, no. 8, pp. 60-67, August 2010.
- [3] K. I. Pedersen *et al.*, “Carrier aggregation for LTE-advanced: functionality and performance aspects”, *IEEE Commun. Mag.*, vol. 49, no. 6, pp. 89-95, June 2011.
- [4] *3GPP Spec. LTE; Evolved Universal Terrestrial Radio Access (E-UTRA); User Equipment (UE) radio transmission and reception (3GPP TS 36.101 version 11.2.0 Release 11)*, Nov. 2012.
- [5] V. Lehtinen *et al.*, “Gating factor analysis of maximum power reduction in multicarrier LTE-A uplink transmission”, in *Proc. IEEE Radio and Wireless Symposium (RWS'13)*, Austin, TX, Jan. 2013.
- [6] Ericsson and ST-Ericsson, *R4-126964, REFSENS with one UL carrier for NC intra-band CA*, [WWW], available http://www.3gpp.org/ftp/tsg_ran/wg4_radio/TSGR4_65/Docs/, referenced 01.07.2013.
- [7] M. Omer *et al.*, “A compensation scheme to allow full duplex operation in the presence of highly nonlinear microwave components for 4G systems,” in *Proc. IEEE MTT-S Int. Microwave Symp. Dig.*, June 2011.
- [8] A. Frotzschner and G. Fettweis, “Digital compensation of transmitter leakage in FDD zero-IF receivers,” *Trans. Emerging Telecommun. Tech.*, vol. 23, no. 2, pp. 105-120, March 2012.
- [9] C. Lederer and M. Huemer, “Simplified complex LMS algorithm for the cancellation of second-order TX intermodulation distortions in homodyne receivers,” in *Proc. 45th Asilomar Conf. Signals, Syst. and Comput. (ASILOMAR)*, pp. 533-537, Nov. 2011.
- [10] M. Isaksson, D. Wisell, and D. Rönnow, “A comparative analysis of behavioral models for RF power amplifiers,” *IEEE Trans. Microw. Theory Tech.*, vol. 54, no. 1, pp. 348-359, Jan. 2006.

Publication 6

A. Kiayani, M. Abdelaziz, L. Anttila, V. Lehtinen, and M. Valkama, “DSP-Based Suppression of Spurious Emissions at RX Band in Carrier Aggregation FDD Transceivers,” in *Proceedings of 22nd European Signal Processing Conference (EUSIPCO 2014)*, pp. 591-595, Sept. 2014.

Copyright ©2014 IEEE. Reprinted, with permission, from the proceedings of 22nd European Signal Processing Conference.

In reference to IEEE copyrighted material which is used with permission in this thesis, the IEEE does not endorse any of Tampere University of Technology's products or services. Internal or personal use of this material is permitted. If interested in reprinting/republishing IEEE copyrighted material for advertising or promotional purposes or for creating new collective works for resale or redistribution, please go to http://www.ieee.org/publications_standards/publications/rights/rights_link.html to learn how to obtain a License from RightsLink

DSP-BASED SUPPRESSION OF SPURIOUS EMISSIONS AT RX BAND IN CARRIER AGGREGATION FDD TRANSCEIVERS

Adnan Kiayani, Mahmoud Abdelaziz, Lauri Anttila, Vesa Lehtinen and Mikko Valkama

Department of Electronics and Communications Engineering,
Tampere University of Technology, FI-33101, Tampere, Finland.
contact email: mikko.e.valkama@tut.fi

ABSTRACT

In frequency division duplex transceivers employing non-contiguous carrier aggregation (CA) transmission, achieving sufficient isolation between transmit and receive chains using radio frequency filtering alone is increasingly difficult. Particularly challenging problem in this context is spurious intermodulation (IM) components due to nonlinear power amplifier (PA), which may easily overlap the receiver band. With realistic duplex filters, the residual spurious IM at RX band can be several dBs stronger than the thermal noise floor, leading to own receiver desensitization. In this paper, we carry out detailed signal modeling of spurious emissions due to wideband PAs at the third-order IM band. Stemming from this modeling, and using the known transmit data, we present an efficient nonlinear digital identification and cancellation technique to suppress the unwanted IM components at RX band. The proposed technique is verified with computer simulations, showing excellent calibration properties, hence relaxing filtering and duplexing distance requirements in spectrally-agile CA transceivers.

Index Terms— Cancellation, carrier aggregation, duplexer isolation, frequency division duplexing, intermodulation, LTE-Advanced, power amplifier, spurious emissions.

1. INTRODUCTION

In order to cope with the ever increasing demands of mobile users for multimedia and other broadband services, the 3rd Generation Partnership Project (3GPP) in its Release 10 Long Term Evolution-Advanced (LTE-A) standard has introduced Carrier Aggregation (CA) [1], which enables scalable bandwidth expansion beyond 20 MHz by aggregating two or more component carriers (CCs). Besides spectral efficiency and offering data rates of up to 1 Gbps in downlink and 500 Mbps in uplink, other key features of LTE-A include flexible bandwidths, low latency, multi-antenna transmission, and backward compatibility to Release 8/9 [2]. While CA is supported

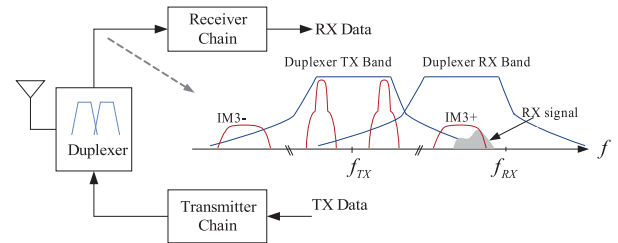


Fig. 1. Illustration of TX induced spurious IM3 emissions at RX band with non-contiguous TX carriers.

by both Frequency Division Duplex (FDD) and Time Division Duplex (TDD) modes of LTE-A, in this article we concentrate on the linearity challenges in CA FDD transceivers and suppression of spurious IM3 emissions at own receiver band.

In mobile radio transceivers operating in FDD mode, a duplexer filter is employed to facilitate simultaneous transmission and reception with a single antenna, while also providing isolation between the TX and RX chains. When emphasizing power efficiency and flexible spectrum use, strong intermodulation distortion (IM) products of the transmit signal, created by a nonlinear power amplifier (PA), result in spurious emissions that may appear in the RX band. This is illustrated in Fig. 1, where positive IM3 components lie at own RX band. Due to finite duplexer filter attenuation [4] and considerably narrow duplexing gaps in systems such as LTE-A, the remaining spurious emissions at the duplexer output at the RX band can potentially be of similar magnitude or even higher than the actual received signal. This can thus lead to own receiver desensitization. To demonstrate the own receiver desensitization phenomenon, consider LTE uplink band 25 [3] and assume intra-band CA with two carriers where duplexing gap is only 15 MHz. Assuming that the unwanted emissions at PA output, prior to duplexer, can in general be up to -30dBm/1MHz [3] (general spurious emission limit), and that duplexer isolation towards receiver at RX band is typically 50 – 60 dB [4], the unwanted emission at RX input can thus be in the order of $-80 \dots -90\text{dBm/1MHz}$. Compared to the effective thermal noise power with nominal 9dB UE RX noise figure, namely $-174 + 60 + 9 = -105\text{dBm/1MHz}$, this

This work was supported by the Academy of Finland (under the project 251138 “Digitally-Enhanced RF for Cognitive Radio Devices”), the Finnish Funding Agency for Technology and Innovation (Tekes, under the project “Cross-Layer Modeling and Design of Energy-Aware Cognitive Radio Networks (CREAM)”), the Linz Center of Mechatronics (LCM) in the framework of the Austrian COMET-K2 programme, and the TUT graduate school.

is substantial interference and can completely block the receiver. Notice also that the general coexistence related emission limit of $-50\text{dBm}/1\text{MHz}$ [3], applicable also at own RX band, is measured at antenna connector, and is thus totally insufficient to protect own RX.

Classical solutions to prevent own receiver desensitization in CA FDD transceivers are to either improve the duplexer TX filtering or to increase the duplex distance. Improving the duplexer filtering is, however, costly and may not be feasible for compact mobile transceivers supporting wider bandwidths and carrier frequencies with small duplexing distance. Alternative solutions using signal processing techniques to suppress the transmitter emissions in the receiver path are proposed in [7], [8] for FDD transceivers. These approaches create a replica of the emitted interference and then use it to suppress the interfering emissions at digital baseband. While [7] assumes known duplexer filter responses and memoryless PA model, the technique presented in [8] estimates the so called *transmitter leakage channel*, which is the collective response of duplexer filters and PA with memory. From the CA perspective, and especially non-contiguous CA transmission, where the total frequency span of the transmit signal can be in the order of 100 MHz or even beyond, these techniques are computationally challenging as they require digital processing of the whole transmission band and do not take the specific frequency-domain structure of the aggregated carriers into account. In contrast to this, we focus in this paper on lower-complexity solution particularly tailored to generic non-contiguous dual-carrier CA transmission scenario where unwanted IM3 spurious emissions desensitize the own receiver. Novel formulation for essential response identification and spurious emission regeneration and cancellation at digital baseband is developed, supporting unknown frequency-selective duplexer response and nonlinear PA with memory. The proposed solution can efficiently prevent own receiver desensitization, and can be seen as a novel extension of the authors' earlier work in [8].

Notations: scalar parameters are represented by lower case letters a and vectors/matrices in boldface letters \mathbf{a} . We distinguish the vectors from matrices by a bold face letter with under-line $\underline{\mathbf{a}}$. The convolution operator is indicated by \star . Superscripts $(\cdot)^T$ and $(\cdot)^H$ denote the transpose and hermitian transpose, respectively, while $(\cdot)^{-1}$ denotes matrix inverse.

2. SIGNAL MODELING FOR TX SPURIOUS EMISSIONS AT RX BAND IN CA FDD TRANSCEIVERS

In a CA FDD transceiver context with small duplexing distance and finite isolation duplexer filter, we consider a scenario where the IM3 band of the transmit signal overlaps with, and therefore creates significant interference, at the RX band. The relative strength of such interference depends in general on the duplexing distance, duplexer filter attenuation, transmit signal strength, and PA characteristics, and is elaborated in more details below.

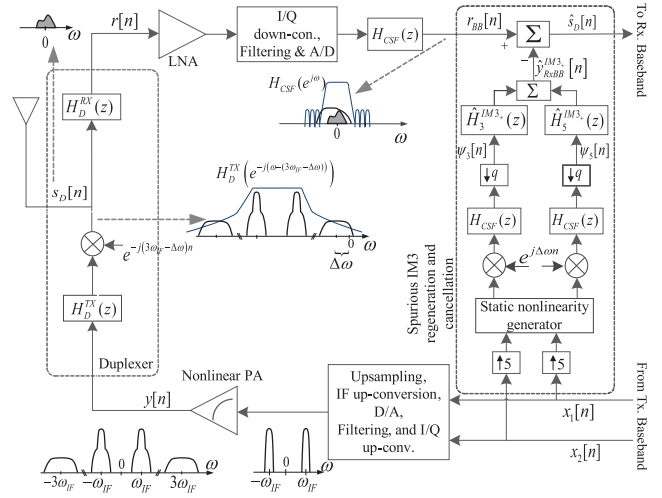


Fig. 2. Discrete-time baseband equivalent model and spectra of nonlinear transmit PA induced spurious emission at receiver band in an CA FDD transceiver. The proposed spurious IM3 emission regeneration and suppression unit operating at digital baseband is also shown, with 3rd and 5th order cancellation units.

In this paper, we assume a general non-contiguous dual-carrier CA FDD transceiver, for which the composite complex baseband/IF transmit signal, denoted by $x[n]$, is composed of two CCs that are separated by $2\omega_{IF}$. The IM3 distortion component, arising primarily due to the nonlinearity of PA and located at three times the IF frequency, may then lie at the RX band. For analysis and modeling purposes, the frequency separation between the center frequencies of the IM3 component and the desired RX signal is denoted by $\Delta\omega$. Fig. 2 shows the discrete-time baseband equivalent model of such scenario and the associated signal spectra, with finite isolation duplexer filters and nonlinear transmitter PA.

In the TX chain, the composite dual-carrier baseband signal is up-converted to the transmitter carrier frequency and the RF signal is then amplified by a PA for transmission. Practical PAs have inherently a nonlinear response and exhibit memory effects for wideband signals. Among numerous models that exist for PAs with memory, we use here the parallel Hammerstein model with polynomial nonlinearities to express the nonlinearity of PA with memory effects, as it has been shown in literature to have very good modeling capabilities for wideband PAs [6]. The baseband equivalent PA input and output are then expressed as

$$x[n] = x_1[n]e^{j\omega_{IF}n} + x_2[n]e^{-j\omega_{IF}n} \quad (1)$$

$$y[n] = \sum_{\substack{p=1 \\ p \text{ odd}}}^P f_p[n] \star (x[n]|x[n]|^{p-1}) \quad (2)$$

where $x_1[n]$ and $x_2[n]$ denote the baseband component carrier waveforms and P denotes the polynomial order. Substituting (1) in (2), the baseband equivalent positive and negative IM3

components, located at $3\omega_{IF}$ and $-3\omega_{IF}$ respectively in the composite signal, read

$$y^{IM3+}[n] = f_3^{IM3+}[n] \star x_1^2[n]x_2^*[n] + 3f_5^{IM3+}[n] \star x_1^2[n]x_2^*[n]|x_2[n]|^2 + 2f_5^{IM3+}[n] \star x_1^2[n]x_2^*[n]|x_1[n]|^2 \quad (3)$$

$$y^{IM3-}[n] = f_3^{IM3-}[n] \star x_1^*[n]x_2^2[n] + 3f_5^{IM3-}[n] \star x_1^*[n]x_2^2[n]|x_2[n]|^2 + 2f_5^{IM3-}[n] \star x_1^*[n]x_2^2[n]|x_1[n]|^2 \quad (4)$$

where nonlinearity orders up to $P = 5$ are considered, and $f_3^{IM3\pm}[n]$; $f_5^{IM3\pm}[n]$ are the corresponding baseband equivalent filters modeling the PA's frequency-responses for 3^{rd} and 5^{th} order nonlinearities at positive and negative IM3 bands, respectively, defined as $f_3^{IM3\pm}[n] = h_{LPF}[n] \star (f_3[n]e^{\mp j3\omega_{IF}n})$; $f_5^{IM3\pm}[n] = h_{LPF}[n] \star (f_5[n]e^{\mp j3\omega_{IF}n})$. For simplicity, we assume below that the positive IM3 term $y^{IM3+}[n]$ appears at the RX operating band and thus focus on its further modeling and cancellation.

The PA output signal then passes through the duplexer to the antenna. A duplexer is constructed with two band pass filters. In the transmitter path, the transmitter duplex filter tries to attenuate the unwanted emissions outside the transmit band, especially the transmitter noise from PA present at the receiver frequency band. The receiver duplex filter then attenuates the transmitter passband signal leaking into the receiver chain. With finite attenuation of duplexing filters, transmitter spurious emissions are not completely suppressed and thus cause self-interference at RX band.

At the receiver input, the baseband equivalent positive IM3 component leaking into the RX band after passing through the cascade of transmitter and receiver duplexer filters can be mathematically expressed as

$$y_{leak}^{IM3+}[n] = h_D[n] \star (y^{IM3+}[n]e^{j\Delta\omega n}). \quad (5)$$

The cumulative duplexer filter response from TX-RX leakage perspective, denoted by $h_D[n]$ in the above equation, is defined as

$$h_D[n] = h_D^{RX}[n] \star (h_D^{TX}[n]e^{-j(3\omega_{IF}-\Delta\omega)n}) \quad (6)$$

where $h_D^{TX}[n]$; $h_D^{RX}[n]$ represent the baseband equivalent lowpass models of the bandpass TX and RX duplexer filters, respectively. In addition to the transmitter spurious emissions, the desired received signal, denoted by $s_D[n]$, and the thermal noise, denoted by $w[n]$, are also present. Thus, the baseband equivalent composite received signal at the receiver input is

$$r[n] = s_D[n] + y_{leak}^{IM3+}[n] + w[n]. \quad (7)$$

This signal is subsequently down-converted from RF to baseband by the receiver local oscillator (LO), followed by the channel selection filtering (CSF), denoted here by $h_{CSF}[n]$. The baseband signal at the CSF output is then given by

$$r_{BB}[n] = h_{CSF}[n] \star r[n] = s_D[n] + y_{RxBB}^{IM3+}[n] + w_{BB}[n] \quad (8)$$

where $y_{RxBB}^{IM3+}[n] \triangleq h_{CSF}[n] \star y_{leak}^{IM3+}[n]$ denotes the unwanted spurious IM3 in the RX baseband and $w_{BB}[n] = h_{CSF} \star w[n]$ is the filtered inband noise.

As discussed already earlier, the transmitter duplexer filter may not have sufficient attenuation to push the transmitter spurious emissions below the thermal noise floor in the transceivers of next generation wireless systems such as LTE-A. Hence, in the following, we develop an efficient digital technique for dynamically regenerating the spurious IM3 component at the RX band and then subsequently suppressing it inside the FDD transceiver.

3. PROPOSED SPURIOUS IM3 REGENERATION AND CANCELLATION

Stemming from previous modeling, we now address the regeneration of positive spurious IM3 emission and its cancellation. The proposed framework appropriately estimates the *effective IM3 channel*, a cascade of unknown duplexer filter responses and the unknown nonlinear PA with memory at positive IM3 band. The estimated effective IM3 channel filters together with the known transmit data are used to create a replica of transmitter spurious emission at IM3 band.

3.1. Linear-in-Parameters Model of Spurious IM3

We first write the spurious IM3 emission term $y_{RxBB}^{IM3+}[n]$ in (8) in its equivalent form as

$$\begin{aligned} y_{RxBB}^{IM3+}[n] &= h_{CSF}[n] \star y_{leak}^{IM3+}[n] \\ &= h_3^{IM3+}[n] \star \psi_3[n] + h_5^{IM3+}[n] \star \psi_5[n] \end{aligned} \quad (9)$$

where $h_p^{IM3+}[n]$, $p = 3, 5$ denote the effective IM3 channels, with subscript p representing the 3^{rd} and 5^{th} order PA nonlinearity filters, defined as

$$\begin{aligned} h_3^{IM3+}[n] &\triangleq e^{j\Delta\omega n} (h_D[n] \star f_3^{IM3+}[n]) \\ h_5^{IM3+}[n] &\triangleq e^{j\Delta\omega n} (h_D[n] \star f_5^{IM3+}[n]), \end{aligned} \quad (10)$$

and the known component carrier baseband waveforms, duplexing distance, and CSF filter response are combined together to form the *modified filtered basis functions*, defined below as

$$\begin{aligned} \psi_3[n] &\triangleq h_{CSF}[n] \star (x_1^2[n]x_2^*[n])e^{j\Delta\omega n} \\ \psi_5[n] &\triangleq h_{CSF}[n] \star \left(\frac{3x_1^2[n]x_2^*[n]|x_2[n]|^2 + 2x_1^2[n]x_2^*[n]|x_1[n]|^2}{2} \right) e^{j\Delta\omega n}. \end{aligned} \quad (11)$$

With the linear-in-parameters model at last row of (9), the proposed IM3 regeneration and cancellation algorithm requires only estimation of the coefficients of effective IM3 channel filters $h_p^{IM3+}[n]$, as other parameters such as the duplexing distance, digital transmit data, and the CSF filter response are known inside the transceiver. The principal regeneration and cancellation structure, stemming from above formulation, is also illustrated in Fig.2. Notice that the sample rate in the

modified filtered basis functions generation is only relative to bandwidths of the individual component carriers instead of the total aggregate bandwidth as in [8]. Furthermore, the cancellation is performed at the sample rate of the receiver chain.

3.2. LS Estimation of Effective IM3 Channel Filters

For parameter estimation of effective IM3 channels, we switch to vector-matrix notations and consider N -samples of each CC. By modeling both nonlinearity orders with N_h -taps, the effective IM3 channel filter vector is then of dimension $2N_h \times 1$. The spurious IM3 term in (9) then takes the form

$$\begin{aligned} \mathbf{y}_{RxBB}^{IM3+} &= \mathbf{\Psi}_3 \mathbf{h}_3^{IM3+} + \mathbf{\Psi}_5 \mathbf{h}_5^{IM3+} = [\mathbf{\Psi}_3 \quad \mathbf{\Psi}_5] \begin{bmatrix} \mathbf{h}_3^{IM3+} \\ \mathbf{h}_5^{IM3+} \end{bmatrix} \\ &= \mathbf{\Psi} \mathbf{h}^{IM3+} \end{aligned} \quad (12)$$

where $\mathbf{\Psi}_p, p = 3, 5$, in $\mathbf{\Psi}$ is a matrix of dimension $(N + N_h - 1) \times N_h$, defined as

$$\mathbf{\Psi}_p = \begin{bmatrix} \psi_p[0] & 0 & \cdots & 0 \\ \psi_p[1] & \psi_p[0] & \cdots & 0 \\ \vdots & 0 & \cdots & 0 \\ \psi_p[N-1] & \vdots & \ddots & \vdots \\ 0 & \psi_p[N-1] & \cdots & \psi_p[N-N_h] \\ 0 & 0 & \cdots & \psi_p[N-N_h+1] \\ \vdots & \vdots & \ddots & \vdots \\ 0 & 0 & \cdots & \psi_p[N-1] \end{bmatrix}. \quad (13)$$

The total baseband received signal then becomes

$$\mathbf{r}_{BB} = \mathbf{s}_D + \mathbf{\Psi} \mathbf{h}^{IM3+} + \mathbf{w}_{BB}. \quad (14)$$

Now, to estimate the effective IM3 channel parameters, we re-write (14) as

$$\mathbf{r}_{BB} = \mathbf{\Psi} \mathbf{h}^{IM3+} + \mathbf{w}_1 \quad (15)$$

where $\mathbf{w}_1 = \mathbf{s}_D + \mathbf{w}_{BB}$. The LS parameter estimate of \mathbf{h}^{IM3+} is then given directly by [9]

$$\hat{\mathbf{h}}^{IM3+} = (\mathbf{\Psi}^H \mathbf{\Psi})^{-1} \mathbf{\Psi}^H \mathbf{r}_{BB}. \quad (16)$$

Finally, the estimates of effective IM3 channel filters are then used in the spurious IM3 emission regeneration and cancellation, as shown in Fig. 2.

4. SIMULATION RESULTS

In this section, we demonstrate the effectiveness of the proposed estimation and cancellation algorithm in a dual-carrier CA FDD transceiver. The simulation chain is set up according to Fig. 2, where the baseband transmit signal is a dual-carrier LTE-A uplink SC-FDMA signal. Each CC is allocated 50 resource blocks (RBs) that are separated by 50

MHz, and subcarrier modulation is QPSK. In the transmitter chain, PA with memory is modeled as a 5th order Wiener system with a linear filter, whose impulse response is $\mathbf{h}_{wiener} = [1 \ 0.2 \ 0.34 \ 0.068 \ 0.0136 \ 0.0027 \ 0.0005]^T$, and the memoryless nonlinearity coefficients are calculated from PA gain, IIP3, and 1-dB compression point, which are 20 dB, 17 dBm, and 26 dBm, respectively. The mismatch between actual and assumed PA model is to mimic a practical scenario. The duplexer filter is modeled to have an average attenuation of 50 dB at the IM3 band, containing also frequency selectivity. We assume that the frequency separation between the center frequencies of positive IM3 component and the desired RX signal is $\Delta f = 2$ MHz. The RX signal is an LTE-A downlink OFDM(A) signal with 50 RBs, QPSK subcarrier modulation. The reference thermal noise power level at receiver input is assumed to be -104 dBm per 10 MHz bandwidth, RX noise figure (NF) is 4.5 dB, and the reference sensitivity level is -93.5 dBm. For the estimation and cancellation processing, we use sampling frequency $f_s = 30.72$ MHz which is only 2 times the nominal baseband sampling frequency of the individual TX and RX carriers. A block of 50 k samples of filtered baseband received signal \mathbf{r}_{BB} and the modified filtered basis function $\mathbf{\Psi}$ are used for estimating the effective IM3 channel parameters, which is modeled with 16-taps ($N_h = 8$). The estimated filter parameters are used to regenerate the interfering IM3 component which is then subtracted from the composite baseband received signal.

In Fig. 3, we plot the essential power spectra before and after the proposed digital cancellation. The actual received signal and noise, both of which are ON during the parameter estimation, are also shown in the figure. It can be observed that with small duplexing distance and finite duplexer isolation, the strong spurious IM3 completely masks the received signal and corrupts the reception heavily. However, the proposed technique is able to push this undesired self-interference below the thermal noise floor in the receiver band when a proper set of nonlinear filters is used. It is interesting to note that considering only the third order PA nonlinearity already gives substantial improvement in performance but there is still some residual interference left in the RX signal band. Whereas, taking into account also the fifth order PA nonlinearity at IM3 band effectively mitigates the total interference.

To further quantify the performance, the desired received signal-to-interference plus noise ratio (SINR) is evaluated against different TX power levels. The SINR curves with different RX signal levels are depicted in Fig. 4. The results indicate that for transmit power levels less than 12 dB, the power of interfering spurious IM3 at the receiver band is negligibly small and does not deteriorate SINR. However, higher transmission levels generate more powerful spurious IM3 component which consequently degrades the receiver SINR. Nevertheless, the proposed technique is able to reduce the interference and to enhance SINR. With practical 23 dBm

TX power, the difference between interference free SNR and SINR with interference is about 30 dB. This difference reduces to less than 1 dB when the cancellation technique is employed. Furthermore, note that for TX powers > 21 dB, both 3rd and 5th order PA nonlinearities should be considered in the estimation and regeneration to effectively remove the interference. The simulation example further demonstrates that the proposed technique is able to efficiently estimate the IM3 leakage filters even in the presence of strong RX signal. Thus, the effectiveness of proposed solution is evident.

5. CONCLUSION

This paper addressed the problem of spurious IM3 emissions at receiver band in CA FDD transceivers. More specifically, the combination of small duplex gaps, practical PAs exhibiting memory effects, and practical duplexers with limited isolation may result in significant spurious emissions falling at the RX band and can easily lead to own receiver desensitization. A nonlinear estimation and regeneration procedure was proposed, where first the unknown duplexer response and unknown nonlinear PA with memory response at IM3 band are estimated, and then used to reproduce and suppress the unwanted spurious IM3 components at own receiver digital baseband. This enables efficient mitigation of spurious IM3 emissions hence relaxing duplex distance and duplexer filtering requirements and thereby increasing the flexibility of the transceiver. The proposed technique was evaluated with computer simulations showing that spurious emissions can be effectively suppressed below the noise floor. Future work will focus on a prototype implementation and RF measurements to demonstrate the suppression properties of the proposed algorithms with real RF duplexers and PAs.

REFERENCES

- [1] M. Iwamura *et al.*, "Carrier aggregation framework in 3GPP LTE-advanced", *IEEE Commun. Mag.*, vol. 48, no. 8, pp. 60-67, August 2010.
- [2] S. Sesia, I. Toufik, and M. Baker, *LTE-The UMTS Long Term Evolution, From Theory to Practice*, Chichester, West Sussex, John Wiley & Sons Ltd., 2008.
- [3] 3GPP "TS 36.101: Evolved Universal Terrestrial Radio Access (E-UTRA); User Equipment (UE) radio transmission and reception", Release 11, Nov. 2012.
- [4] Ericsson and ST-Ericsson, *R4-126964, REFSENS with one UL carrier for NC intra-band CA*.
- [5] "Evolved Universal Terrestrial Radio Access (E-UTRA); Radio Frequency (RF) system scenarios", 3GPP Tech. Report v. 10.2.0, Release 10, TR 36.942, May 2011.
- [6] M. Isaksson, D. Wisell, and D. Rönnow, "A comparative analysis of behavioral models for RF power amplifiers," *IEEE Trans. Microw. Theory Tech.*, vol. 54, no. 1, pp. 348359, Jan. 2006.
- [7] M. Omer *et al.*, "A compensation scheme to allow full duplex operation in the presence of highly nonlinear microwave components for 4G systems," in *Proc. IEEE MTT-S Int. Microwave Symp. Dig.*, June 2011.
- [8] A. Kiayani, L. Anttila, and M. Valkama, "Digital suppression of power amplifier spurious emissions at receiver band in FDD transceivers," *IEEE Signal Processing Letters*, vol. 21, no. 1, pp. 69-73, Jan. 2014.
- [9] S. Haykin, *Adaptive Filter Theory*, 4th ed. Upper Saddle River, NJ: Prentice-Hall, 2002.

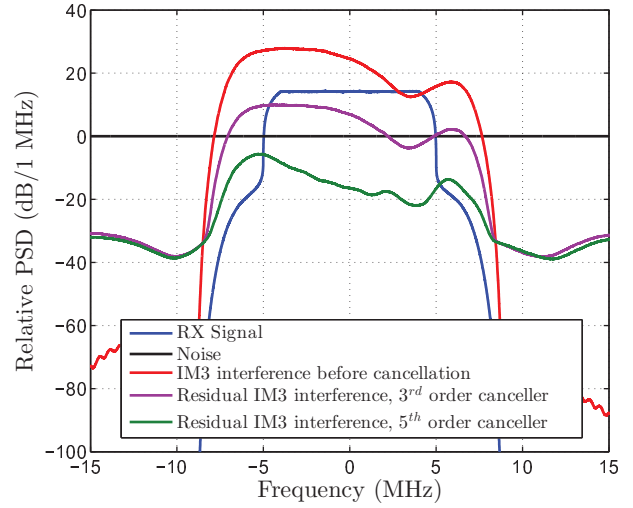


Fig. 3. Spurious IM3 emission at RX band before and after cancellation with 23 dBm TX Power and 5th-order Wiener PA. The RX signal is 10 dB above the REFSENS level. PSDs are normalized to the noise power.

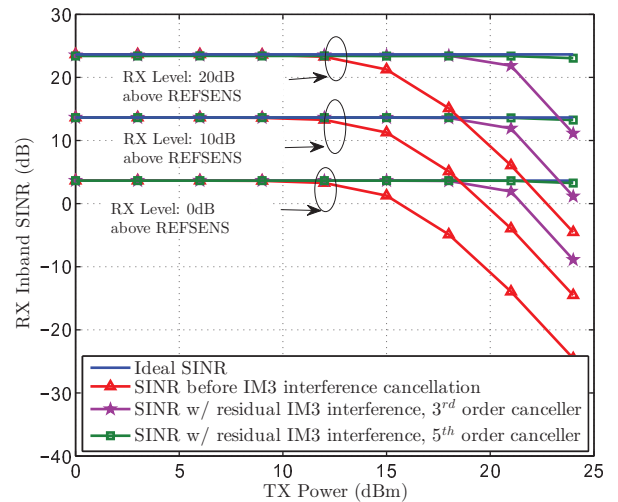


Fig. 4. Comparison of average SINR vs. TX power before and after cancellation with different RX signal strengths.

Publication 7

A. Kiayani, L. Anttila, Y. Zou, and M. Valkama, "Channel Estimation and Equalization in Multi-User Uplink OFDMA and SC-FDMA Systems Under Transmitter RF Impairments," *IEEE Transactions on Vehicular Technology*, DOI: 10.1109/TVT.2015.2397277, 2015.

Copyright ©2015 IEEE. Reprinted, with permission, from Transactions on Vehicular Technology, 2015.

In reference to IEEE copyrighted material which is used with permission in this thesis, the IEEE does not endorse any of Tampere University of Technology's products or services. Internal or personal use of this material is permitted. If interested in reprinting/republishing IEEE copyrighted material for advertising or promotional purposes or for creating new collective works for resale or redistribution, please go to http://www.ieee.org/publications_standards/publications/rights/rights_link.html to learn how to obtain a License from RightsLink.

Channel Estimation and Equalization in Multi-User Uplink OFDMA and SC-FDMA Systems Under Transmitter RF Impairments

Adnan Kiayani, *Student Member, IEEE*, Lauri Anttila, *Member, IEEE*, Yaning Zou, *Member, IEEE*,
and Mikko Valkama, *Member, IEEE*

Abstract—Single-carrier frequency division multiple access (SC-FDMA), a modified form of orthogonal frequency division multiple access (OFDMA), has been adopted as the uplink physical layer radio access technique for the 3GPP Long Term Evolution (LTE) and LTE-Advanced. Radio transceiver implementations for such OFDM-based systems with the direct-conversion architecture are desirable to enable small size, low-cost and low power consumption terminals. However, the associated circuit impairments stemming from the processing of analog radio frequency (RF) signals, such as in-phase and quadrature phase (I/Q) imbalance and carrier frequency offset (CFO) errors, can severely degrade the obtainable link performance. In this paper, we analyze the effects of these radio impairments in multi-user SC-FDMA uplink system, and present digital signal processing (DSP)-based methods for the joint estimation and equalization of impairments and channel distortions on the receiver side with arbitrary number of receiver antennas. For the equalization, linear equalizers such as the zero-forcing (ZF) and the minimum mean-square error (MMSE) equalizers that utilize pairs of mirror subcarriers are formulated, and the MMSE equalizer is developed to effectively handle mirror sub-band users with different power levels. Furthermore, for reduced computational complexity, the joint channel and impairments filter responses are efficiently approximated with polynomial-based basis function models. The parameters of the basis functions are then estimated by exploiting the time multiplexed reference symbols in the LTE uplink sub-frame structure. The performance of the proposed estimation and equalization methods is assessed with extensive multi-user link simulations, with both single-antenna and dual-antenna base station receivers, and the results show that the proposed algorithms are able to significantly reduce the impact of channel distortions and radio impairments. The resulting receiver implementation with the proposed techniques enables improved uplink link performance even when the mobile terminals fulfill their emission requirements, in terms of I/Q images, without any changes in the LTE standard's frame and pilot structures.

Index Terms—CFO, channel estimation, direct-conversion transceivers, I/Q imbalance, intercarrier interference (ICI), inter-

user interference (IUI), least-squares (LS) estimation, long term evolution (LTE), minimum mean-square error (MMSE) equalization, orthogonal frequency-division multiple access (OFDMA), single-carrier frequency-division multiple access (SC-FDMA), SIMO, zero-forcing (ZF) equalization.

I. INTRODUCTION

THE next generation of wireless systems is expected to provide enhanced data services to users by employing higher data rates and higher bandwidths. This drives the need for increased flexibility in RF spectrum use together with the use of higher order modulation techniques. In recent years, orthogonal frequency division multiplexing (OFDM) has received much attention as a physical layer technology for the future wireless systems, and is being adopted in existing as well as emerging communication systems, such as WLAN IEEE 802.11a/g/n/ac [1], WiMAX IEEE 802.16 [2], DVB-T [3], DVB-H [4], and 3GPP LTE [5]. In the context of 3GPP LTE (Third Generation Partnership Project Long Term Evolution), the target data rates are 100Mbps in downlink and 50Mbps in uplink, and other system features include flexible bandwidths, and moderate power consumption of mobile terminals [5],[6]. While the previous 3GPP generations, namely 3G UMTS and 3.5G HSPA, rely on code division multiple access (CDMA), LTE adopts orthogonal frequency division multiple access (OFDMA) based technologies for its uplink and downlink [6]-[7]. Due to high peak-to-average power ratio (PAPR) of OFDMA signals, the single-carrier frequency division multiple access (SC-FDMA), also known as DFT-spread OFDMA, has been selected for the uplink transmission in 3GPP LTE systems. SC-FDMA has similar throughput performance as OFDMA but with lower PAPR to increase power efficiency, and is less sensitive to frequency synchronization errors, which makes it favorable for mobile terminals [5]-[7].

Meanwhile the implementation of radio devices with low-cost, small size, and low power consumption transceiver architectures is desirable for mass production. Among several radio architectures, the direct-conversion (or zero-IF) architecture represents the most promising solution, offering the advantages of low power consumption and small size by avoiding bulky image rejection filters, and consequently decreasing cost, size, and hardware complexity of the transceiver [13], [14]. One performance limiting issue of the direct-conversion

This work was supported by the Academy of Finland (under the projects 251138 “Digitally-Enhanced RF for Cognitive Radio Devices” and 138424 “Joint Analysis and DSP-Based Mitigation of Multiple RF Impairments in Future Radio Devices”), the Finnish Funding Agency for Technology and Innovation (Tekes, under the project “Cross-Layer Modeling and Design of Energy-Aware Cognitive Radio Networks (CREAM)”), the Linz Center of Mechatronics (LCM) in the framework of the Austrian COMET-K2 programme, the Graduate School TISE, and the TUT graduate school.

Copyright (c) 2013 IEEE. Personal use of this material is permitted. However, permission to use this material for any other purposes must be obtained from the IEEE by sending a request to pubs-permissions@ieee.org.

The authors are with the Department of Electronics and Communications Engineering, Tampere University of Technology, Tampere, FI-33101, Finland (e-mail: adnan.kiayani@tut.fi, lauri.anttila@tut.fi, yaning.zou@tut.fi, mikko.e.valkama@tut.fi).

architecture is, however, its vulnerability to unavoidable hardware inaccuracies, stemming from the impairments of analog RF components. The most pronounced radio impairment in direct-conversion architecture based radios is in-phase and quadrature-phase (I/Q) imbalance, i.e., amplitude, phase, and impulse response mismatches between the I- and Q- branch signals [15]-[21]. Such I/Q imbalances result in mirror frequency interference between the subcarriers located symmetrically around the center frequency, and depending on the user's spectral location cause inter-carrier interference (ICI) through own signal image or inter-user interference (IUI) through the image signal of users located on the mirror sub-bands. The minimum uplink I/Q image suppression defined in the current 3GPP standardization is only 25 dB [9],[10] which, as also verified with simulations in Section VI, can form a performance bound in uplink transmission. This is due to the fact that considerable power level differences may exist among the uplink users and the powerful users may cause strong interference to weak users located on mirror band. Therefore, extra enhancement at the base station (BS) RX side is an interesting option to improve the link and system performance, as mobile transmitter vendors anyway only seek to comply with emission specifications which, as described above, are fairly loose from the I/Q imaging perspective.

While the direct conversion radios are vulnerable to I/Q imbalance, OFDM-based systems are also sensitive to frequency synchronization errors, often called carrier frequency offset (CFO). The CFO arises due to the misalignment between TX and RX local RF oscillators and/or mobility of users, and destroys orthogonality between subcarriers. For an uplink scenario, each user experiences different CFO which leads to ICI as well as IUI [25]-[27]. It is worth noting that the 3GPP LTE standardization dictates fairly tight synchronization of the mobile terminal's local oscillators (LOs) to the base station LO and the specified maximum transmitter LO error is only ± 0.1 ppm of carrier frequency [9], [10].

The presence of radio impairments also complicates the fairly simple task of channel estimation, where now the overall effective channel with TX and RX impairments included must be estimated and equalized to recover the transmitted data. In general, there exists abundant literature on the digital estimation and compensation of RF impairments in OFDM systems, see e.g. [15] - [17] and references therein for such joint estimation and compensation techniques. The I/Q imbalance correction approaches proposed in these references are, however, not applicable to the *multi-user* uplink OFDMA type systems, because I/Q imbalances in uplink induce both ICI and IUI between mirror sub-band users, as opposed to classical ICI in OFDM systems. The effect of I/Q imbalances in multi-user SC-FDMA and OFDMA systems has been considered to some extent in recent literature, e.g. in [18] - [24], but, as elaborated below, have limited application in practical systems such as LTE where flexible bandwidth assignment and fast scheduling results in (i) possible reallocation of bandwidths and subcarrier locations of each terminal every 1 msec and (ii) possibility of having multiple mirror band terminals simultaneously. In [18], the channel and TX I/Q imbalances are estimated and equalized in OFDMA systems using a group of mirror subcarrier

pairs located symmetrically around the center subcarrier. This technique has poor spectral efficiency due to large number of specific pilots being used for the efficient channel estimation, and also LTE standard does not support such pilot structure. The effect of IUI due to TX I/Q imbalances in OFDMA and SC-FDMA systems is discussed in [19] and a widely-linear minimum-mean square error (WLMMSE) equalizer is proposed when channel and TX I/Q imbalance parameters are known at the BS RX. The authors have also proposed a subcarrier mapping scheme to avoid IUI created by the TX I/Q imbalances. The subcarrier mapping scheme cannot be deployed in, for example, uplink 3GPP LTE systems where localized subcarrier mapping is adopted and multiple users are sharing the whole bandwidth. Also, with known TX I/Q imbalance parameters at the receiver, [20] proposed a turbo equalizer for the multi-user multiple input multiple output (MU-MIMO) SC-FDMA systems. Additionally, only frequency independent I/Q imbalance models are considered in [18] - [20] which limits their applicability in wideband radio systems. A circularity based compensation scheme for receiver I/Q imbalance in SC-FDMA systems is presented in [21]. The impact of joint frequency selective TX and RX I/Q imbalances on the error vector magnitude (EVM) is investigated in [23], but no estimation or compensation method is proposed. Recently, a joint channel and I/Q imbalance and propagation delay estimation technique for multi-user asynchronous uplink OFDMA systems is proposed in [24] but assumes distributed subcarrier assignments with mirror subcarriers being always allocated to the same user.

In this article, in multi-user system context, uplink SC-FDMA channel and impairment estimation techniques are proposed when frequency-selective TX I/Q imbalances and small CFOs are present, being generally different for different terminals. The estimation and compensation are carried out at the base station RX by utilizing its computing resources, therefore having no effect on the cost of the mobile terminals. The focus is on uplink SC-FDMA systems, *nevertheless, the proposed methods are also equally applicable to OFDMA systems, as long as the system employs time multiplexed pilots.* We capitalize on the preliminary work in [22] (where a compensator structure for the mitigation of TX I/Q imbalances and small CFOs was initially presented) and develop joint channel and impairment estimation techniques. The treatment for the joint estimation and compensation of channel distortions and radio impairments presented in this paper is essentially LTE standard-compliant and has several advantages over the existing literature. The main contributions are summarized as follows:

- 1) An analytic expression for the received signal as a function of the transmitted uplink signals, the TX-RX I/Q imbalances, CFOs, and channel distortions is derived. This mathematical framework provides deep insight into the detrimental effects of these radio impairments on the performance of multiuser radio systems, particularly of TX I/Q imbalances. It is further shown that the signal model can be simplified, by invoking practical considerations of small uplink CFOs and RX I/Q imbalance

compensation *a priori*. This simplified model is then used to derive efficient joint estimation and equalization algorithms. These working assumptions are strongly motivated by 3GPP standardization specifications for mobile transmitters [9],[10], in terms of I/Q imaging and carrier frequency synchronization.

- 2) A compensation structure is presented that utilizes pairs of mirror subcarriers, and two alternative joint channel and impairment equalization schemes, stemming from the zero-forcing (ZF) and minimum mean-square error (MMSE) principle, are discussed. The joint mirror carrier MMSE equalizer is derived to effectively handle the situations when uplink mirror sub-band users have different power levels, and is shown to be function of joint channel and impairments filter parameters and the mirror channel signal-to-noise ratios (SNRs). The presence of power level differences among uplink users is a practical scenario (e.g. the inband dynamic range for a 3GPP LTE BS RX is 21.5 dB [12]) whereas the existing equalization methods for multiuser uplink systems, such as in [18]-[20], assume equal average received power at the BS RX. The proposed estimation and equalization schemes are also generalized to multi-antenna receiver systems, which in practice can provide significant performance gain over the single-antenna receiver systems.
- 3) The estimation of channel distortions and impairments under TX I/Q imbalances and small CFOs is carried out jointly using embedded LTE reference symbols in a single uplink signal sub-frame, covering all simultaneously scheduled terminals. In practice, the joint estimation of channels with TX I/Q imbalances and small CFOs is very challenging due to large number of parameters to be estimated and insufficient number of equations to solve for the estimation parameters. In the existing literature, it is often assumed that the joint channel and impairment responses are known (e.g [19] and [20]) or a large number of specifically designed pilots are utilized for estimation (such as in [18]). In contrast, the leading principle for the joint estimation, in this paper, is to reduce the number of essential parameters by characterizing the channel and impairment filters with basis functions models, where the filters are equivalently expressed as products of known basis function matrices and unknown small size coefficient vectors. Three different basis function models, namely polynomial, piecewise polynomial, and splines, are discussed, and it is shown that the basis function model yields an efficient and feasible estimation solution, supporting parameter estimation with LTE-compliant reference symbol structure. The base station RX then performs the estimation of the coefficient vectors for all simultaneously scheduled user equipments (UEs) using least-squares (LS) model fitting principle. The performance of all different estimation and equalization algorithms is evaluated with extensive computer simulations. The obtained results indicate that the proposed algorithms can effectively reduce the impact of channel distortions and radio

impairments. Furthermore, they can be directly applied in the base station RXs without any modification in the design of RF transceiver or in LTE standardization.

Preliminaries: The notations used in this paper are as follows. Time domain quantities are represented by lower case letters a and frequency domain quantities with upper case letters A . We denote time domain vectors/matrices by $\underline{a}/\underline{A}$, while the frequency domain vectors/matrices are represented by $\underline{A}/\underline{A}$. Superscripts $(\cdot)^T, (\cdot)^H$ and $(\cdot)^*$ denote the transpose, hermitian transpose, and conjugate of a vector, a scalar, or a matrix, respectively, while $(\cdot)^{-1}$ denotes matrix inverse. The convolution operation is indicated by \star and the operators $\mathbb{E}[\cdot]$ and $|\cdot|$ denote the expectation and the absolute value, respectively. \mathbf{I}_N and $\mathbf{0}_N$ denote the $N \times N$ identity and all zeros matrices, respectively. If $\underline{A} = [A(1) \ A(2) \ \dots \ A(N/2) \ \dots \ A(N)]^T$ is a frequency domain vector with N subcarriers then $\underline{A}^\# = [A(1)^* \ A(N)^* \ \dots \ A(N/2)^* \ \dots \ A(2)^*]^T$ denotes the conjugate of the mirror subcarriers vector. $\mathfrak{D}\text{diag}(\cdot)$ and $\mathfrak{B}\mathfrak{D}\text{diag}(\cdot)$ denote square diagonal and block diagonal matrices, respectively.

The rest of the paper is organized as follows. Section II introduces the essential signal models. In Section III, we describe the joint mirror subcarrier ZF and MMSE equalization schemes for receivers with arbitrary number of receiver antennas. In Section IV, the basis function approximation of direct and mirror channel filters is formulated and different basis function models and their comparison are presented. In Section V, we first shortly review the LTE frame and reference symbol structures, and then describe in detail the proposed estimation methods. The performance analysis and comparison of proposed estimation and equalization algorithms are given in Section VI, and finally the conclusions are drawn in Section VII. Some further details of the MMSE equalization are given in Appendix.

II. MULTI-USER UPLINK SIGNAL MODELING UNDER RF IMPAIRMENTS

The system model of multi-user uplink SC-FDMA radio link with radio impairments, channels, and the corresponding estimation and compensation blocks is shown in Fig. 1. We assume that U -users are communicating simultaneously with a single BS RX with N_{RX} receiving antennas through their independent multi-path channels. For notational simplicity, we present below the received signal models from an arbitrary receiver antenna perspective.

A. Principal Signal Models

Assume that each user transmits its data in a single uplink subframe using one or more resource blocks (RBs), where a resource block size N_{SC}^{RB} occupies twelve subcarriers in LTE. For a user- i , a block of $N_i = m_i N_{SC}^{RB}$, $m_i \in \{1, 2, \dots\}$ data symbols $\underline{s}^i = [s^i(0), s^i(1), \dots, s^i(N_i - 1)]^T$ drawn from a quadrature amplitude modulation (QAM) constellation is first transformed to the frequency domain by means of an N_i -point DFT, such that

$$S^i(\kappa) = \sum_{p=0}^{N_i-1} s^i(p) e^{-j2\pi \frac{p\kappa}{N_i}}, \quad 0 \leq \kappa \leq N_i - 1. \quad (1)$$

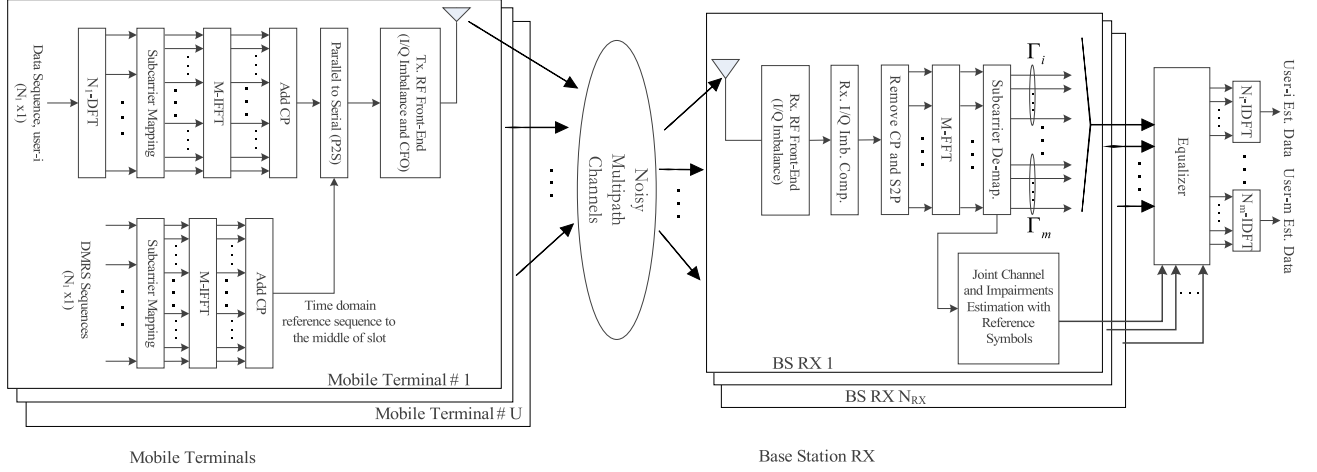


Fig. 1. Block diagram of SC-FDMA uplink system with RF impairments and their corresponding equalization/compensation blocks in the base station receiver.

The output sample $S^i(\kappa)$ is mapped to the k^{th} OFDMA subcarrier, denoted here as $X^i(k) = S^i(\kappa)$ such that $k \in \Gamma_N^i$, where Γ_N^i denotes the N_i element set that contains the indices of subcarriers allocated to i^{th} -user. The subcarrier sets satisfy $\Gamma_N^i \cap \Gamma_N^j = \emptyset$ if $i \neq j$. If the elements in Γ_N^i are arranged consecutively then the subcarrier assignment is referred to as localized mapping. Otherwise, it is called distributed mapping. In this work, we study the SC-FDMA system with localized subcarrier mapping which is the current subcarrier mapping scheme in 3GPP LTE [6], [7], [11]. The subcarrier mapping is followed by an M -point inverse fast Fourier transform (IFFT) to convert the data into a time domain signal. After the cyclic prefix (CP) insertion of length N_g , the time domain signal for a user- i can be written as

$$x^i(t) = \sum_{k \in \Gamma_N^i} X^i(k) e^{j2\pi \frac{tk}{M}}, \quad -N_g \leq t \leq M-1. \quad (2)$$

The complex baseband signal travels through the RF module for up-conversion where it is distorted by the TX I/Q imbalance. The baseband equivalent of the impaired TX RF signal can then be expressed as [15]-[17]

$$\tilde{x}^i(t) = g_{1T}^i(t) \star x^i(t) + g_{2T}^i(t) \star x^i(t)^* \quad (3)$$

with the complex imbalance filters $g_{1T}^i(t), g_{2T}^i(t)$ of the i^{th} -user's TX front-end, defined as $g_{1T}^i(t) \triangleq [\delta(t) + g_T^i \exp(j\phi_T^i) h_T^i(t)]/2$ and $g_{2T}^i(t) \triangleq [\delta(t) - g_T^i \exp(j\phi_T^i) h_T^i(t)]/2$ with $\delta(t), g_T^i, \phi_T^i, h_T^i(t)$ denoting the unit impulse function, gain imbalance, phase imbalance, and relative non-ideal impulse response between the I- and Q- paths of the modulator, respectively, and where $\delta(t)$ denotes an impulse function [17]. The signal then propagates through a multi-path block fading channel whose delay spread is assumed to be shorter than the CP length. The overall received signal is composed of the signals received from U -users and additive noise, written as

$$r(t) = \sum_{i=1}^U r^i(t) + n(t) \quad (4)$$

with

$$r^i(t) = \sum_{l=0}^{N_{ch}-1} h^i(l) \tilde{x}^i(t-l) \quad (5)$$

where $n(t)$ is the additive white Gaussian noise (AWGN) with zero mean and variance σ_n^2 , $h^i(l)$ denotes the i^{th} user channel impulse response with N_{ch} complex taps, and $r^i(t)$ is the received signal of i^{th} user.

Assuming that the local oscillator in the base station is not perfectly synchronized with the oscillators in the UE, there exist CFOs. Assume further that the BS I/Q down-conversion stage is not ideal and also induces I/Q imbalance. The composite received signal in (4) can then be re-written as

$$y(t) = g_{1R}(t) \star \left(\sum_{i=1}^U r^i(t) e^{j2\pi \frac{\epsilon^i t}{M}} \right) + g_{2R}(t) \star \left(\sum_{i=1}^U r^i(t) e^{j2\pi \frac{\epsilon^i t}{M}} \right)^* + \tilde{n}(t) \quad (6)$$

where ϵ^i is the normalized CFO of i^{th} -user relative to the subcarrier spacing, $g_{1R}(t); g_{2R}(t)$ are RX complex imbalance filters, defined as $g_{1R}(t) \triangleq [\delta(t) + g_R \exp(-j\phi_R) h_R(t)]/2$ and $g_{2R}(t) \triangleq [\delta(t) - g_R \exp(j\phi_R) h_R(t)]/2$ with $g_R, \phi_R, h_R(t)$ denoting the gain imbalance, phase imbalance, and relative non-ideal impulse response between the demodulator's quadrature branches [17], and $\tilde{n}(t) = g_{1R}(t) \star n(t) + g_{2R}(t) \star n(t)^*$ is the noise term under RX I/Q imbalance. The frequency domain baseband signal of the user- i at the k^{th} subcarrier after CP removal, FFT, and subcarrier demapping is then given by (7) [22], where $-k = M - k$ denotes the mirror subcarrier, superscript m refers to the user located on the mirror sub-band of user- i , $H^i(k), H^m(k)$ are the channel responses of user- i and user- m at the k^{th} subcarrier, $G_{1T}^i(k), G_{2T}^i(k)$ are the frequency domain responses of the TX I/Q imbalance filters of user- i , $G_{1R}(k), G_{2R}(k)$ are the frequency domain responses of the RX I/Q imbalance filters, and $\tilde{N}^i(k) = G_{1R}(k) N^i(k) + G_{2R}(k) N^m(-k)^*$ represents the noise at k^{th} subcarrier of i^{th} user under RX I/Q imbalance. The CFO

$$\begin{aligned}
Y^i(k) = & G_{1R}(k) \left\{ \begin{aligned} & H^i(k)G_{1T}^i(k)X^i(k)\Omega(k, k, \epsilon^i) + H^m(k)G_{2T}^m(k)X^m(-k)^*\Omega(k, k, \epsilon^m) + \\ & \sum_{l \in \Gamma^i, l \neq k} H^i(l)G_{1T}^i(l)X^i(l)\Omega(l, k, \epsilon^i) + \\ & \sum_{l \in \Gamma^i, l \neq k} H^m(l)G_{2T}^m(l)X^m(-l)^*\Omega(l, k, \epsilon^m) + \\ & \sum_{j=1, j \neq i}^U \sum_{l \in \Gamma^j} H^j(l)G_{1T}^j(k)X^j(l)\Omega(l, k, \epsilon^j) + \\ & \sum_{j=1, j \neq m}^U \sum_{l \in \Gamma^j} H^j(l)G_{2T}^j(l)X^j(-l)^*\Omega(l, k, \epsilon^j) \end{aligned} \right\} \\
& + G_{2R}(k) \left\{ \begin{aligned} & H^i(-k)^*G_{2T}^i(-k)^*X^i(k)\Omega(-k, -k, \epsilon^i)^* + \\ & H^m(-k)^*G_{1T}^m(-k)^*X^m(-k)^*\Omega(-k, -k, \epsilon^m)^* + \\ & \sum_{l \in \Gamma^i, l \neq k} H^i(-l)^*G_{2T}^i(-l)^*X^i(l)\Omega(-l, -k, \epsilon^i)^* + \\ & \sum_{l \in \Gamma^i, l \neq k} H^m(-l)^*G_{1T}^m(-l)^*X^m(-l)^*\Omega(-l, -k, \epsilon^m)^* + \\ & \sum_{j=1, j \neq i}^U \sum_{l \in \Gamma^j} H^j(-l)^*G_{2T}^j(-l)^*X^j(l)\Omega(-l, -k, \epsilon^j)^* + \\ & \sum_{j=1, j \neq m}^U \sum_{l \in \Gamma^j} H^j(-l)^*G_{1T}^j(-l)^*X^j(-l)^*\Omega(-l, -k, \epsilon^j)^* \end{aligned} \right\} \\
& + \tilde{N}^i(k) \quad k \in \Gamma^i
\end{aligned} \tag{7}$$

leakage coefficients in (7) are defined as

$$\Omega(l, k, \epsilon^i) = \frac{1}{M} \sum_{q=0}^{M-1} e^{j2\pi \frac{q}{M} (l + \epsilon^i - k)}. \tag{8}$$

B. Impact of Radio Impairments and Simplified Signal Model

Equation (7) describes the IUI generated by the image of mirror user m as a result of TX and RX I/Q imbalances and CFOs, as well as the ICI generated by the i^{th} user itself as a result of CFOs. In general, the focus in this article is on the uplink transmission impaired by the transmitter RF imperfections. The related topic such as RX I/Q imbalance is out of the scope of this paper and is thus assumed reasonably well compensated, using, e.g., the technique presented in [21], [28] that can blindly compensate for the RX I/Q imbalance even in the presence of TX I/Q imbalances and CFOs. However, to realistically quantify the results, the effect of a calibrated residual RX I/Q imbalance with an image rejection ratio (IRR) of 55 dB [21], [28], [29] is included in the performance simulations later in this paper. Moreover, following the guidelines of 3GPP LTE specifications for the uplink carrier frequency synchronization error, we assume that the CFO is relatively small, i.e., ± 0.1 ppm of carrier frequency [9], [10]. Hence, CFO does not induce considerable ICI from user's own neighboring subcarriers as well as negligibly small IUI because most of the interference energy originates from the neighboring subcarriers which are allocated to the same user in localized mapping and affects much less the users located far away [23], [25]. All these assumptions are plausible for the uplink transmission and simplify equation (7) to

$$\begin{aligned}
Y^i(k) \approx & H^i(k)G_{1T}^i(k)X^i(k)\Omega(k, k, \epsilon^i) + \\ & H^m(k)G_{2T}^m(k)X^m(-k)^*\Omega(k, k, \epsilon^m) + N^i(k)
\end{aligned} \tag{9}$$

which can also be written in its equivalent form as

$$Y^i(k) = X^i(k)G_D^i(k) + X^m(-k)^*G_M^i(k) + N^i(k) \tag{10}$$

where

$$\begin{aligned}
G_D^i(k) &\triangleq H^i(k)G_{1T}^i(k)\Omega(k, k, \epsilon^i) \\
G_M^i(k) &\triangleq H^m(k)G_{2T}^m(k)\Omega(k, k, \epsilon^m)
\end{aligned}$$

denote the direct and mirror channel responses of user- i , respectively, and $N^i(k)$ represents noise at k^{th} subcarrier of i^{th} -user, assuming calibrated RX I/Q imbalance.

Sidenote about OFDMA: SC-FDMA is in general a modified form of OFDMA that employs single carrier transmission by pre-coding the data symbols with DFT. Due to the close resemblance between SC-FDMA and OFDMA systems, the above formulated signal models can be directly used also in the context of OFDMA with the substitution $S^i(\kappa) \leftarrow s^i(n)$. In addition, since the proposed estimation and equalization are carried out in the frequency domain after the M -point FFT calculation at the RX, the subsequent algorithms are also applicable to uplink OFDMA systems.

Next, we formulate the channel and impairment effects over the user bandwidth with vector-matrix algebra, and describe the impact of IUI due to TX I/Q imbalances in multi-user system context, incorporating also the flexible bandwidth allocation aspect which in general leads to scenarios where a single UE may have multiple UEs at its image band.

C. Role of TX I/Q Imbalances

We now switch to vector-matrix notations, and denote the M samples of frequency domain composite received signal vector after CP removal and FFT by $\mathbf{Y} = [Y(0) \ Y(1) \ Y(2) \ \dots \ Y(M-1)]^T$. The received signal vector of user- i , denoted by \mathbf{Y}^i and containing the samples of (10), is obtained by left multiplying the composite received signal vector \mathbf{Y} with the demapping matrix for user- i , denoted by \mathbf{M}^i , which has following form

$$\mathbf{M}^i = \begin{bmatrix} \mathbf{0}_{N_i \times (\Gamma_N^i(1)-1)} & \mathbf{I}_{N_i \times N_i} & \mathbf{0}_{N_i \times (M-\Gamma_N^i(N_i))} \end{bmatrix}. \tag{11}$$

Then, the vector \mathbf{Y}^i of samples of the signal in (10) is given by

$$\begin{aligned}
\mathbf{Y}^i &= \mathbf{M}^i \mathbf{Y} = \mathbf{X}^i \mathbf{G}_D^i + \mathbf{M}^i (\mathbf{X}^{\#} \mathbf{G}_M) + \mathbf{N}^i \\ &= \mathbf{X}^i \mathbf{G}_D^i + \mathbf{X}^{m\#} \mathbf{G}_M^i + \mathbf{N}^i = \tilde{\mathbf{X}} \mathbf{G}^i + \mathbf{N}^i
\end{aligned} \tag{12}$$

where

$$\tilde{\mathbf{X}} \triangleq \begin{bmatrix} \mathbf{X}^i & \mathbf{X}^{m\#} \end{bmatrix}; \quad \mathbf{G}^i \triangleq \begin{bmatrix} (\mathbf{G}_D^i)^T & (\mathbf{G}_M^i)^T \end{bmatrix}^T.$$

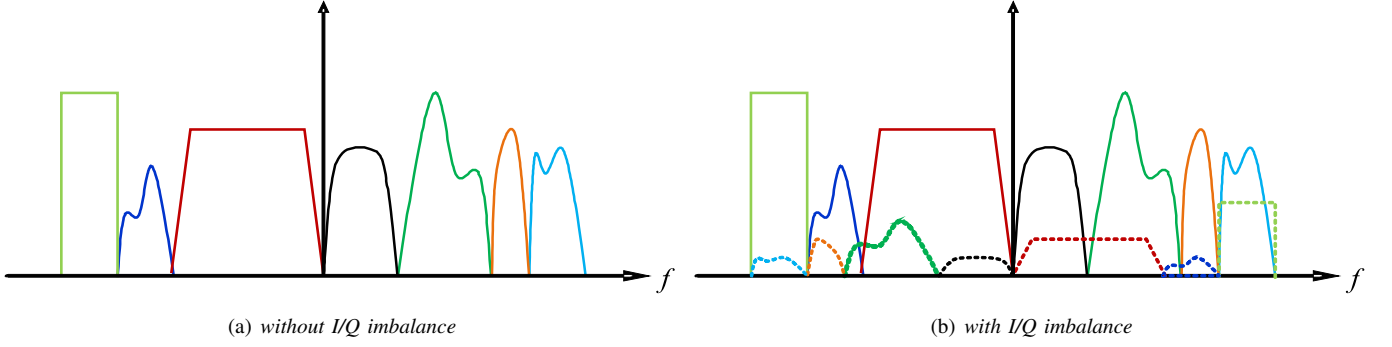


Fig. 2. Example spectral illustration of seven uplink users (different colors) in localized mode with different bandwidths and power levels. The image signal of a user produced due to TX I/Q imbalance (shown as dashed lines) appears at the mirror sub-band and causes interference to user(s) located at that band. Note that depending on the bandwidth allocations, an individual user can be subject to IUI from many users.

In (12), \mathbf{X}^i and $\mathbf{X}^{m\#}$ are diagonal matrices of DFT pre-coded transmitted data symbols of dimension $N_i \times N_i$ and the direct and mirror channel filter vectors \mathbf{G}_D^i and \mathbf{G}_M^i are of length $N_i \times 1$.

In the context of multi-user uplink transmission, the exact structure of the matrix $\mathbf{X}^{m\#}$ and the vector \mathbf{G}_M^i depends on the bandwidth occupancy of direct and mirror channel users. In the example case depicted in Fig. 2, the wideband user-3 (dark red) has more than one user on its mirror band, and thus the overall interference comes from user-4 (black) and partially from user-5 (green), both of which have generally different power levels. The narrow band users, in turn, have the interference coming from the wideband user. In order to model such a general scenario where the bandwidths of uplink users are not equal, we denote the number of users located on the mirror sub-band of user- i by N_u . This results in the following structure of $\mathbf{X}^{m\#}$ and \mathbf{G}_M^i :

$$\mathbf{X}^{m\#} = \text{Diag} \left(\left[\left(\mathbf{X}^{m_1\#} \right)^T \left(\mathbf{X}^{m_2\#} \right)^T \dots \left(\mathbf{X}^{m_{N_u}\#} \right)^T \right]^T \right)$$

$$\mathbf{G}_M^i = \left[\left(\mathbf{G}_M^{i_1\#} \right)^T \left(\mathbf{G}_M^{i_2\#} \right)^T \dots \left(\mathbf{G}_M^{i_{N_u}\#} \right)^T \right]^T. \quad (13)$$

This implies that for decoding an individual terminal signal, the mirror channel responses and transmitter impairment parameters need to be estimated for multiple mirror UEs.

The above discussion assumes that with current I/Q imaging and CFO specifications in the 3GPP LTE standardization for user equipments, the TX I/Q imbalances are expected to play a bigger role than CFOs. This will also be verified with link level simulations in Section VI. In general, the presence of channel distortions and radio impairments causes severe performance degradation in LTE uplink and it is therefore imperative to estimate and thereafter compensate them to minimize their impact. We first formulate the compensation solutions with known parameters in Section III below, and address then the challenging multi-transmitter parameter estimation with LTE compliant reference symbols in detail in Sections IV and V.

III. JOINT EQUALIZATION OF TX I/Q IMBALANCES, SMALL CFOs, AND CHANNEL DISTORTIONS

The task of the equalizer is to reconstruct the frequency domain symbol $X^i(k)$ in (10) from the impaired received signal $Y^i(k)$. As we have observed, the TX I/Q imbalance causes interference between the users located on mirror sub-bands, hence we propose to construct a *total channel matrix* that consists of the channel and impairment responses from the users on mirror sub-bands, and eliminate the impairments by processing the mirror channel subcarrier pairs of the received signals. In order to build such a channel matrix, we stack the i^{th} -user received signal at k^{th} subcarrier $Y^i(k)$ and the complex conjugate of its mirror subcarrier $Y^m(-k)^*$ as

$$\tilde{\mathbf{Y}}(k) = \tilde{\mathbf{G}}(k)\tilde{\mathbf{X}}(k) + \tilde{\mathbf{N}}(k) \quad (14)$$

where

$$\tilde{\mathbf{Y}}(k) \triangleq \begin{bmatrix} Y^i(k) & Y^m(-k)^* \end{bmatrix}^T$$

$$\tilde{\mathbf{X}}(k) \triangleq \begin{bmatrix} X^i(k) & X^m(-k)^* \end{bmatrix}^T$$

$$\tilde{\mathbf{G}}(k) \triangleq \begin{bmatrix} \mathbf{G}_D^i(k) & \mathbf{G}_M^i(k) \\ \mathbf{G}_M^{m*}(-k)^* & \mathbf{G}_D^m(-k)^* \end{bmatrix}$$

$$\tilde{\mathbf{N}}(k) \triangleq \begin{bmatrix} N^i(k) & N^m(-k)^* \end{bmatrix}^T.$$

The total channel matrix $\tilde{\mathbf{G}}(k)$ represents the joint effect of TX I/Q imbalances, small CFOs, and channel distortions for the received signals at mirror subcarriers. When the coefficients of $\tilde{\mathbf{G}}(k)$ are known, the transmitted data symbols can be estimated by employing a linear equalizer such as the ZF equalizer or the MMSE equalizer. In the following subsections, we shortly formulate the principles of these linear equalizers.

A. Joint Mirror Carrier ZF Equalizer (J-ZF eq.)

The ZF equalizer nulls the impairments and channel effects by applying the inverse of total effective channel matrix to the received signal. The J-ZF equalizer builds on the inverse of the matrix $\tilde{\mathbf{G}}(k)$ and processes the mirror subcarrier pair as

$$\begin{bmatrix} \hat{X}_{ZF}^i(k) \\ \hat{X}_{ZF}^m(-k)^* \end{bmatrix} = \tilde{\mathbf{W}}_{ZF}(k) \begin{bmatrix} Y^i(k) \\ Y^m(-k)^* \end{bmatrix}$$

$$= \tilde{\mathbf{G}}^{-1}(k) \begin{bmatrix} Y^i(k) \\ Y^m(-k)^* \end{bmatrix}. \quad (15)$$

In favorable channel conditions, the J-ZF equalizer efficiently eliminates the undesired effect of impairments and channel distortions. However, it is known to suffer from the noise enhancement problem where the additive noise in the received signal is strongly increased and degrades the equalizer performance heavily. Contrary to OFDM systems, the IDFT operation in SC-FDMA systems spreads the noise over all the symbols and noise amplification for deep fades has greater impact on the performance [8].

B. Joint Mirror Carrier MMSE Equalizer (J-MMSE eq.)

Alternatively, we can employ the MMSE equalizer principle which, in addition to the channel matrix, utilizes the information of signal-to-noise ratio (SNR) of mirror users to jointly equalize the radio impairments and channel distortions. MMSE equalizer alleviates the noise enhancement problem associated with the ZF equalizer. It uses an equalization filter $\tilde{\mathbf{W}}_{MMSE}(k)$ which filters the received signal as

$$\begin{bmatrix} \hat{X}_{MMSE}^i(k) \\ \hat{X}_{MMSE}^m(-k)^* \end{bmatrix} = \tilde{\mathbf{W}}_{MMSE}(k) \begin{bmatrix} Y^i(k) \\ Y^m(-k)^* \end{bmatrix}. \quad (16)$$

The filter $\tilde{\mathbf{W}}_{MMSE}(k)$, derived in the appendix, minimizes the mean-square error (MSE) between the DFT spread transmitted samples and the DFT-spread equalized samples, and is of the following form

$$\tilde{\mathbf{W}}_{MMSE}(k) = \begin{bmatrix} \left(\Xi^{-1}(k) \begin{bmatrix} G_D^i(k)^* \\ G_M^m(-k) \end{bmatrix} \right)^T \\ \left(\Xi^{-1}(k) \begin{bmatrix} G_M^i(k)^* \frac{\Upsilon^m(-k)}{\Upsilon^i(k)} \\ G_D^m(-k) \frac{\Upsilon^i(k)}{\Upsilon^m(-k)} \end{bmatrix} \right)^T \end{bmatrix} \quad (17)$$

where $\Upsilon^i(k)$; $\Upsilon^m(-k)$ denote the per subcarrier SNR of direct and mirror users at k^{th} and $(-k)^{th}$ subcarriers, defined in (A.9), and the matrix $\Xi(k)$ is defined by equation (A.11).

C. Extension to Multi-Antenna Receiver

While the above derivations are formulated for a single, yet arbitrary, receiver antenna, we now consider explicitly the case when the BS RX is equipped with multiple receiving antennas, as shown also in Fig. 1. Thus, the signal transmitted by a user from its antenna arrives at the RX antennas through different channels. We assume that the channels between the user's TX antenna and each RX antenna are uncorrelated. With multiple differently faded copies of the same transmit signal, RX can then exploit diversity and thus improves the performance considerably.

Assuming now that the RX has N_{RX} antennas, the received signal at k^{th} subcarrier of user- i and its mirror user- m in (14) can be re-written by stacking the mirror subcarrier pairs from all N_{RX} antennas as

$$\underbrace{\begin{bmatrix} \tilde{\mathbf{Y}}_1(k) \\ \vdots \\ \tilde{\mathbf{Y}}_{N_{RX}}(k) \end{bmatrix}}_{\tilde{\mathbf{Y}}_{SIMO}(k)} = \underbrace{\begin{bmatrix} \tilde{\mathbf{G}}_1(k) \\ \vdots \\ \tilde{\mathbf{G}}_{N_{RX}}(k) \end{bmatrix}}_{\tilde{\mathbf{G}}_{SIMO}(k)} \tilde{\mathbf{X}}(k) + \underbrace{\begin{bmatrix} \tilde{\mathbf{N}}_1(k) \\ \vdots \\ \tilde{\mathbf{N}}_{N_{RX}}(k) \end{bmatrix}}_{\tilde{\mathbf{N}}_{SIMO}(k)} \quad (18)$$

where

$$\begin{aligned} \tilde{\mathbf{Y}}_{\chi}(k) &= [Y_{\chi}^i(k) \ Y_{\chi}^m(-k)^*]^T \\ \tilde{\mathbf{G}}_{\chi}(k) &= \begin{bmatrix} G_{D,\chi}^i(k) & G_{M,\chi}^i(k) \\ G_{M,\chi}^m(-k)^* & G_{D,\chi}^m(-k)^* \end{bmatrix} \\ \tilde{\mathbf{N}}_{\chi}(k) &= [N_{\chi}^i(k) \ N_{\chi}^m(-k)^*]^T \\ \chi &\in \{1, 2, \dots, N_{RX}\}. \end{aligned} \quad (19)$$

The ZF and MMSE equalizers are then given directly by

$$\begin{bmatrix} \hat{X}_{ZF}^i(k) \\ \hat{X}_{ZF}^m(-k)^* \end{bmatrix} = \left(\tilde{\mathbf{G}}_{SIMO}^H(k) \tilde{\mathbf{G}}_{SIMO}(k) \right)^{-1} \times \tilde{\mathbf{G}}_{SIMO}^H(k) \tilde{\mathbf{Y}}_{SIMO}(k) \quad (20)$$

and

$$\begin{bmatrix} \hat{X}_{MMSE}^i(k) \\ \hat{X}_{MMSE}^m(-k)^* \end{bmatrix} = \tilde{\mathbf{W}}_{MMSE}(k) \tilde{\mathbf{Y}}_{SIMO}(k) \quad (21)$$

where $\tilde{\mathbf{W}}_{MMSE}(k)$ is given by equation (A.7). These represent multi-antenna receiver generalizations of the previous single-antenna equalizers in (15) and (16).

In general, the representation of the total channel matrix by merging pairs of mirror subcarriers is a widely adopted approach, e.g. the works in [15], [17], [18], and [19] use similar effective channel matrix concept to model and compensate for certain radio impairments. We emphasize, however, that while the proposed J-ZF equalizer is essentially similar to the one reported in [17]-[19], the proposed J-MMSE equalizer is fundamentally different from the widely linear (WL) MMSE equalizer of [19]. In [19], the WL MMSE equalizer is derived under the assumption that uplink users have equal average received powers. The proposed J-MMSE equalizer, on the other hand, takes into account the power level differences among the uplink users. Such unequal received power levels is, indeed, a practical scenario as reported, e.g., in [12].

Above equalizer formulations in (15) - (17), (20), (21) assume that the essential responses and parameters are known, while in practice they need to be estimated in the receiver simultaneously for all the active terminals. In Section IV, we present basis function representations of the effective channel response vectors, in order to reduce the estimation complexity. The estimation methods are then presented in detail in Section V.

IV. EFFICIENT RESPONSE REPRESENTATION WITH BASIS FUNCTIONS

In this section, we describe how the effective direct and mirror channel response filters for a signal received at an arbitrary receiver antenna in (12) may be modeled with *basis functions*, where each response filter is expressed as a product of a *basis function matrix* and a *coefficient vector*. In the existing literature, the methods of basis functions are widely used to estimate frequency selective and time varying channels, e.g. see references [32], [34], [35], [36], [37]. The motivation for this representation in the context of joint channel and impairments responses estimation is twofold. The first is that equation (12) cannot be even solved in its existing form as the number of parameters to be estimated is double the

number of available equations. The other motivating factor comes from the fact that the basis function representations can be used to greatly reduce the size of the parameter space and consequently the involved computations, thus enabling efficient receiver implementation.

A. Basis Function Model for Effective Direct and Mirror Channel Responses

Fundamentally, the subspace spanned by the basis vectors is sufficient to approximate the responses, given that a sufficiently large number of basis functions is used. This number effectively depends on the response characteristics - the longer the time dispersion is, the lower the correlation between the adjacent subcarrier responses, thus generally implying a larger number of basis functions for an accurate approximation. Since the basis function matrix is generally known and can be pre-calculated, the estimation problem then reduces to estimating only the coefficient vector whose length is, in general, considerably smaller than that of the response vectors.

A simple model of (12) based on representing the effective channel response vectors $\underline{\mathbf{G}}_D^i$ and $\underline{\mathbf{G}}_M^i$ with the basis functions can be obtained as

$$\begin{aligned} \underline{\mathbf{Y}}^i &= \mathbf{X}^i \mathbf{B}_D^i \underline{\mathbf{G}}_{D,B}^i + \mathbf{X}^{m\#} \mathbf{B}_M^i \underline{\mathbf{G}}_{M,B}^i + \underline{\mathbf{N}}^i \\ &= \mathbf{X}^i \mathbf{B}_D^i \underline{\mathbf{G}}_{D,B}^i + \mathbf{X}^{m\#} \mathfrak{B} \text{Diag} \left(\begin{bmatrix} \mathbf{B}_M^{i_1} \\ \mathbf{B}_M^{i_2} \\ \vdots \\ \mathbf{B}_M^{i_{N_u}} \end{bmatrix} \right) \begin{bmatrix} \underline{\mathbf{G}}_{M,B}^{i_1} \\ \underline{\mathbf{G}}_{M,B}^{i_2} \\ \vdots \\ \underline{\mathbf{G}}_{M,B}^{i_{N_u}} \end{bmatrix} + \underline{\mathbf{N}}^i \\ &= \tilde{\mathbf{X}} \tilde{\mathbf{B}}^i \underline{\mathbf{G}}_B^i + \underline{\mathbf{N}}^i \end{aligned} \quad (22)$$

where

$$\begin{aligned} \mathbf{B}_D^i &= [\mathbf{B}_{D,0}^i \quad \mathbf{B}_{D,1}^i \quad \cdots \quad \mathbf{B}_{D,N_D}^i] \\ \mathbf{B}_M^i &= [\mathbf{B}_{M,0}^{i_p} \quad \mathbf{B}_{M,1}^{i_p} \quad \cdots \quad \mathbf{B}_{M,N_M}^{i_p}] \\ \underline{\mathbf{G}}_{D,B}^i &= [G_{D,B,1}^i \quad G_{D,B,2}^i \quad \cdots \quad G_{D,B,N_D}^i]^T \\ \underline{\mathbf{G}}_{M,B}^{i_p} &= [G_{M,B,1}^{i_p} \quad G_{M,B,2}^{i_p} \quad \cdots \quad G_{M,B,N_M}^{i_p}]^T \\ \tilde{\mathbf{B}}^i &= \begin{bmatrix} \mathbf{B}_D^i & \mathbf{0}_{N_i \times N_M} \\ \mathbf{0}_{N_i \times N_D} & \mathbf{B}_M^i \end{bmatrix} \\ \tilde{\mathbf{G}}_B^i &\triangleq \begin{bmatrix} (\underline{\mathbf{G}}_{D,B}^i)^T & (\underline{\mathbf{G}}_{M,B}^{i_p})^T \end{bmatrix}^T \\ p &\in \{1, 2, \dots, N_u\} \end{aligned} \quad (23)$$

The matrices $\mathbf{B}_D^i, \mathbf{B}_M^i, \mathbf{B}_M^{i_p}$ are of size $N_i \times N_D; N_i \times N_M; N_i^{i_p} \times N_M^{i_p}$, respectively, that collect the N_D -th; N_M -th; and $N_M^{i_p}$ -th order basis function vectors as columns, and vectors $\underline{\mathbf{G}}_{D,B}^i, \underline{\mathbf{G}}_{M,B}^{i_p}, \underline{\mathbf{G}}_{M,B}^{i_{N_u}}$ represent the $N_D \times 1; N_M \times 1; N_M^{i_p} \times 1$ basis function coefficient vectors, respectively. It can be seen from (22) that the procedure is to transform the $N_i \times 1$ -vectors $\underline{\mathbf{G}}_D^i, \underline{\mathbf{G}}_M^i$ into $N_D \times 1$ and $N_M \times 1$ -vectors $\underline{\mathbf{G}}_{D,B}^i, \underline{\mathbf{G}}_{M,B}^{i_p}$ for the estimation purposes. We also note from (22) that there are now N_i equations with $N_D + N_M$ unknowns, hence given that $N_D + N_M \leq N_i$ the estimation problem is well-defined.

In the following, we shortly review the *polynomial*, *piecewise polynomial*, and *splines* basis models for the basis func-

tion matrices.

B. Polynomials Basis Model

One way to capture or approximate the frequency-selective behavior of frequency responses is to project them onto a set of polynomial basis functions for approximation [37], [39]. Using a monomial form for the basis, the matrices $\mathbf{B}_D^i, \mathbf{B}_M^{i_p}$ are expressed as

$$\begin{aligned} \mathbf{B}_D^i(N_i, N_D) &= \begin{bmatrix} 1 & 1 & 1 & \cdots & 1 \\ 1 & 2 & 2^2 & \cdots & 2^{N_D-1} \\ \vdots & \vdots & \vdots & \ddots & \vdots \\ 1 & N_i & N_i^2 & \cdots & N_i^{N_D-1} \end{bmatrix} \\ \mathbf{B}_M^{i_p}(N_i^{i_p}, N_M^{i_p}) &= \begin{bmatrix} 1 & 1 & 1 & \cdots & 1 \\ 1 & 2 & 2^2 & \cdots & 2^{N_M^{i_p}-1} \\ \vdots & \vdots & \vdots & \ddots & \vdots \\ 1 & N_i^{i_p} & (N_i^{i_p})^2 & \cdots & (N_i^{i_p})^{N_M^{i_p}-1} \end{bmatrix} \end{aligned} \quad (24)$$

Matrices of this form are called *Vandermonde matrix* and they are increasingly ill-conditioned as the degree of polynomial increases. An orthonormal set of basis vectors can be obtained by taking the QR-decomposition of the basis matrices [38], such that $\mathbf{B}_D^i = \mathbf{Q}_D^i \mathbf{R}_D^i, \mathbf{B}_M^{i_p} = \mathbf{Q}_M^{i_p} \mathbf{R}_M^{i_p}$ and (22) is transformed to

$$\begin{aligned} \underline{\mathbf{Y}}^i &= \mathbf{X}^i \mathbf{Q}_D^i \mathbf{R}_D^i \underline{\mathbf{G}}_{D,B}^i + \mathbf{X}^{m\#} \mathbf{Q}_M^i \mathbf{R}_M^i \underline{\mathbf{G}}_{M,B}^i + \underline{\mathbf{N}}^i \\ &= \mathbf{X}^i \mathbf{Q}_D^i \mathbf{R}_D^i \underline{\mathbf{G}}_{D,B}^i + \mathfrak{B} \text{Diag} \left(\begin{bmatrix} \text{Diag}(\mathbf{X}^{m_1\#}) \mathbf{Q}_M^{i_1} \\ \text{Diag}(\mathbf{X}^{m_2\#}) \mathbf{Q}_M^{i_2} \\ \vdots \\ \text{Diag}(\mathbf{X}^{m_{N_u}\#}) \mathbf{Q}_M^{i_{N_u}} \end{bmatrix} \right) \begin{bmatrix} \mathbf{R}_M^{i_1} \underline{\mathbf{G}}_{M,B}^{i_1} \\ \mathbf{R}_M^{i_2} \underline{\mathbf{G}}_{M,B}^{i_2} \\ \vdots \\ \mathbf{R}_M^{i_{N_u}} \underline{\mathbf{G}}_{M,B}^{i_{N_u}} \end{bmatrix} + \underline{\mathbf{N}}^i \\ &= \Psi_D^i \Phi_D^i + \mathfrak{B} \text{Diag} \left(\begin{bmatrix} \Psi_M^{i_1} \\ \Psi_M^{i_2} \\ \vdots \\ \Psi_M^{i_{N_u}} \end{bmatrix} \right) \begin{bmatrix} \Phi_M^{i_1} \\ \Phi_M^{i_2} \\ \vdots \\ \Phi_M^{i_{N_u}} \end{bmatrix} + \underline{\mathbf{N}}^i \\ &= \Psi_D^i \Phi_D^i + \Psi_M^i \Phi_M^i + \underline{\mathbf{N}}^i \\ &= \tilde{\Psi}^i \tilde{\Phi}^i + \underline{\mathbf{N}}^i \end{aligned} \quad (26)$$

where

$$\begin{aligned} \Psi_D^i &= \mathbf{X}^i \mathbf{Q}_D^i; \quad \Psi_M^{i_p} = \mathbf{X}^{m_p\#} \mathbf{Q}_M^{i_{N_p}} \\ \Phi_D^i &= \mathbf{R}_D^i \underline{\mathbf{G}}_{D,B}^i; \quad \Phi_M^{i_p} = \mathbf{R}_M^{i_p} \underline{\mathbf{G}}_{M,B}^{i_p} \\ \tilde{\Psi}^i &\triangleq [\Psi_D^i \quad \Psi_M^i]; \quad \tilde{\Phi}^i \triangleq [(\Phi_D^i)^T \quad (\Phi_M^i)^T]^T \end{aligned} \quad (27)$$

and now the coefficient vectors to be estimated are Φ_D^i and Φ_M^i . The polynomial basis model approximates the effective response with an N^{th} degree polynomial, and is therefore sensitive to the choice of polynomial order. For a *smoothly varying* response, the polynomial approximation is optimal. However, if the effective response to be approximated has a deep fade at any point in the approximation interval then the

$$\begin{aligned}\mathbf{B}_D^i &= \left[\mathbf{1}, \underline{\xi}_D, \underline{\xi}_D^2, \dots, \underline{\xi}_D^{N_S}, \left(\underline{\xi}_D - \lambda_1 \right)_+^{N_S}, \dots, \left(\underline{\xi}_D - \lambda_{N_D^k} \right)_+^{N_S} \right]; \\ \mathbf{B}_M^i &= \left[\mathbf{1}, \underline{\xi}_M, \underline{\xi}_M^2, \dots, \underline{\xi}_M^{N_S}, \left(\underline{\xi}_M - \lambda_1 \right)_+^{N_S}, \dots, \left(\underline{\xi}_M - \lambda_{N_M^k} \right)_+^{N_S} \right]\end{aligned}\quad (29)$$

resulting approximation is poor [39].

C. Piece-wise (PW) Polynomial Basis Model

To overcome the limitations of polynomial basis, piece-wise polynomial model can be used where the effective response is sliced into small pieces and each slice is modeled with a low degree polynomial. The piece-wise polynomial modeling approach can better approximate a *highly frequency-selective* response than the polynomial, but the size of associated coefficient vectors is larger. In this paper, the response over one resource block N_{SC}^{RB} , which contains twelve subcarriers in LTE, is projected onto a small set of polynomial basis functions such that the basis function matrices of (22) take the form

$$\mathbf{B}_{D;M}^i = \begin{bmatrix} \tilde{\mathbf{B}}(N_{D;M}) & \mathbf{0} & \dots & \mathbf{0} \\ \mathbf{0} & \tilde{\mathbf{B}}(N_{D;M}) & \dots & \mathbf{0} \\ \vdots & \vdots & \ddots & \vdots \\ \mathbf{0} & \mathbf{0} & \dots & \tilde{\mathbf{B}}(N_{D;M}) \end{bmatrix} \quad (28)$$

where

$$\tilde{\mathbf{B}}(N_{D;M}) = \begin{bmatrix} 1 & 1 & 1^2 & \dots & 1 \\ 1 & 2 & 2^2 & \dots & 2^{N_{D;M}} \\ 1 & \vdots & \vdots & \ddots & \vdots \\ 1 & N_{SC}^{RB} & (N_{SC}^{RB})^2 & \dots & (N_{SC}^{RB})^{N_{D;M}} \end{bmatrix}.$$

In general, piece-wise polynomials are simpler to implement than ordinary polynomial, but they suffer from the discontinuities at the connecting region between the slices (i.e. resource blocks). Hence, the piece-wise polynomial model is not efficient for estimating a longer channel response.

D. Splines Basis Model

In order to have least possible oscillations in a way that polynomials in connecting regions join as smoothly as possible while keeping the size of coefficient vectors reasonably small, spline basis model is now reviewed. Among its many other applications such as in computer aided design and in image processing [33], splines model is also well known and widely used for the identification of frequency selective and time varying channels [34] - [36].

Splines are also piece-wise polynomials with continuity constraints between the connecting pieces. The connecting points are called *knots* and the interval between two knots is called a *knot interval* (which is equal to N_{SC}^{RB} subcarriers in this paper). Each segment of a spline of degree N_S is an N_S^{th} -degree polynomial, and the polynomials in any connecting interval have the same f^{th} derivative, $f \in \{0, 1, \dots, N_S - 1\}$, at the knot, thus resulting in a continuous

curve. Defining the spline over the user bandwidth of N_i subcarriers for which the basis function matrices are given by (29), where $\underline{\xi}_D = [1, 2, \dots, N_i]^T$, $\underline{\xi}_M = [1, 2, \dots, N_i^{i_p}]^T$, λ_a is the index in a^{th} knot with total N_D^k knots for the direct channel response vector and N_M^k knots for the mirror channel response vector, and

$$(\underline{\xi} - \lambda_i)_+^n = \begin{cases} (\underline{\xi} - \lambda_i)^n & \text{if } \underline{\xi} \geq \lambda_i \\ 0 & \text{otherwise.} \end{cases} \quad (30)$$

Another way of defining alternative splines basis functions is to use *B-splines* that have better numerical properties than normal splines. They are also characterized for a given set of knots with symmetrical bell-shaped functions, which can be found using the Cox-de Boor recursion formula [39].

E. Basis Models Comparison

In order to quantify the modeling accuracy of above discussed different basis function approximations, we carry out MATLAB simulations where basis functions are used to approximate the frequency responses over different resource block lengths of a multipath fading channel with maximum delay spread of $2.5\mu\text{sec}$ and power delay profile following the Extended Vehicular A model as described in [30]. For fair comparison, the number of model parameters (i.e. the size of coefficient vectors) is kept small relative to the number of RBs. The average normalized mean-squared error (NMSE) of the approximated channel response over 10 000 independent channel realizations is calculated at SNR = 30 dB and presented in Table-I. The resulting NMSE values suggest that the proposed basis function approximation techniques are able to accurately estimate the channel responses. The results of this experiment are also in excellent agreement with the discussion in previous subsections. For a given length of resource blocks, spline approximation has the best performance among the approximation techniques. The piece-wise polynomial approximation performs better than the polynomial for larger RB lengths but requires considerably higher number of parameters for efficient approximation. On the other hand, we notice that the number of estimated parameters is significantly small, e.g., a channel response over 50 RBs (= 600 subcarriers) can be efficiently approximated with splines model that requires only 53 parameters. Thus, the effectiveness and practical applicability of proposed techniques is evident, and are taken in use in the next sections in estimating effective direct and mirror channels for all simultaneously scheduled UEs.

TABLE I
NMSE BETWEEN TRUE AND APPROXIMATED CHANNEL RESPONSES
(EXTENDED VEHICULAR A MODEL) FOR DIFFERENT NUMBER OF
CONSECUTIVE RBs

# of RBs	No. of model parameters			NMSE (1×10^{-3})		
	Poly.	Spline	PW Poly.	Poly.	Spline	PW Poly.
1	4	4	4	0.3	0.3	0.3
5	8	8	10	0.6	0.6	1.9
10	13	13	20	2.5	1.0	1.5
15	18	18	30	4.6	1.1	1.4
20	23	23	40	5.2	1.1	1.4
25	28	28	50	6.8	1.1	1.3
30	33	33	60	14.8	1.1	1.3
35	38	38	70	20.2	1.1	1.3
40	43	43	80	22.3	1.1	1.3
45	48	48	90	24.1	1.1	1.3
50	53	53	100	28.3	1.1	1.2

V. JOINT ESTIMATION OF TRANSMITTER I/Q IMBALANCES, SMALL CFOS, AND CHANNELS USING LTE UPLINK REFERENCE SIGNALS

In this section, we first shortly review the LTE frame and uplink reference signal structures that are exploited in the estimation, and then describe the overall estimation algorithm in detail.

A. LTE Frame and Uplink Reference Signal Structures

The data transmission in LTE uplink is arranged in radio frames where each radio frame is 10 msec in duration and is divided into ten subframes. A subframe is of 1 msec duration and consists of two slots, each of which is 0.5 msec in duration [11]. With the normal CP configuration, a slot carries seven SC-FDMA symbols with six data symbols and one time-multiplexed reference symbol located in the middle. Compared to the data symbols which are pre-coded by DFT, the reference symbols are mapped directly to the subcarriers in the uplink transmission as shown in Fig. 1.

In the reference signal generation context, LTE physical layer specifications [11] define two types of reference signals—the demodulation reference signals (DMRS) and the sounding reference signals (SRS). The DMRS of a user— i , say $r_{u,v}^{i,\alpha}(p)$, are used for the i^{th} user's channel estimation and are defined by the cyclic shift α of the base sequence $\bar{r}_{u,v}^i(p)$ as

$$r_{u,v}^{i,\alpha}(p) = e^{j\alpha n} \bar{r}_{u,v}^i(p), \quad 0 \leq p \leq N_i - 1 \quad (31)$$

where $u \in \{0, 1, 2, \dots, 29\}$ is the group number of the base sequence, v is the serial number within the group, and $N_i = m_i N_{SC}^{RB}$, $m_i \in \{1, 2, \dots\}$ is DMRS length [11], [31]. A physical resource block in LTE is defined for one slot and consists of $N_{SC}^{RB} = 12$ subcarriers. The base sequences $\bar{r}_{u,v}^i(p)$ are generated from *Zadoff-Chu* sequences and have the properties of constant amplitude resulting in efficient power amplifier (PA) usage with low peak-to-average power ratio

(PAPR), zero circular autocorrelation and low cross correlation between different sequences. In reference [31] exact procedure of generating LTE reference signals is described based on 3GPP specifications [11], detailing how the base sequences of different lengths are derived from Zadoff-Chu sequences.

B. Frequency Domain Least Squares Parameter Estimation with LTE Reference Signals

In LTE, 1 msec subframe forms a transmission time interval (TTI). By exploiting the two received DMRS symbols in a TTI, the proposed estimator, operating in frequency domain, estimates the coefficient vectors of all simultaneously scheduled uplink users within a single LTE subframe. A natural approach for estimating the basis function coefficient vectors \mathbf{G}_B^i of (22) is to use the LS estimator. During the DMRS transmission, the received signal vector of user- i in (22) becomes

$$\begin{aligned} \mathbf{Y}_{DMRS(\varrho)}^i &= \mathbf{X}_{DMRS(\varrho)}^i \mathbf{B}_D^i \mathbf{G}_{D,B-DMRS(\varrho)}^i + \\ &\quad \mathbf{X}_{DMRS(\varrho)}^{m\#} \mathbf{B}_M^i \mathbf{G}_{M,B-DMRS(\varrho)}^i + \mathbf{N}^i \quad (32) \\ &= \tilde{\mathbf{X}}_{DMRS(\varrho)}^i \tilde{\mathbf{B}}^i \tilde{\mathbf{G}}_{B-DMRS(\varrho)}^i + \mathbf{N}^i \end{aligned}$$

where $\varrho \in \{1, 2\}$ denotes the DMRS index within a 1 msec subframe. The LS estimator [40] of coefficient vectors at the reference symbol positions ϱ is then given by

$$\begin{aligned} \hat{\mathbf{G}}_{B-DMRS(\varrho)}^i &= \begin{bmatrix} \hat{\mathbf{G}}_{D,B-DMRS(\varrho)}^i \\ \hat{\mathbf{G}}_{M,B-DMRS(\varrho)}^i \end{bmatrix} \\ &= \left(\tilde{\mathbf{B}}^i \tilde{\mathbf{X}}_{DMRS(\varrho)}^H \tilde{\mathbf{X}}_{DMRS(\varrho)}^i \tilde{\mathbf{B}}^i \right)^{-1} \times \\ &\quad \tilde{\mathbf{B}}^i \tilde{\mathbf{X}}_{DMRS(\varrho)}^H \mathbf{Y}_{DMRS(\varrho)}^i \end{aligned} \quad (33)$$

which is implemented for all simultaneously scheduled users $i = 1, 2, \dots, U$ within a subframe, and independently per each receiver antenna in case of multi-antenna receiver. The actual effective direct and mirror channel filters can then be computed by multiplying the basis function coefficient vectors with the basis functions matrices, as shown in (22). Once the estimates of channel filters on both DMRS symbols are obtained, the effective channel responses over all the data-bearing SC-FDMA symbols and subcarriers are obtained through linear interpolation and extrapolation within the subframe. The estimation procedure is executed independently at every subframe. The estimated direct and mirror channel filter responses are then substituted in (15), (16), (20), or (21) to detect the actual transmitted data.

VI. SIMULATION RESULTS AND ANALYSIS

A. System Parameters for Simulations

We consider an uplink multi-user SC-FDMA system whose parameters are chosen according to 3GPP LTE 10 MHz carrier bandwidth. There are in total $M = 1024$ subcarriers, of which 600 are active subcarriers. The total number of resource blocks is thus 50, and each user may occupy one or more resource blocks. The subcarrier spacing is $f_s = 15$ kHz and the total active bandwidth is 9 MHz. The mobile station TX gain

and phase imbalance values are randomly generated in each simulation realization in the range of $g_T = 3\% \cdots 13\%$ and $\phi_T = -5^\circ \cdots 5^\circ$, respectively, while the inphase and quadrature branch filters are modeled with 3-taps and their coefficients are $\mathbf{h}_{I,T} = [0.998, 0.07, 0]^T$, $\mathbf{h}_{Q,T} = [1, -0.02, 0.01]^T$. The basic sample rate in the waveform processing is $1024 \times 15e3 = 15.36$ MHz, and the I/Q imbalance values correspond to an average front-end IRR of $23 \cdots 27$ dB within the system BW and represent a challenging yet practical example case. The BS RX I/Q imbalance is considered calibrated and has an IRR in the order of 55 dB [21], [28], [29]. The in-channel selectivity requirements [12] address the reception of simultaneous users with different power levels at the LTE BS and the typical inband dynamic range for the BS RX is in the order of 21.5 dB. To model such dynamic range at the BS receiver input, the uplink users are scaled properly, and the relative power levels are randomly chosen in the range of $-25 \cdots 0$ dB. All the transmitted signals pass through independent block-fading multipath channels with maximum delay spread of $2.5\mu\text{s}$ and power delay profile following the Extended Vehicular A model [30]. Furthermore, channel responses between a user transmitter and each receiver antenna are independent and uncorrelated. The carrier frequency is 2 GHz and according to the specified uplink carrier frequency synchronization requirements for LTE [9], [10], the CFO is in the range of $-200 \cdots 200$ Hz. Aiming at feasible complexity in the parameter estimation, the estimator order of direct and mirror channels for a user- i with polynomial approximation is defined as: $(N_i/N_{SC}^{RB}) + 3$. For splines and piece-wise polynomial, each RB is estimated separately with a cubic polynomial giving $(N_i/N_{SC}^{RB}) + 3$ and $(N_i/N_{SC}^{RB}) \times 3$ parameters, respectively.

B. Simulation Setup

We assume that all scheduled users transmit their data in one uplink subframe that consists of two DMRS symbols and twelve data symbols. For each simulation realization, TX I/Q imbalances, CFOs, and channel impulse responses are independently generated for each user and their effects are introduced to the uplink signals. The received signal is then a sum of impaired UE signals. As shown in Fig.1, the proposed receiver extracts the DMRS symbols from the received data after M-point FFT and estimates the joint channel and impairment responses, as elaborated in Sections IV and V. The compensator then utilizes the estimated and interpolated coefficients of direct and mirror channel filters and applies the joint mirror-carrier ZF or MMSE equalization scheme of Section III to detect the transmitted data of each user. In the following figures, “SER” refers to the symbol error rate of data bearing symbols \mathbf{s}^i whereas axis labels “Average RX SNR” and “RX SNR of Target UE” refer simply to the overall received signal power relative to total receiver noise power and average received power of target user vs. noise power calculated over the target UE bandwidth, respectively. Moreover, we illustrate the results by plotting the uncoded SER and evaluate the performance at $\text{SER} = 10^{-2}$, which is of practical interest for uncoded evaluations. We realize and

clearly acknowledge that all practical communication systems deploy also error control coding, in order to reduce the symbol and bit error rates. However, as demonstrated in the following simulation examples, the detrimental effects of mirror UE interference with inband dynamic range in the order of 20 dB or so at the BS RX input and with UE transmitters’ inband I/Q imaging still being within the standardized emissions, the weaker UE uncoded SER is practically flat, and saturates to a very high level independently of the thermal noise SNR. Hence, in such challenging yet realistic scenarios, error control coding cannot certainly compensate all the degradation, while more detailed evaluations with coded transmission are left for future work. To obtain valid statistics, all simulation figures are plotted by averaging results of 3000 independent channel and other parameters realizations.

C. Impact of Transmitter I/Q Imbalances and CFOs

To demonstrate the detrimental effects of IUI due to mobile transmitter I/Q imbalances, we first report a simulation scenario where classical per-subcarrier linear MMSE equalizer with known channel estimates is deployed for channel equalization and without any more elaborate processing against TX impairments. Fig. 3 displays the numerical results for the average SER as a function of SNR for a two users uplink SC-FDMA system with single input single output (SISO) and 1×2 single input multiple output (SIMO) antenna configurations. The target user in this example is a weaker user which is on average 20 dB weaker than the mirror band UE. The subcarrier modulation for both UEs is 16-QAM. In addition to normal channel equalization, the common phase error is corrected when CFO is present. An immediate conclusion that can be drawn from both plots is the huge signal distortion brought by the TX I/Q imbalances, when no impairment suppression is deployed, while the effect of CFO error is negligibly small, when the system parameters conform to LTE standardization. This result verifies the assumptions made in Section II that IUI induced by TX I/Q imbalances heavily affects the performance whereas the localized subcarrier mapping is fairly immune to small CFO errors. Also notice that the SER curves become practically saturated at a very high level when TX I/Q imbalance is present and increasing the SNR does not improve SER. Furthermore, in case of ideal system, substantial diversity gain of 1×2 SIMO can be observed over SISO, nevertheless, SER remains high with no impairments compensation. It is thus obvious that the uplink performance can be heavily influenced by the TX I/Q imbalances, even though within LTE specifications, especially when there is considerable dynamic range at the input of the BS RX. Thus additional enhancement through efficient and sophisticated estimation and compensation algorithms can substantially improve the link performance. This is demonstrated here by the solid blue J-MMSE curve, where ideal channel response and impairment knowledge is assumed.

D. Performance of Proposed Estimation and Compensation Techniques for SISO antenna configuration

The performance of proposed estimation and equalization algorithms for single antenna receiver is next demonstrated

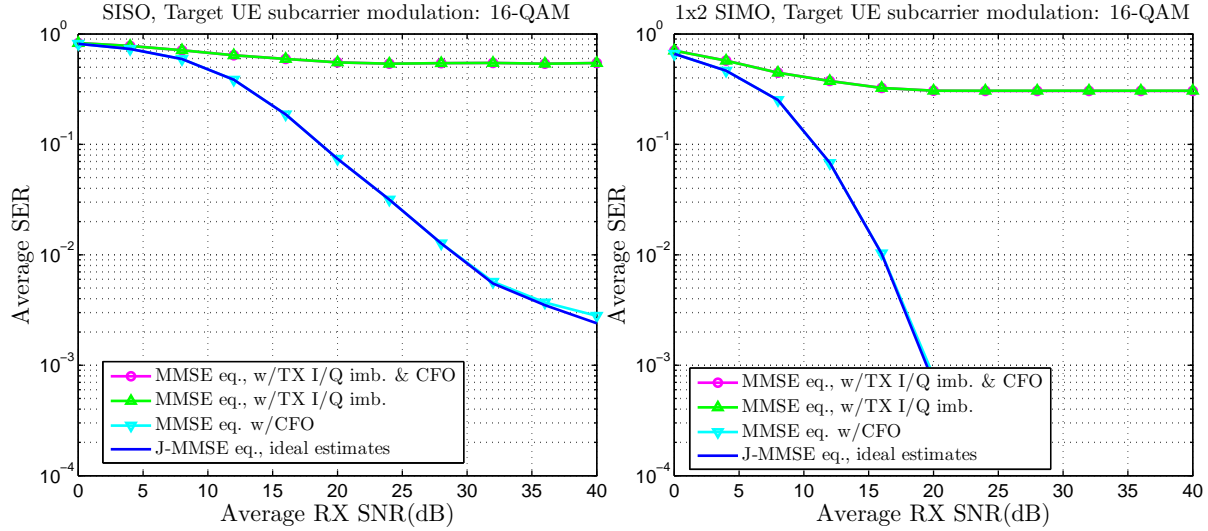


Fig. 3. Average SER performance with SISO and 1×2 SIMO antenna configurations of the target user without impairment estimation and equalization in an uplink SC-FDMA system with 20 dB stronger mirror band UE. CFOs $\in [-200, 200]$ Hz, transmitter I/Q imbalances: 23...27dB, Veh. A channel model with maximum delay spread of 2.5μ sec. The curves were obtained by averaging results of 3000 independent channel, CFO, and I/Q imbalance parameter realizations. Also the performance of joint subcarrier processing based equalization, with ideal parameter knowledge, is shown for reference.

in this sub-section, where an uplink multi-user SC-FDMA system is again simulated and the performance is compared to the receiver which has perfectly known total channel matrix (i.e. channel responses, TX I/Q imbalances, and CFOs are known). Conceptually, the performance of a system with known estimates is similar to the one with no front-end radio impairments and for which perfect channel estimates are available. Three difference cases, based on different uplink user settings and baseband modulations, are simulated and are presented in detail as follows. The fundamental parameters of these simulation scenarios are also listed in Table-II, and are referred to figure captions for better readability.

1) Two UEs Experiment with Fixed Dynamic Range:

We first consider a simple scenario where two wideband uplink users of equal bandwidths, each spanning 24 RBs, are communicating with a BS RX. The first user is assumed to be a weaker user and is the *target user* in this example, as being more sensitive to any additional distortion and interference. The second user at the image band of target user is assumed to be stronger and employs 16-QAM baseband modulation. The received power level of stronger UE is assumed to be on average 15 dB higher than that of the target UE. Fig. 4 shows the average uncoded SER performance of the target user with different baseband modulations. The x-axis in the figures represents the RX SNR of the target user. For comparison purposes, the solid blue curve with ideal channel estimates and perfect impairment knowledge is also plotted. In all plots, without impairment processing, we observe significant performance degradation due to IUI from the strong UE located on the image band. On the other hand, the proposed methods are able to greatly reduce SER. Focusing first on the estimation quality of various channel response approximation methods, LS estimation with splines is shown to outperform other channel response approximation methods. We have already shown in Section IV-E that the spline approximation is efficient

TABLE II
SIMULATION SCENARIOS FOR SINGLE ANTENNA RX CASE

scenario-1	Two UEs experiment with fixed dynamic range <ul style="list-style-type: none"> • Weaker target UE and stronger mirror band UE, each with BW: 24 RBs. • Target UE modulation: 16-QAM & 64-QAM, Mirror band UE modulation: 16-QAM. • Received power level difference: 15 dB.
scenario-2	Two UEs experiment with varying dynamic range and modulations <ul style="list-style-type: none"> • Target UE modulation: 16-QAM, Mirror band UE modulation: QPSK, 16-QAM, or 64-QAM (varies depending on the power difference between two UEs).
scenario-3	Multi UEs experiment with varying bandwidths & dynamic range <ul style="list-style-type: none"> • Total BW: 50 RBs, and each UE bandwidth: 1 RB - 25 RBs (randomly chosen in each simulation realization). • Modulation of each UE: 16-QAM. • RX inband dynamic range: 25 dB.

both in terms of approximation accuracy and complexity, whereas the polynomial approximation is not very efficient for

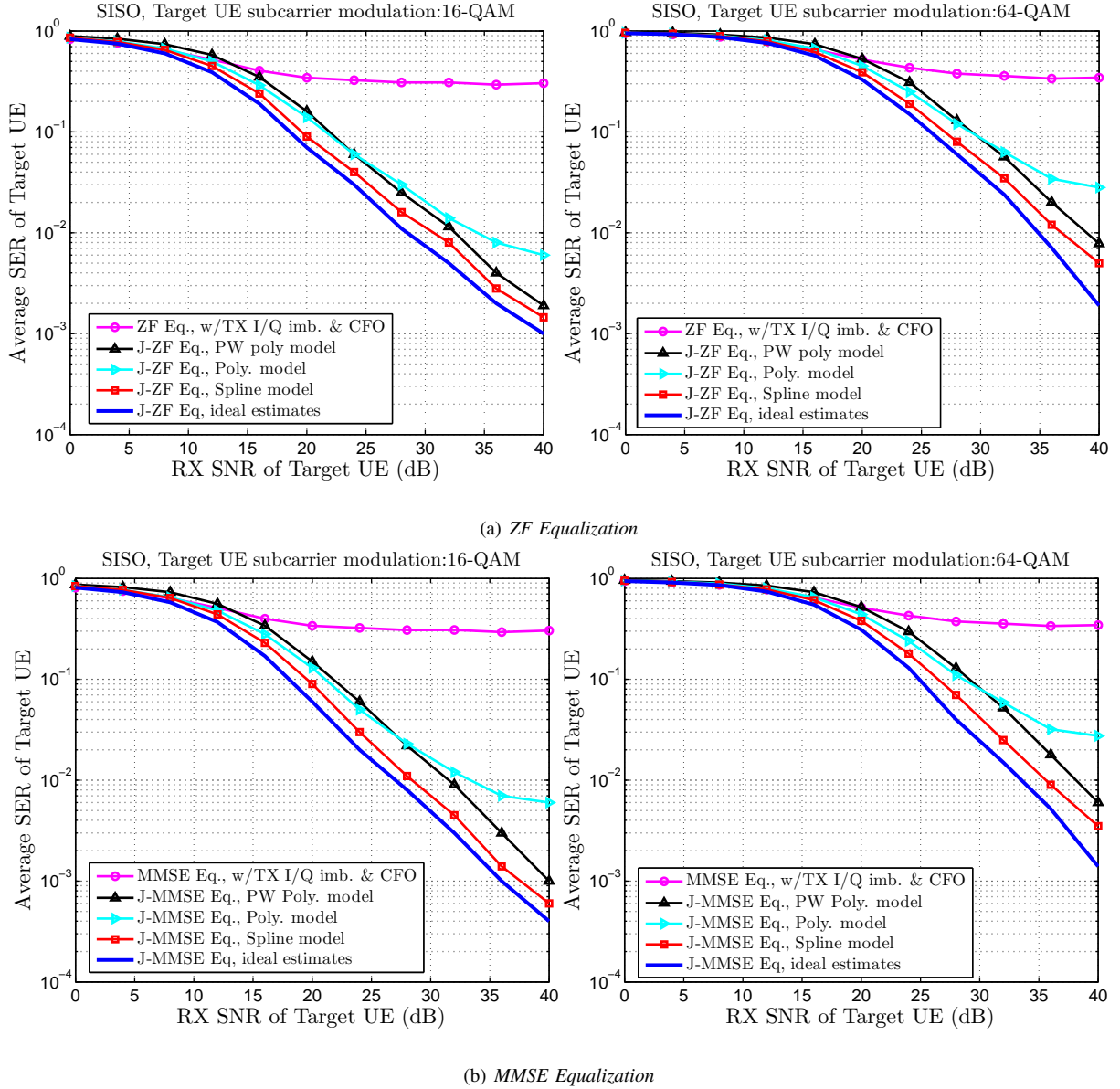


Fig. 4. Average SER performance of the target user for single antenna RX after estimation and equalization in an uplink SC-FDMA system with 15 dB stronger mirror band UE. CFOs $\in [-200, 200]$ Hz, transmitter I/Q imbalances: 23 \dots 27 dB, veh. A channel model with maximum delay spread of $2.5\mu\text{sec}$. The curves were obtained by averaging results of 3000 independent channel, CFO, and I/Q imbalance parameter realizations (scenario-1).

approximating effective channel responses over larger bandwidths. At uncoded SER of 10^{-2} , LS spline approximation has about 1.2 dB and 0.8 dB degradation for 16-QAM and 2.5 dB and 2 dB for 64-QAM compared with the ideal reference system when J-ZF and J-MMSE equalization are used, respectively. Furthermore, J-MMSE equalization gives about 2.5–4 dB improvement in SNR over the J-ZF equalizer.

2) *Two UEs Experiment with Varying Dynamic Range and Modulations*: To further quantify the performance, the target user SER is evaluated against the power level difference for the image band UE. Here, 16-QAM baseband modulation is used for the target user, whereas the image band UE modulation is varied depending on the power level difference. When the target user is actually stronger and the power level difference is smaller than -5 dB, QPSK modulation is employed. For the power level difference in the range of

$-5 \dots 5$ dB, implying increased received power for the mirror band UE, 16-QAM modulation is used, and for more than 5 dB difference, 64-QAM baseband modulation is used. For the mirror UE, this is reflecting the link adaptation of the true system which controls the modulation and coding scheme depending on the received inband SNR. The average uncoded SER curves of the target user with different SNRs are depicted in Fig. 5. The results suggest that even a fairly weak image band UE can cause serious interference to the target user band. The proposed estimation and equalization methods, on the other hand, are shown to reduce SER for wide receiver inband dynamic range. Furthermore, the J-MMSE equalization is again shown to improve the SER compared to the J-ZF equalizer.

3) *Multi UEs Experiment with Varying Bandwidths and Dynamic Range*: Finally, we consider a more complex scenario,

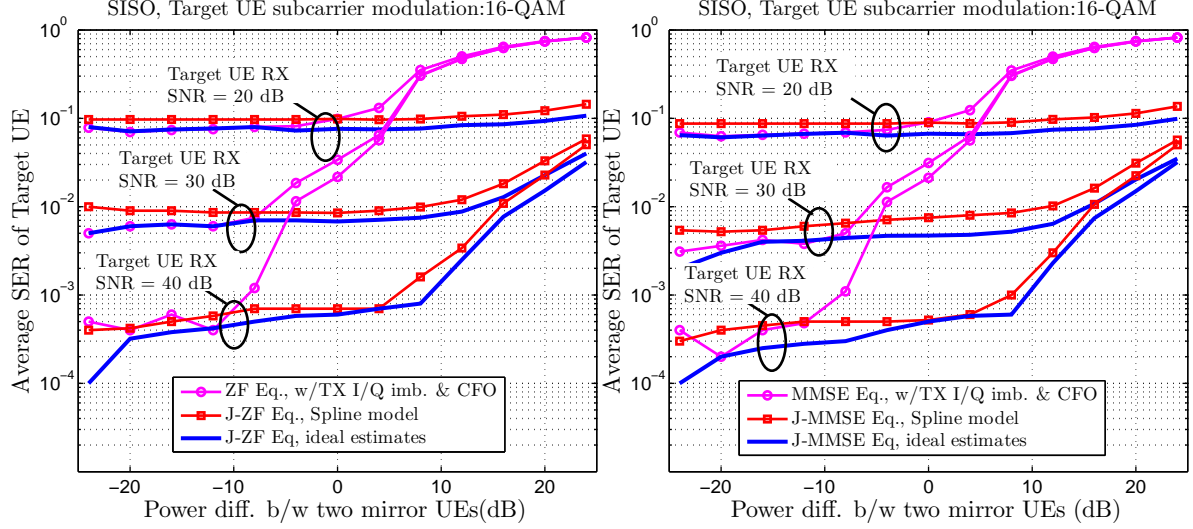


Fig. 5. Average SER performance of the target user for single antenna RX after estimation and equalization in an uplink SC-FDMA system vs. power level difference of the mirror UEs. CFOs $\in [-200, 200]$ Hz, transmitter I/Q imbalances: $23 \dots 27$ dB, veh. A channel model with maximum delay spread of $2.5 \mu\text{sec}$. The curves were obtained by averaging results of 3000 independent channel, CFO, and I/Q imbalance parameter realizations (scenario-2).

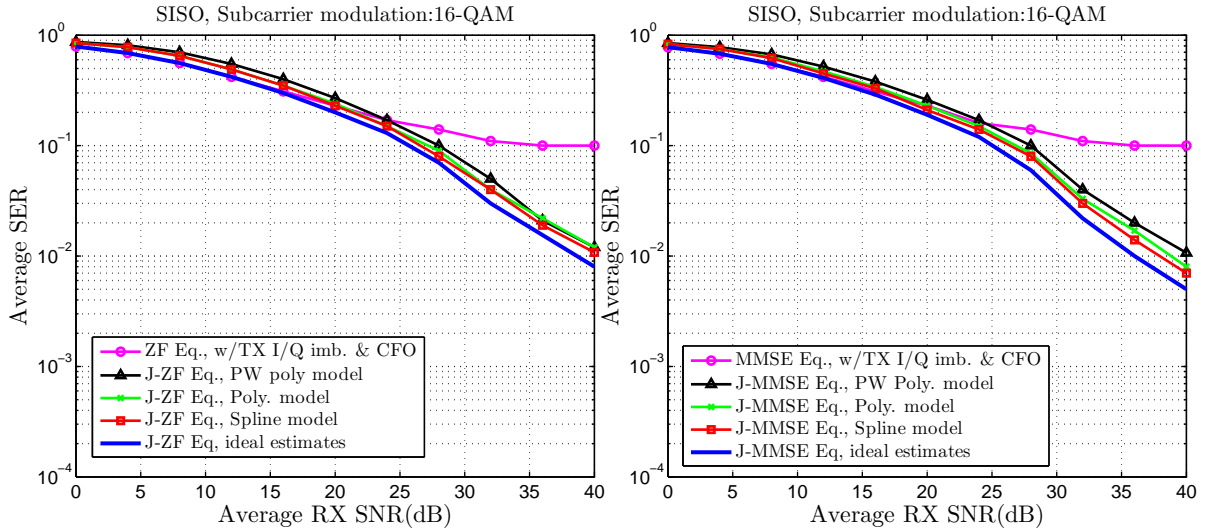


Fig. 6. Average SER performances of single antenna RX over all UEs after estimation and equalization of uplink SC-FDMA system with different number of users of different transmission power levels in each channel realizations. The maximum allowed inband dynamic range at BS input is 25 dB. CFOs $\in [-200, 200]$ Hz, transmitter I/Q imbalances: $23 \dots 27$ dB, Veh. A channel model with maximum delay spread of $2.5 \mu\text{sec}$. The curves were obtained by averaging results of 3000 independent channel, CFO, and I/Q imbalance parameter realizations (scenario-3).

where the total number of uplink users and correspondingly their bandwidths are different in each channel realization. Each user is allocated from one RB to a maximum of 25 RBs, and the baseband symbols are drawn from 16-QAM constellation. Also, we allocate different power levels randomly generated within the specified receiver inband dynamic range of $-25 \dots 0$ dB, together with CFOs and TX I/Q imbalances whose parameters are also generated randomly in each channel realization. The interference falling in the band of a single UE may now originate from one or more users of possibly different power levels located on the mirror sub-band. Fig. 6 characterizes the overall average sensitivity of such uplink SC-FDMA

system to radio impairments and the improvement achieved by the proposed estimation and equalization approaches. As the results suggest, the uplink transmission is susceptible to radio impairments and for $\text{SNR} \geq 30$ dB, the SER curve, representing the case when no compensation is deployed, saturates at a considerably high SER in the order of 10^{-1} . Comparing the performance of the proposed algorithms with the ideal reference system, shown with the blue solid curve and representing the case of compensation with known ideal estimates, proves that the proposed techniques significantly improve the system performance and reduce SER. Considering first the equalizers performance, the J-MMSE equalization

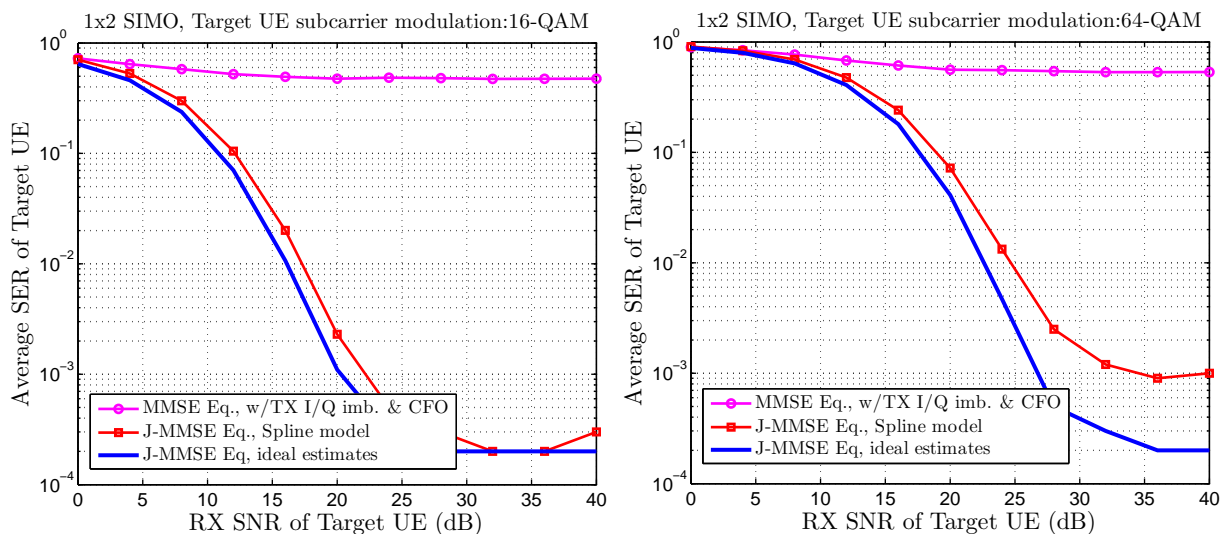


Fig. 7. Average SER performance in dual antenna RX setup of the target user after estimation and equalization in an uplink SC-FDMA system with 25 dB stronger mirror band UE. CFOs $\in [-200, 200]$ Hz, transmitter I/Q imbalances: $23 \cdots 27$ dB, veh. A channel model with maximum delay spread of $2.5 \mu\text{sec}$. The curves were obtained by averaging results of 3000 independent channel, CFO, and I/Q imbalance parameter realizations.

gives about 2.5 – 3 dB improvement in SNR over the J-ZF equalizer. When comparing the performance of estimator with different response approximation methods presented in Section V, the LS estimator with proposed channel response approximation techniques yields performance close to the reference system. Thus, it can be concluded that the detrimental effects of radio impairments can be efficiently suppressed using the proposed estimation and equalization methods even in the presence of considerable inband dynamic range and mirror UE interference stemming simultaneously from multiple UEs. Notice that x-axis in Fig. 6 represents average received SNR over all users.

E. Performance of Proposed Estimation and Compensation Techniques For 1×2 SIMO antenna configuration

In this subsection, we present the performance results for an uplink multi-user SC-FDMA system with a dual antenna receiver, and compare again the performance of proposed estimation and equalization algorithms with a reference system which has perfect channel and impairments knowledge. For compactness of presentation, we consider only the two users experiment with challenging receiver inband dynamic range in the order of 25 dB. The first user, assumed target user, is a weaker user whereas the mirror band second user is stronger and employs 16-QAM baseband modulation. The average uncoded SER performance of the target user with different baseband modulations is shown in Fig. 7. The first observation is the steep slope of the ideal and compensated curves indicating the diversity gain achieved with SIMO. However, in this challenging yet realistic scenario, the target user SER is practically flat when no impairments compensation scheme is employed even though SIMO antenna configuration is adopted. The proposed estimation and equalization technique is again shown to greatly improve the link performance being very close to the ideal system performance bound. Notice that a

residual error noise floor is observed in Fig. 7 at high SNR region. This is due to the ICI terms that were neglected in simplifying the basic system equations from (7) to (9), and is now more clearly visible due to basic diversity gain and challenging power difference of 25 dB between the UEs. Nevertheless, substantial improvement through the proposed techniques is anyway clearly demonstrated also in case of dual-antenna BS receiver.

F. Summary of Simulation Results

It can be established from the results of these experiments that RF impairments can severely limit the obtainable link performance, while the proposed methods can essentially handle realistic transmission and impairment scenarios. The proposed response approximation methods are shown to approximate the direct and mirror channel filter responses with high accuracy and feasible complexity. The spline approximation not only approximates the responses more accurately than the piece-wise polynomial and the polynomial approximation, but also requires considerably less model parameters than the piece-wise polynomial approximation. On the other hand, the computational complexity of all proposed estimation methods is, in general, feasible for the current state-of-the-art signal processing implementation platforms. To illustrate this, the computational complexities of different parameter estimation cases over one resource block, in terms of elementary floating point operations (flops), can be easily evaluated and are summarized in Table III. Notice that the basis function matrices are fixed and can thus be pre-calculated. It is further shown that J-MMSE equalization gives more than 3 dB performance gain over the J-ZF equalization. Since the channel and impairments are estimated and equalized jointly in the digital domain, the proposed algorithms can thus be directly used in the BS RX without any modification in uplink LTE pilot structure or analog/RF hardware design.

TABLE III
PARAMETER ESTIMATION COMPLEXITY PER RESOURCE BLOCK IN
SOLVING (33), USING EITHER NORMAL EQUATIONS APPROACH OR QR
DECOMPOSITION [42].

	Poly. (flops)	Spline (flops)	PW Poly. (flops)
Normal Equations	7595	7595	4320
QR factorization	11691	11691	6912

VII. CONCLUSIONS AND FUTURE WORK

This paper addressed selected radio impairment problems in uplink multi-user SC-FDMA systems. Analytic signal models of the received signal when the uplink transmissions are impaired by TX and RX I/Q imbalances, CFOs, and channel distortions were derived. It was shown that I/Q imbalances and CFO cause IUI and ICI, where IUI due to TX I/Q imbalances is more severe and critical to consider when uplink users have localized mapping and different transmission powers. Two practical assumptions were then made to simplify the signal model- (i) CFO is relatively small in the uplink and (ii) RX I/Q imbalance has already been reasonably well calibrated at the BS. Based on the simplified signal model, a compensation structure operating in the digital baseband of the RX was then proposed for the joint mitigation of TX I/Q imbalances, small CFOs, and channel distortions. The compensation structure operates on the pairs of mirror subcarriers and employs linear equalizers, most notably the ZF and the MMSE equalizer. The derivation of the joint mirror carrier MMSE equalizer with arbitrary number of receiver antennas and different power levels of mirror sub-band UE signals is one key contribution of this paper, and shown to clearly outperform the ZF solution. We also showed that the joint channel and considered RF impairments responses can be effectively modeled with appropriate basis functions, which leads to less complex and more efficient parameter estimation. The parameter estimation was then formulated and solved by utilizing DMRS reference symbols in the LTE uplink sub-frame, enabling response and parameter estimation of all simultaneously scheduled UEs. The derivation of joint channel and impairments estimation techniques with 3GPP LTE compliant reference symbols is another key contribution of this paper. Excellent compensation properties of the proposed estimation and equalization schemes were demonstrated through computer simulations under realistic signals, radio impairments, and channel models. In particular, the Spline-based estimation solution combined with joint mirror-carrier MMSE equalization was shown to offer good balance between the modeling accuracy, receiver performance and complexity. Future work will focus on generalizing the signal models, estimation, and compensation techniques, as well as performance evaluations, to coded MIMO-SC-FDMA/OFDMA type systems.

APPENDIX JOINT MIRROR CARRIER MMSE EQUALIZER FOR SIGNALS WITH DIFFERENT RECEIVED POWER LEVELS

Here we derive the joint MMSE equalizer that can process mirror sub-band user signals having different power levels and incorporating arbitrary number of receiver antennas. The J-MMSE equalization filter $\tilde{\mathbf{W}}_{MMSE}(k)$ derived here is used in (16) and (21) for the frequency domain joint equalization of channels and impairments.

A. J-MMSE Equalizer for Multi Antenna RX

Recall first from (18) that the received signal vector for mirror subcarrier pairs with N_{RX} receiver antennas is given by

$$\tilde{\mathbf{Y}}_{SIMO}(k) = \tilde{\mathbf{G}}_{SIMO}(k)\tilde{\mathbf{X}}(k) + \tilde{\mathbf{N}}_{SIMO}(k). \quad (\text{A.1})$$

Our task is then to design a filter $\tilde{\mathbf{W}}(k)$ that minimizes the cost function

$$\mathbf{J} = \mathbb{E} \left\{ \left\| \tilde{\mathbf{X}}(k) - \tilde{\mathbf{W}}(k)\tilde{\mathbf{Y}}_{SIMO}(k) \right\|^2 \right\}$$

$$\tilde{\mathbf{W}}_{MMSE}(k) = \arg \min_{\tilde{\mathbf{W}}(k)} \mathbb{E} \left\{ \left\| \tilde{\mathbf{X}}(k) - \tilde{\mathbf{W}}(k)\tilde{\mathbf{Y}}_{SIMO}(k) \right\|^2 \right\}, \quad (\text{A.2})$$

for which, the J-MMSE equalization filter is given by [41]

$$\tilde{\mathbf{W}}_{MMSE}(k) = \mathbf{R}_{\mathbf{X}\mathbf{Y}}(k)\mathbf{R}_{\mathbf{Y}\mathbf{Y}}^{-1}(k) \quad (\text{A.3})$$

where

$$\mathbf{R}_{\mathbf{X}\mathbf{Y}}(k) = \mathbb{E} \left\{ \tilde{\mathbf{X}}(k)\tilde{\mathbf{Y}}_{SIMO}^H(k) \right\} = \mathbf{R}_{\mathbf{X}\mathbf{X}}(k)\tilde{\mathbf{G}}_{SIMO}^H(k)$$

$$\mathbf{R}_{\mathbf{Y}\mathbf{Y}}(k) = \mathbb{E} \left\{ \tilde{\mathbf{Y}}_{SIMO}(k)\tilde{\mathbf{Y}}_{SIMO}^H(k) \right\}$$

$$= \tilde{\mathbf{G}}_{SIMO}(k)\mathbf{R}_{\mathbf{X}\mathbf{X}}(k)\tilde{\mathbf{G}}_{SIMO}^H(k) + \mathbf{R}_{\mathbf{N}\mathbf{N}} \quad (\text{A.4})$$

are the cross-covariance matrix between $\tilde{\mathbf{X}}(k)$ and $\tilde{\mathbf{Y}}_{SIMO}(k)$, and the auto-covariance matrix of $\tilde{\mathbf{Y}}_{SIMO}(k)$, respectively. Furthermore, $\mathbf{R}_{\mathbf{X}\mathbf{X}}(k) = \mathbb{E} \left\{ \tilde{\mathbf{X}}(k)\tilde{\mathbf{X}}^H(k) \right\}$ and $\mathbf{R}_{\mathbf{N}\mathbf{N}} = \mathbb{E} \left\{ \tilde{\mathbf{N}}_{SIMO}(k)\tilde{\mathbf{N}}_{SIMO}^H(k) \right\}$ are diagonal auto-covariance data matrix and noise matrix, respectively, defined as

$$\mathbf{R}_{\mathbf{X}\mathbf{X}}(k) = \mathfrak{D} \text{diag} \left(\sigma_x^{i^2}(k), \sigma_x^{m^2}(-k) \right)$$

$$\mathbf{R}_{\mathbf{N}\mathbf{N}} = \mathfrak{D} \text{diag} \left(\sigma_{n,1}^2, \sigma_{n,1}^2, \dots, \sigma_{n,N_{RX}}^2, \sigma_{n,N_{RX}}^2 \right). \quad (\text{A.5})$$

where $\sigma_x^{i^2}(k) = \mathbb{E} \left\{ |X^i(k)|^2 \right\}$ and $\sigma_x^{m^2}(-k) = \mathbb{E} \left\{ |X^m(-k)|^2 \right\}$ represent the direct and mirror channel signal powers at k^{th} and its mirror $(-k)^{th}$ subcarrier, respectively, and $\sigma_{n,\chi}^2 = \mathbb{E} \left\{ |N_\chi(k)|^2 \right\}$ represents the noise power at receiver χ , at an individual subcarrier, which is assumed equal on all subcarriers of a single receiver. The J-MMSE

$$\Xi(k) = \begin{bmatrix} |G_D^i(k)|^2 + |G_M^i(k)|^2 \frac{\Upsilon^m(-k)}{\Upsilon^i(k)} + \frac{1}{\Upsilon^i(k)} & (G_D^{i*}(k)G_M^{m*}(-k)) + (G_M^{i*}(k)G_D^{m*}(-k)) \frac{\Upsilon^m(-k)}{\Upsilon^i(k)} \\ ((G_D^i(k)G_M^m(-k)) + (G_M^i(k)G_D^m(-k)) \frac{\Upsilon^m(-k)}{\Upsilon^i(k)} & |G_M^{m*}(-k)|^2 + |G_D^{m*}(-k)|^2 \frac{\Upsilon^m(-k)}{\Upsilon^i(k)} + \frac{1}{\Upsilon^m(-k)} \end{bmatrix}. \quad (\text{A.11})$$

equalization filter in (A.3) can thus be expressed as

$$\tilde{\mathbf{W}}_{MMSE}(k) = \mathbf{R}_{\mathbf{XX}}(k) \tilde{\mathbf{G}}_{SIMO}^H(k) \times \left(\tilde{\mathbf{G}}_{SIMO}(k) \mathbf{R}_{\mathbf{XX}}(k) \tilde{\mathbf{G}}_{SIMO}^H(k) + \mathbf{R}_{\mathbf{NN}} \right)^{-1}, \quad (\text{A.6})$$

which can be further re-expressed using the matrix inversion lemma as

$$\tilde{\mathbf{W}}_{MMSE}(k) = \left(\tilde{\mathbf{G}}_{SIMO}^H(k) \mathbf{R}_{\mathbf{NN}}^{-1} \tilde{\mathbf{G}}_{SIMO}(k) + \mathbf{R}_{\mathbf{XX}}^{-1}(k) \right)^{-1} \times \tilde{\mathbf{G}}_{SIMO}^H(k) \mathbf{R}_{\mathbf{NN}}^{-1}. \quad (\text{A.7})$$

B. J-MMSE Equalizer for Single Antenna RX

For single antenna receiver, $\mathbf{R}_{\mathbf{NN}} = \sigma_n^2 \mathbf{I}$ and the J-MMSE equalization filter in (A.7) can be given in an equivalent form as

$$\tilde{\mathbf{W}}_{MMSE}(k) = \left(\tilde{\mathbf{G}}^H(k) \tilde{\mathbf{G}}(k) + \Lambda_{SNR}^{-1}(k) \right)^{-1} \tilde{\mathbf{G}}^H(k) \quad (\text{A.8})$$

where $\Lambda_{SNR}(k) = \text{Diag}(\Upsilon^i(k), \Upsilon^m(-k))$ is a diagonal matrix with direct and mirror channel per subcarrier SNRs being the diagonal elements, defined as

$$\begin{aligned} \Upsilon^i(k) &\triangleq \frac{\sigma_x^2(k)}{\sigma_n^2} \\ \Upsilon^m(-k) &\triangleq \frac{\sigma_x^2(-k)}{\sigma_n^2}. \end{aligned} \quad (\text{A.9})$$

A more explicit form of J-MMSE equalization filter in terms of total channel matrix responses and SNRs can be obtained through direct evaluation of (A.8), which yields

$$\tilde{\mathbf{W}}_{MMSE}(k) = \begin{bmatrix} \left(\Xi^{-1}(k) \begin{bmatrix} G_D^{i*}(k) \\ G_M^m(-k) \end{bmatrix} \right)^T \\ \left(\Xi^{-1}(k) \begin{bmatrix} G_M^{i*}(k) \frac{\Upsilon^m(-k)}{\Upsilon^i(k)} \\ G_D^m(-k) \frac{\Upsilon^m(-k)}{\Upsilon^i(k)} \end{bmatrix} \right)^T \end{bmatrix} \quad (\text{A.10})$$

where $\Xi(k)$ is defined in (A.11). Notice also that in case of multi-antenna receiver with N_{RX} antennas, if one assumes that the noise power is identical in each receiver, it results in $\mathbf{R}_{\mathbf{NN}} = \sigma_n^2 \mathbf{I}$ and thus the general J-MMSE equalizer in (A.7) can be re-expressed as

$$\tilde{\mathbf{W}}_{MMSE}(k) = \left(\tilde{\mathbf{G}}_{SIMO}^H(k) \tilde{\mathbf{G}}_{SIMO}(k) + \Lambda_{SNR}^{-1}(k) \right)^{-1} \times \tilde{\mathbf{G}}_{SIMO}^H(k). \quad (\text{A.12})$$

This can be manipulated further and finally expressed in a form similar to (A.10) or (A.11), incorporating the effects of

all effective channels between the UE transmitters and parallel receiver antennas.

This concludes the proof and derivations.

REFERENCES

- [1] *Wireless LAN medium access control (MAC) and physical layer (PHY) specifications: high speed physical layer in 2.4 GHz band*, IEEE, April 1999.
- [2] *IEEE standard for local and metropolitan area networks part 16: air interface for fixed broadband wireless access systems*, IEEE 802.16, 2004.
- [3] U. Ladebusch, C. A. Liss, "Terrestrial DVB (DVB-T): A broadcast technology for stationary portable and mobile use," *Proc. IEEE*, vol.94, no.1, pp.183-193, Jan. 2006.
- [4] G. Faria, J. A. Henriksson, E. Stare, and P. Talmola, "DVB-H: digital broadcast services to handheld devices," *Proc. IEEE*, vol.94, no.1, pp.194-209, Jan. 2006.
- [5] A. B. Ericsson, "Long term evolution (LTE): an introduction," *White paper*, Oct. 2007.
- [6] J. Zyren, "Overview of the 3GPP long term evolution physical layer," *White Paper*, July 2007.
- [7] S. Sesia, I. Toufik, and M. Baker, *LTE - The UMTS Long Term Evolution: From Theory to Practice*, Chichester: Wiley, 2009.
- [8] F. E. A. El-Samie, F. S. Al-kamali, Z. Y. Al-Nahari, and M. I. Dessouky, *SC-FDMA for Mobile Communications*, CRC press, 2013.
- [9] "Evolved Universal Terrestrial Radio Access (E-UTRA); User Equipment (UE) Radio Transmission and Reception," 3GPP Tech. Spec. V10.3.0, Release 10, Tech. Spec. TS36.101, Nov. 2013.
- [10] "Evolved Universal Terrestrial Radio Access (E-UTRA); User Equipment (UE) Conformance Specification; Radio Transmission and Reception" 3GPP Tech. Spec. V11.2.0, Release 11, Tech. Spec. TS36.521-1, Oct. 2013.
- [11] "Evolved Universal Terrestrial Radio Access (E-UTRA); Physical Channels and Modulation," 3GPP Tech. Spec. Group Radio Access Network, V9.1.0, Release 9, Tech. Spec. TS36.211, March 2010.
- [12] "Evolved Universal Terrestrial Radio Access (E-UTRA); Base Station (BS) Transmission and Reception," 3GPP Tech. Spec. V10.2.0, Release 10, Tech. Spec. TS36.104, May 2011.
- [13] S. Mirabbasi and K. Martin, "Classical and modern receiver architectures," *IEEE Commun. Mag.*, vol. 38, no. 11, pp. 132-139, Nov. 2000.
- [14] A. A. Abidi, "Direct-conversion transceivers for digital communications," *IEEE J. Solid-State Circuits*, vol. 30, no. 12, pp. 1399-1410, Dec. 1995.
- [15] A. Tarighat and A. H. Sayed, "Joint compensation of transmitter and receiver impairments in OFDM systems," *IEEE Trans. Wireless Commun.*, vol. 6, no. 1, pp.240-247, Jan. 2007.
- [16] Y. H. Chung, and S. M. Phoong, "Joint estimation of transmitter and receiver I/Q imbalances, CFO, and channel response for OFDM systems," in *Proc. Int. Conf. Green Circuits and Systems (ICGCS)*, pp. 247-252, June 2010.
- [17] A. Kiayani, L. Anttila, Y. Zou, and M. Valkama, "Advanced receiver design for mitigating multiple RF impairments in OFDM systems: algorithms and RF measurements," *J. of Elect. Comput. Eng.*, vol. 2012.
- [18] H. A. Mahmoud, H. Arslan, M. K. Ozdemir, and F. E. Retnasothie, "IQ imbalance correction for OFDMA uplink systems," in *Proc. IEEE Int. Conf. Commun. (ICC)*, pp. 1-5, June 2009.
- [19] Y. Yoshida, K. Hayashi, H. Sakai, and W. Bocquet, "Analysis and compensation of transmitter IQ imbalances in OFDMA and SC-FDMA Systems," *IEEE Trans. Signal Process.*, vol. 57, no. 8, pp. 3119-3129, Aug. 2009.
- [20] R. Liu, X. Li, L. Ding, and X. Gao, "Low complexity turbo equalization for LTE uplink with transmitter IQ imbalance," in *Proc. Int. Conf. Wireless Commun. and Signal Process. (WCSP'10)*, pp. 1-6, Oct. 2010.
- [21] L. Anttila, M. Valkama, and M. Renfors, "3.9G Radio reception with SC-FDMA waveforms under I/Q imbalance," in *Proc. IEEE Int. Symp. Circuits and Syst. (ISCAS)*, pp. 25-28, May 2007.

- [22] A. Kiayani, L. Anttila, and M. Valkama, "Mobile transmitters I/Q imbalances in LTE uplink: Analysis and digital mitigation," in *Proc. IEEE Int. Conf. Commun. Syst. (ICCS)*, pp. 125-129, Nov. 2012.
- [23] A. Gomaa and N. Al-Dhahir, "Multi-user SC-FDMA systems under IQ imbalance: EVM and subcarrier mapping impact," in *Proc. IEEE Global Telecommun. Conf.(GLOBECOM)*, pp. 1-5, Dec. 2011.
- [24] M. Marey and N. Steendam, "Novel Data Detection and Channel Estimation Algorithms for BICM-OFDMA Uplink Asynchronous Systems in the Presence of IQ Imbalance," *IEEE Trans. Wireless Commun.*, vol. 13, no. 5, pp. 2706-2716, May 2014.
- [25] A. Gomaa and N. Al-Dhahir, "SC-FDMA performance in presence of oscillator impairments: EVM and subcarrier mapping impact," in *Proc. IEEE Global Telecommun. Conf.(GLOBECOM)*, pp. 1-5, Dec. 2011.
- [26] M. Morelli, "Timing and frequency synchronization for the uplink of an OFDMA system," *IEEE Trans. Commun.*, vol. 52, no. 2, pp. 296-306, Feb. 2004.
- [27] X. P. Zhang and H. G. Ryu, "Suppression of ICI and MAI in SC-FDMA communication system with carrier frequency offsets," *IEEE Trans. Consum. Electron.*, vol. 56, no. 2, pp. 359-365, May 2010.
- [28] L. Anttila and M. Valkama, "On circularity of receiver front-end signals under RF impairments," in *Proc. European Wireless Conf.*, pp. 1-8, April 2011.
- [29] A. Yamaoka, K. Yamaguchi, T. Kato, Y. Tanabe, "Experimental performance evaluation of IQ imbalance and DC offset estimation and compensation technique for 3GPP LTE base station," in *Proc. 2010 IEEE MTT-S Intl. Microwave Symposium Digest (MTT)*, pp. 268-271, May 2010.
- [30] T. B. Sorensen, P. E. Mogensen, and F. Frederksen, "Extension of the ITU channel models for wideband (OFDM) systems," in *Proc. IEEE Veh. Technology Conf. (VTC'05)*, pp. 392-396, Sept. 2005.
- [31] X. Li and C. Tong, "DSP implementation of DMRS in PUSCH within the LTE system," in *Proc. Intl. Conf. Bus. Computing and Global Informatization (BCGIN'11)*, pp. 528-531, July 2011.
- [32] Y. Zhang, Q. Yin, and W. Han, "Piece-wise polynomial approximation based channel estimation for high-mobility OFDM," in *Proc. IEEE Int. Conf. Comm. (ICC'10)*, pp. 1-4, June 2011.
- [33] M. Unser, "Splines: a perfect fit for signal and image processing," *IEEE Signal Processing Mag.*, vol. 16, no. 6, pp. 22-38, Nov. 1999.
- [34] N. Mai, Y. V. Zakharov, and A. G. Burr, "Iterative channel estimation based on B-splines for fast flat fading channels," *IEEE Trans. Wireless Commun.*, vol. 6, no. 4, pp. 1224-1229, April 2007.
- [35] Y. V. Zakharov, and T. C. Tozer, "Local spline approximation of time-varying channel model," *Electron. Lett.*, vol. 37, no. 23, pp. 1408-1409, Nov. 2001.
- [36] R. N. Khal, Y. V. Zakharov, and J. Zhang, "B-spline based joint channel and frequency offset estimation in doubly-selective fading channels," in *Proc. IEEE Int. Conf. Acoustic Speech and Signal Process. (ICASSP'10)*, pp. 3214-3217, March 2010.
- [37] D. K. Borah and B. D. Hart, "Frequency-selective fading channel estimation with a polynomial time-varying channel model," *IEEE Trans. Commun.*, vol. 47, no. 6, pp. 862-873, June 1999.
- [38] L. S. Scharf, *Statistical Signal Processing*, Reading, MA: Addison-Wesley, 1991.
- [39] C. Boor, *A Practical Guide to Splines*, New York: Springer-Verlag, 1978.
- [40] S. Haykin, *Adaptive Filter Theory*, 4th ed. Upper Saddle River, NJ: Prentice-Hall, 2002.
- [41] S. M. Kay, *Fundamentals of Statistical Signal Processing: Estimation Theory*, Upper Saddle River, NJ: Prentice-Hall, 1993.
- [42] G. Golub and C. F. Van Loan, *Matrix Computations*, Johns Hopkins University Press, 3rd edition, 1996.



Adnan Kiayani was born in Rawalpindi, Pakistan, on December 17, 1985. He received the B. Sc degree in Electrical Engineering from COMSATS Institute of Information Technology, Islamabad, Pakistan, in 2006, and the M. Sc. degree (with honors) in Radio Frequency (RF) Electronics from Tampere University of Technology (TUT), Tampere, Finland, in 2009. He is currently a doctoral student in the Department of Electronics and Communications Engineering at TUT. His general research interests include analysis and signal processing algorithms for RF impairments mitigation in modern radio systems, and currently his research work focuses on the self-interference cancellation in frequency division duplex (FDD) transceivers.



Lauri Anttila received the M.Sc. degree and D.Sc. (Tech) degree (with honors) in electrical engineering from Tampere University of Technology (TUT), Tampere, Finland, in 2004 and 2011. Currently, he is a postdoctoral research fellow at the Department of Electronics and Communications Engineering at TUT. He has published over 40 articles in international peer-reviewed journals and conferences, as well as two book chapters. His research interests include statistical and adaptive signal processing for communications, digital front-end signal processing

in flexible radio transceivers, power-efficient transmitter structures, and full-duplex radio systems.



Yaning Zou received her Bachelor Degree in communications engineering from University Electronic Science and Technology of China (UESTC), Chengdu, China, in 2002, and the M.Sc. and Ph.D. Degrees in electrical engineering from Tampere University of Technology (TUT), Tampere, Finland, in 2005 and 2009, respectively. She was a visiting researcher with DICE GmbH, Linz, Austria, in 2008, and Vodafone Chair Mobile Communication Systems, Technical University of Dresden, Germany, in 2013. Currently, she continues to work as research fellow at the Department of Electronics and Communications Engineering in TUT. Her current research interests are in efficient transceiver design and algorithm development for meeting RF/antenna implementation challenges in different multi-antenna systems.



Mikko Valkama was born in Pirkkala, Finland, on November 27, 1975. He received the M.Sc. and Ph.D. Degrees (both with honors) in electrical engineering (EE) from Tampere University of Technology (TUT), Finland, in 2000 and 2001, respectively. In 2002, he received the Best Ph.D. Thesis -award by the Finnish Academy of Science and Letters for his dissertation entitled "Advanced I/Q signal processing for wideband receivers: Models and algorithms". In 2003, he was working as a visiting researcher with the Communications Systems and Signal Processing

Institute at SDSU, San Diego, CA. Currently, he is a Full Professor and Department Vice-Head at the Department of Electronics and Communications Engineering at TUT, Finland. He has been involved in organizing conferences, like the IEEE SPAWC'07 (Publications Chair) held in Helsinki, Finland. His general research interests include communications signal processing, estimation and detection techniques, signal processing algorithms for software defined flexible radios, cognitive radio, full-duplex radio, radio localization, 5G mobile cellular radio, digital transmission techniques such as different variants of multicarrier modulation methods and OFDM, and radio resource management for ad-hoc and mobile networks.

Tampereen teknillinen yliopisto
PL 527
33101 Tampere

Tampere University of Technology
P.O.B. 527
FI-33101 Tampere, Finland

ISBN 978-952-15-3598-7
ISSN 1459-2045